



UNIVERSIDADE FEDERAL DE SANTA CATARINA
CENTRO TECNOLÓGICO
PROGRAMA DE PÓS-GRADUAÇÃO EM ENGENHARIA MECÂNICA

LUCAS MEIRELLES PEREIRA

**HIGH-FIDELITY NUMERICAL SIMULATIONS OF
ACOUSTIC LINERS UNDER GRAZING FLOW**

FLORIANÓPOLIS

2023

Lucas Meirelles Pereira

**HIGH-FIDELITY NUMERICAL SIMULATIONS OF ACOUSTIC LINERS
UNDER GRAZING FLOW**

Dissertação submetida ao Programa de Pós-Graduação em Engenharia Mecânica da Universidade Federal de Santa Catarina como requisito parcial para a obtenção do Grau de Mestre em Engenharia Mecânica.

Orientador: Prof. Andrey R. da Silva, Ph.D.

Coorientador: Prof. Júlio A. Cordioli, Dr.Eng.

Florianópolis

2023

Ficha de identificação da obra elaborada pelo autor,
através do Programa de Geração Automática da Biblioteca Universitária da UFSC.

Pereira, Lucas Meirelles

High-Fidelity Numerical Simulations of Acoustic Liners
Under Grazing Flow / Lucas Meirelles Pereira ; orientador,
Andrey Ricardo da Silva, coorientador, Júlio Apolinário
Cordioli, 2023.

162 p.

Dissertação (mestrado) - Universidade Federal de Santa
Catarina, Centro Tecnológico, Programa de Pós-Graduação em
Engenharia Mecânica, Florianópolis, 2023.

Inclui referências.

1. Engenharia Mecânica. 2. Simulações de Alta Fidelidade.
3. Método de Lattice Boltzmann. 4. Liners Acústicos. 5.
Escoamento Tangencial. I. Silva, Andrey Ricardo da. II.
Cordioli, Júlio Apolinário. III. Universidade Federal de
Santa Catarina. Programa de Pós-Graduação em Engenharia
Mecânica. IV. Título.

Lucas Meirelles Pereira

High-Fidelity Numerical Simulations of Acoustic Liners under Grazing Flow

O presente trabalho em nível de mestrado foi avaliado e aprovado por banca examinadora composta pelos seguintes membros:

Prof. Andrey Ricardo da Silva, Ph.D.
Universidade Federal de Santa Catarina

Prof. Francesco Avallone, Ph.D.
Politecnico di Torino

Paul B. Murray, Ph.D.
University of Southampton

Certificamos que esta é a **versão original e final** do trabalho de conclusão que foi julgado adequado para obtenção do título de Mestre em Engenharia Mecânica.

Prof. Henrique Simas, Dr. Eng.
Coordenador do Programa

Prof. Andrey R. da Silva, Ph.D.
Orientador

Florianópolis, 2023.

A quem me apoiou.

ACKNOWLEDGEMENTS

I would like to address a few words to my family and friends. For that reason, some of the following paragraphs are written in Portuguese.

Sou grato por ter tido o apoio e a compreensão da minha família e dos meus amigos para que eu pudesse conduzir o mestrado. Este documento sintetiza os dois anos de trabalho dedicados a esta causa.

Agradeço aos meus pais e irmãos, em especial, pelo suporte e pela compreensão. Particularmente, sou grato a meu pai por ter me ajudado a estabelecer um novo lar em Florianópolis.

Me empenhar para concluir o mestrado foi mais fácil porque encontrei o amor no caminho. Obrigado, Carolina, por tornar meus dias mais leves.

Agradeço à minha madrinha Geruza pelas palavras e atitudes de incentivo durante o mestrado.

Aos amigos que fiz nesta trajetória, deixo meu muito obrigado. O grupo de aeroacústica do LVA e seus agregados foram parte fundamental neste processo. Em especial, agradeço ao Bonomo pela parceria e por todo o auxílio técnico, ao Nicolas por manter o Sol presente em nossas vidas e por todos os dados experimentais fornecidos, ao Colombo pelos momentos de descontração e de reflexão, e à Racquel, que me apoiou nesta caminhada desde o primeiro até o último dia do mestrado.

Agradeço aos professores, mestres e doutores que contribuíram para que eu chegasse até aqui. Em especial, sou grato aos professores Andrey Ricardo da Silva e Júlio Apolinário Cordioli, da Universidade Federal de Santa Catarina, pela orientação e pela oportunidade de fazer parte deste projeto. Ademais, agradeço aos professores Marco Túlio Santana Alves e Armando Sá Ribeiro Júnior, da Universidade Federal da Bahia, pelos conselhos que guiaram minha vida acadêmica. Agradeço também a Ronei Maciel, amigo e peça fundamental nesta caminhada. A todos, obrigado por confiarem em meu potencial.

Thank you, Prof. Francesco Avallone, for all the hours spent teaching me how to handle PowerFLOW. Also, thank you for this partnership and for believing in my work.

This work is part of the scope of a collaboration project between the Laboratory of Vibration and Acoustics (LVA) at UFSC (Brazil) and Delft University of Technology (The Netherlands). This study was financed in part by the Coordenação de Aperfeiçoamento de Pessoal de Nível Superior – Brasil (CAPES) – Finance Code 001. The author acknowledges

the AeroAcoustics Research Consortium (AARC) for supporting this work financially. The author acknowledges PRACE for awarding access to Prometheus at PSNC@CYFRONET, Poland. The author acknowledges the support from the Research Laboratories for Emerging Technologies in Cooling and Thermophysics (UFSC). The experimental data used in this work was obtained from equipment partially financed by the Brazilian funding agencies Conselho Nacional de Desenvolvimento Científico e Tecnológico (CNPq) and Financiadora de Estudos e Projetos (FINEP).

“I am an old man now, and when I die and go to Heaven there are two matters on which I hope enlightenment. One is quantum electro-dynamics and the other is turbulence of fluids. About the former, I am really rather optimistic.”

(Sir Horace Lamb, 1932) ([GOLDSTEIN, 1969](#))

RESUMO

Liners acústicos são soluções amplamente adotadas para redução efetiva de ruído em motores aeronáuticos modernos do tipo *turbofan*. A caracterização dos *liners* é usualmente realizada por meio de sua impedância acústica, em bancadas para testes de *liners* com indução de escoamento de ar tangencial à amostra. O escoamento tangencial de ar influencia significativamente os mecanismos de dissipação de energia acústica dos *liners*. Diferentes técnicas de medição da impedância podem ser aplicadas nas bancadas de testes, sendo que algumas (denominadas técnicas de educação) representam o *liner* como uma condição de contorno localmente reativa. Publicações anteriores exibiram uma dependência aparente da impedância educida em relação à direção de propagação relativa entre a onda sonora e o escoamento tangencial, o que viola a hipótese localmente reativa. Embora esta violação tenha sido atribuída a uma falha da condição de contorno utilizada, um comportamento semelhante foi observado em medições realizadas com outra técnica, que não emprega nenhuma condição de contorno. Isto sugere que os mecanismos reativos e dissipativos dos *liners* nem sempre são independentes da direção de propagação da onda sonora, e questiona a hipótese localmente reativa. Além disso, questiona-se a representatividade da física de dissipação do *liner* nos modelos existentes. Na tentativa de contribuir ao conhecimento sobre a interação entre escoamento e perturbação sonora e sobre o comportamento não-linear dos *liners*, este trabalho busca desenvolver um modelo de simulação de alta fidelidade para *liners* acústicos na presença de um escoamento tangencial turbulento, através da abordagem de simulações de grandes escalas. Para tanto, um *solver* comercial do método de lattice Boltzmann é utilizado para modelar explicitamente *liners* tridimensionais de múltiplas cavidades, no domínio do tempo. A impedância acústica é medida com diferentes técnicas (a técnica *in-situ*, o método do acoplamento modal e o algoritmo de Kumaresan-Tufts), na ausência e na presença de escoamento tangencial subsônico, considerando diferentes frequências, níveis de pressão sonora e posições da fonte acústica. Os resultados das simulações são comparados com dados experimentais e com predições de um modelo semiempírico, e apresentam concordância razoável na ausência de escoamento. Na presença de escoamento, o modelo numérico captura o aumento da resistência característico deste cenário, embora superestime consideravelmente os dados de referência. A convergência dos resultados numéricos em relação ao refino da malha sugere que uma melhor discretização do modelo pode melhorar a sua concordância com os valores de referência. Ademais, a representação adequada da geometria dos orifícios da amostra real se mostra fundamental para a reprodução dos resultados experimentais de impedância no modelo. Ainda assim, o modelo captura de forma satisfatória as tendências da impedância em função da frequência e pode ser considerado útil para a avaliação da interação entre escoamento e perturbação sonora nas regiões próximas aos orifícios, onde a dissipação de energia acústica acontece majoritariamente. A análise da velocidade induzida pela onda sonora nos orifícios sugere que a porcentagem de área aberta efetiva, onde a oscilação fluidodinâmica acontece em resposta da perturbação acústica, é drasticamente reduzida pelo efeito do escoamento tangencial. Ademais, a velocidade acusticamente induzida nos orifícios, diretamente relacionada à impedância do *liner*, exibe pouca dependência da direção de propagação acústica em relação ao escoamento.

Palavras-chave: Simulações de alta fidelidade. Método de lattice Boltzmann. *Liners* acústicos. Impedância acústica. Escoamento tangencial.

RESUMO EXPANDIDO

Introdução

O ruído proveniente de operações com aeronaves comerciais afeta negativamente comunidades em todo o mundo, principalmente em zonas adjacentes a aeroportos. Os níveis admissíveis para o ruído gerado pelas aeronaves são definidos com base nas diretrizes da Organização da Aviação Civil Internacional, que considera a redução do ruído emitido pela fonte como medida prioritária. Uma das fontes sonoras mais proeminentes em aeronaves comerciais modernas é o motor *turbofan*, cujo ruído possui forte característica tonal, ou seja, cuja energia sonora se concentra em faixas estreitas de frequência. Por este motivo, é comum que as paredes internas das naceles dos motores *turbofan* sejam revestidas por painéis acústicos chamados *liners*. Estes painéis são particularmente eficientes na atenuação de ruídos tonais, e sua construção tipicamente consiste em uma placa perfurada, exposta ao escoamento gerado pelo motor, separada de uma placa sólida por um núcleo em forma de colmeia. Matematicamente, os *liners* são modelados como uma superfície localmente reativa e são caracterizados por sua impedância acústica. Entretanto, sua caracterização é uma tarefa complexa, já que sua impedância varia de acordo com as condições de operação, como a velocidade do escoamento tangencial. Por este motivo, é comum que os *liners* sejam caracterizados em bancadas experimentais especiais, que possibilitam a determinação da impedância na presença de escoamento tangencial sobre a placa perfurada da amostra. Diferentes técnicas podem ser aplicadas para determinação da impedância, sendo que um grupo de técnicas denominadas "métodos de educação de impedância" são comumente empregadas. Contudo, estes métodos necessitam de condições de contorno para a representação do *liner*, e conseqüentemente para o cálculo de sua impedância. Recentemente, discrepâncias foram verificadas em experimentos realizados com *liners* sujeitos a escoamento tangencial: verificou-se uma dependência aparente da impedância eduzida em função da direção de propagação relativa entre a onda sonora e o escoamento, o que viola a hipótese localmente reativa. Embora esta violação tenha sido atribuída a uma falha da condição de contorno utilizada, um comportamento semelhante foi observado em medições realizadas com outra técnica, que não emprega nenhuma condição de contorno. Isto sugere que os mecanismos reativos e dissipativos dos *liners* podem não serem independentes da direção de propagação da onda sonora, e questiona a hipótese localmente reativa. Além disso, questiona-se a representatividade da física de dissipação do *liner* nos modelos matemáticos existentes. Neste contexto, simulações numéricas de alta fidelidade podem contribuir para esclarecer a interação entre escoamento tangencial e perturbações acústicas, principalmente na placa perfurada dos *liners*, onde a maior parte da energia acústica é dissipada.

Objetivos

Diversos trabalhos envolvendo simulações numéricas de *liners* acústicos estão disponíveis na literatura. Embora estes trabalhos tenham contribuído de forma significativa para o conhecimento sobre a física que envolve a dissipação de energia acústica nos *liners*, nenhum deles apresentou resultados de um *liner* tridimensional com múltiplas cavidades, simulado explicitamente na presença de escoamento tangencial. Isto impediu a investigação das discrepâncias encontradas nos resultados de impedância obtidos pelos métodos de educação, como também limitou o estudo de *liners* representativos com múltiplas cavidades. Desta forma, o principal objetivo deste trabalho é a avaliação da impedância acústica de um *liner* tridimensional com múltiplas cavidades na presença de escoamento turbulento tangencial subsônico, através de simulações numéricas de alta fidelidade.

Metodologia

Inicialmente, este trabalho apresenta uma breve revisão bibliográfica contemplando a teoria básica de *liners* acústicos e métodos experimentais para determinação de sua impedância acústica. A revisão aborda ainda modelos semiempíricos aplicados a *liners* e trabalhos envolvendo simulações numéricas encontrados na literatura, que serviram de base para o desenvolvimento deste documento. No presente trabalho apresenta-se um modelo computacional desenvolvido em um software comercial de fluidodinâmica, baseado no método de lattice Boltzmann. O software emprega a equação de lattice Boltzmann em um espaço de velocidades tridimensional, discretizado em 19 direções. Utiliza-se a aproximação de Bhatnagar, Gross e Krook para modelagem do operador de colisão da equação de Boltzmann. Para solução das escalas turbulentas, emprega-se uma abordagem de simulação de grandes escalas, enquanto as escalas de submalha são levadas em consideração por um modelo de turbulência de duas equações, incorporado ao tempo de relaxação do modelo de lattice Boltzmann. O software utiliza ainda um modelo de parede para consideração da condição de não escorregamento na subcamada limite viscosa. O modelo foi construído para replicar parcialmente as condições de escoamento encontradas na bancada de testes de *liners* acústicos da Universidade Federal de Santa Catarina, onde dados experimentais de impedância foram obtidos para a validação dos resultados numéricos. Para o cálculo da impedância, diferentes métodos foram considerados em ambos os experimentos e simulações, sendo estes: a técnica *in-situ*, o método do acoplamento modal e o algoritmo de Kumaresan-Tufts. Simulações foram realizadas na ausência e na presença de escoamento tangencial subsônico, considerando diferentes frequências, níveis de pressão sonora e posições da fonte acústica. Além disto, diferentes níveis de discretização foram aplicadas ao modelo para avaliação da convergência dos resultados.

Resultados e Discussão

Os resultados obtidos para a impedância na ausência de escoamento tangencial mostram boa correlação aos dados de referência. Verificou-se convergência de malha para uma discretização de pelo menos 20 elementos ao longo do orifício do *liner*. Os efeitos não-lineares causados pela incidência de altos níveis de pressão sonora na amostra são capturados pelo modelo computacional. As diferentes técnicas de medição da impedância entregam resultados ligeiramente divergentes, especialmente em regime não-linear, em ambos os experimentos e simulações. Por outro lado, na presença de escoamento tangencial os resultados numéricos apresentaram boa correlação com os dados de referência apenas para a reatância, já que a resistência foi consideravelmente superestimada. Entretanto, as simulações foram capazes de capturar o principal efeito do escoamento tangencial sobre a placa perfurada, que se traduz em um aumento significativo da resistência do *liner*. As simulações numéricas realizadas na presença de escoamento tangencial consideraram uma resolução máxima entre 40 e 50 elementos ao longo do orifício do *liner*, que não foram suficientes para verificação da convergência de malha nestes casos. Os resultados sugerem que futuras investigações com este modelo são necessárias considerando níveis ainda maiores de discretização, que podem contribuir para melhor correlação entre os resultados numéricos e os dados de referência. No entanto, imagens obtidas por microscopia óptica da amostra de referência testada na bancada experimental revelaram que as bordas dos orifícios são arredondadas, o que não foi considerado originalmente no modelo. Simulações adicionais, realizadas com nível de discretização moderado e considerando as bordas dos orifícios arredondadas, evidenciaram que os resultados de impedância são altamente sensíveis a estas particularidades da geometria. Para estes casos, houve redução drástica da

resistência medida, o que sugere que a representação mais adequada da geometria do *liner* no modelo pode contribuir significativamente para a correlação dos resultados numéricos aos dados experimentais. Ademais, as simulações foram capazes de capturar a física de interação entre escoamento tangencial e perturbações acústicas. Os resultados numéricos obtidos se mostraram sensíveis à posição relativa da fonte sonora em relação ao *liner* e ao escoamento, reproduzindo tendências obtidas experimentalmente. A análise dos perfis de escoamento induzidos nos orifícios pelas perturbações sonoras, diretamente relacionada à impedância do *liner*, sugere pouca dependência da direção de propagação acústica em relação ao escoamento. Contudo, esta análise possibilitou a verificação de que a possível causa do aumento de resistência do *liner* induzido pela presença do escoamento tangencial sobre a amostra é a redução da área aberta efetiva, onde a oscilação fluidodinâmica acontece em resposta da perturbação acústica. Ademais, verificou-se que o fluxo de massa induzido no orifício pela perturbação acústica é função da frequência incidente quando não há escoamento tangencial. Em contrapartida, além de reduzir o fluxo de massa em termos absolutos, a presença do escoamento tangencial praticamente elimina sua dependência em relação à frequência. Resultados locais de impedância calculados numericamente na placa perfurada evidenciam que a impedância do *liner* varia consideravelmente no espaço, não somente entre diferentes cavidades, mas também em uma mesma cavidade. Isto foi verificado para casos na ausência e na presença de escoamento, destacando que resultados obtidos localmente não são representativos de toda a amostra. Além disso, observou-se que a reatância, particularmente, exibe tendências que variam em função da posição da fonte sonora, tanto nos resultados numéricos quanto em dados experimentais.

Considerações Finais

Este trabalho apresenta resultados de simulações numéricas de alta fidelidade para a impedância acústica de *liners* aeronáuticos na ausência e na presença de escoamento subsônico tangencial. Os resultados numéricos são obtidos por três técnicas diferentes, as quais também são empregadas na bancada experimental utilizada como referência para análise da precisão do modelo computacional. Os efeitos da frequência, nível de pressão sonora e posição da fonte são investigados. O modelo fornece resultados representativos dos dados de referência, embora não seja verificada concordância razoável em termos absolutos para todos os casos estudados. Entretanto, evidências sugerem que estas discordâncias podem ser resultado de uma representação inapropriada da real geometria de referência. Ainda assim, o modelo é capaz de fornecer informações importantes sobre a interação local entre escoamento tangencial e perturbação acústica, embora não sejam verificadas evidências sólidas que justifiquem a discrepância entre impedâncias obtidas para diferentes posições relativas da fonte sonora. Para possíveis trabalhos futuros, sugere-se: (i) a realização de simulações com fontes sonoras de banda-larga; (ii) simulações considerando um *liner* de maior comprimento, na tentativa de melhorar a acurácia dos resultados em baixas frequências; (iii) a melhoria do método de imposição da perturbação acústica no domínio da simulação, de modo a reduzir o custo computacional e aumentar o tempo de amostragem; (iv) a avaliação do efeito de diferentes perfis de camada-limite do escoamento tangencial no escoamento induzido pelas perturbações acústicas dentro dos orifícios; (v) simulação de um *liner* devidamente caracterizado em termos da forma de seus orifícios.

Palavras-chave: Simulações de alta fidelidade. Método de lattice Boltzmann. *Liners* acústicos. Impedância acústica. Escoamento tangencial.

ABSTRACT

Acoustic liners have become a widely adopted technological solution for effectively reducing noise in modern turbofan engines. The characterization of liners in terms of their impedance is commonly performed in grazing flow testing facilities, as the grazing flow significantly influences the acoustic dissipation mechanisms of the liner. Different impedance measurement techniques can be employed for the characterization of the liner, some of which represent it as a locally-reactive impedance boundary condition, named eduction methods. Several works have shown apparent dependence of the educed impedance on the direction of acoustic propagation relative to the grazing flow, which violates the locally-reactive hypothesis. Although it has been argued that a failure in the boundary conditions is the cause for this dependence, it has also been recently observed with other techniques, which do not consider any boundary condition. This suggests that the liners' reactive and dissipative mechanisms might not always be independent of the wave propagation direction, and questions the locally-reactive hypothesis. Furthermore, it is questionable whether the liner's physics in the presence of grazing flow is properly captured by existing models. In the attempt to provide insights into the flow-acoustics interaction and non-linear behaviour of liners, this work focuses on the development of a high-fidelity numerical model for acoustic liners in the presence of a turbulent grazing flow, with a very large eddy simulation approach. For this purpose, a commercial lattice Boltzmann solver is employed to model explicitly three-dimensional multi-cavity liners in the time domain. The acoustic impedance is assessed by different techniques (the in-situ technique, the mode matching method and the Prony-like Kumaresan-Tufts algorithm), both in the absence and in the presence of a subsonic grazing flow, considering different frequencies, sound pressure levels and acoustic source positions. The simulation results are compared with experimental data and with predictions from a semiempirical model, and present reasonable agreement for the cases in which the mean flow is absent. When the grazing flow is present, the model is sensitive enough to capture the increase in resistance, although it overestimates considerably the reference data. The convergence trends of the numerical results regarding the grid refinement suggest that increasing the resolution might improve the simulation results in the presence of grazing flow. Moreover, it is fundamental to accurately incorporate the actual geometry of the liner's orifices into the model in order to achieve good agreement between numerical and experimental results. Nevertheless, the model adequately captures the impedance trends with respect to frequency. As a result, it is a valuable tool for assessing the flow-acoustics interactions in the near-orifice regions, where the main acoustic dissipation takes place. The assessment of the acoustic-induced velocity inside the liner's orifices reveals that the effective open area, where the oscillating flow movement occurs in response to incident acoustic waves, is drastically reduced by the effect of grazing flow. Furthermore, the acoustic-induced velocity profiles inside the orifices, which are directly related to the liner's impedance, show little dependence on the direction of propagation of the acoustic waves relative to the grazing flow.

Keywords: High-fidelity simulations. Lattice Boltzmann method. Acoustic liners. Acoustic impedance. Grazing flow.

LIST OF FIGURES

Figure 1 – Relevant noise sources of conventional mid-range transport aircraft.	27
Figure 2 – Typical turbofan engine: locations where acoustic liners are installed.	28
Figure 3 – Typical single degree of freedom acoustic liner.	29
Figure 4 – Main acoustic energy dissipation mechanisms within liners.	34
Figure 5 – Drainage holes located at the bottom of the honeycomb cells.	35
Figure 6 – Typical impedance plot for acoustic liners.	37
Figure 7 – Schematic representation of the UFSC liner test rig.	39
Figure 8 – Energy dissipation mechanisms under high sound pressure level excitation.	45
Figure 9 – Typical lattice Boltzmann numerical model of grazing flow test rigs.	47
Figure 10 – Impedance predictions for a liner reported in previous literatures.	49
Figure 11 – Steady mean flow inside the resonator: vortical regions.	50
Figure 12 – Self-noise generation mechanism.	51
Figure 13 – Schematic of the triple decomposition of the velocity field.	54
Figure 14 – Schematic application of the in-situ technique.	57
Figure 15 – Schematic of the mode matching method for impedance measurements.	59
Figure 16 – Schematic of the Prony’s algorithm for impedance measurements.	60
Figure 17 – UFSC liner test rig.	62
Figure 18 – Microphones in the UFSC liner test rig.	62
Figure 19 – Experimental setup for the in-situ measurements.	63
Figure 20 – Schematic of the location of the flow velocity assessments.	64
Figure 21 – Experimental assessment of the flow inside the UFSC test rig.	65
Figure 22 – Liner samples for the experimental testing campaign.	67
Figure 23 – Facesheets of the two samples tested.	67
Figure 24 – Position of the facesheet probes for the experimental tests.	68
Figure 25 – Lattice element from a D3Q19 numerical scheme.	70
Figure 26 – Typical surface boundary conditions for the lattice Boltzmann method.	73
Figure 27 – Periodic boundary condition for the lattice Boltzmann method.	73
Figure 28 – Variable resolution in the lattice grid.	73
Figure 29 – Comparison between real Sample B and the modelled one.	75
Figure 30 – Numerical models of the liner geometries.	75
Figure 31 – Computational domain for the simulations with Sample A.	76

Figure 32 – Turbulence trigger (zigzag strip).	76
Figure 33 – Artificial variation of the fluid’s viscosity in the absorbent regions.	77
Figure 34 – Computational domain for the simulations with Sample B.	78
Figure 35 – Variable resolutions of the Sample B numerical model.	78
Figure 36 – Position of the facesheet probes in the numerical models.	80
Figure 37 – Location and length of the streamwise measurement planes.	80
Figure 38 – Measurement planes for the simulations with Sample A.	81
Figure 39 – Measurement planes for the simulations with Sample B.	81
Figure 40 – Acoustic harmonic perturbations superimposed in the simulations.	82
Figure 41 – Impedance results for $M = 0$ cases with different SPLs (Sample A).	86
Figure 42 – Turbulent boundary layer contour plot (Sample A).	89
Figure 43 – Assessment of the turbulent boundary layers for Sample A.	89
Figure 44 – Contour plot of the flow inside the cavities of Sample A.	91
Figure 45 – Impedance results for $M = 0.3$ cases with upstream source (Sample A).	93
Figure 46 – Up and downstream impedance results for $M = 0.3$ cases (Sample A).	95
Figure 47 – Effects of the grid resolution on the $M = 0.3$ results (Sample A).	97
Figure 48 – Convergence of the impedance results for $M = 0$ cases (Sample B).	99
Figure 49 – Impedance results for $M = 0$ cases with different SPLs (Sample B).	102
Figure 50 – Turbulent boundary layer contour plot (Sample B).	103
Figure 51 – Overview of the turbulent boundary layers for Sample B.	104
Figure 52 – Detail of the turbulent boundary layers for Sample B.	105
Figure 53 – Contour plots of the flow inside the cavities of Sample B.	106
Figure 54 – Convergence of the impedance results for $M = 0.32$ cases (Sample B).	108
Figure 55 – Schematic representation of the liner Sample B partially covered with speed tape.	109
Figure 56 – Effect of the liner length on the $M = 0.32$ experimental results.	110
Figure 57 – Up and downstream impedance results for $M = 0.32$ cases (Sample B).	111
Figure 58 – Computational cost of the acoustic simulations.	115
Figure 59 – Detail of the real liners’ orifice shapes.	116
Figure 60 – Alternative liner geometry with rounded orifice edges.	117
Figure 61 – Effect of the orifice shape on the impedance results for $M = 0$	118
Figure 62 – Effect of the orifice shape on the impedance results for $M = 0.32$	119
Figure 63 – Contour plots on the facesheet. $M = 0$ at 1400 Hz and 145 dB.	122

Figure 64 – Location of the facesheet probes along the sample for the line plots of SPL, resistance and reactance.	123
Figure 65 – Results along the liner length. $M = 0$ at 1400 Hz and 145 dB.	124
Figure 66 – Results along the liner length. $M = 0$ at 2000 Hz and 145 dB.	125
Figure 67 – Results along the liner length. $M = 0$ at 800 Hz and 145 dB.	125
Figure 68 – Sound pressure level close to the acoustic source and on the facesheet. .	126
Figure 69 – Predictions from the semiempirical model with corrected SPL values. .	127
Figure 70 – Sound pressure level along the liner length. $M = 0.32$ at 1400 Hz and 145 dB.	127
Figure 71 – Contour plots of the resistance on the facesheet. $M = 0.32$ at 1400 Hz and 145 dB.	128
Figure 72 – Contour plots of the reactance on the facesheet. $M = 0.32$ at 1400 Hz and 145 dB.	128
Figure 73 – Resistance along the liner length. $M = 0.32$ at 1400 Hz and 145 dB. . .	129
Figure 74 – Reactance along the liner length. $M = 0.32$ at 1400 Hz and 145 dB. . .	130
Figure 75 – Positions of the facesheet probes for the additional campaign.	130
Figure 76 – Experimental and numerical assessment of the effect of the facesheet probe on the impedance obtained for $M = 0$	131
Figure 77 – Effect of the facesheet probe location on the impedance obtained for $M = 0.32$ (upstream source).	132
Figure 78 – Effect of the facesheet probe location on the impedance obtained for $M = 0.32$ (downstream source).	132
Figure 79 – Contour plot of the acoustic-induced velocity magnitude. $M = 0$ at 1400 Hz and 145 dB.	133
Figure 80 – Contour plot of the acoustic-induced velocity magnitude. $M = 0.32$ at 1400 Hz and 145 dB.	134
Figure 81 – Contour plot of the y component of the acoustic-induced velocity at the most upstream cavity. 1400 Hz and 145 dB.	135
Figure 82 – Contour plot of the y component of the acoustic-induced velocity at the most downstream cavity. 1400 Hz and 145 dB.	136
Figure 83 – In-orifice velocity profiles at inflow and outflow cycles.	137
Figure 84 – Estimation of the discharge coefficient for different cases.	139
Figure 85 – Comparison of the estimated discharge coefficients with reference data.	140

Figure A.1–Two-dimensional model of the duct acoustic field.	159
Figure B.1–Contour plot of the y component of the acoustic-induced velocity at the most upstream cavity. 800 Hz and 145 dB.	161
Figure B.2–Contour plot of the y component of the acoustic-induced velocity at the most downstream cavity. 800 Hz and 145 dB.	161
Figure B.3–Contour plot of the y component of the acoustic-induced velocity at the most upstream cavity. 2000 Hz and 145 dB.	162
Figure B.4–Contour plot of the y component of the acoustic-induced velocity at the most downstream cavity. 2000 Hz and 145 dB.	162

LIST OF TABLES

Table 1 – Streamwise coordinates of the microphones used for the experimental impedance eduction procedures.	63
Table 2 – Geometric parameters of the liner samples tested experimentally.	67
Table 3 – Geometric parameters of the modelled liner samples.	75
Table 4 – Size of the finest elements considered in the simulations.	79
Table 5 – Global parameters and initial conditions for the simulations.	83
Table 6 – Test matrix for the simulations with both liner samples.	83
Table 7 – Characteristics of the turbulent boundary layers for Sample A.	90
Table 8 – Characteristics of the turbulent boundary layers for Sample B.	106
Table 9 – Computational cost of 15×10^{-3} seconds of simulation time with the Sample B setup.	115

LIST OF ABBREVIATIONS AND ACRONYMS

BC	boundary condition
BE	Boltzmann equation
BGK	Bhatnagar, Gross and Krook
BPF	blade-passage frequency
CFD	computational fluid dynamics
DNS	direct numerical simulation
GFIT	Grazing Flow Impedance Tube, at the NASA Langley Research Center
ICAO	International Civil Aviation Organization
KT	Kumaresan-Tufts
LVA	Laboratory of Vibration and Acoustics
LBM	lattice Boltzmann method
LEE	linearized Euler equations
LNSE	linearized Navier-Stokes equations
MM	mode matching
NASA	National Aeronautics and Space Administration
NIT	normal impedance tube
NSE	Navier-Stokes equation
POA	percentage of open area
PIV	particle image velocimeter
RANS	Reynolds averaged Navier-Stokes
RMS	root mean squared
RNG	Renormalization Group Theory

SDOF	single degree of freedom
SPL	sound pressure level
TBL	turbulent boundary layer
VLES	very large eddy simulation
VR	variable resolution
UFSC	Federal University of Santa Catarina

LIST OF SYMBOLS

Mathematical symbols

A	acoustic mode amplitude
C	BGK collision operator
C_D	discharge coefficient
C_μ	constant closure coefficient
\mathbf{c}	discrete particle velocity
$c_s = 1/\sqrt{3}$	isothermal speed of sound, lattice units
c_0	characteristic speed of sound in the air at 25°C, m s^{-1}
D	diameter of the inscribed circumference in the cavity, m
d	orifice diameter, m
\mathbf{f}	particle distribution function
f	frequency, Hz
f_c	transverse modes cut-on frequency, Hz
H	modelled channel's height, m
\tilde{H}	transfer function between facesheet and backplate pressures
h	cavity depth, m
$i = \sqrt{-1}$	imaginary unit
K	von Kármán constant
k	free-field wavenumber
L	liner sample length, m
\mathcal{L}	model's order
l	cavity width, m

M	channel's cross-sectional maximum streamwise flow Mach number
\overline{M}	channel's cross-sectional mean streamwise flow Mach number
\mathcal{M}	number of microphones in the lined section of the test rig
\mathcal{N}	model's maximum order
\mathbf{n}	facesheet normal unity vector
P_o	maximum amplitude of the acoustic pressure on the facesheet, Pa
p	acoustic pressure, Pa
\tilde{p}	complex acoustic pressure, Pa
Q	quality factor
q	number of microphones in each rigid section of the test rig
R	air's specific gas constant, $\text{J kg}^{-1} \text{K}^{-1}$
r	orifice radius, m
S	cross-sectional area of the orifice, m^2
T	local mean temperature, K
t	time, s
U	channel's cross-sectional streamwise flow velocity, m s^{-1}
\overline{U}	channel's cross-sectional mean streamwise flow velocity, m s^{-1}
U_∞	channel's cross-sectional maximum streamwise flow velocity, m s^{-1}
\mathbf{u}	local mean velocity, m s^{-1}
\bar{u}	streamwise mean flow velocity, m s^{-1}
$\bar{\bar{u}}$	streamwise acoustic-induced velocity, m s^{-1}
\tilde{u}	complex acoustic particle velocity, m s^{-1}
u_τ	flow friction velocity, m s^{-1}

V	volume of the cavity, m^3
\bar{v}	wall-normal mean flow velocity, m s^{-1}
$\bar{\bar{v}}$	wall-normal acoustic-induced velocity, m s^{-1}
v_{ac}	acoustic-induced ideal flow velocity, m s^{-1}
W	modelled channel's width, m
\mathcal{W}	measurement noise
w	weighing coefficient
w_p	cavities' partition walls thickness, m
\bar{w}	spanwise mean flow velocity, m s^{-1}
$\bar{\bar{w}}$	spanwise acoustic-induced velocity, m s^{-1}
x	streamwise (axial) coordinate, m
y	wall-normal coordinate, m
\tilde{Z}	specific acoustic impedance (normalized by Z_0)
Z_0	characteristic specific acoustic impedance of air, Pa s m^{-1}
z	spanwise coordinate, m

Greek symbols

α	transverse wavenumber
γ	air's specific heat ratio
Δt	timestep, lattice units
Δx	size of the grid element, lattice units
Δ_x	streamwise distance between two consecutive microphones, m
δ	boundary layer thickness, m
δ_1	boundary layer displacement thickness, m

δ_2	boundary layer momentum thickness, m
ε	turbulent energy dissipation
ϵ	orifice end correction
ζ	axial wavenumber
$\tilde{\eta}$	correction term for local strain, vorticity and helicity effects
θ	specific acoustic resistance (normalized by Z_0)
κ	turbulent kinetic energy
$\kappa_0 = \omega_0 h / c_0$	constant, refer to Equation 2.4
λ	acoustic wavelength, m
ν	kinematic viscosity, $\text{m}^2 \text{s}^{-1}$
ξ	particle velocity, lattice units
ρ	local mass density, kg m^{-3}
ρ_0	characteristic mass density of air at 25°C, kg m^{-3}
σ	cavity's open area ratio, i.e., the POA
τ	facesheet thickness, m
τ_e	effective facesheet thickness, m
τ	relaxation time constant
χ	specific acoustic reactance (normalized by Z_0)
ψ	acoustic mode shape
Ω	collision operator
ω	angular frequency, rad s^{-1}
ω_0	liner's resonance angular frequency, rad s^{-1}

Subscripts

b	backplate
eff	effective
f	facesheet
HR	Helmholtz resonator
L	in lattice units
max	maximum
mea	measured
MM	theoretical value, obtained with the mode matching method
PL	phase-locked, or phase-averaged

Superscripts

eq	equilibrium
o	temporary
*	refer to the real liner sample
–	negative direction of propagation
+	positive direction of propagation
†	refer to the dimensionless scale of the inner boundary layer

Semiempirical model parameters

R_{cm}	normalized grazing flow induced resistance
S_m	non-linear reactance slope
S_r	non-linear resistance slope
V_p	root mean squared acoustic particle velocity
Z_{of}	normalized linear impedance term

CONTENTS

1	INTRODUCTION	27
1.1	MOTIVATION	27
1.2	AIM AND OBJECTIVES	31
1.3	DOCUMENT STRUCTURE	31
2	LITERATURE REVIEW	33
2.1	ACOUSTIC LINERS THEORY: AN OVERVIEW	33
2.2	EXPERIMENTAL ASSESSMENT OF A LINER IMPEDANCE	37
2.3	SEMIEMPIRICAL MODELS	41
2.4	NUMERICAL SIMULATIONS OF ACOUSTIC LINERS	43
2.4.1	Acoustic simulations without mean flow effects	44
2.4.2	Grazing flow effects on acoustic simulations	48
3	METHOD	56
3.1	IMPEDANCE MEASUREMENT TECHNIQUES	56
3.1.1	The In-Situ Technique	56
3.1.2	Mode Matching Method	58
3.1.3	The Prony-like Algorithm	60
3.2	EXPERIMENTAL SETUP	61
3.2.1	Turbulent Boundary Layer Assessment	64
3.2.2	Liner Geometries and Test Conditions	66
3.3	NUMERICAL METHOD	68
3.3.1	The Lattice Boltzmann Method	69
3.3.2	Characteristics of the Solver	73
3.3.3	Computational Domain and Simulation Procedures	74
4	ACOUSTIC IMPEDANCE RESULTS	85
4.1	LINER SAMPLE A	85
4.1.1	Impedance in the Absence of Grazing Flow	85
4.1.2	Comparison of the Turbulent Boundary Layers	88
4.1.3	Impedance in the Presence of Grazing Flow	91

4.2	LINER SAMPLE B	98
4.2.1	Impedance in the Absence of Grazing Flow	98
4.2.2	Comparison of the Turbulent Boundary Layers	103
4.2.3	Impedance in the Presence of Grazing Flow	107
4.3	A BRIEF DISCUSSION ABOUT THE MODEL'S CAPABILITIES	112
4.3.1	General Parameters of the Model and Their Effects	113
4.3.2	Effect of the Orifice Shape on the Acoustic Results	115
5	INSIGHTS ON SOUND ABSORPTION MECHANISMS OF LINERS	121
5.1	IMPEDANCE VARIATION ALONG THE LINER'S FACESHEET	121
5.2	IN-ORIFICE FLOW INDUCED BY ACOUSTICS	132
5.3	ASSESSMENT OF THE DISCHARGE COEFFICIENT	137
6	CONCLUSIONS	142
6.1	FUTURE WORKS	144
	Bibliography	146
	APPENDIX A – TWO-DIMENSIONAL DUCT ACOUSTIC PROPAGATION MODEL WITH LINERS	159
	APPENDIX B – CONTOUR PLOTS OF THE IN-ORIFICE ACOUSTIC-INDUCED VELOCITY	161

1 INTRODUCTION

1.1 MOTIVATION

Aircraft noise is a primary concern all over the world as it affects communities negatively in several ways, from sleep disturbance to children’s learning interference (SPARROW et al., 2019). General standards for noise regulation in aircraft’s operations are provided by the International Civil Aviation Organization (ICAO), which are used as reference by countries to establish their own noise regulation policy¹.

The first ICAO standards for aircraft noise regulation were published in the late 1960’s. Since then, civil aviation agencies have been working with aerospace organizations to mitigate the impacts of aircraft noise on the environment, especially in areas close to airports. The ICAO guidelines specify the reduction of noise generation at the source as the main goal (ICAO, 2019, p. 46), since harsh measures (i.e., operational restrictions) would affect the aviation market economically and cause other social impacts. Figure 1 depicts the most relevant noise sources in a typical aircraft, among which the engine-related ones (in red color) are of primary interest (HUFF, 2007; BERTSCH et al., 2019).

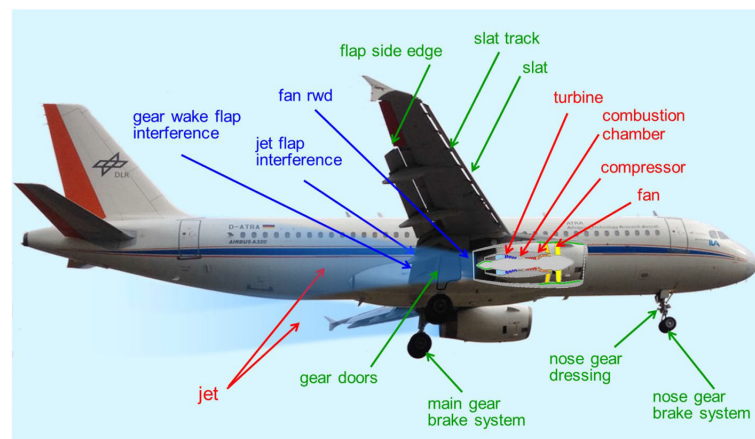


Figure 1 – Depiction of the most relevant noise sources on-board of conventional mid-range transport aircraft. Source: Bertsch et al. (2019).

Modern aircraft engines are typically turbofans with high bypass ratios, as shown in Figure 2. One of the most dominant sources in the engine is the fan, whose noise signature is marked by tonal components related to the blade-passage frequency (BPF) and by broadband components induced by turbulence (SMITH, 1989, p. 62-64). Inflow distortions and the interaction of fan-blade wakes with downstream guiding vanes are some

¹ <https://www.icao.int/about-icao/Pages/default.aspx>. Access on October 31st, 2022.

fan-related physical phenomena responsible for the generation of the tonal components in turbofans (SMITH, 1989, p. 135-137). For this reason, it is common that the inner walls of the engine's nacelles are acoustically treated with panels, named liners (SMITH, 1989; ROLLS-ROYCE LTD., 1996).

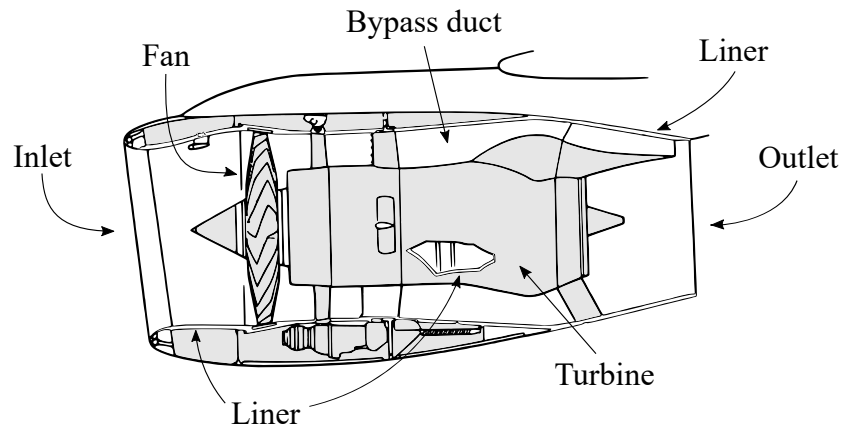


Figure 2 – Typical turbofan engine: locations where acoustic liners are installed. Source: adapted from Bonomo (2021, p. 20).

In its typical construction, the acoustic liner is built as a perforated plate (known as the facesheet) supported by a honeycomb structure at a specified distance from a solid plate, known as the backplate. This is called a single degree of freedom (SDOF) liner, which is essentially an arrangement of Helmholtz resonators (BONOMO, 2021, p. 25), as shown in Figure 3. Apart from the SDOF liner, different assemblies can be found in the literature (e.g., the double degree of freedom liner) (SMITH, 1989, p. 143). The liners must withstand harsh environments, with temperatures ranging from -50°C , of the intake air flow at high altitudes, to 500°C , due to the hot gases in the exhaust system. At the same time, these panels must be sufficiently light, as weight is a major concern for aircraft fuel efficiency, and effective for noise attenuation (SMITH, 1989, p. 141).

In general, the geometric parameters of the liners are tuned to provide optimal sound attenuation over a narrow frequency bandwidth centered in the BPF. However, as aircraft designs evolve towards better fuel efficiency, future engines are expected to have different characteristics and operational conditions, hence new noise signatures (CASALINO; DIOZZI, et al., 2008). Future turbofan engines are expected to have an increased rotor diameter, as well as a smaller length-to-diameter ratio. These aspects translate into both lower frequency blade passage tones, which are harder to be absorbed by typical passive liners, and in a reduction of the available area for the acoustic treatment, consequently reducing the attenuation efficiency. These trends present challenges to the

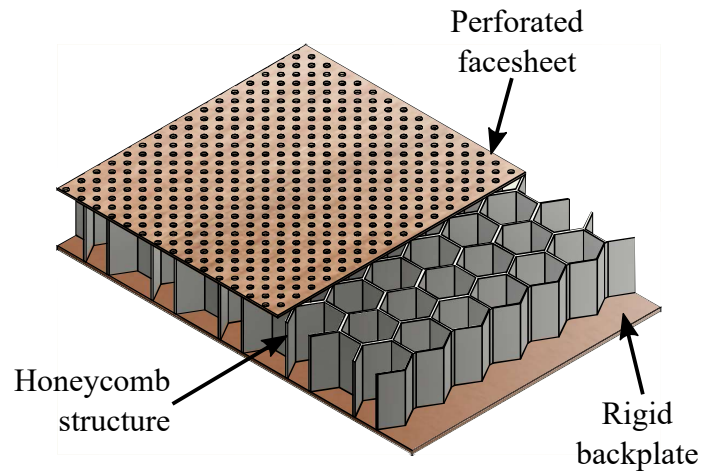


Figure 3 – Typical single degree of freedom acoustic liner. Source: Adapted from [Bonomo \(2021, p. 26\)](#).

engine’s noise control and will motivate the development new solutions, e.g., novel concepts of acoustic liners ([BAKE; KNOBLOCH, 2019](#)). In this sense, it is important to have a thorough understanding of the typical SDOF liner’s physics, so as to provide a background for novel concepts ([MURRAY; DI GIULIO, 2022](#)).

Liners are usually modelled as a locally-reactive surface (i.e., its acoustic response depends only on the local pressure), and are characterized by their impedance. Their characterization is not a simple task, since operational conditions change the liner’s acoustic response and its impedance. Among the parameters that affect the liner’s response are the liner’s geometry ([GUESS, 1975; JONES; TRACY, et al., 2002](#)), grazing flow velocity ([EVERSMAN, 1970; BONOMO; QUINTINO; SPILLERE, et al., 2022](#)), boundary layer parameters ([KOOI; SARIN, 1981](#)), temperature ([MÉRY et al., 2019](#)) and both sound pressure level (SPL) and frequency of the incident acoustic wave ([MURRAY; ASTLEY, 2012](#)).

Grazing flow impedance tubes have been used to assess liners’ acoustic response in conditions as close as possible to the operational ones ([JONES; WATSON, 2011; LÉON et al., 2019; LAFONT et al., 2021](#)). Different techniques can be applied to measure the acoustic impedance of liners in such facilities ([DEAN, 1974; ELNADY; BODÉN; ELHADIDI, 2009; WATSON; CARPENTER, et al., 2015](#)). A group of these techniques, named eduction methods, are commonly applied to determine the liner’s impedance, based on measurements of the acoustic field inside the duct. For that purpose, these methods make use of acoustic propagation models and proper boundary conditions, which assume a set of hypotheses.

Recently, discrepancies were found in experiments with liners in the presence of grazing flow, as the educed impedance changed with respect to the acoustic source position relative to the liner sample (RENOU; AURÉGAN, 2011). This contested the locally-reactive hypothesis, even though the hypothesis is considered by the eduction methods. This discrepancy was attributed to limitations of the wall boundary condition used to model the liner mathematically. However, it has been shown that even in the case of local impedance measurements (e.g., the in-situ technique), which does not rely on any boundary condition, a dependence exists on the relative directions of mean flow and main direction of propagation of the acoustic waves (BODEN et al., 2017; BONOMO; QUINTINO; SPILLERE, et al., 2022). This indicates that liners' reactive and dissipative mechanisms might not always be independent of the wave propagation direction, and questions the locally-reactive hypothesis.

Evidence suggest that the liner's physics in the presence of grazing flow is still not fully captured by existing models. In this context, high-fidelity numerical simulations have the potential to provide valuable insights into the flow-acoustics interaction and non-linear behaviour of the liner. These simulations can provide a detailed description of the pressure and velocity fields in the near-orifice regions, where most of the dissipation of the acoustic energy takes place, which can be used to improve the existing low-order models and to develop new ones.

A set of works on numerical simulations of liners is available in the literature (TAM; PASTOUCHENKO, et al., 2014; ZHANG; BODONY, 2016; AVALLONE; MANJUNATH, et al., 2019; SCHROEDER et al., 2021). Although these studies have provided important information on the physics of liners, none of them have simulated explicitly a three-dimensional multi-cavity liner geometry in the presence of grazing flow. This limitation has prevented the application of eduction methods to numerical data and the attempt to assess numerically the discrepancies between upstream and downstream measurements observed in experiments based on those methods.

The aim of this work is to develop a high-fidelity computational model for simulations of realistic multi-cavity acoustic liners in the presence of a turbulent grazing flow, in line with previous efforts to develop a representative numerical model for liners found in the literature. The goal is to reproduce the experimental data obtained at the Federal University of Santa Catarina (UFSC) liner test rig with the simulations. For that purpose the numerical model is built to replicate the test rig conditions. The simulation results are

used to assess near-wall flow-acoustics interactions, and to measure the liner's impedance with different approaches, including the in-situ technique and eduction methods.

1.2 AIM AND OBJECTIVES

The aim of this work is to assess the impedance of three-dimensional multi-cavity acoustic liners in the presence and in the absence of a subsonic turbulent grazing flow, with high-fidelity numerical simulations.

In order to achieve that the following objectives are established:

- To develop a computational setup based on the lattice Boltzmann method, by using the commercial solver *3DS-Simulia PowerFLOW6-2022R1*;
- To assess the turbulent flow parameters in the simulations and compare them with experimental data, obtained at the UFSC test rig;
- To calculate the acoustic impedance of the liner samples in different scenarios (varying the position, frequency and sound pressure level of the acoustic source), with different methods;
- To compare the impedance results with experimental data obtained at the UFSC test rig, considering the same methods, and with a semiempirical model;
- To assess the model's capabilities and opportunities to improve the agreement between the numerical and the experimental results;
- To evaluate aspects of the interaction between the grazing flow and the acoustic waves in the liner's near-orifice regions.

1.3 DOCUMENT STRUCTURE

This document is structured as follows.

Chapter 2 presents a literature review covering some basics of the acoustic liners theory. Additionally, some key aspects of the experimental characterization of liners are covered, especially in the presence of grazing flow, which are motivation for this work. The semiempirical model used to provide baseline results for the comparisons with the numerical simulations is presented. Lastly, a longer section discusses previous works on

high-fidelity numerical simulations of liners, with focus on their contributions to the overall knowledge of the liners' absorption mechanisms.

Chapter 3 focuses on the method used in this work. The impedance assessment techniques are explored, and their mathematical expressions are given. The experimental procedures employed to obtain the reference data are discussed, together with a brief presentation of the UFSC test rig. Also, the liner geometries chosen for the purposes of this work are described. Moreover, the chapter follows up with the presentation of the numerical procedures. First, the general aspects of the lattice Boltzmann method are explored. Later, the characteristics of the solver considered are presented. Lastly, the computational domain built to replicate the UFSC test rig and to simulate the liner geometries is explained.

Chapter 4 contains the results from the simulations carried out with the liner geometries in different scenarios, which includes the absence and the presence of the turbulent grazing flow, different sound pressure levels and frequencies and different positions for the acoustic source, relative to the flow direction. These results, which are obtained by three impedance measurement methods, are compared with the experimental data and with the semiempirical model's predictions. The results are assessed in terms of their agreement to the baselines and in terms of the physical phenomena they represent. Furthermore, discussions on the model's capabilities and glitches are carried out.

Chapter 5 is dedicated to explore some key aspects of the liners' absorption mechanisms in the near-orifice regions, such as the spatial dependence of the impedance along the sample, the in-orifice flow characteristics and the resultant discharge coefficient. These aspects are related to the behaviour observed for the impedance in the previous chapter.

Chapter 6 presents the main conclusions of this work. Additionally, some suggestions for related future works are given.

2 LITERATURE REVIEW

2.1 ACOUSTIC LINERS THEORY: AN OVERVIEW

The acoustic liner is an important noise control feature of the modern turbofan engine. The acoustic energy dissipation within liners is usually represented by its impedance, a parameter that includes the effects of two main physical mechanisms of these perforated panels: a resistive damping effect and a reactive effect. In this sense, the impedance is usually represented by a complex number $\tilde{Z} = \theta + i\chi$, in which the real part is the resistive term, or resistance θ , and the imaginary part is the reactive term, or reactance χ . A simple analogy to the typical acoustic liner (see Figure 3) is the Helmholtz resonator, which consists of a rigid-walled volume connected to the external environment by a small opening (also called orifice). Figure 4 represents schematically the main sound attenuation mechanisms of liners. The pressure gradients generated by an incident acoustic wave of frequency f induce an alternating movement of the air through the facesheet openings. This leads to the development of shear stresses within the fluid, due to viscosity, mainly in the near-wall regions, which dissipate acoustic energy in the form of heat, by momentum diffusion and by vortex shedding¹, the latter in the case of high SPL incident waves. The resistive damping is inversely proportional to the porosity of the facesheet, such that aerospace liners often have a low percentage of open area (POA), around 5%. Additionally, a reactive effect of the incident sound-wave can occur inside the resonator, due to the reflected waves at the bottom of the cavity. This reactive behaviour is frequency-dependent, and the depth of the cavity can be adjusted to provide optimum attenuation at a specific frequency, with reasonable efficiency over one octave bandwidth (MOTSINGER; KRAFT, 1991, p. 167). As shown in Figure 4, complete cancellation of the incident wave is provided by the resonator in an ideal condition when the cavity depth h is equivalent to a quarter of the acoustic wavelength $\lambda = c_0/f$, where c_0 is the local speed of sound, which is the resonance condition of the system (SMITH, 1989, p. 143-145).

To determine the liner's impedance is not a simple task. For plane wave excitations, if the dimensions of the resonators are much smaller than the acoustic wavelength, one may consider the pressure as uniform at a sufficient distance from the opening (PIERCE, 1989, p. 324-325). This allows for the application of the following definition for the resonators'

¹ This effect is also known as *acoustic streaming* (LIGHTHILL, 1978).

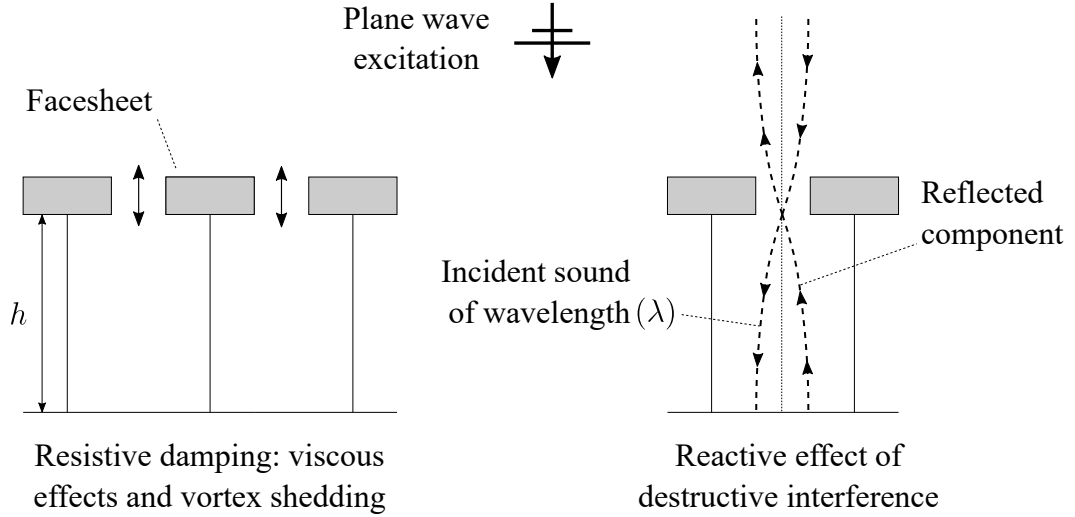


Figure 4 – Main acoustic energy dissipation mechanisms within liners.

surface specific acoustic impedance, normalized by the characteristic specific acoustic impedance of the air $Z_0 = \rho_0 c_0$, given by

$$\tilde{Z}(\omega) = \frac{1}{Z_0} \frac{\tilde{p}(\omega)}{\tilde{\mathbf{u}}(\omega) \cdot \mathbf{n}}, \quad (2.1)$$

where ρ_0 is the local air density, $\omega = 2\pi f$ is the angular frequency of the incident sound wave, $\tilde{p}(\omega)$ is complex pressure amplitude, $\tilde{\mathbf{u}}(\omega)$ is the complex acoustic particle velocity and \mathbf{n} is the normal vector on the outer surface of the perforated panel (PIERCE, 1989, p. 107, 331). In this work, \tilde{Z} is referred to only as normalized impedance.

The definition given by Equation 2.1 implies that the liners are considered locally-reactive surfaces (MOTSINGER; KRAFT, 1991; RENO; AURÉGAN, 2011). In classical acoustics, the locally-reactive condition means that $\tilde{Z}(\omega)$ must be independent of the angle of incidence of the acoustic wave, or that $\tilde{\mathbf{u}}(\omega)$ depends only on the local value of $\tilde{p}(\omega)$. Specifically for liners, this assumption means that the liner's cavities must be completely separated from each other, so as to prevent sound from propagating laterally within the panel (MOTSINGER; KRAFT, 1991, p. 171). Examples of non-locally-reactive liners can be found in real applications inside turbofan's nacelles, in which drainage holes connect adjacent cavities to prevent them from flooding with liquids (e.g., water from rain), as shown in Figure 5. Both locally and non-locally-reacting liners are used as acoustic treatments in nacelles (SPILLERE, 2017, p. 43), but the latter are out of the scope of this work.

Explicit relations for the impedance of acoustic liners are not straightforward to determine. For the simplest case of a single Helmholtz resonator in the linear regime, one

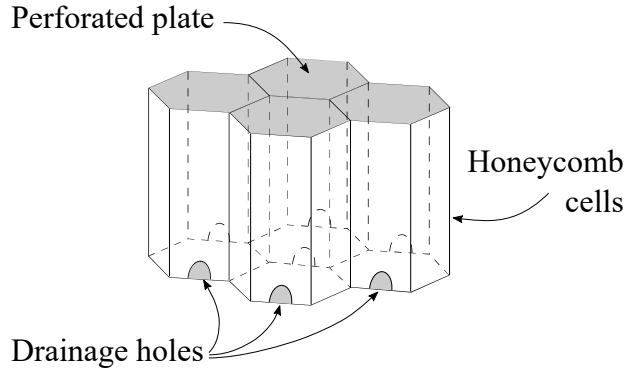


Figure 5 – Drainage holes located at the bottom of the honeycomb cells. Source: [Spillere \(2017, p. 43\)](#).

can obtain a straightforward expression for its impedance (\tilde{Z}_{HR}) by making an analogy to a SDOF damped mass-spring forced system, where the fluid inside the orifice represents an oscillating mass and the apparent spring is represented by the compressible fluid inside the cavity. This justifies why typical liner geometries are known as SDOF liners. In this case, as per [Temkin \(1981, p. 92\)](#),

$$\tilde{Z}_{\text{HR}} = \theta + i\rho_0 \left(\frac{c_0^2 S}{\omega V} - \omega\tau_e \right), \quad (2.2)$$

where S is the cross-sectional area of the opening, V is the volume of the cavity and τ_e is an effective facesheet thickness ([TEMKIN, 1981, p. 306](#)), given the facesheet thickness τ . If one considers an ideal fluid, the energy dissipation in the resonator happens exclusively due to acoustic radiation, therefore it is possible to state $\theta = \rho_0 c_0 k^2 / 2\pi$ ([TEMKIN, 1981, p. 306](#)), where $k = \omega/c_0$ is the free-field wavenumber. The resonance condition is established when the frequency of the incident sound wave matches the resonance frequency of the system, that is when $\lambda = 4h$. In this scenario, the amplitude of $\tilde{\mathbf{u}}(\omega)$ reaches a maximum, such that the resonance frequency of the Helmholtz resonator can be defined as

$$\omega_{\text{HR}} = c_0 \sqrt{\frac{S}{\tau_e V}}. \quad (2.3)$$

The substitution of ω_{HR} in Equation 2.2 leads to the conclusion that, near the resonance frequency, $\chi \rightarrow 0$ ([TEMKIN, 1981, p. 92, 306](#)).

Analytical predictions for the impedance of real liners are much harder to make, and several aspects contribute to enhance the complexity of such predictions. Real aerospace liners consist of multiple cavities covered by a facesheet with several orifices, which interact with each other. Moreover, the effective POA of real liners is not constant over all cavities, since the blockage of some orifices by the partition walls of the honeycomb during the

assembly of the panel is rather difficult to avoid (SMITH, 1989, p. 145). Furthermore, non-linearities of different sources become evident in their operation. These panels are installed inside the ducts of turbofans and are subjected to harsh environments, which change with respect to the operational condition of the engine. For this reason, a proper liner design process must take into account the liner's geometry (GUESS, 1975; JONES; TRACY, et al., 2002), grazing flow velocity (EVERSMAN, 1970; BONOMO; QUINTINO; SPILLERE, et al., 2022), boundary layer parameters (KOOI; SARIN, 1981), temperature (MÉRY et al., 2019) and both SPL and frequency of the incident acoustic waves (MURRAY; ASTLEY, 2012). Hence, liner's properties assessments are usually done experimentally, in test rigs that aim to reproduce their operational conditions as close as possible. Further discussions about experimental characterization of liners will be presented in Section 2.2.

The resonance frequency of an acoustic liner can be estimated by the numerical solution of the equation

$$\kappa_0 \tan \kappa_0 = \frac{\sigma h}{\tau_e}, \quad (2.4)$$

which is based on the work of Rienstra and Singh (2018) and was reported in the work of Léon et al. (2019). In Equation 2.4, σ is the cavity's open area ratio (i.e., the POA) and $\kappa_0 = \omega_0 h / c_0$, where ω_0 is the liner's resonance angular frequency. It is worth mentioning that the τ_e considered by Léon et al. (2019) is different from the one presented by Temkin (1981, p. 306) for a single Helmholtz resonator. Analytical models to estimate the impedance of realistic liners are also available, despite their relative high complexity (MOTSINGER; KRAFT, 1991, p. 176-189). These are based on the derivation of analytical solutions for the viscous, radiation and backing impedance contributions and on the adjustment of non-linear coefficients to experimental data (SPILLERE; REIS, et al., 2016), therefore are known as semiempirical models.

A semiempirical model is used in this work to assess the accuracy of the simulation results, in addition to experimental data. Section 2.3 will cover the main aspects of this model. However, at this point it might be important for the reader to get familiar with a typical impedance plot for acoustic liners, shown in Figure 6. These results were generated considering the liner in the absence of grazing flow with acoustic excitation in the linear regime (120 dB, $p_{\text{ref}} = 2 \times 10^{-5}$ Pa) (MELLING, 1973), using the semiempirical model by Yu et al. (2008). The geometric parameters of the liner used to generate the results in Figure 6 were selected to match the characteristics of one of the liners considered in this

work (Sample B, as further presented in Section 3.2.2), with a POA of 6.3%, $h = 38.1$ mm, $\tau = 0.635$ mm, and considering facesheet orifices of diameter d equal to 0.9906 mm.

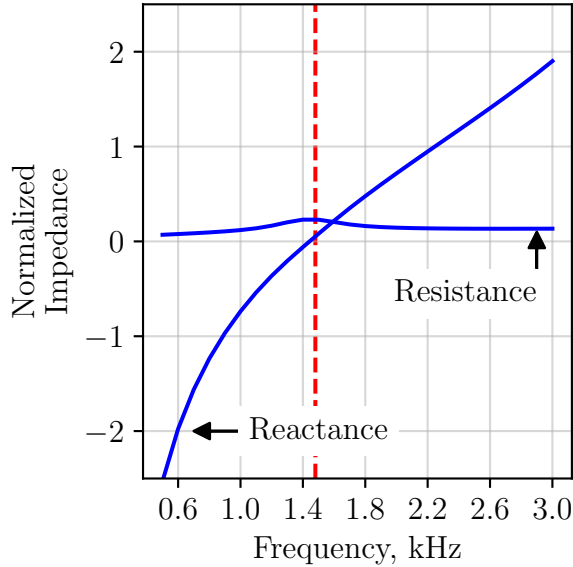


Figure 6 – Typical impedance plot for acoustic liners. Resonance frequency of the liner estimated with Equation 2.4 (---).

It can be seen that, in these conditions, resistance is almost constant over a large frequency range, except for a small bump near the resonance. Reactance, on the other hand, follows a slightly modified cotangent curve, as a function of frequency (MOTSINGER; KRAFT, 1991, p. 174). However, these trends change in the presence of other non-linear sources common to a liner’s operational environment, and different impedance measurement techniques may deliver different results, to some extent. The resonance of the liner is around 1440 Hz, according to the impedance results (i.e., $\chi \rightarrow 0$), while the resonance frequency estimated with Equation 2.4 is approximately 1480 Hz, which shows reasonable agreement with the semiempirical model’s predictions.

2.2 EXPERIMENTAL ASSESSMENT OF A LINER IMPEDANCE

To measure experimentally the impedance of acoustic liners, ideally, one should replicate the operational conditions of the panels as close as possible, to allow for a proper characterization of their acoustic response. In this sense, several experiments reported in the literature are designed to induce non-linear responses from the liner, e.g., by imposing a high incident SPL and/or turbulent grazing flow over the sample, which are the typical conditions inside turbofan nacelles. These factors, besides the relative small dimensions of the resonators, make it unfeasible to assess the impedance of the liner by measuring

directly the acoustic pressure and particle velocity on the facesheet, as given by the \tilde{Z} definition (Equation 2.1). For that matter, alternative techniques are commonly applied both in normal impedance tubes (NIT) and grazing flow test facilities, which are the most common experimental setups used to assess liners' properties (SPILLERE; BRAGA, et al., 2021).

Although important contributions have come from experiments with a NIT (MELLING, 1973; TAM; KURBATSKII, et al., 2001; JONES; BROWN, et al., 2019), this work focuses on grazing flow effects on the liner's response, and so only grazing flow test facilities will be discussed.

Grazing flow test facilities are ducts (typically with squared cross-sections) connected to an air flow source. The UFSC has grazing flow test facility, also referred to as the UFSC liner test rig, shown schematically in Figure 7. Several other facilities of this kind can be found around the world, each of them with its specific dimensions and features (KOOI; SARIN, 1981; JONES; WATSON, et al., 2004; LÉON et al., 2019). However, the general aspects of these test rigs are the same: the duct is commonly divided into sections, bolted to each other, in which equipment such as acoustic drivers and microphones are flush-mounted; special sections to place the liner sample to be tested are needed; anechoic terminations are used to prevent acoustic waves from reflecting back towards the sample, which could affect the quality of the measurements. The impedance assessment of the sample can be made in the absence or in the presence of grazing air flow inside the duct, which is usually subsonic.

Different impedance measurement methods can be applied in grazing flow test rigs. Dean's technique (also known as in-situ technique) was one of the first methods proposed, and has been widely used in previous investigations of acoustic liners (DEAN, 1974; KOOI; SARIN, 1981; FERRANTE et al., 2016; BONOMO; QUINTINO; SPILLERE, et al., 2022). The method is based on the measurement of the transfer function between the acoustic pressure at the facesheet and at the backplate of the liner, and therefore it requires instrumentation of the liner sample. Apart from the Dean's method, a group of measurement techniques, named eduction methods, are commonly employed to determine the liner's impedance, based on duct acoustic propagation models (JING et al., 2008; ELNADY; BODÉN; ELHADIDI, 2009; WATSON; CARPENTER, et al., 2015; SPILLERE; MEDEIROS, et al., 2018). Some of these impedance measurement methods are used in this work, and will be discussed in Section 3.1.

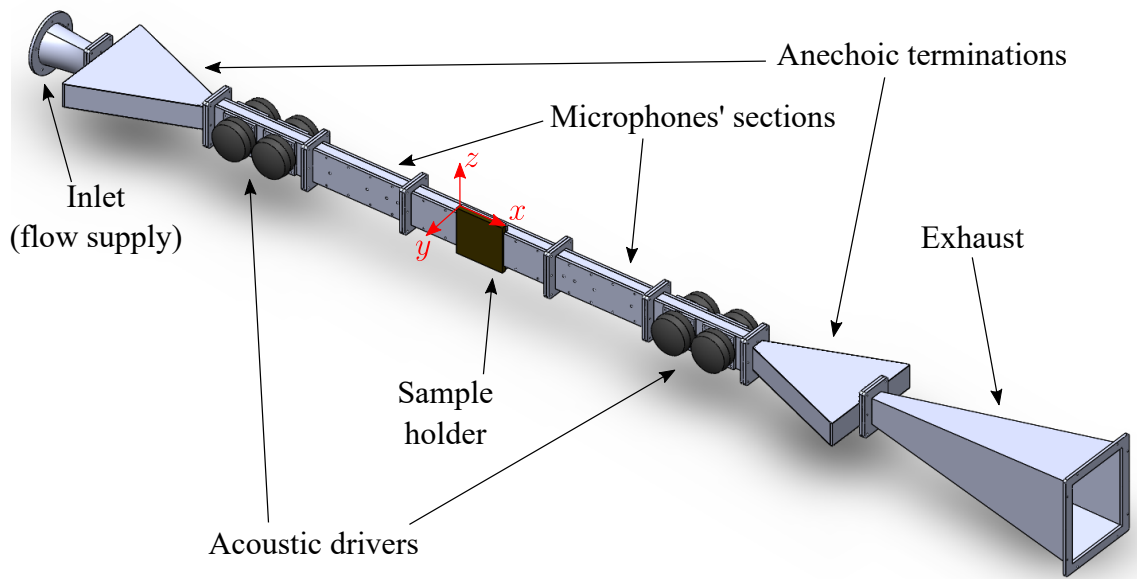


Figure 7 – Schematic representation of the UFSC liner test rig.

The experimental works considering the presence of grazing flow have provided important contributions to the understanding of sound absorption in liners. [Eversman \(1970\)](#) showed that the frequency of optimum attenuation of a typical liner changes when there is grazing flow over the facesheet, and this behaviour is dependent on both the flow velocity and the direction of propagation of the sound with respect to the flow. Generally, if the sound propagates in the same direction of the flow, the peak attenuation frequency increases with increasing flow velocity, and it decreases otherwise. Also, the higher the grazing flow velocity, the greater is the change in the frequency of peak attenuation. [Dean \(1974\)](#) evaluated the effect of the grazing flow speed on both resistance and reactance. It was observed that, for typical liners, the greater the grazing flow speed is, the higher the resistance values get. As for the reactance, as the flow speed increases, reactance values tend to zero. Further work by [Kooi and Sarin \(1981\)](#) showed a dependence of the liner's properties on the flow turbulent boundary layer (TBL) parameters. By measuring the impedance using Dean's method, it was found that, for a given free-stream flow velocity, an increase in the ratio between the boundary layer displacement thickness and the liner's orifices diameter (δ_1/d) results in lower values for the liner resistance, while reactance tends to increase. However, the former was shown to be more sensitive to changes in the TBL parameters.

In recent experimental works, impedance reduction techniques have been used very often ([JONES; PARROTT, et al., 2003](#); [JING et al., 2008](#); [ELNADY; BODÉN; ELHADIDI,](#)

2009). As eduction methods rely on the measurement of the acoustic field inside the duct to determine the liner's impedance, adequate boundary conditions are required to represent the viscous boundary layer on the interface between the mean flow and the liners' facesheet. In the presence of grazing flow, a common mathematical model for the liner's impedance is the Ingard-Myers boundary condition (BC) (INGARD, 1959; MYERS, 1980), given by

$$\frac{\partial \tilde{p}}{\partial y} = \frac{1}{i\omega \tilde{Z}} \left(i\omega + \overline{M} \frac{\partial}{\partial x} \right)^2 \tilde{p}, \quad (2.5)$$

where x and y are the streamwise and wall-normal coordinates (see Figure 7), respectively, and $\overline{M} = \overline{U}/c_0$ is the mean flow Mach number, \overline{U} being the mean flow streamwise velocity. This formulation assumes a set of hypotheses, namely: shear flow can be represented by a uniform flow and the viscous boundary layer is assumed to be infinitely thin; the liner can be modelled as a locally-reactive surface; the liner's reactive and dissipative mechanisms are independent of the wave propagation direction (BODEN et al., 2017). Renou and Aurégan (2011) reported differences in measured impedance from eduction methods when changing the relative direction of propagation of the acoustic wave with respect to the mean flow, while investigating locally-reactive liners inside grazing flow duct facility. This discrepancy was first attributed to a failure in the Ingard-Myers BC, and it is often referred as the upstream-downstream discrepancy.

The dependence of the measured impedance on the propagation direction violated the hypotheses of the Ingard-Myers BC, even though it was used in the acoustic propagation model, and was supposedly related to a non-complete description of the propagation in shear flow. Alternative boundary conditions have been proposed to represent the liner in the presence of sheared flow (AURÉGAN et al., 2001; BRAMBLEY, 2011), but none was found to be truly predictive, as discussed by Spillere, Bonomo, et al. (2020). Dai and Aurégan (2016) further studied this issue with a simplified 2D numerical model governed by linearized Euler equations (LEE) with the consideration of a sheared flow profile. Although several important effects were not taken into account (e.g., viscosity, turbulence and non-linear effects), the acoustic propagation in the sheared profile was completely described in this work. Mismatched impedance values were still obtained for different relative directions of mean flow and acoustic waves, suggesting that the cause might be related to a more fundamental issue. Weng et al. (2018) evaluated the impedance of liner samples by using two eduction methods, together with the full linearized Navier-Stokes equations (LNSE). Although in this case viscous effects, neglected by Dai and Aurégan

(2016), were taken into account with turbulence modelling, the upstream-downstream discrepancy was still not eliminated. Roncen et al. (2020) concluded that the calculation of the wavenumbers in the eduction procedures should take into account the flow profile in the whole cross-section of the rigs, which was shown to reduce the upstream-downstream discrepancy, but not to eliminate it. The residual mismatch was attributed either to experimental uncertainties or to a failure of the impedance boundary condition. Recent works have shown that even in the case of local impedance measurements (which do not depend on any BC, e.g., the in-situ technique) there is dependence on the relative directions of mean flow and acoustic waves propagation (BODEN et al., 2017; BONOMO; QUINTINO; SPILLERE, et al., 2022). This indicates that liners' reactive and dissipative mechanisms might not always be independent of the wave propagation direction, and that further investigations are necessary.

In this context, high-fidelity numerical simulations may be able to provide valuable insights, as one seeks to better understand the liner's dissipative and reactive mechanisms. However, current high-fidelity models are neither simple nor quick, which hinders their direct application on the design process of new liners.

In order to design liners effectively, it is important to assess their performance under various operational conditions. However, experimental test campaigns often fail to provide results quickly and inexpensively. Current high-fidelity simulations are also inadequate for early liner project phases, due to their complexities. Consequently, designers commonly rely on semiempirical models as an initial approach. These models allow for a rapid determination of the liner characteristics required to achieve a desired impedance, considering specific duct geometries. It's worth noting that these models are typically limited to certain liner geometries and operational conditions, as they are calibrated based on experimental data. The subsequent Section 2.3 will provide a brief discussion of these models.

2.3 SEMIEMPIRICAL MODELS

Semiempirical models are mathematical expressions developed to relate explicitly the geometric parameters of the liner, the environmental conditions and the acoustic impedance of the panel. These models are generally based on the analytical solution of viscous, radiation and rigid-wall reflection contributions for the impedance, while non-linear

effects are modelled by numerical fitting to experimental data (SPILLERE, 2017, p. 59). The majority of semiempirical models available in the literature are suitable for SDOF liners, and are useful as a baseline for both experimental and numerical results (GUESS, 1975; KOOI; SARIN, 1981; MOTSINGER; KRAFT, 1991).

In this work, the Goodrich liner impedance model, presented by Yu et al. (2008), is used as a reference to assess the numerical results from the simulations. This formulation was chosen because it captures both high SPL and grazing flow linear and non-linear effects, as well as TBL parameter contributions, to the predicted impedance. The Goodrich model was built upon experimental data obtained by a two-microphone method (KRAFT et al., 1997). Its was validated with experimental results obtained in the National Aeronautics and Space Administration (NASA) grazing flow impedance tube, by an eduction method based on a finite element approach (YU et al., 2008).

Considering the case of a liner whose $\tau/d \leq 1$, the general expression for the liner's impedance, given by Yu et al. (2008), is

$$\tilde{Z} = \tilde{Z}_{\text{of}} + S_r V_p + R_{\text{cm}} + i [S_m V_p - \cot(kh)], \quad (2.6)$$

where \tilde{Z}_{of} is a normalized linear contribution term without grazing flow, S_r is a non-linear resistance slope term (in s/cm), V_p is the root mean squared (RMS) acoustic particle velocity (in cm/s), R_{cm} is a normalized grazing flow induced resistance linear term and S_m is a non-linear reactance slope term (in s/cm). In Equation 2.6, the linear term \tilde{Z}_{of} is given by

$$\tilde{Z}_{\text{of}} = \frac{i\omega}{F(k_s r)} \left(\frac{\tau + \epsilon d}{c_0 \sigma} \right), \quad (2.7)$$

where ϵ is called 'orifice end correction', as presented by Guess (1975), and it is given by

$$\epsilon = \frac{1 - 0.7\sqrt{\sigma}}{1 + 305\overline{M}^3}. \quad (2.8)$$

The equation for $F(k_s r)$ represents the cross-sectional averaged velocity profile of the orifice, equal to

$$F(k_s r) = 1 - \frac{2J_1(k_s r)}{k_s r J_0(k_s r)}, \quad (2.9)$$

where r is the orifice radius, J_0 and J_1 are zero and first order Bessel functions, respectively, and $k_s = -i\omega/\nu$, ν being the fluid's kinematic viscosity. The non-linear resistance slope term S_r , given in Equation 2.6, is defined as

$$S_r = \frac{1.336541 (1 - \sigma^2)}{2c_0 C_D^2 \sigma^2}, \quad (2.10)$$

where C_D is the discharge coefficient, given by

$$C_D = 0.80695 \sqrt{\sigma^{0.1} / \exp(-0.5072\tau/d)}, \quad (2.11)$$

which can be interpreted as an orifice open-area correction, due to the formation of the *vena contracta* during inflow and outflow phases (SPILLERE, 2017, p. 63). Finally, the normalized grazing flow induced resistance and non-linear reactance slope terms, in Equation 2.6, are given by

$$R_{\text{cm}} = \frac{\overline{M}}{\sigma(2 + 1.256\delta_1/d)}, \quad (2.12)$$

and

$$S_m = -2.07 \times 10^{-5} k / \sigma^2, \quad (2.13)$$

respectively.

The solution for the liner's impedance by the Goodrich model requires an optimization routine, because the model explicitly depends on the V_p on the facesheet, which cannot be determined at first, since the impedance \tilde{Z} is not known. The strategy is to guess an initial value for V_p , namely V_i , by considering $\tilde{Z} = \tilde{Z}_i = 1$, in such a way that $V_i = \langle \tilde{p}_f \rangle \left(|\tilde{Z}_i| Z_0 \right)^{-1}$ can be determined, since the RMS value of the pressure on the facesheet $\langle \tilde{p}_f \rangle$ can be estimated from the incident SPL. An optimization routine is then performed to minimize the cost-function

$$\mathcal{C} = V_p - \frac{1}{Z_0} \frac{\langle \tilde{p}_f \rangle}{|\tilde{Z}_{\text{prev}}|}, \quad (2.14)$$

in which \tilde{Z}_{prev} is the impedance calculated with the previous guess for V_p .

Semiempirical models can benefit from numerical simulations results, as these simulations allow for a detailed assessment of the liner's physics and can be used to derive more representative models. A discussion on numerical simulations of liners is presented in the following Section 2.4.

2.4 NUMERICAL SIMULATIONS OF ACOUSTIC LINERS

Direct experimental assessment of the flow field around and inside resonant liners' openings is a challenging task, due to the small dimensions of the perforated orifices. Until about two decades ago, most of the knowledge regarding acoustic liners was based on either theoretical models or large-scale experimental setups, which exhibit different Reynolds numbers from the real phenomena. Recent works involving high-fidelity numerical

simulations allowed for better understanding of liner’s dissipation mechanisms, since very small scale structures of the flow field can be resolved and studied under a representative Reynolds number (TAM; KURBATSKII, 2000). A summary of the state-of-the-art regarding low to high-fidelity tools for acoustic liners is available in the work of Winkler et al. (2021). This section is dedicated to highlight some of the insights on the physics of acoustic liners provided by previous works involving high-fidelity simulations.

2.4.1 Acoustic simulations without mean flow effects

One of the first numerical investigations of the energy dissipation mechanisms within liners was performed by Tam and Kurbatskii (2000), who simulated a cavity resonator with a single orifice under acoustic excitation without mean flow. A Direct Numerical Simulation (DNS) approach was considered for the solution of the two-dimensional compressible Navier–Stokes and energy equations. Different sound pressure levels ranging from 120 dB to 160 dB were considered, which allowed for the observation of linear and non-linear regimes. In the non-linear regime, strong oscillatory ‘jetlike’ boundary layers were observed inside and out of the opening. Time-averaged results showed that, in the linear regime, most of the acoustic energy dissipation due to viscosity effects takes place near the walls of the resonator’s opening, which was caused by the shear gradient of the unsteady boundary layer. Other interesting findings of this work were that, under sufficiently high SPLs and near the resonance frequency, the main dissipation mechanism of the cavity became vortex shedding, which was associated with high acoustic particle velocities, up to $M = 0.2$ at 150 dB. These vortices were the result of the conversion of incident acoustic kinetic energy into rotational kinetic energy, which could not be converted back into sound. This makes vortex shedding an efficient dissipation mechanism. As schematically shown in Figure 8, two main causes were identified for the vortices’ generation at the resonator’s opening: an internal vortex is shed when the incoming flow separates from the wall on the corner of the opening; external vortex forms when flow leaving the orifice separates from the opening’s wall. Internal vortices were found to be usually trapped inside the opening until dissipated by viscous losses, while external vortices usually moved away from the resonator in the form of mutual induced motion counter-rotating pairs. This phenomena happened alternately, due to the oscillating pressure outside the resonator, and the vortices were generated both inside and outside the cavity, based on the pressure gradient. These

numerical simulations were further validated by [Tam, Kurbatskii, et al. \(2001\)](#) in terms of calculated absorption coefficients with a NIT experimental setup, which included a particle image velocimeter (PIV) and special cameras that allowed for flow visualizations. The experiments confirmed vortex shedding as an important acoustic energy dissipation mechanism in the non-linear regime and in the absence of mean flow.

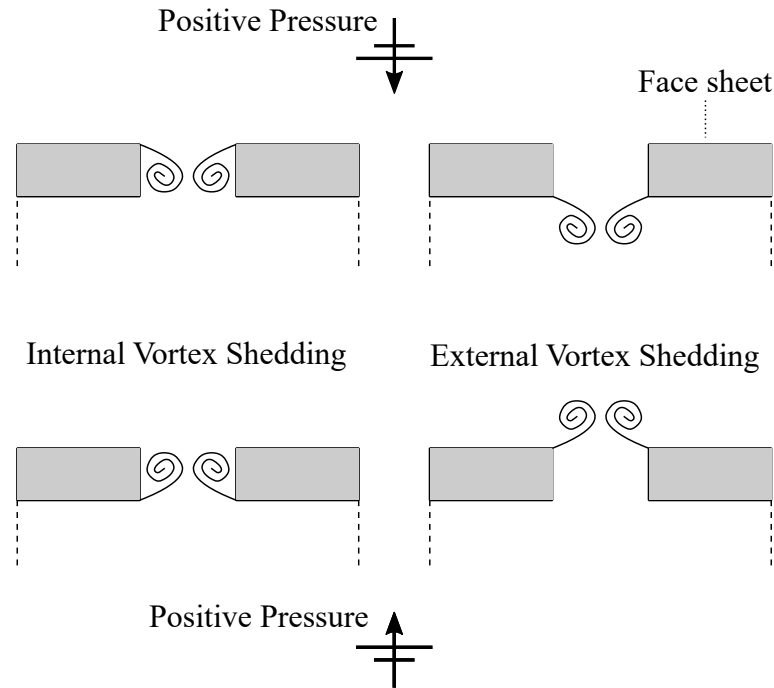


Figure 8 – Vortex shedding mechanisms in the resonator's opening under high sound pressure level excitation.

Further correlated numerical and experimental studies involving slit resonators mounted in a NIT setup were presented by [Tam, Ju, Jones, et al. \(2005\)](#) and [Tam, Ju, Jones, et al. \(2010\)](#), who performed two and three-dimensional simulations, respectively, with the same DNS approach to solve the compressible Navier-Stokes equations presented by [Tam and Kurbatskii \(2000\)](#). These works have provided better understanding of the vortex shedding phenomena, and proved that the DNS was a reliable and accurate strategy to assess liner's design. The assessment of different slit's geometries on the acoustic properties of resonators showed that the use of a 45° beveled slit, instead of a conventional 90° squared opening, would significantly increase the occurrence of vortex shedding, consequently increasing the resistance associated with higher acoustic energy absorption for a given slit width ([TAM; JU; JONES, et al., 2005](#)). Previous two-dimensional simulations had shown a rather chaotic motion of the shed vortices ([TAM; KURBATSKII, 2000; TAM; JU; JONES, et al., 2005](#)). The three-dimensional setup allowed for the

observation of ring vortices, which were regularly shed under discrete frequency excitation, in contrast with the chaotic line vortices generation. The regularity of the vortex shedding phenomena under discrete frequency excitation was related to the opening's aspect ratio, with large aspect ratio slits (inherent to two-dimensional setups) leading to fairly random behaviour. Randomness in the vortex shedding was also verified for the three-dimensional resonator under broadband acoustic excitation, even for low aspect ratio slits (TAM; JU; JONES, et al., 2010).

A more recent effort to simulate a NIT setup was made by Mann et al. (2013), who performed three-dimensional Very Large Eddy Simulations (VLES) with a commercial solver based on the lattice Boltzmann method (LBM) (KRÜGER et al., 2017). They have assessed numerically the acoustic properties of different liner configurations, and used semiempirical models to validate the results (MELLING, 1973; MOTSINGER; KRAFT, 1991). The effect of the numerical grid refinement on the impedance was evaluated and higher resistance values were found for lower resolutions. This was attributed to numerical dissipation, which is more significant for low resolution levels in the vicinity of the perforated facesheet orifices. Moreover, it was found that low resolution led to higher reactance predictions and the resonance frequency of the cavity was underestimated. Overall, as a consequence of insufficient grid refinement, the flow inside the orifices was not well resolved, and impedance could not be correctly predicted. For this NIT setup, convergence of the simulation results was verified for a grid considering approximately 19 cells/mm in the near-orifice region.

The LBM commercial solver employed by Mann et al. (2013) was also used by Manjunath et al. (2018) and Schroeder et al. (2021) to assess the impedance of liners excited by grazing acoustic waves. These models were built to replicate grazing flow facilities, the former based on the Grazing Flow Impedance Tube (GFIT) at the NASA Langley Research Center (JONES; WATSON, 2011), and the latter based on the UFSC liner test rig (BONOMO; QUINTINO; SPILLERE, et al., 2022). However, both works have presented acoustic results only in the absence of grazing flow. As shown schematically in Figure 9, the liners were positioned on the top wall of the computational domain, which was set as a no-slip wall. The bottom wall was positioned to replicate the facility duct's cross section height, and it was set as a slip wall. Periodic BC was applied to the sides of the computational domain, in order to minimize the computational costs, and the width of the duct was restricted to the liner's cavity width. Absorbent regions were established in

the duct's terminations to dissipate the acoustic waves and prevent reflections. A variable resolution scheme was used for the grid generation, with higher resolution applied to the near-orifice regions.

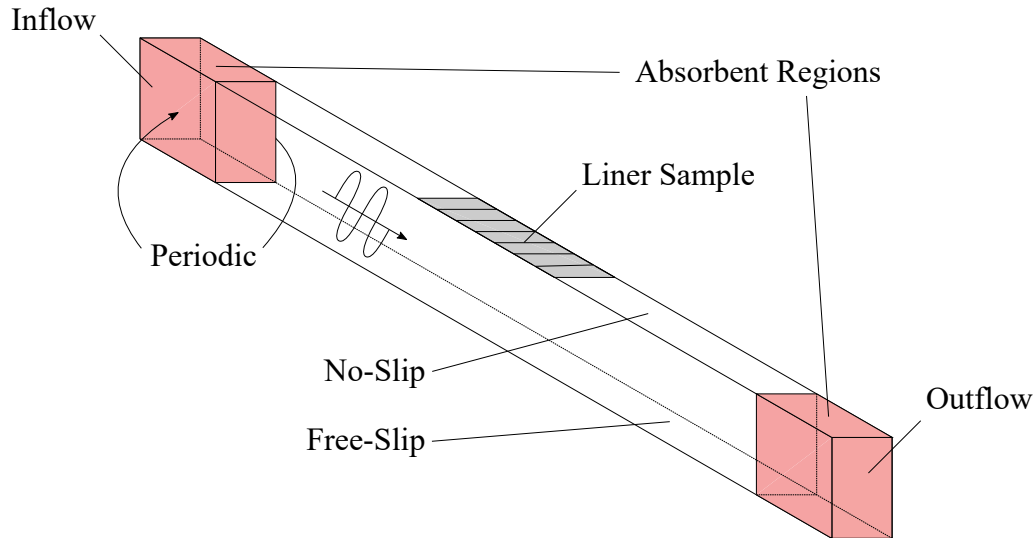


Figure 9 – Typical lattice Boltzmann numerical model of grazing flow test rigs.

Manjunath et al. (2018) studied two single cavity liners found in the literature (JONES; WATSON, et al., 2004; ZHANG; BODONY, 2016), and presented impedance measurements with the in-situ technique for a single frequency at different SPLs, covering linear and non-linear regimes. The resistance results were in good agreement with DNS, experimental and semiempirical reference data, while only fair agreement was verified for the reactance. Phase-averaged results allowed for the observation of the acoustically induced mean flow profile inside the orifices, and higher velocity values were found for excitation near the resonance frequency. These near-resonance profiles were also found to be less uniform, which is likely to be the result of the strong vortices generated in this scenario. A grid refinement study was performed, and the optimal resolution in terms of results convergence and computational effort was found to be approximately 42 cells/mm in the near-orifice region.

Schroeder et al. (2021) investigated a realistic acoustic liner with multiple cavities. However, only a single row of eleven cavities was simulated to save computational resources, as opposed to the eighteen cavities found in the streamwise direction of the real sample (SPILLERE; BRAGA, et al., 2021). Impedance was measured by both in-situ technique and by an eduction method for three frequencies, at both 130 dB and 150 dB. The impedance calculated with the in-situ technique were presented in the form of an averaged

result over all cavities, and it was in good agreement with the experimental data for the 130 dB case. For the acoustic source at 150 dB, the simulation overestimated the resistance obtained experimentally. The probes positioned in all cavities showed that the measured SPL tends to drop along the liner length, as does the resistance, while reactance tends to increase. The impedance measured with the eduction method presented only fair agreement with the experimental data. The mismatches found between the numerical and experimental results were partially attributed to the relative low refinement of the simulations, which is a reasonable hypothesis given the resolutions considered by previous works (MANJUNATH et al., 2018; AVALLONE; DAMIANO, 2021). Schroeder et al. (2021) worked with a resolution of approximately 26 cells/mm in the near-orifice region. For the eduction mismatch, the difference in the number of cavities between simulations and experiments was also considered an error source.

Previous works had shown that, as the SPL drops along the liner, the discharge coefficient should increase as a consequence of smaller orifice boundary layers and velocity magnitudes (ZHANG; BODONY, 2012). This would lead to smaller resistance and higher reactance, which was observed in the in-situ measurements of Schroeder et al. (2021).

It is worth highlighting that there was a mismatch between the facesheet thickness of the liner simulated by Schroeder et al. (2021) and the real sample used for the results' comparisons, as per Spillere, Braga, et al. (2021). The real sample had a facesheet thickness of $\tau = 1.00$ mm, while the numerical geometry was modelled with $\tau = 0.80$ mm. The effect of this mismatch on the impedance was estimated with the semiempirical model presented by Yu et al. (2008), and it is shown in Figure 10. According to this model, the effect of the thinner facesheet would be minor on the simulation results, although it is likely that the resistance measurements would drop and reactance would raise, especially for the high SPL case.

2.4.2 Grazing flow effects on acoustic simulations

Similar two-dimensional DNS to the ones presented by Tam and Kurbatskii (2000) and Tam, Ju, Jones, et al. (2005) were carried out by Tam, Ju, and Walker (2008), who assessed the effects of grazing flow on liners' dissipative mechanisms. In that work, a channel was modelled with a resonator placed on the bottom wall and the acoustic source on the top wall. A sheared flow profile of maximum Mach number $M = 0.2$ was considered,

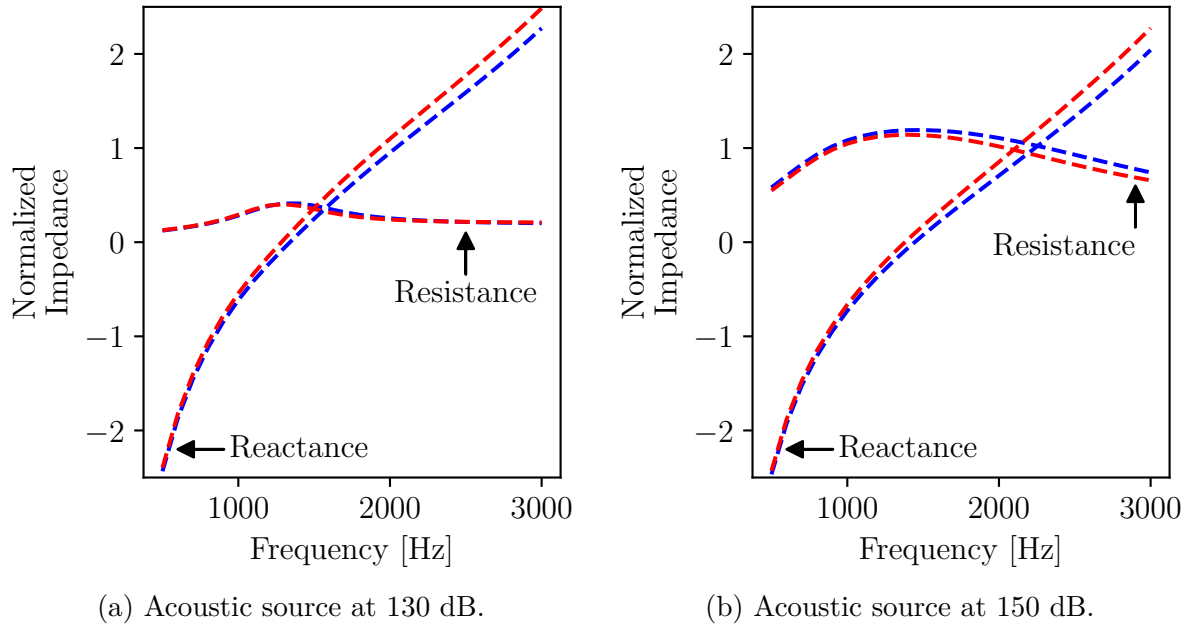


Figure 10 – Predicted impedance for the liner considered by [Schroeder et al. \(2021\)](#) with a facesheet thickness of 0.80 mm (blue) and 1.00 mm (red). Impedance estimated by the semiempirical model described in [Yu et al. \(2008\)](#).

although only the TBL on the bottom wall was resolved. Steady state results (without acoustic excitation) showed recirculation inside the resonator. As shown schematically in [Figure 11](#), at the opening of the resonator, clockwise vortical flow (identified as ‘A’) is induced by the free-stream flow. This further induces the development of large counter-clockwise vortical flow (identified as ‘B’), that fulfills the entire cavity. Secondary clockwise vortical flows (identified as ‘C’) develop adjacent to the upper corners of the resonator, as a consequence of the ‘B’ vortex. Observations made under low SPL excitation showed that when the pressure outside the resonator decreases, outflow from the cavity pushes the ‘A’ vortex towards the downstream wall of the opening, where it eventually vanishes. When pressure increases outside the resonator, the incoming flow generates a new ‘A’ vortex in the opening. Under high SPL excitation it was observed that, even under laminar grazing flow, vortex shedding is still the main acoustic energy dissipation mechanism. However, due to the presence of grazing flow, strong merged vortices ejected from the resonator’s opening during the outflow cycle are carried away downstream, trapped inside the boundary layer for long distances, which affect the flow-acoustic interaction in subsequent orifices. [Zhang and Bodony \(2011\)](#), who performed similar simulations with grazing flow speed up to $M = 0.85$, concluded that the velocity at which these vortices convect depends on their distance to the wall. Furthermore, it was observed that the higher the grazing flow speed,

the closer these vortices tend to stay to the wall, confined within the boundary layer. Smaller grazing flow speeds would allow for the vortices to be convected away vertically and most probably not interact with adjacent resonators. Impedance measurements using the Dean's method showed dependence on the facesheet probe location (ZHANG; BODONY, 2011).

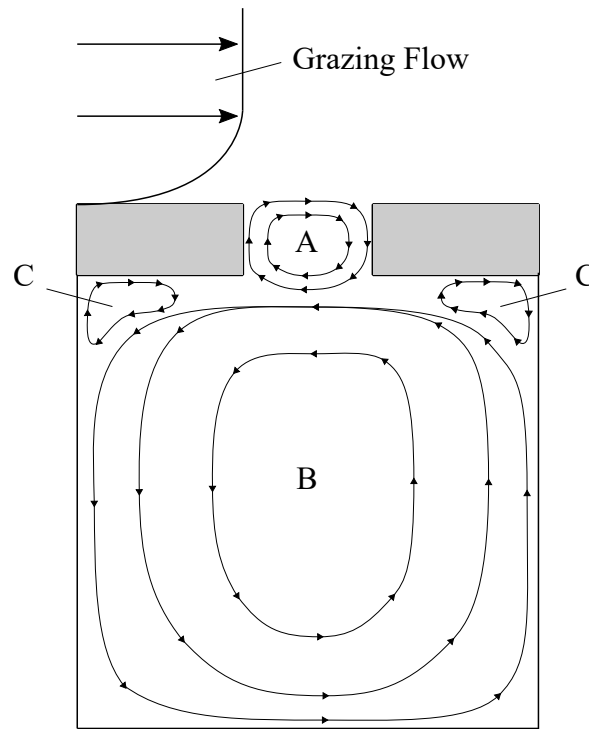


Figure 11 – Steady mean flow inside the resonator: vortical regions.

Tam, Pastouchenko, et al. (2014) carried out a coordinated experimental and numerical simulation study of a multi-cavity liner under grazing flow, in which Reynolds Averaged Navier-Stokes (RANS) equations were solved with a turbulent eddy viscosity model. The liner geometry used in this study was a single array of eight squared cavities completely separated from each other, and a single high aspect ratio slit was drilled in the facesheet for each cavity. The liner was acoustically excited by grazing tonal waves of at least 140 dB, covering a wide frequency range, and impedance was calculated by an eduction method (WATSON; JONES, et al., 2005). Additionally to a no-flow scenario, the effects of a $M = 0.3$ turbulent grazing flow were assessed. In the numerical simulations, the problem was simplified as two-dimensional to save computational resources. The simulations showed that the mean flow induced the same recirculation regions as represented in Figure 11, although they were neither symmetrically positioned nor identical from one cavity to another. The interaction between the mean flow and the slits was responsible for very

high frequency noise (29 kHz) generation, beyond normal hearing range, with relative low SPL. The authors classified this phenomena as a self-noise liner generation, since it was found to be completely unrelated to the incident grazing acoustic wave. As shown in Figure 12, the mean flow promotes the generation of a thin shear layer in the upstream edge of the resonator orifice, which is unstable due to Kelvin-Helmholtz instabilities. The instability waves grow in amplitude, as they propagate downstream, and eventually roll up to a vortex structure, which strikes the downstream edge of the orifice creating an acoustic pulse. This acoustic pulse propagates upstream and further excites the shear layer, closing the feedback loop. This constant impingement of vortices in the downstream edges of the orifices is responsible for an increase in the drag force of about 4%, considering a conventional liner with 10% POA. Although these phenomena have not been observed experimentally yet, their effects might be significant in terms turbofan’s efficiency.

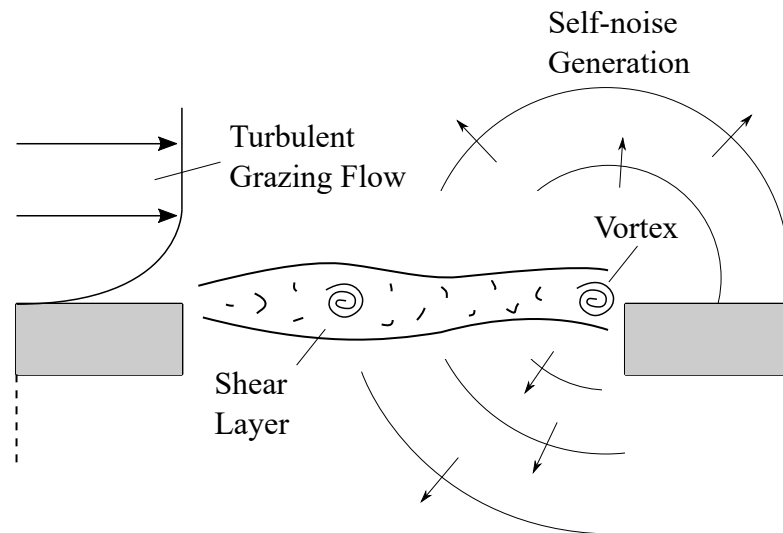


Figure 12 – Self-noise generation mechanism.

Zhang and Bodony (2016) performed three-dimensional DNS by solving the compressible Navier-Stokes equations, which aimed to reproduce the testing conditions of the GFIT liner test section under turbulent grazing flow of $M = 0.5$. However, a prior RANS analysis conducted with a commercial solver showed the Reynolds number to be too large for the DNS approach, and so the Reynolds number was artificially lowered while keeping other important parameters constant (e.g., the momentum thickness to orifice diameter ratio). This was considered a reasonable approximation, taking into account the important turbulence scales involved in the problem. The computational domain was composed by a rectangular volume containing a single hexagonal resonator covered by

a perforated facesheet with only one orifice, which were centered on the bottom wall. It was found that the grazing flow is responsible for asymmetry of the acoustically induced flow inside the orifice, which is an important observation of the flow-acoustics interaction from the impedance point of view. Phase-averaged results were used to assess the peak in velocity induced in the orifice by the acoustic waves. These results were compared with analytical predictions for the velocity based on a SDOF system analogy, which was found to underestimate the peak velocity for the case with a turbulent grazing flow. Impedance numerical assessments in the presence of grazing flow were made for three frequencies at 130 dB and compared against experimental data in the form of porosity-scaled measurements, due to the differences in the POA between the real sample and the modelled liner. This approach was supported by previous works ([MELLING, 1973](#); [HERSH et al., 2003](#); [SINGH; RIENSTRA, 2014](#)). The numerical results were found to be within the scatter of the experimental data. The authors highlighted that the experimental data used for the comparisons were obtained by eduction methods, while in the numerical simulations the Dean's method was used. This difference might be significant due to the fact that impedance changes along the liner sample, due to the change in SPL and flow parameters.

Recent efforts were made with LBM-VLES of three-dimensional liners in the presence of turbulent grazing flow, using similar computational domains as the one represented in [Figure 9](#). [Avallone, Manjunath, et al. \(2019\)](#) and [Avallone and Damiano \(2021\)](#) considered a previously studied multi-orifice single resonator under a $M = 0.3$ flow profile ([JONES; WATSON, et al., 2004](#)), similar to the one measured experimentally at the GFIT. The transition to turbulence and the resolution of the turbulent scales by the VLES algorithm was triggered by a zigzag strip included in the setup, at an specific streamwise position. The simulation procedure was divided into steps: first the statistical convergence of the TBL was assessed and the fluid domain was exported; second, a periodic pressure signal was superimposed to the fluid domain at an upstream position of the sample; last, the modified domain was simulated and the acoustic waves propagated towards the sample with the grazing flow. Impedance was measured by the in-situ technique with probes positioned at several facesheet locations, to assess the effects of the interaction between the grazing flow and the orifices on the results.

The acoustic simulations performed by [Avallone, Manjunath, et al. \(2019\)](#) considered a single frequency at 130 dB, and reasonable agreement was found between eduction experimental data and the numerical impedance values obtained with the in-situ technique.

The results showed dependence on the probing position, with resistance being more sensitive than the reactance. Two potential causes were given for such spatial scattering of the impedance results: the turbulent wake generated behind each orifice might increase the velocity and pressure fluctuations induced by the acoustic waves; large scale vortex motions generated by the interaction between the flow and the orifices might affect the ejection of acoustically-induced vorticity within the orifice, which could affect the pressure signal at the backplate. Visual results of the flow-acoustics interaction in the near-orifice region showed that the pressure increase due to the acoustic wave passage over the orifice was responsible for the generation of vorticity inside the orifices. It was possible to observe that the grazing flow interacts with the orifices and generates a wake, which affects the vortex shedding pattern on downstream orifices. The flow inside the cavity was found to be strongly three-dimensional, and this could affect the discharge coefficient among different orifices and the impedance measurements in different positions. This study was performed with a resolution of approximately 30 cells/mm in the near-orifice region.

[Avallone and Damiano \(2021\)](#) performed acoustic simulations of a single frequency for a no-flow scenario at different SPLs, ranging from 130 dB to 160 dB. Grazing flow simulations ($M = 0.3$) were performed for three frequencies at the same SPLs. The impedance results showed that the non-linear effects related to the SPL were dominant in the no-flow case, with higher SPL leading to significantly higher resistance and lower reactance. In the presence of grazing flow, the flow linear and non-linear effects become more important and dominate. In this case, the increase in SPL led to only slight increase in the resistance for very high SPL (about 160 dB), while the reactance remained fairly constant. The impedance results showed variation as a function of the probe position on the facesheet for the grazing flow cases, with the resistance increasing from the most upstream positions to the most downstream positions. Meanwhile, reactance tends to decrease towards the downstream direction. The acoustic-induced velocity within the liner orifice was assessed by means of a triple decomposition procedure, based on time synchronous averaging of the signals ([HOCHMANN; SADOK, 2004](#); [RANDALL, 2021](#)). This procedure, which is schematically represented in [Figure 13](#), consisted of the following steps: a phase-average is performed in the time signal acquired from the simulation, resulting in the phase-locked velocities u_{PL} , v_{PL} and w_{PL} for the x , y and z directions, respectively; the phase-locked velocities are averaged, leading to the mean velocities \bar{u} , \bar{v} , \bar{w} ; the subtraction of the mean velocities from the phase-locked results in the acoustic-induced velocities $\bar{\bar{u}}$, $\bar{\bar{v}}$, $\bar{\bar{w}}$.

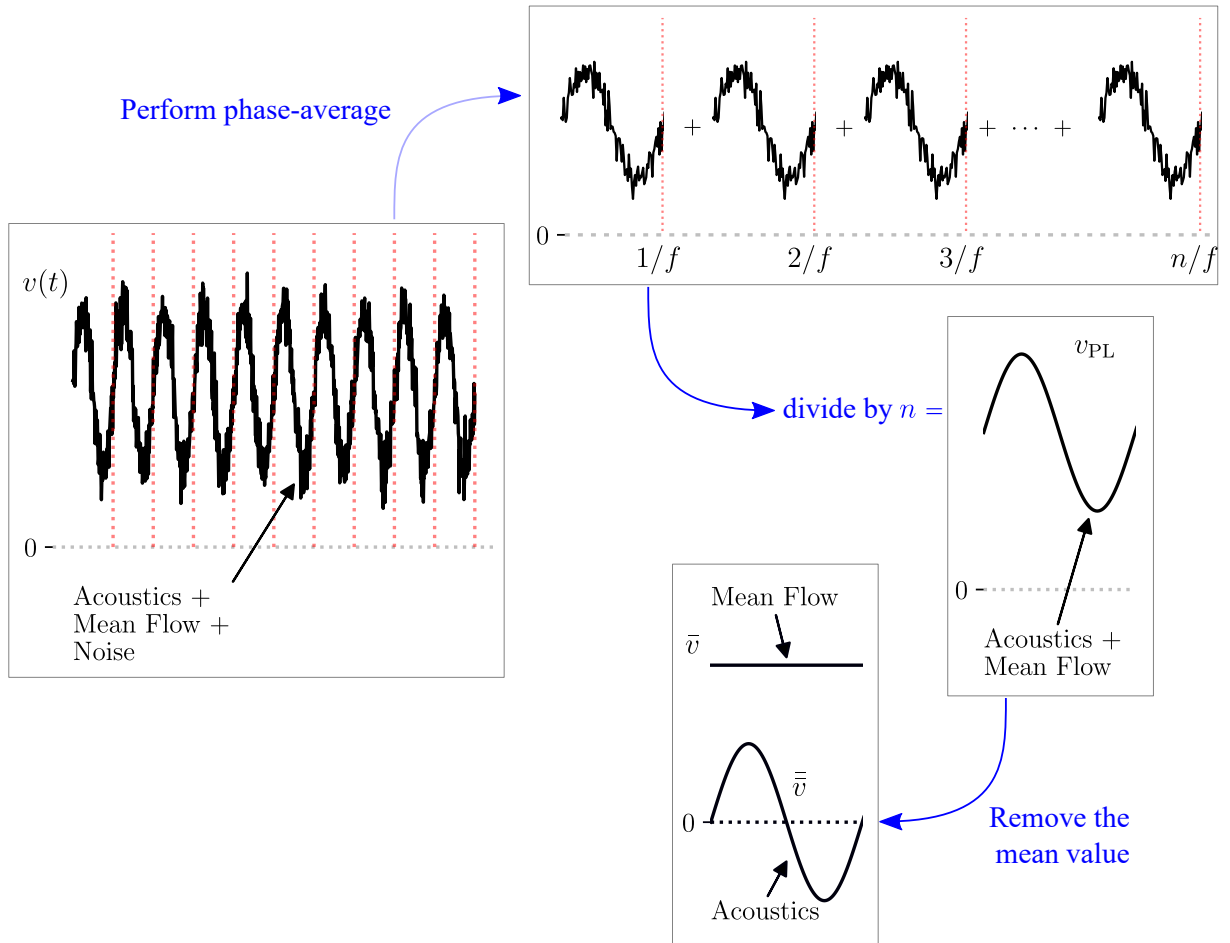


Figure 13 – Schematic of the triple decomposition of the velocity field.

The recirculation inside the orifices was stated as a quasi-steady vortex, as it slightly oscillates when it interacts with incident acoustic waves. This vortex was observed to act like a barrier to the acoustic wave, since periodic oscillations of the acoustic-induced velocity were seen only at the downstream portion of the orifice. These findings agree with the previous numerical study of [Zhang and Bodony \(2016\)](#) and with the PIV experimental observations from [Léon et al. \(2019\)](#). This condition was said to be valid as long as $\bar{v} < \bar{u}$, which is essentially a function of the SPL. The work showed that the peak values of \bar{v} are not altered by the presence of the grazing flow with respect to the no-flow cases, at least for that specific combination of POA, Mach number and frequency. The main effect of the grazing flow is the change in the spatial distribution of \bar{v} . Since periodic oscillations occur only in the downstream portion of the orifice, there is an effective reduction in the cross-sectional area seen by the acoustic wave, and this explains the increase in resistance measured. In that work, the grid resolution was approximately 40 cells/mm in the near-orifice region.

The numerical studies presented in this section have provided important insights on the physics of liners. However, to address numerically some of the gaps still present in the literature, as discussed previously, better representation of the real liner absorption mechanisms in the simulations is desirable. None of the works discussed in this section has considered simulating explicitly a three-dimensional multi-cavity liner geometry in the presence of grazing flow. Such limitations have prevented the assessment of key aspects regarding liners' absorption mechanisms. For example, the discrepancies between upstream and downstream measurements observed in experiments based on eduction methods have not been assessed numerically yet. In this sense, this work aims to develop a high-fidelity computational model for simulations of realistic multi-cavity acoustic liners in the presence of a turbulent grazing flow.

3 METHOD

3.1 IMPEDANCE MEASUREMENT TECHNIQUES

This Section is devoted to present the impedance measurement techniques used in this work, which are used to obtain both the experimental and the numerical results. Overall, three methods were considered, all of which are indirect techniques, such that the impedance is calculated by the measurement of other variables (in this case, acoustic pressure). The methods considered include the in-situ technique, which is a two-microphone method; and two eduction methods, which determine the impedance of the liner based on measurements of the acoustic field in the duct of the test rigs.

3.1.1 The In-Situ Technique

The in-situ technique is a two-microphone method to measure the liner's local impedance, presented by Dean (1974). This technique was developed mainly to address duct acoustic propagation problems in high speed flow environments, such as gas turbines applied to aircraft propulsion. The operational conditions of aircraft engines involve both high speed grazing flow and high SPL, which were known by the time this technique was presented as non-linear sources in the liner's response (EVERSMAN, 1970; MELLING, 1973; DEAN, 1974).

The in-situ technique is the simplest among the impedance measurement methods considered in this work. It relies on acoustic pressure measurements on the facesheet \tilde{p}_f and inside the cavity, usually on the backplate \tilde{p}_b , simultaneously. Figure 14 presents a scheme of the application of this technique in a resonant cavity, where the two measurement points are shown. The formulation considers that the liner is locally-reactive¹ and that only plane acoustic waves propagate inside the cavity (i.e., the acoustic wavelength is much larger than the cavity's cross section dimensions).

Taking the coordinate system on Figure 14 as reference, consider the incident acoustic wave $\tilde{p}^+ = pe^{i(\omega t - ky)}$ is totally reflected by the rigid backplate in the bottom of the liner's cavity in the form of the $\tilde{p}^- = pe^{i(\omega t + ky)}$ component. The acoustic field inside the cavity is

¹ In the case of the in-situ technique, the concept of locally-reactive acoustic liner refers specifically to the no energy transmission through the cavity walls condition (DEAN, 1974).

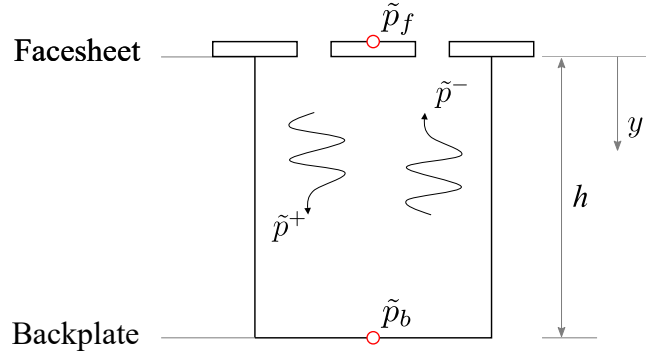


Figure 14 – Schematic application of the in-situ technique.

the sum of both \tilde{p}^+ and \tilde{p}^- components, or

$$\tilde{p} = 2pe^{i\omega t} \cos ky. \quad (3.1)$$

The application of linear momentum conservation, given by $\rho_0 \partial \tilde{u} / \partial t = -\partial \tilde{p} / \partial y$, leads to the acoustic particle velocity expression

$$\tilde{u} = -i \frac{2p}{\rho_0 c_0} e^{i\omega t} \sin ky. \quad (3.2)$$

The specific acoustic impedance on the facesheet in terms of the local acoustic pressure is given by the ratio $\tilde{Z}_f = \tilde{p}_f / \tilde{u}_f$. However, it is not feasible to measure the acoustic particle velocity experimentally. An alternative relation can be derived by mathematical manipulation to express \tilde{Z}_f in terms of the pressure measurements on both the facesheet and the backplate, or

$$\tilde{Z}_f = -i\tilde{H} \frac{1}{\sin kh}, \quad (3.3)$$

where $\tilde{H} = \tilde{p}_f / \tilde{p}_b$ is the transfer function between facesheet and backplate measurements.

Among the hypotheses considered by this model is that there is a simple relation between the acoustic pressure and the acoustic particle velocity inside the cavity, which in practice limits the application of this technique to conventional SDOF liners (e.g., without any porous material inside the cavity (ELNADY; BODÉN, 2004)), and that the facesheet is ‘acoustically thin’, such that there is continuity of acoustic particle velocity along the facesheet thickness (DEAN, 1974).

The application of the in-situ technique to measure acoustic impedance of real liner samples has been proven effective (BONOMO; QUINTINO; SPILLERE, et al., 2022). However, there are some observations to the in-situ measurement procedure: the assembly of the microphones (or probes) in the sample is a delicate process that causes permanent damage to the liner (BONOMO, 2021); the facesheet microphone has to be inserted

through a hole in the backplate and flush-mounted on the outer perforate surface, which results in a change in the effective volume inside the cavity that needs to be corrected (FERRANTE et al., 2016); ideally, one should make sure that the interface between the facesheet microphone and the facesheet is sealed, such that any leakage is prevented, and this is a challenging task (the same applies to the backplate and the microphone flush-mounted on it); signal to noise ratio issues are expected in the facesheet measurements due to the influence of the TBL, and are more likely to occur as the grazing flow speed increases (DEAN, 1974; ELNADY; BODÉN, 2004).

Important factors related to the confidence level of the measurements made with the in-situ technique should also be highlighted. It is expected a change in impedance in the streamwise direction of the sample, due to the SPL attenuation of consecutive cavities, as per Motsinger and Kraft (1991, p. 168) and Schroeder et al. (2021). Since the in-situ technique evaluates the impedance locally, the result might not be representative for the whole sample. Trustful results depend directly on the sample setup procedures, e.g., the facesheet microphone should be placed far enough from the orifices to avoid the ‘hydrodynamic field’ pressure gradient but close enough with respect to the wavelength (DEAN, 1974; SCHROEDER et al., 2021).

3.1.2 Mode Matching Method

The mode matching (MM) method is an inverse impedance eduction method for acoustic liners. It requires the use of numerical optimization routines to obtain a theoretical acoustic field that matches the reference measured acoustic field (BONOMO, 2021). The theoretical acoustic field is modelled as described in Appendix A. The MM method was first proposed by Elnady and Bodén (2004), and validated by Elnady, Bodén, and Elhadidi (2009) later on. This approach was developed as an alternative method to the in-situ technique, whose drawbacks have been discussed in the previous Section.

In this work, a modified version of the original MM method is used, where only plane waves propagation is considered (ZHOU; BODÉN, 2015). Viscothermal energy dissipation is considered by corrections in the axial wavenumber (SPILLERE; BONOMO, et al., 2020). For the impedance eduction procedure, the acoustic field is measured at different positions upstream and downstream of the liner sample, as shown schematically in Figure 15.

From the decomposition of the measured acoustic field the amplitudes of the modes

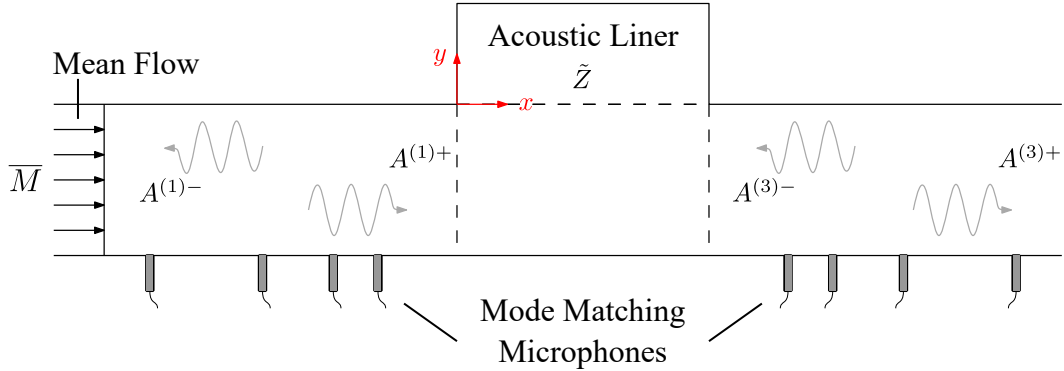


Figure 15 – Schematic representation of the mode matching method application for liner impedance measurements.

which propagate towards the sample in sections (1) and (3) ($A^{(1)+}$ e $A^{(3)-}$) are obtained, by solving an overdetermined linear system. For example, in section 1

$$\begin{bmatrix} \exp(-i\zeta^{(1)+}x_1) & \exp(-i\zeta^{(1)-}x_1) \\ \exp(-i\zeta^{(1)+}x_2) & \exp(-i\zeta^{(1)-}x_2) \\ \vdots & \vdots \\ \exp(-i\zeta^{(1)+}x_q) & \exp(-i\zeta^{(1)-}x_q) \end{bmatrix} \begin{bmatrix} A^{(1)+} \\ A^{(1)-} \end{bmatrix} = \begin{bmatrix} \tilde{p}_1 \\ \tilde{p}_2 \\ \vdots \\ \tilde{p}_q \end{bmatrix}, \quad (3.4)$$

where q is the number of microphones in in each section. In general, the higher q is, the smaller the influence of random noise (like turbulent flow induced noise) in the results (HOLMBERG et al., 2011; SPILLERE; MEDEIROS, et al., 2018). A similar set of equations must be solved for section 3. The modal amplitudes are given as input to the optimization routine of the MM method with an initial guess for the liner's impedance, usually calculated with semiempirical models to improve convergence (SPILLERE; BONOMO, et al., 2020).

The mode coupling in the two lined-rigid interfaces considers mass and momentum conservation, as proposed by Gabard and Astley (2008) and described by Spillere, Bonomo, et al. (2020). The solution for the coupling equations is obtained by an iterative algorithm, and allows the reconstruction of the acoustic field. The liner's impedance is obtained by the optimization of the cost-function

$$\mathcal{F}(\tilde{Z}, \omega) = \sum_{i=1}^q \left| \frac{\tilde{p}_{i,\text{mea}}(\omega) - \tilde{p}_{i,\text{MM}}(\tilde{Z}, \omega)}{\tilde{p}_{i,\text{mea}}(\omega)} \right|, \quad (3.5)$$

where $\tilde{p}_{i,\text{mea}}$ and $\tilde{p}_{i,\text{MM}}$ are the measured and theoretical acoustic pressure, respectively, at each microphone. Once convergence criteria is achieved, the liner's impedance is deduced. The Levenberg-Marquadt algorithm (LEVENBERG, 1944; MARQUARDT, 1963), available for Python3 in the `scipy.optimize` library (SCIPY..., 2022), is used to optimize the \mathcal{F} function.

3.1.3 The Prony-like Algorithm

The use of the Prony's method to measure impedance of liners was first presented by [Jing et al. \(2008\)](#). This approach was considered a straightforward impedance eduction method, as opposed to inverse techniques (e.g., the mode matching method), because it does not rely on optimization routines. This approach has some advantages over the inverse techniques: its computational cost is smaller and it is not affected by convergence and/or initial guess problems.

The Prony's algorithm educes the liner's impedance by fitting a linear combination of damped complex exponentials to the pressure field, sampled by equally spaced microphones in the lined section of the duct ([JING et al., 2008](#)), as shown in Figure 16.

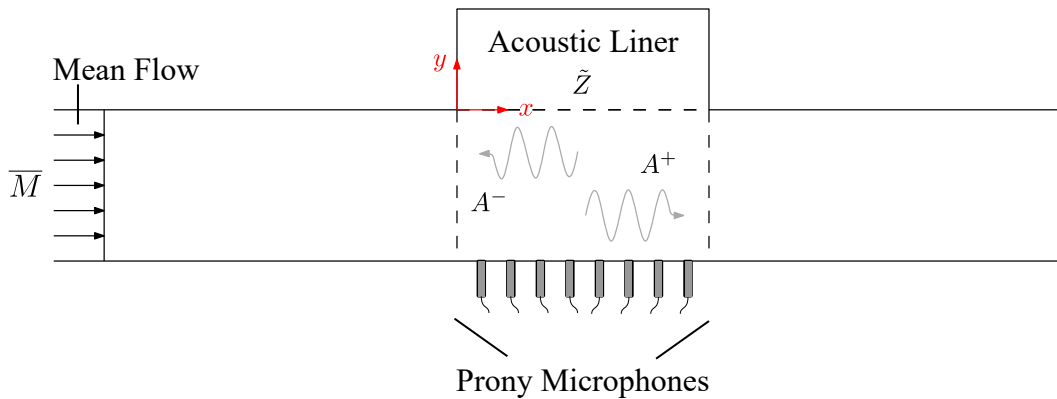


Figure 16 – Schematic representation of the Prony algorithm application for liner impedance measurements.

The method considers that the acoustic field at the lined channel is a linear combination of damped complex exponentials

$$\tilde{p}_i = \sum_{m=1}^{\mathcal{N}} A_m^{\pm} e^{-i\zeta_m^{\pm} \Delta_x}, \quad i = 0, 1, \dots, \mathcal{M} - 1, \quad (3.6)$$

where \tilde{p}_i is the pressure at the i -th microphone, ζ_m^{\pm} are the axial wavenumbers, Δ_x is the streamwise distance between two consecutive microphones and \mathcal{M} is the total number of microphones. From this expression, the application of the Prony's method allows for the determination of the axial wavenumbers from the pressure signals.

Given that the acoustic field in the channel can be represented in a similar way as that described in Appendix A, the application of the Ingard-Myers BC for the lined wall and $\partial\tilde{p}/\partial y = 0$ for the opposite rigid wall leads to the eigenvalue problem given by

$$\frac{ik}{\tilde{Z}} \left\{ \frac{1}{1 - \overline{M}^2} \left[1 \mp \overline{M} \sqrt{1 - \frac{1 - \overline{M}^2}{k^2} (\alpha_m^{\pm})^2} \right] \right\}^2 = \alpha_m^{\pm} \tan(\alpha_m^{\pm} 2H). \quad (3.7)$$

In Equation 3.7, α_m^\pm are the m -th transverse wavenumbers, which can be related to the axial wavenumbers by the dispersion relation (JING et al., 2008):

$$\zeta_m^\pm = \frac{-\overline{M}k \pm \sqrt{k^2 - (1 - \overline{M}^2)(\alpha_m^\pm)^2}}{1 - \overline{M}^2}. \quad (3.8)$$

From application of the Prony's algorithm in Equation 3.6, the axial wavenumbers are known. Consequently, it is straightforward to obtain the liner's impedance with Equations 3.7 and 3.8. Note that the sum in Equation 3.6 has been truncated at the maximum mode order \mathcal{N} , which is dependent on the number of pressure signals available.

A modified version of this method has been proposed by Watson, Carpenter, et al. (2015), which included the effect of measurement noise \mathcal{W} to the description of the pressure field, in the form of

$$\tilde{p}_i = \sum_{m=1}^{\mathcal{L}} A_m^\pm e^{-i\zeta_m^\pm \Delta x} + \mathcal{W}_i, \quad i = 0, 1, \dots, \mathcal{M} - \mathcal{L} - 1. \quad (3.9)$$

To educe the liner's impedance with this expression, Watson, Carpenter, et al. (2015) used the method described by Kumaresan and Tufts (1982) and Kumaresan (1983) to separate the effect of the noise from the pressure field exponentials, and this approach is usually referred as the Prony-like KT algorithm. However, the model order needs to be reduced to \mathcal{L} , such that $\mathcal{N} \leq \mathcal{L} \leq \mathcal{M} - \mathcal{N}$ (BONOMO; SPILLERE, et al., 2020).

3.2 EXPERIMENTAL SETUP

This work aims to develop a numerical model for acoustic liners in the presence of grazing flow. To assess the accuracy of the model, experiments were carried out with real liners in the UFSC liner test rig. The test rig is located at the Laboratory of Vibration and Acoustics (LVA), and its current assembly is composed by seven sections, which can be seen in Figure 17.

There are eight beyrna CP-855Nd acoustic drivers mounted on the walls of the rig, four upstream from the sample and four downstream, which allow for measurements with SPL up to 150dB. A National Instruments PXI is used to both generate the acoustic excitation and to sample the B&K 4944-A 1/4" pressure field microphones, at a 25.6 kHz sampling rate. Excitation signals are amplified by B&K 2716-C power amplifiers. Figure 18 shows in detail the microphones' sections of the rig, and also where the pressure field is measured for the application of each one of the eduction methods, presented in Section 3.1.

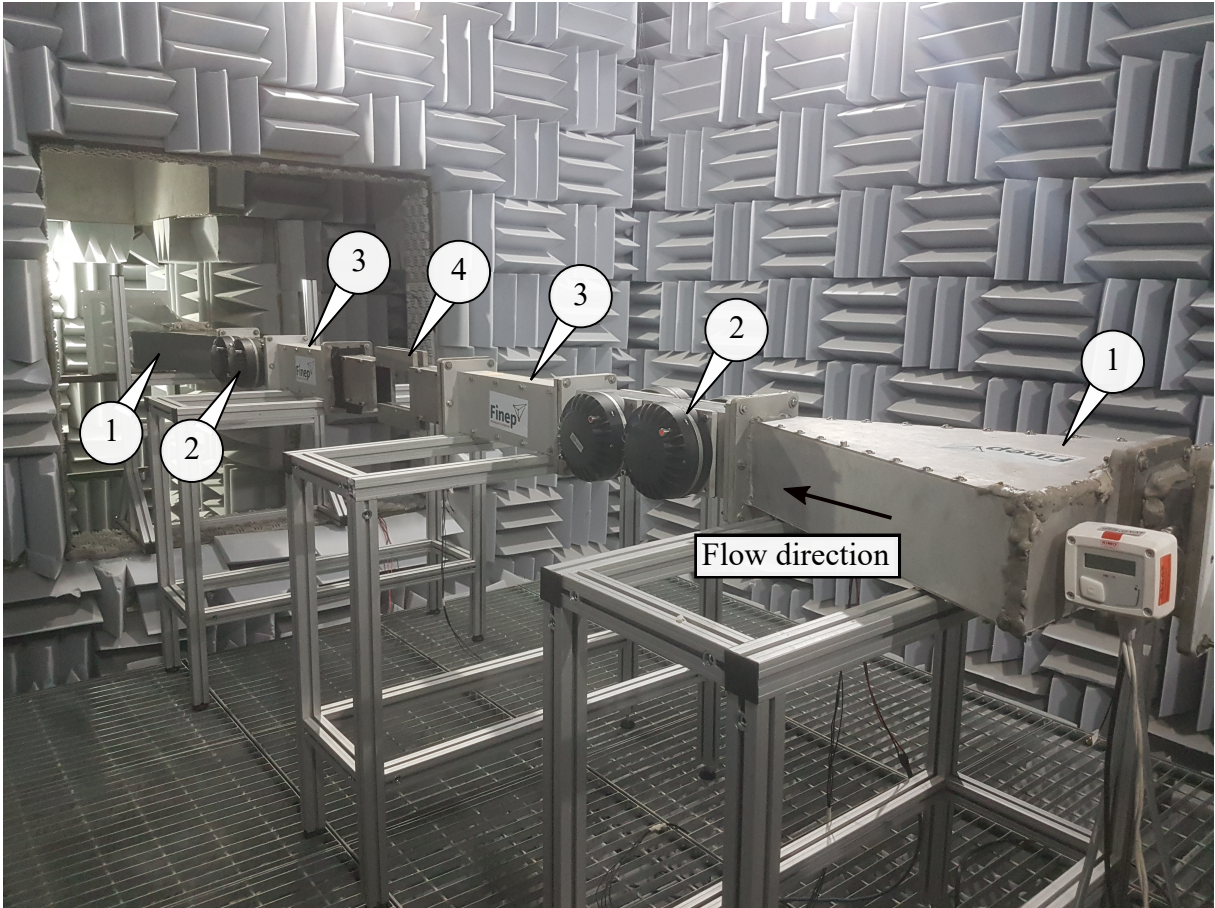


Figure 17 – UFSC liner test rig: (1) quasi-anechoic terminations; (2) acoustic drivers' sections; (3) microphones' sections; (4) sample holder.

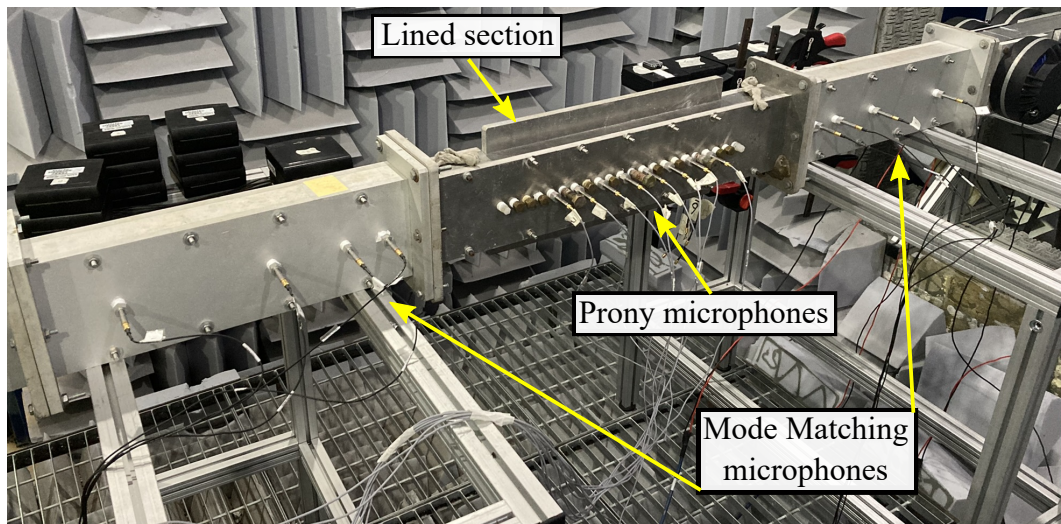


Figure 18 – Microphone slots for the impedance education techniques in the UFSC test rig.

For the MM method education procedure, eight unequally spaced flush-mounted microphones are considered, four upstream and four downstream from the sample holder. The microphones used for the Prony/KT method are flush-mounted on the rigid wall of the sample holders, opposite to the liner, and are equally spaced. Table 1 exhibits the

streamwise coordinates of these microphones in the UFSC test rig.

Table 1 – Streamwise coordinates of the microphones used for the experimental impedance eduction procedures.

	Mic. 1	Mic. 2	Mic. 3	Mic. 4	Mic. 5	Mic. 6	Mic. 7	Mic. 8
MM method (x), m	-0.48	-0.31	-0.22	-0.17	0.59	0.64	0.73	0.90
KT algorithm (x), m	0.08	0.12	0.16	0.20	0.24	0.28	0.32	0.36

The in-situ technique measurements are performed with the use of the same B&K 4944-A 1/4" microphones, mounted on stainless steel capillary probes with a 1.6 mm external diameter, coupled to a brass adapter to attach the 1/4" microphone. The microphones are calibrated systematically, and this procedure is described in more detail by [Bonomo, Quintino, Spillere, et al. \(2022\)](#). The probes, shown in Figure 19a, are properly flush-mounted on the backplate inside the cavity, and on the facesheet. The assembly of the capillary probes are shown in detail in Figure 19b, and the top view of the facesheet showing the flush mounted probe in place is shown in Figure 19c. Note that, to perform the in-situ measurements, it is necessary to drill the liner sample, which damages it permanently.

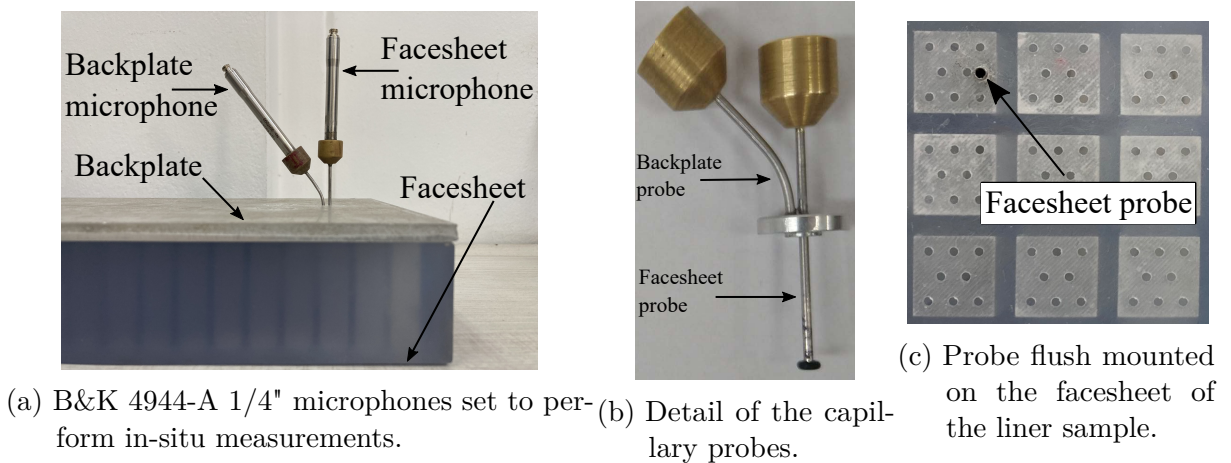


Figure 19 – Experimental setup for the in-situ measurements.

The duct of the test rig has a rectangular cross-section which is 100 mm wide and 40 mm high, for which the first transverse mode in the absence of grazing flow occurs at about 1700 Hz. However, since the microphones are positioned at half the duct width, they lie on the nodal line of this first transverse mode, whose effect is not captured during the measurements ([SPILLERE; BONOMO, et al., 2020](#)). The cut-on frequency for the second transverse mode in the no flow condition is about 3400 Hz, but it drops

to approximately 3270 Hz for a $\overline{M} = 0.3$ grazing flow condition (see Equation A.2). For this reason, measurements in the UFSC test rig are typically kept under 3000 Hz. The inlet of the rig is connected to a compressed air system, which can supply grazing air flow inside the test sections at speeds up to $\overline{M} = 0.6$, and the available sample holders allow for the impedance measurement of liner samples up to 420 mm long, while the width of the samples is limited to the cross-section's width (100 mm). Further information about the UFSC test rig can be found in Spillere, Braga, et al. (2021) and Bonomo, Quintino, Spillere, et al. (2022).

3.2.1 Turbulent Boundary Layer Assessment

The liner's dissipation mechanisms occur at the turbulent boundary layer scale, and are strongly influenced by the grazing flow parameters (KOOI; SARIN, 1981; AVALONE; DAMIANO, 2021; BONOMO; QUINTINO; SPILLERE, et al., 2022), so a good correlation between the experimental and numerical TBLs is of primary importance in the attempt to replicate the experimental impedance results in the numerical model. In this work, the comparison between the two TBLs is performed by comparing the x component of the streamwise flow velocity U , at the upstream end of the liner sample ($x = 0$), as shown in Figure 20.

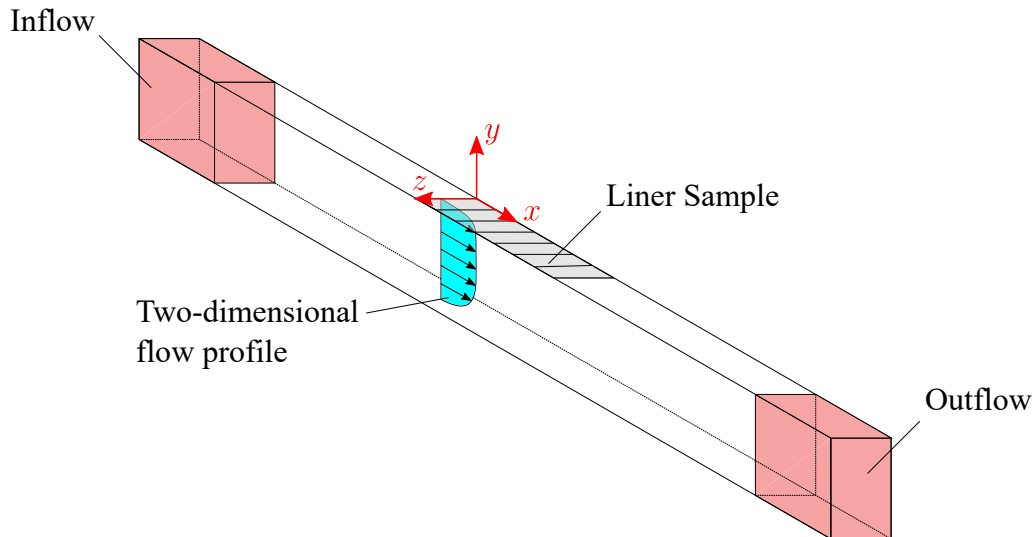
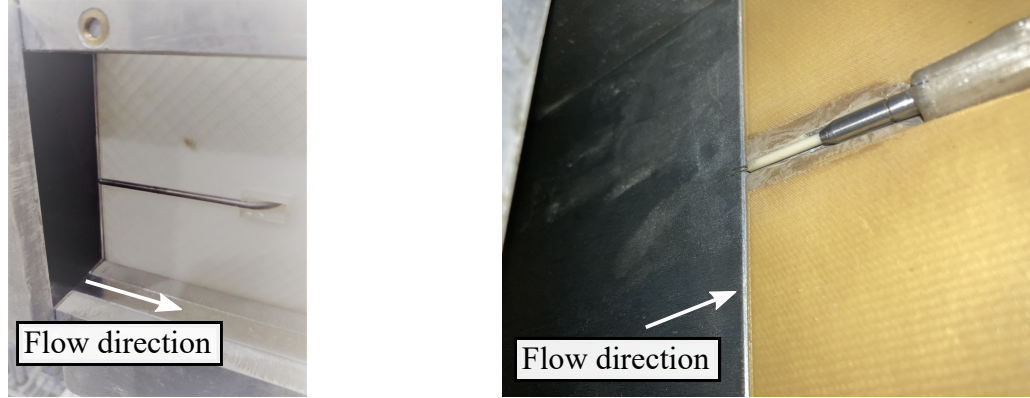


Figure 20 – Schematic representation of the location of the flow velocity field assessments.

To measure the flow experimentally, the liner sample is replaced by a customized 3D printed apparatus, designed to hold a Pitot tube or a hot-wire anemometer, as shown in Figure 21. The apparatus allow for the measuring probe to move in the y direction, along

which a set of measurements are made in the central z section of the duct. In this case, although the flow profile is three dimensional and TBLs also develop in the z direction, these features are not captured by the current measurement setup. It is worth highlighting that the experimental flow measurements are performed slightly upstream of the $x = 0$ position, in order to avoid any interference of the presence of the apparatus on the TBL parameters.



(a) Pitot tube with 3 mm external diameter.

(b) Hot-wire anemometer.

Figure 21 – Experimental assessment of the flow inside the UFSC test rig.

The analytical model presented by [Schlichting and Gersten \(2017\)](#) is used for the TBL characterization through a numerical least-square fitting procedure. The flow profile definition relies on the adjustment of two parameters: the friction velocity u_τ and the boundary layer thickness δ . It is worth mentioning that δ is very difficult to determine, thus it is often approximated by δ_{99} , i.e., the y coordinate in which $U(y) \approx 0.99U_\infty$, being U_∞ the free-stream velocity. However, this is a conceptual definition, since the choice of the 99% parameter is arbitrary and any other value (for example 98%) can be chosen, although it is usually set between 95% and 99.5% ([KUNDU et al., 2015](#), p. 475).

Taking the coordinate system of [Figure 20](#) as reference, the flow profile, as per [Schlichting and Gersten \(2017\)](#), is defined by:

$$u^\dagger = y^\dagger, \quad y^\dagger < 5; \quad (3.10a)$$

$$u^\dagger = \frac{\mathcal{K}}{\Lambda} + \frac{1}{4K} \ln(1 + KB y^{\dagger 4}), \quad 5 < y^\dagger < 70; \quad (3.10b)$$

$$u^\dagger = \frac{1}{K} \ln y^\dagger + C, \quad y^\dagger > 70; \quad (3.10c)$$

where

$$\mathcal{K} = \frac{1}{3} \left(\ln \frac{\Lambda y^\dagger + 1}{\sqrt{(\Lambda y^\dagger)^2 - \Lambda y^\dagger + 1}} \right) + \frac{1}{\sqrt{3}} \left(\tan^{-1} \frac{2\Lambda y^\dagger - 1}{\sqrt{3}} + \frac{\pi}{6} \right). \quad (3.11)$$

The flow variables indicated by the superscript ‘†’ refer to the dimensionless scale of the inner boundary layer. In Eq. 3.10, $y^\dagger = |y| u_\tau / \nu$, where ν is the fluid’s kinematic viscosity. Similarly, U relates to u^\dagger by $u^\dagger = U / u_\tau$. The other parameters are the von Kármán constant $K = 0.41$, $A = 6.1 \times 10^{-4}$, $B = 1.43 \times 10^{-3}$ and $\Lambda = (A + B)^{1/3}$, which gives $C = 5$. These parameters were defined by extensive numerical evaluations and experimental measurements (SCHLICHTING; GERSTEN, 2017).

Relevant parameters of the TBL which do not depend on any arbitrariness are the displacement thickness δ_1 and the momentum thickness δ_2 . The former represents the thickness of a zero-velocity layer that has the same velocity deficit as the actual boundary layer, while the latter expresses the momentum loss in the flow due to the presence of the boundary layer. The two parameters are defined as

$$\delta_1 = \int_{y=0}^{\infty} \left(1 - \frac{U(y)}{U_\infty} \right) dy, \quad (3.12)$$

and

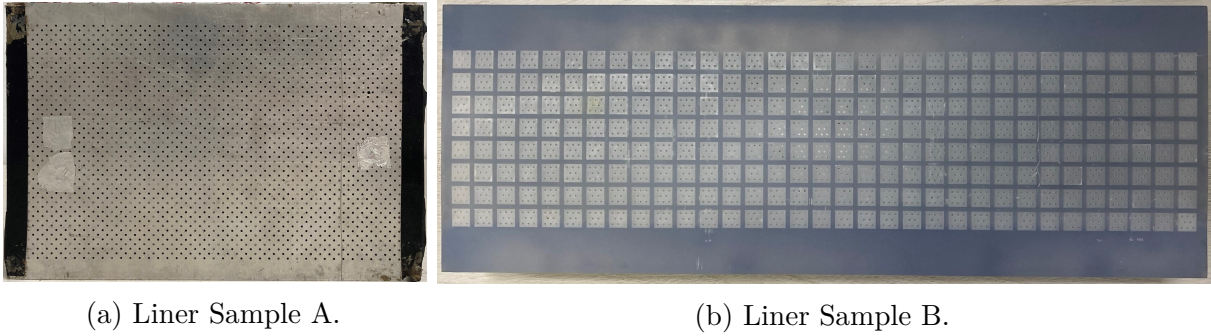
$$\delta_2 = \int_{y=0}^{\infty} \frac{U(y)}{U_\infty} \left(1 - \frac{U(y)}{U_\infty} \right) dy, \quad (3.13)$$

respectively. These parameters are calculated by numerical integration of the measured profiles, both in the experiments and in the simulations, and although well defined, their accuracy are still dependent on the spatial resolution of the measurements along the TBL.

3.2.2 Liner Geometries and Test Conditions

Two liner geometries were tested as part of the experimental campaigns for this work. The first one, called Sample A, is the same liner tested previously by Spillere, Braga, et al. (2021), made of aluminum alloy. The second sample, Sample B, was 3D printed by stereolithography process (HUANG, 2020), specifically for the scope of this work. Sample A consists of 12 rows with 18 squared cavities, each, which gives a total of 216 cavities. Sample B consists of 8 rows with 33 squared cavities, each, which gives a total of 264 cavities. The two samples are shown in Figure 22.

The following geometric parameters of the two samples are described in Table 2: sample total length L^* ; cavity width l , facesheet thickness τ ; partition walls thickness w_p ; orifices diameter d ; cavities depth h ; nominal percentage of open area σ ; effective percentage of open area σ_{eff} . The estimate resonance frequencies for Samples A and B in a static environment are approximately 1315 Hz and 1481 Hz, respectively, as per Equation 2.4.



(a) Liner Sample A.

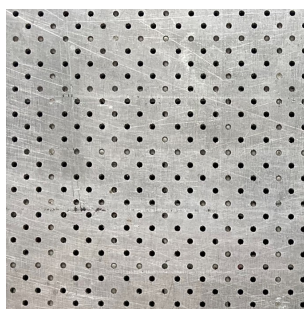
(b) Liner Sample B.

Figure 22 – Liner samples for the experimental testing campaign.

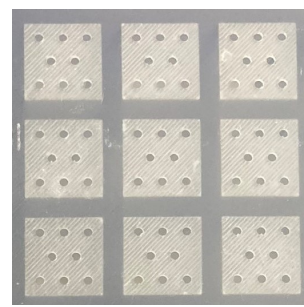
Table 2 – Geometric parameters of the liner samples tested experimentally.

	L^* [mm]	l [mm]	τ [mm]	w_p [mm]	d [mm]	h [mm]	σ [%]	σ_{eff} [%]
Sample A	210.00	9.20	1.00	0.80	1.00	38.50	5.67	4.60
Sample B	420.00	9.906	0.635	2.54	0.9906	38.10	6.30	4.20

Figure 23 exhibits in detail the facesheets of both samples. A closer look into the facesheet of Sample A reveal that some orifices are blocked by the cavity walls, which is related to its manufacturing process (SMITH, 1989, p. 145). This is not the case for Sample B, which was specially designed to avoid this issue, which affects the POA of the liner. The POA can be divided into nominal and effective, where the former is an estimate of a single cavity open area ratio and the latter relates to the whole facesheet. In the case of Sample B, both POAs can be calculated precisely, while for Sample A this is not straightforward (SPILLERE; BRAGA, et al., 2021).



(a) Facesheet of Sample A.



(b) Facesheet of Sample B.

Figure 23 – Comparison between the facesheets of the two samples tested.

The impedance of both samples was measured in the UFSC test rig by the three methods referred to in Section 3.1, in the absence and in the presence of grazing flow. Also, for the grazing flow cases, results were collected considering the acoustic sources at an upstream position relative to the liner and at a downstream position. The impedance measurements were carried out for frequencies ranging from 500 Hz to 2500 Hz. The power

of the acoustic sources was configured to provide the desired SPL at the sample upstream end. In this work, both 130 dB and 145 dB SPLs were considered.

Specifically for the in-situ measurements, it is worth mentioning that the choice of which cavity to install the probes is preferably near the end of the sample which is closer to the acoustic source, such that the effects of the liners' attenuation on the measured SPL and impedance are avoided. In this sense, Figure 24 exhibits more precisely the location on the facesheet of both Samples A and B where the experimental in-situ measurements were performed. In the case of Sample A (Figure 24a), the probes were installed in the second cavity nearest to the acoustic source in the x direction. As for Sample B, (Figure 24a), the probes were installed in the third cavity nearest to the acoustic source in the x direction, at a central spanwise position in the z direction.

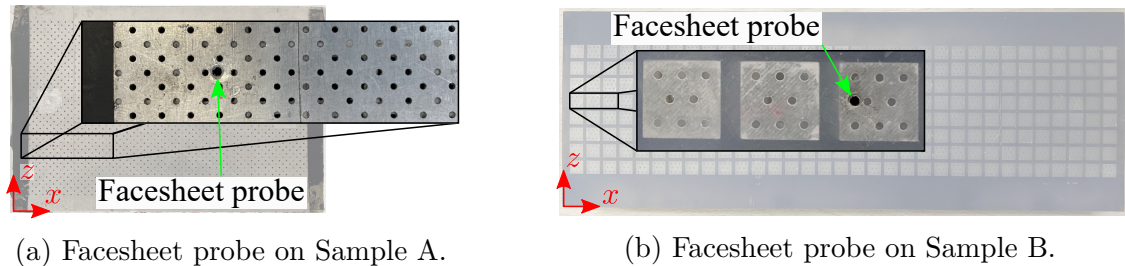


Figure 24 – Position of the facesheet probes for the experimental assessment of the liners' impedance with the in-situ technique

3.3 NUMERICAL METHOD

Mathematical representations of fluid dynamic systems are normally complex and, in most cases, lack an analytical solution. For this reason, a common approach to this kind of problem is the use of numerical schemes, known as Computational Fluid Dynamics (CFD), which can provide reasonable approximate solutions to the mathematical representations for engineering applications (GUO; SHU, 2013, p. 8).

Most of CFD schemes are continuum-based approaches, which means that the governing equations are obtained from a macroscopic description of the fluid, based on the conservations of mass, momentum and energy. In these models, molecular interaction are represented by transport coefficients, e.g., viscosity and thermal conductivity, which is a valid approach given that the Knudsen number is sufficiently small, i.e., if the particle mean free path is sufficiently smaller than the characteristic length of the system (GUO; SHU, 2013, p. 6).

Conversely, microscopic models capture the fluid dynamic behaviour by modelling each fluid particle individually, and the macroscopic parameters, such as pressure, are recovered by statistical methods. However, the applications of such approach are limited to nanometric systems with temporal scales in the order of picoseconds, due to the number of variables involved in the molecules physical state description (GUO; SHU, 2013, p. 9). In this context, there is a growing interest for multiple scales systems, for which the macro and microscopic models are both inadequate, due to the high Knudsen number in the regions with small characteristic lengths and to the high computational cost, respectively (GUO; SHU, 2013, p. 8). An appealing alternative to multiple scales systems is the use of numerical schemes at a mesoscopic scale, such as the lattice Boltzmann method.

3.3.1 The Lattice Boltzmann Method

The lattice Boltzmann method (LBM) is a computational mesoscopic method applied to the solution of fluid dynamic problems based on the first order approximation of the Boltzmann equation (GUO; SHU, 2013, p. 3-16). This section gives a general description of the LBM formulations and definitions, that can be found in more details in texts like Succi (2001), Guo and Shu (2013) and Krüger et al. (2017).

The LBM has its origins in the molecular kinetic theory of gases, commonly applied to model dilute monoatomic gases, in which the state of the fluid is given statistically in terms of the particle distribution function $\mathbf{f} = \mathbf{f}(\mathbf{x}, \boldsymbol{\xi}, t)$, which provides a statistical measure of the number of particles per unity of volume in the phase-space. In other words, \mathbf{f} defines the particle density in the \mathbf{x} coordinate moving with velocity $\boldsymbol{\xi}$ at a certain time t . The time and spacial evolution of \mathbf{f} is given by the Boltzmann equation (BE)

$$\frac{\partial \mathbf{f}}{\partial t} + \boldsymbol{\xi} \frac{\partial \mathbf{f}}{\partial \mathbf{x}} + \frac{d\boldsymbol{\xi}}{dt} \frac{\partial \mathbf{f}}{\partial \boldsymbol{\xi}} = \Omega(\mathbf{f}), \quad (3.14)$$

where $\Omega(\mathbf{f}) = d\mathbf{f}/dt$ is a source term called the collision operator, which represents the local redistribution of the particles due to their collisions. Nevertheless, the analytical solution of the BE is rather difficult, even harder than it is to solve the Navier-Stokes equation (NSE). On the other hand, numerical schemes for the discretized form of the BE are considerably simple to implement. Moreover, this approach is able to provide straightforward solutions for the fluid's advection terms, as opposed to the traditional continuum-based CFD techniques. These can be considered the main advantages of using the LBM over conventional CFD solvers (KRÜGER et al., 2017, p. 62). Recent works

have demonstrated the potential and robustness of the LBM in applications related to fluid dynamics and aeroacoustics (MANJUNATH et al., 2018; CASALINO; HAZIR, et al., 2018; SILVA; GRECO, 2019).

Numerically, the continuous velocity space is discretized by Hermite orthogonal polynomials expansions into a finite number of directions, so as to provide the discrete-velocity distribution function $\mathbf{f}_i(\mathbf{x}, t)$, where the subindex i denotes a discrete velocity direction \mathbf{c}_i (SHAN et al., 2006). The distribution of particles, given by \mathbf{f}_i , is stored in a Cartesian mesh, known as lattice. Each numerical scheme has its dimensionality and its finite number i of velocity directions, that gives the scheme's designation. For three-dimensional systems, a common numerical scheme is the D3Q19, which consists of 19 velocity directions. Figure 25 shows a lattice element from the D3Q19 scheme, where the 19th velocity component is located at the centre of the element and represents a resting group of particles.

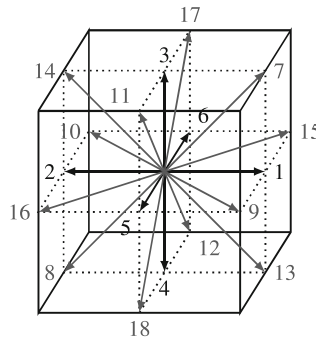


Figure 25 – Lattice element from a D3Q19 numerical scheme. Source: Krüger et al. (2017, p. 87).

The numerical solution by the LBM follows a time-marching scheme dictated by a discrete form of the BE, written as

$$\mathbf{f}_i(\mathbf{x} + \mathbf{c}_i \Delta t, t + \Delta t) - \mathbf{f}_i(\mathbf{x}, t) = C_i(\mathbf{x}, t), \quad (3.15)$$

where Δt is the time increment (or time step) and $C_i(\mathbf{x}, t)$ is a simplified collision term proposed by Bhatnagar et al. (1954), also known as the Bhatnagar, Gross and Krook (BGK) collision operator. The BGK operator is given by

$$C_i(\mathbf{x}, t) = -\frac{\Delta t}{\tau} [\mathbf{f}_i(\mathbf{x}, t) - \mathbf{f}_i^{\text{eq}}(\mathbf{x}, t)], \quad (3.16)$$

where τ is a time constant, called relaxation time (SILVA; GRECO, 2019). This constant determines the rate in which the system evolves towards an equilibrium state, and it is

directly related to macroscopic transport coefficients, e.g., viscosity and heat diffusivity. The equilibrium state, which is achieved by the gas if it has been left alone for a sufficient amount of time, is given by the equilibrium distribution functions \mathbf{f}^{eq}_i . In the equilibrium state, the system becomes isotropic in the velocity space, which means that $\mathbf{f}_i = \mathbf{f}^{\text{eq}}_i$ (KRÜGER et al., 2017, p. 22-23). The \mathbf{f}^{eq}_i functions play a role in every time step of a LBM solution, which consists of two sub-steps: collision (or relaxation) and streaming (KRÜGER et al., 2017, p. 65-66). In the relaxation sub-step, the system is forced to reach a local thermodynamic equilibrium state, by means of the BGK collision operator, and a new temporary distribution function is defined

$$\mathbf{f}_i^{\circ}(\mathbf{x}, t) = \mathbf{f}_i(\mathbf{x}, t) + C_i(\mathbf{x}, t). \quad (3.17)$$

Later, in the streaming sub-step, the time increment (Δt) is applied to the system by forcing every \mathbf{f}_i° to advect from one element of the grid to an adjacent one, in the direction of the respective \mathbf{c}_i component, as per

$$\mathbf{f}_i(\mathbf{x} + \mathbf{c}_i \Delta t, t + \Delta t) = \mathbf{f}_i^{\circ}(\mathbf{x}, t). \quad (3.18)$$

The \mathbf{f}^{eq}_i are defined as a discrete form of the Maxwell distribution function, derived by the application of the maximum entropy principle based on mass and momentum conservation constraints, given by

$$\mathbf{f}^{\text{eq}}_i = \rho_0 w_i \left(1 + \frac{\mathbf{c}_i \cdot \mathbf{u}}{T} + \frac{(\mathbf{c}_i \cdot \mathbf{u})^2}{2T^2} - \frac{\mathbf{u}^2}{2T} + \frac{(\mathbf{c}_i \cdot \mathbf{u})^3}{6T^3} - \frac{\mathbf{c}_i \cdot \mathbf{u}}{2T^2} \mathbf{u}^2 \right), \quad (3.19)$$

where ρ , \mathbf{u} and T are the fluid's macroscopic local mass density, mean velocity and temperature, respectively (WOLF-GLADROW, 2006; SILVA; GRECO, 2019). The w_i constants are weighing coefficients for the \mathbf{c}_i velocities, which in the case of the D3Q19 scheme are defined as

$$w_i = \begin{cases} 1/18 & \text{for } i = 1, 2, \dots, 6; \\ 1/36 & \text{for } i = 7, 8, \dots, 18; \\ 1/3 & \text{for } i = 19. \end{cases} \quad (3.20)$$

It is possible to obtain macroscopic parameters of the system, which are more suitable for engineering applications, through the moments of the discrete-velocity distribution function, e.g, the macroscopic mass density

$$\rho(\mathbf{x}, t) = \sum_i \mathbf{f}_i(\mathbf{x}, t), \quad (3.21)$$

and the macroscopic momentum density,

$$\rho(\mathbf{x}, t) \mathbf{u}(\mathbf{x}, t) = \sum_i \mathbf{c}_i \mathbf{f}_i(\mathbf{x}, t). \quad (3.22)$$

One can formally relate the mesoscopic and the macroscopic parameters through a scale expansion technique, known as the Chapman-Enskog analysis (CHEN; CHEN, et al., 1992). As a result, the relation between the relaxation time and the fluid's kinematic viscosity can be written as

$$\nu = c_s^2 \left(\tau - \frac{\Delta t}{2} \right), \quad (3.23)$$

where $c_s = 1/\sqrt{3}$ is the model's isothermal speed of sound. The c_s parameter is defined in lattice units, which is a dimensionless auxiliary unit system, set to ease the model's implementation. One can define $c_s^2 = \Delta x^2 / (3\Delta t^2)$, given that $\Delta x = 1$ is the lattice element size, $\Delta t = 1$ is the solution's time increment, $\rho_L = 1$ is the fluid's mass density and $T_L = 1/3$ is the fluid's temperature, all of which are in lattice units (SILVA; GRECO, 2019). From the isothermal equation of state, it is also possible to state the relation $p = c_s^2 \rho$ (KRÜGER et al., 2017, p. 63-65).

The interaction between a fluid particle and any solid surface inside the solution's domain can be dictated by two boundary conditions: the slip and the no-slip. The slip BC enforces only the normal component of the fluid velocity to be zero while placing no restrictions on the tangential fluid velocity. On the other hand, the no-slip BC restricts both the normal and tangential components of the fluid velocity on the wall. Figure 26a represents the collision of particles with a surface set as a slip BC, represented by the dashed line. In this case, the particles advect to the adjacent node with the normal velocity components flipped in time $t + \Delta t$, with respect to the time instant t . Figure 26b represents the collision of particles with a no-slip wall, represented by the bold solid line, that enforces the particles' velocity to be totally reflected.

A third boundary condition widely used in LBM numerical schemes is the periodic BC, which is usually applied to pairs of opposite limits of the computational domain. In this case, fluid particles leaving the domain on one side will re-enter at the opposite side, instantaneously. This BC conserves mass and momentum at all times (KRÜGER et al., 2017, p. 171). Figure 27 represents the interaction between particles and the periodic BC.

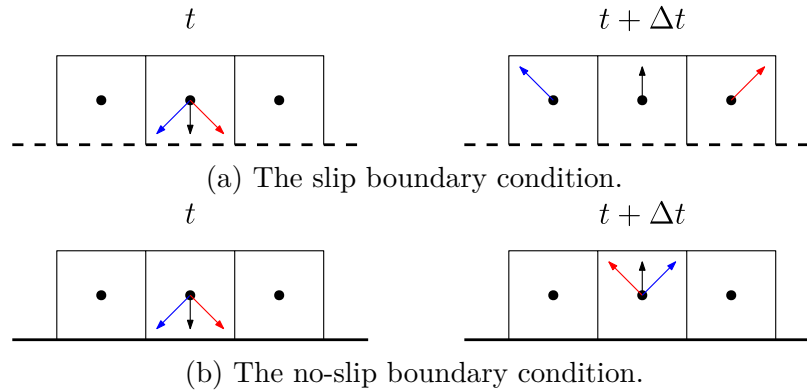


Figure 26 – Typical surface boundary conditions for the lattice Boltzmann method.

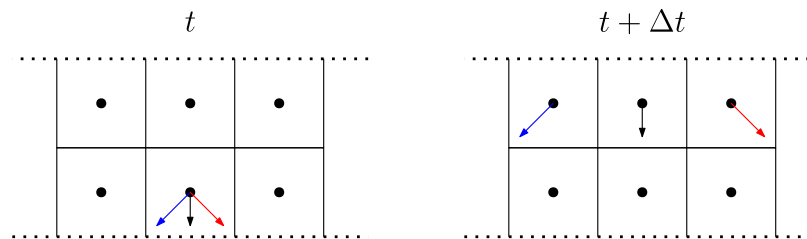


Figure 27 – Periodic boundary condition for the lattice Boltzmann method.

3.3.2 Characteristics of the Solver

In this work, the numerical simulations are performed with the commercial LBM package *3DS-Simulia PowerFLOW v.6*, which uses a D3Q19 lattice scheme to discretize the three-dimensional numerical domain. This solver applies a variable resolution (VR) scheme for the lattice grid, that can be used to provide better refinement in specific regions of the computational domain. Each increase in the grid refinement is defined by the division of the adjacent elements' size by a factor of 2, as represented by Figure 28. The conservation of mass and momentum between the different VRs is ensured by the grid refinement algorithm presented by [Chen, Filippova, et al. \(2006\)](#).

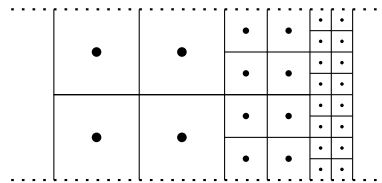


Figure 28 – Variable resolution in the lattice grid.

Because of the high Reynolds number found in the cases of interest, a VLES approach is adopted. This means that only large turbulent scales are resolved, while the effects of sub-grid scales are modelled using statistical representations for the turbulence. A turbulence model based on the two-equation Renormalization Group Theory (RNG) $\kappa - \varepsilon$

is used in the solution to account for sub-grid turbulent scales (YAKHOT; ORSZAG, 1986). This is done by incorporating an effective relaxation time, which adjusts the Boltzmann model to the characteristic turbulent time scale, and it is given by

$$\tau_{\text{eff}} = \tau + C_{\mu} \frac{\kappa^2 / \varepsilon}{T (1 + \tilde{\eta}^2)^{1/2}}, \quad (3.24)$$

where C_{μ} is a constant closure coefficient and $\tilde{\eta}$ is a correction term to account for local strain, vorticity and helicity effects (KOTAPATI et al., 2009; SILVA; GRECO, 2019). The equations for the turbulent kinetic energy κ and the dissipation ε are obtained from the modified RNG turbulence model (TEIXEIRA, 1998).

The high Reynolds numbers imply high velocity gradients at the inner regions of the viscous boundary layer, in the wall normal direction. Because of nature of the LBM formulation, it is necessary to incorporate a wall model to account for the no-slip BC on solid walls. This is achieved by a pressure-gradient-extended wall-model, that is assumed to obey a universal flow velocity profile, known as the Law of the Wall (TEIXEIRA, 1998; AVALONE; MANJUNATH, et al., 2019; SCHROEDER et al., 2021).

3.3.3 Computational Domain and Simulation Procedures

The computational domain used in this study was developed to mimic the UFSC test rig. However, in order to save computational resources, the test rig and the liner geometries were simplified for the purpose of the simulations. Taking as reference the coordinate system presented in Figure 7, only a single row of eleven cavities was considered in the model in the streamwise direction (x axis). This way, the width W of the modelled rig (z axis) was limited to the width of the cavity, plus the partition walls thickness. Periodic BCs were applied, as shown in Figure 29, in the z direction, which is a consistent approach found in several works (MANJUNATH et al., 2018; AVALONE; MANJUNATH, et al., 2019; AVALONE; DAMIANO, 2021; SCHROEDER et al., 2021).

Two liner geometries were simulated, as previously mentioned in Section 3.2.2. Because of the simplifications made in the numerical approach, the modelled geometries had slightly different parameters than the ones presented in Table 2, for the real samples. The main differences were related to the streamwise length of the sample L . Since only eleven cavities of each liner were considered in the streamwise direction, the ratio L/L^* was approximately 0.52 for Sample A and only 0.33 for Sample B. In the case of Sample A, other differences can be highlighted. The model for Sample A is the same as the one used

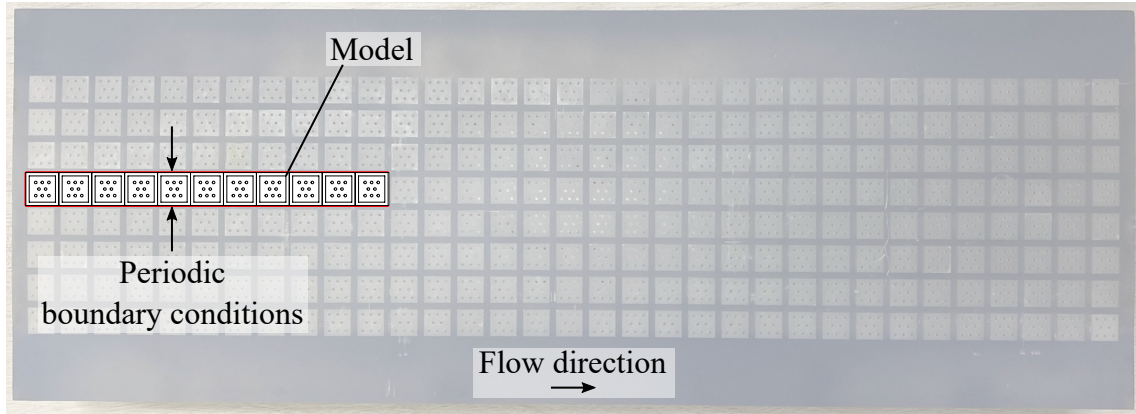


Figure 29 – Comparison between the real Sample B and the modelled geometry for the simulations.

by [Schroeder et al. \(2021\)](#), and so the model's facesheet was 0.2 mm thinner than that found in the real sample. Nevertheless, since the effect of these differences on the measured impedance are minor (see Section 2.4.1), the results for this sample were still considered for the purposes of this work. Furthermore, the nominal percentage of open area in the real Sample A is not constant over all cavities. Due to the manufacturing process, some orifices end up partially or completely blocked, and this characteristic is not represented in the numerical model. Figure 30 shows the simulated liner geometries, while Table 3 describes their geometric parameters.

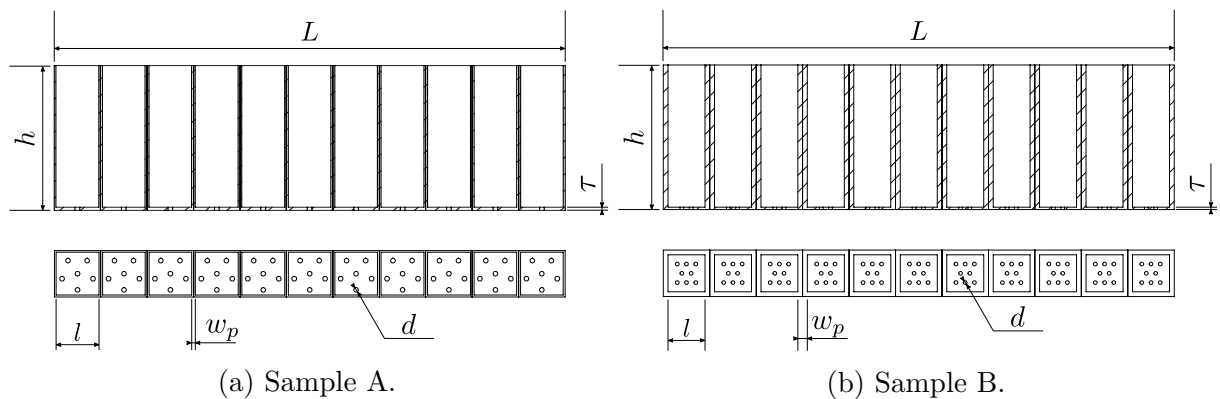


Figure 30 – Numerical models of the liner geometries.

Table 3 – Geometric parameters of the modelled liner samples.

	L [mm]	l [mm]	τ [mm]	w_p [mm]	d [mm]	h [mm]	σ [%]
Sample A	110.00	9.20	0.80	0.80	1.00	38.50	5.60
Sample B	136.906	9.906	0.635	2.54	0.9906	38.10	6.30

The computational domains used to simulate Samples A and B were slightly different.

The reason is that the simulations with Sample A were conducted prior to the beginning of the studies with Sample B, so there were few modifications in this process, as attempts to improve impedance results (as it will be further explored in Chapter 4).

Figure 31 shows the whole computational domain used to simulate Sample A. The channel's inlet and outlet are represented by the orange rectangles. A prescribed velocity BC was used at the inlet, where a proper target value was set in order to initiate the grazing flow. As for the outlet, a static pressure BC was prescribed, equal to the typical ambient pressure (101325 Pa, or 1 atm).

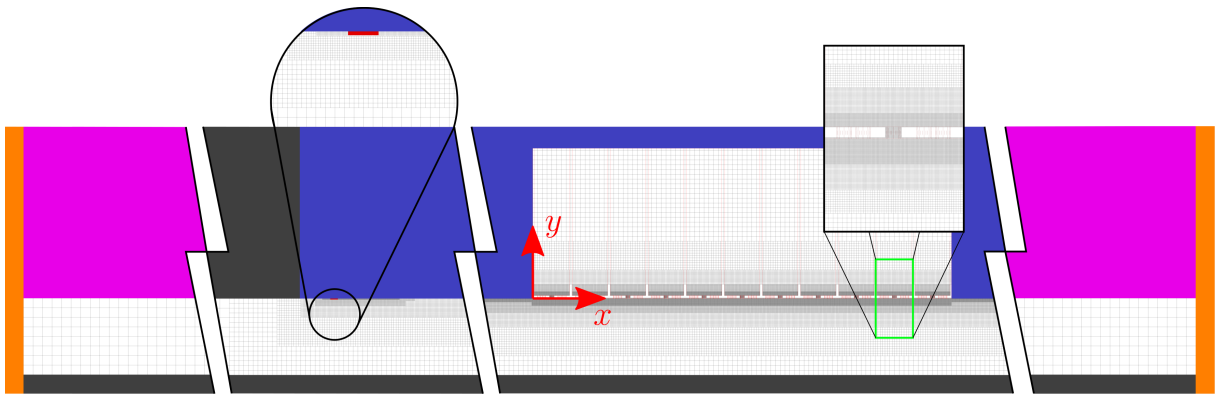


Figure 31 – Computational domain for the simulations with Sample A.

As shown in Figure 31, the lattice generation uses a VR scheme. The finest resolutions were set in the near-wall regions to provide a proper solution of the TBL, including the regions inside the liner's orifices. The finest resolution level in the liner's orifices was used as reference for the discretization of the domain. Taking the highlighted details of Figure 31, a zigzag geometry can be found on the left-hand side, which was placed on the top wall at a specific x position to trigger the VLES algorithm. The zigzag geometry is a turbulence trigger strip, as shown in Figure 32, and its size and position were adjusted manually to provide a proper match between the experimental velocity profile of the UFSC test rig and the one obtained from the simulations at $x = 0$, as it will be shown in Sections 4.1.2 and 4.2.2.

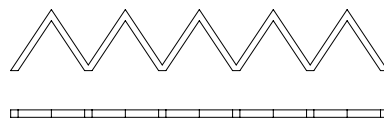


Figure 32 – Turbulence trigger (zigzag strip).

An orifice of the liner is highlighted on the right-hand side of Figure 31. It can be seen that the resolution of the grid is the finest inside the orifice and in its surroundings,

while it becomes coarser inside the cavity and towards the centre line of the channel. Similarly, the refinement of the grid becomes coarser towards the channel's terminations, to save computational resources. Moreover, to ensure a quasi-anechoic condition and prevent acoustic perturbations to be reflected at the channel's terminations, the viscosity of the fluid was significantly raised in the purple regions of Figure 31, creating absorption regions. As shown in Figure 33, this parameter is controlled by the ratio ν/T , which is artificially increased from its default value in the middle of the channel by a factor of one hundred in the absorbent regions. This was done gradually in adjacent regions to the channel's terminations, according to an exponential function of x over a $1.5\lambda_{\max}$ length, where λ_{\max} corresponds to the largest wavelength considered in this set of simulations. The raised ν/T parameter remains constant over a length of $3\lambda_{\max}$, until the end of the channel. This strategy can provide sufficiently high absorption coefficients in the channel's terminations, above 98% for the frequency range considered (AVALLONE; MANJUNATH, et al., 2019; SCHROEDER et al., 2021).

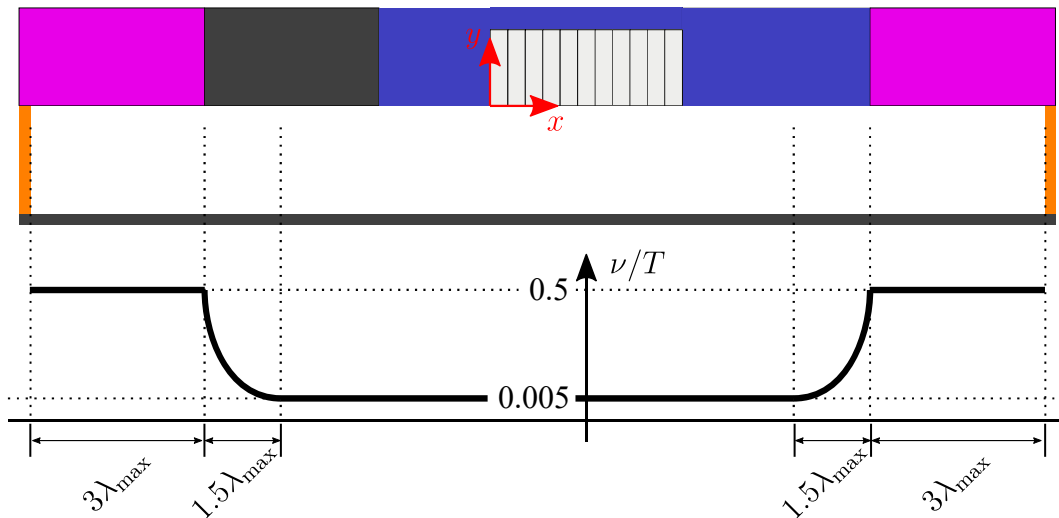


Figure 33 – Artificial variation of the fluid's viscosity in the absorbent regions. Source: adapted from Schroeder (2020, p. 59).

All the walls in the computational domain were set as adiabatic. The grey and blue coloured walls represented in Figures 31 and 33 were set as slip and no-slip BCs, respectively. The top wall was divided into slip and no-slip portions, the latter closer to the liner. This was considered a reasonable approach, as the TBL needs an optimal entrance length to develop and match the experimental flow velocity profile, but at the same time the channel had to be very long for the acoustic simulations, as it will be further explained in this Section. To save computational resources, the TBL on the bottom wall was not

resolved in the setup for Sample A, as shown in Figure 31, since a slip BC was imposed in that region. This meant that only half the height of the UFSC test rig was considered in the model, which was $H = 20$ mm high.

For the simulations with Sample B, the channel was fully modelled in the y direction with a $2H = 40$ mm height, and both the TBLs on the top and bottom walls of the channel were resolved, as shown in Figure 34. For this purpose, the discretization scheme used in the near-wall regions on the top were mirrored to the bottom wall, with the exception of the two finest VRs, applied to the regions near to the liner's orifices and to the turbulence triggers.

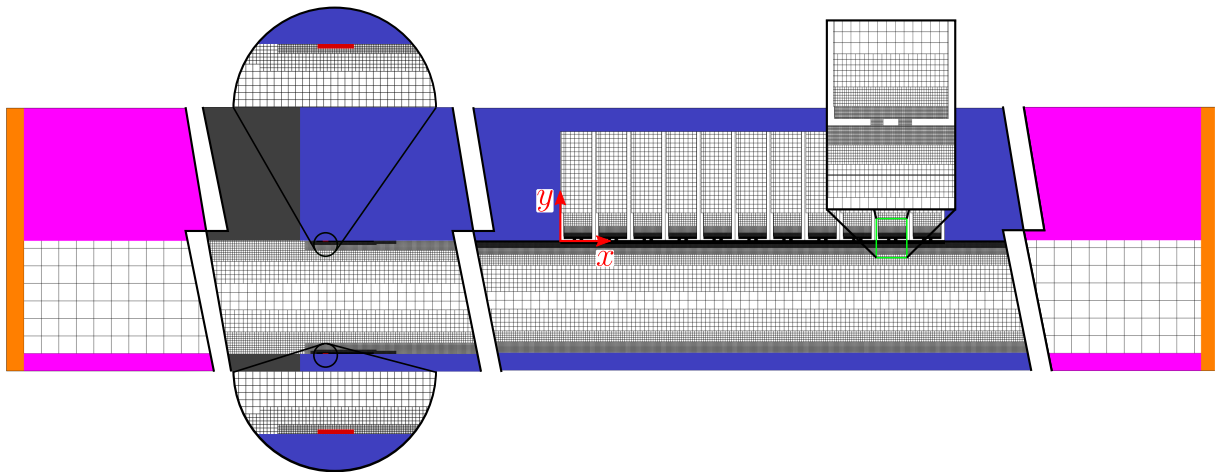


Figure 34 – Computational domain for the simulations with Sample B.

Figure 35 shows the setup for the simulations with Sample B and the different VRs in evidence, where VR 10 is the finest. As mentioned previously in Section 3.3.2, different refinement levels in a lattice are related by a constant factor 2, such that the size of all cells can be obtained from the size of the smallest ones.

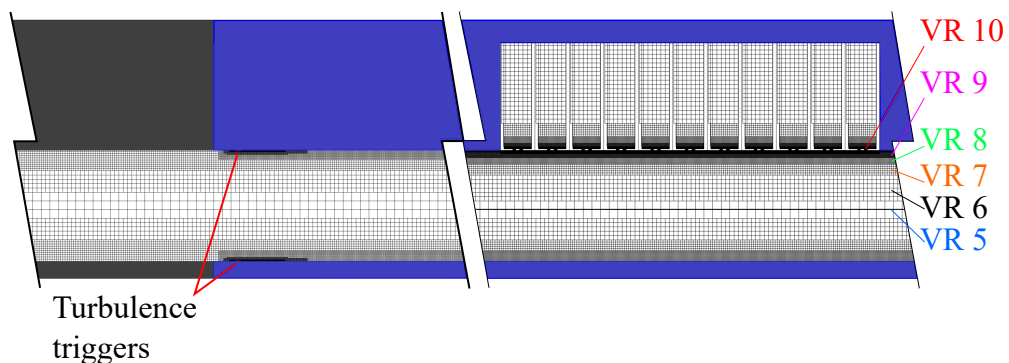


Figure 35 – Variable resolutions of the computational domain for the simulations with Sample B.

The simulations carried out in this work considered different resolution levels, namely

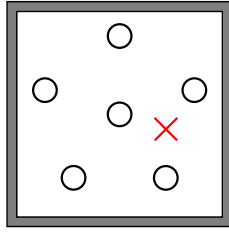
Coarse, Medium and Fine, which were chosen based on previous works involving LBM simulations of acoustic liners (MANJUNATH et al., 2018; AVALLONE; DAMIANO, 2021). However, the resolution levels correspond to different lattice cell sizes regarding the two liners simulated, as described in Table 4.

Table 4 – Discretization levels considered for the simulations: size of the smallest lattice elements (VR10) and number of cells per orifice diameter (in parenthesis).

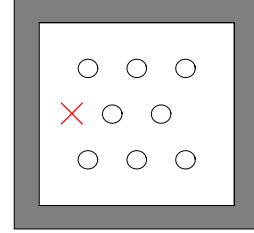
Resolution	Sample A	Sample B
Coarse	-	9.72×10^{-5} m (10 cells/ d)
Medium	3.91×10^{-5} m (25 cells/ d)	4.86×10^{-5} m (20 cells/ d)
Fine	1.95×10^{-5} m (50 cells/ d)	2.43×10^{-5} m (40 cells/ d)

The results of the simulations were assessed by sampling different surfaces from the domain. For the application of the in-situ technique, both the facesheet and the backplate were sampled. Following the same approach as Schroeder et al. (2021), the numerical results presented in this work for Sample A are in the form of an averaged value among all cavities, which were sampled in the facesheet position shown in Figure 36a. However, it is known that both impedance and SPL vary along the liner length, and averaging results over the cavities masks these variations and possibly hinders the comparisons with the experiments. For better consistency, the numerical results from Sample B were obtained for a single facesheet probe placed in a similar position as in the experiments (as depicted in Figure 36b). In the simulations, the first cavity closest to the acoustic source was evaluated, as opposed to the experimental measurements which were obtained in the third cavity. The backplate probes in the simulations were positioned in the centre of the cavities, for both samples. Alternatively, this work also presents impedance contour plots calculated with the in-situ technique, which were obtained by sampling the entire facesheet, as this is possible with the numerical simulations.

In the case of the eduction methods, a streamwise measurement plane was created in the domain, symmetrically positioned in the middle of the sample. The total length considered for this plane was 1.28 m, as shown in Figure 37, which allowed for the extraction of pressure time series in any coordinate within the plane for the post-processing. For the



(a) Facesheet probe on Sample A.



(b) Facesheet probe on Sample B.

Figure 36 – Position of the facesheet probes for the numerical assessment of the liners' impedance with the in-situ technique

MM method impedance education, two arrays of 22 pressure probes are located along the centre line of the channel at $y = -H$ and $z = W/2$, to minimize turbulence noise in the signal. The probes are evenly spaced in the streamwise direction and are positioned at $W \leq |x| \leq W + 2L$, with a spacing of 1/2 inch between each probe. For the KT algorithm procedure, 10 pressure probes are considered, whose x coordinates are aligned with the partition walls of the liner samples, i.e., $x_i = iW$, for $i = 1, 2, \dots, 10$.

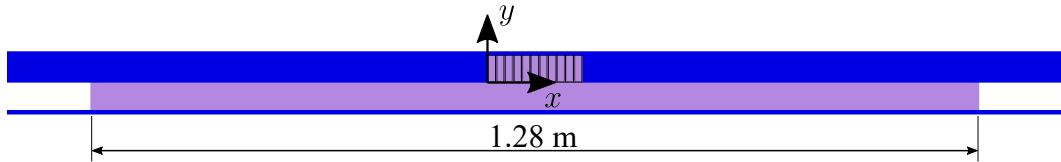
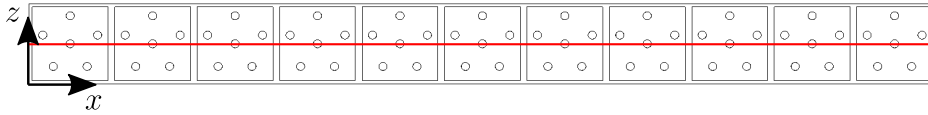


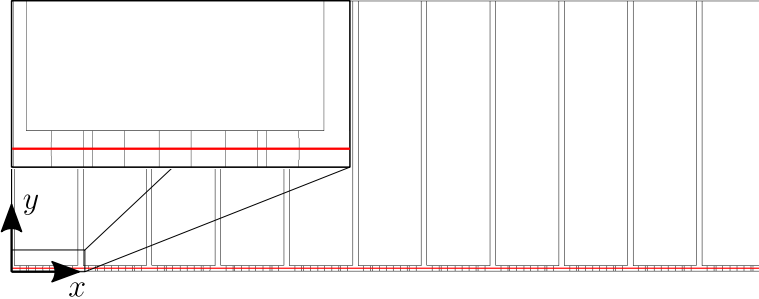
Figure 37 – Location and length of the streamwise measurement planes.

The physical phenomena that takes place near the orifice regions has a strong influence on the liner absorption mechanisms. In this sense, the streamwise plane was set to match the centre of the liner's orifices, to allow for flow visualizations in these regions. Figures 38a and 39a show the streamwise plane set for the simulations with Sample A and B, respectively. Other measurement planes were set in the normal y direction, parallel to the orifices' cross sections, for the evaluation of the acoustically induced velocity profiles and mass flux inside the orifices, as shown by Figures 38b and 39b.

The general procedure for the simulations involving grazing flow was to consider a coarser variation of the setup, that removes near wall high resolution regions, to establish the pressure gradient within the channel. The results of the coarser variation are used to seed higher resolution cases, i.e., the coarser resolution results are the starting point of finer resolution simulations. The statistical convergence of the velocity field is assessed by the evaluation of the time history of the boundary layer thickness δ , the friction velocity u_τ and the maximum Mach number M . It is considered that the flow velocity field has converged

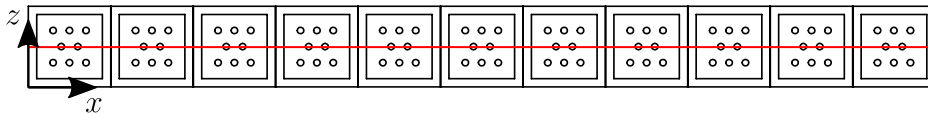


(a) Streamwise measurement plane.



(b) Spanwise measurement plane.

Figure 38 – Measurement planes for the simulations with Sample A.



(a) Streamwise measurement plane.



(b) Spanwise measurement plane.

Figure 39 – Measurement planes for the simulations with Sample B.

after a relative deviation within a 1% range is verified for all parameters simultaneously.

The acoustic simulations were performed by superimposing a harmonic acoustic plane wave to the fluid domain by means of the *OptydB* toolkit (AVALLONE; DAMIANO, 2021), which is an add-on software package for the solver. The general procedure was as follows: first, the statistical convergence of the flow pressure and velocity fields was assessed, as previously described (even for the acoustic simulations without grazing flow effects, still a static fluid domain needs to be generated); second, the fluid domain was exported; the exported fluid domain was modified by the *OptydB fieldmod* algorithm, which imposes a harmonic pressure variation with a specific pure tone frequency and SPL; lastly, the modified fluid domain was used to seed another simulation, and the acoustic waves were

let to propagate within the channel. Figures 40a and 40b show the superimposed harmonic pressure oscillations at upstream and downstream positions, respectively, for a case without grazing flow.

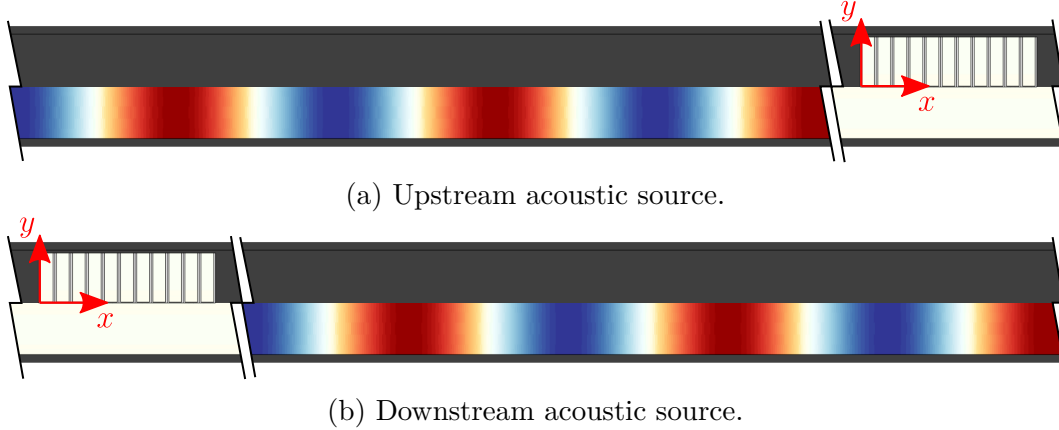


Figure 40 – Acoustic harmonic perturbations superimposed in the computational fluid domain. Red colors denote positive pressure variations, while blue colors are for negative variations.

Considering that the number of acoustic pressure cycles sampled by the planes strongly impacts the frequency domain resolution for post-processing analysis, a very long channel is necessary to accommodate a reasonable number of pressure cycles. In this work, the total length of the modelled channel was approximately 18025 mm, with the liner sample positioned in its midsection. This setup was long enough to accommodate a minimum of 10 acoustic pressure cycles for the lowest frequency considered, which was 800 Hz, in an upstream source case, for which the waves propagate in the same direction as a $M = 0.3$ grazing flow.

Several parameters need to be defined during the setup of the simulations, regarding the fluid properties and the initial conditions. Table 5 describes these parameters, which were applied to the whole fluid domain as initial conditions, except when a simulation was seeded with a previously exported fluid domain. In this case, the initial conditions were suppressed and only the BCs played their roles.

The initial conditions and fluid parameters were chosen to represent the air at 298.15 K, as the fluid for the simulations. The characteristic velocity is the speed of sound $c_0 = \sqrt{\gamma RT}$, where γ is the air's specific heat ratio, R is the air's specific gas constant and T is the temperature.

Overall, 45 scenarios were simulated in this study, which are summarized in Table 6. For the cases involving grazing flow effects, both upstream (U) and downstream (D)

Table 5 – Global parameters and initial conditions for the simulations.

Parameter	Value	Units
Initial Pressure	101325	Pa
Initial x Velocity	Mc_0	m s^{-1}
Initial y Velocity	0.0	m s^{-1}
Initial z Velocity	0.0	m s^{-1}
Initial Temperature	298.15	K
Initial Turbulence Intensity	0.01	-
Initial Turbulence Length Scale	0.1	mm
Characteristic Velocity	346.15	m s^{-1}
Characteristic Viscosity	1.552×10^{-5}	$\text{m}^2 \text{s}^{-1}$
Characteristic Length	L	m
Characteristic Area	LW	m^2
Ideal Gas Constant	8.314	$\text{J K}^{-1} \text{mol}^{-1}$
Molecular Weight	28.965×10^{-3}	kg kmol^{-1}
Air's Specific Gas Constant	287.057	$\text{J kg}^{-1} \text{K}^{-1}$
Specific Heat Ratio	1.4	-
Constant-Pressure Specific Heat	1004.7	$\text{J kg}^{-1} \text{K}^{-1}$
Prandtl Number	0.707	-

acoustic sources were considered. As for the no-flow simulations, only upstream acoustic source cases were simulated, since the change in the position of the acoustic source is not expected to change the measured impedance in this scenario.

Table 6 – Test matrix for the simulations with both liner samples.

	Sample A			Sample B		
	$M = 0$	$M = 0.3$		$M = 0$	$M = 0.32$	
	(U)	(U)	(D)	(U)	(U)	(D)
800 Hz	✓	✓	✓	✓	✓	✓
1100 Hz	✓	✓	✓			
1400 Hz	✓	✓	✓	✓	✓	✓
1700 Hz	✓	✓	✓			
2000 Hz	✓	✓	✓	✓	✓	✓
2300 Hz	✓	✓	✓			

Acoustic sources at both 130 dB
and 145 dB were considered.

The flow and acoustic simulations were conducted with high performance computing clusters, namely: the HPC Prometheus². at PSNC@CYFRONET, located in Poland; the

² <https://www.cyfronet.pl/en/computers/15226,artykul,prometheus.html>. Access on May 25th, 2023.

HPC Snellius³. at SURFsara@SURFsara, located in The Netherlands; the HPC12⁴ of the Flow Physics and Technology department from TU Delft, located in The Netherlands.

³ <https://www.surf.nl/en/dutch-national-supercomputer-snellius>. Access on May 25th, 2023.

⁴ <https://hpcwiki.tudelft.nl/index.php/Introduction>. Access on May 25th, 2023.

4 ACOUSTIC IMPEDANCE RESULTS

In this Chapter, the impedance results obtained with the simulations for Samples A and B are presented. These results are compared with experimental data obtained in the UFSC test rig and with the Goodrich semiempirical model predictions. The results are based on the three impedance measurement techniques described in Section 3.1.

For each liner sample, the subsections are organized as follows: the impedance results in the absence of grazing flow are presented first; then, the turbulent boundary layer obtained from the simulations is compared with experimental measurements from the UFSC test rig flow profile; afterwards, a discussion on the impedance measurements in the presence of grazing flow is carried out for acoustic sources located at both upstream and downstream positions, with respect to the liner; lastly, a summary of the model's capabilities is presented with a description of the different settings that were tested.

4.1 LINER SAMPLE A

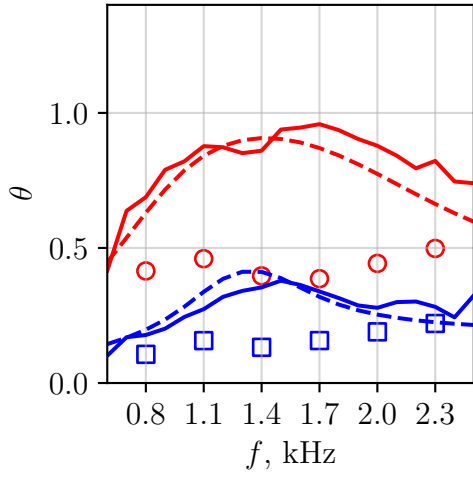
The simulations carried out with Sample A were the starting point of this project. These results were obtained with the 2021-R2 release of the solver ([POWERFLOW...](#), 2021), and are also available in [Pereira, Bonomo, Silva, et al. \(2022\)](#).

4.1.1 Impedance in the Absence of Grazing Flow

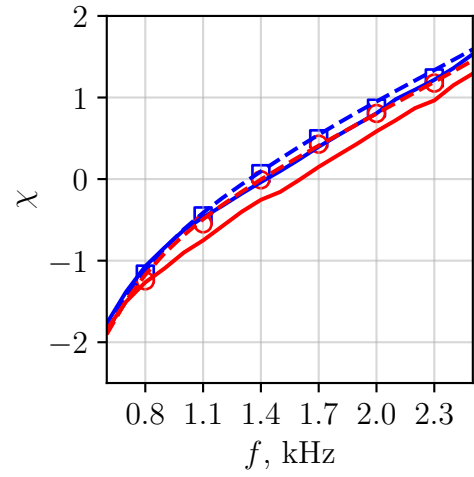
Simulations were performed to evaluate the liner's impedance in the absence of grazing flow. These simulations were carried out with a medium resolution setup (see Table 4), i.e., 25 cells/ d , which was considered a reasonable discretization level by a previous work ([SCHROEDER et al., 2021](#)).

Figure 41 presents the simulations' impedance results obtained for acoustic sources at 130 dB and 145 dB, in comparison with the experimental measurements and with the semiempirical model predictions. From the experiments, it is found that the different impedance measurement techniques deliver different results, even in the case of the acoustic excitation at 130 dB, although all the methods are in a reasonable range of agreement with each other.

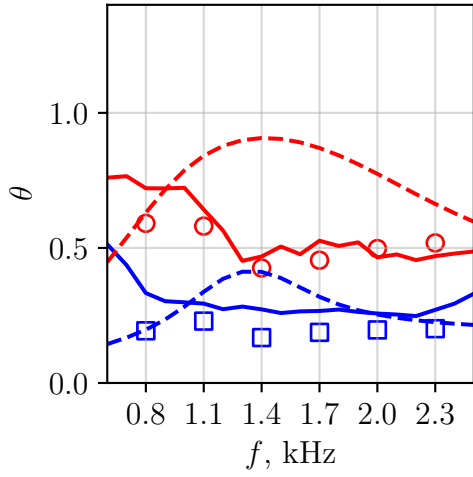
The resistance results obtained experimentally with the in-situ technique (Figure 41a) exhibit a bump near 1400 Hz, which is related to the liner's resonance. The resistance



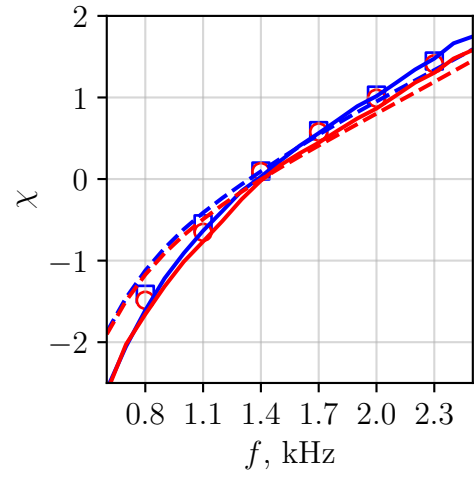
(a) Resistance, In-Situ.



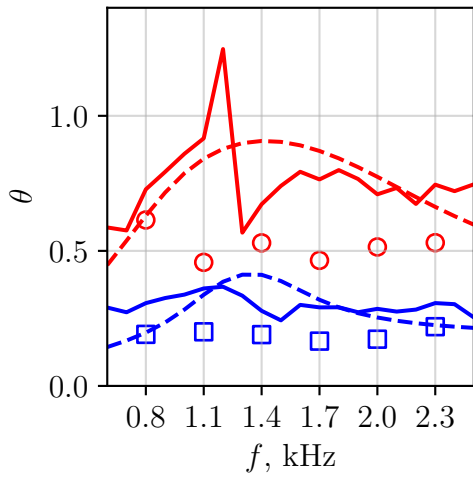
(b) Reactance, In-Situ.



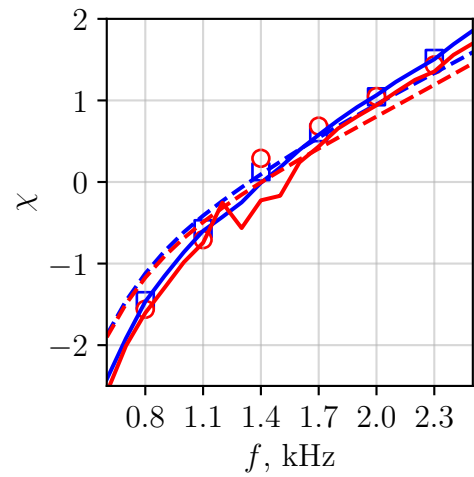
(c) Resistance, MM Method.



(d) Reactance, MM Method.



(e) Resistance, KT Algorithm.



(f) Reactance, KT Algorithm.

Figure 41 – Comparison of the impedance obtained from the $M = 0$ simulations of Sample A. **Blue** refers to the acoustic source at 130 dB, while **red** refers to 145 dB. Experimental (—); semiempirical (---); simulations (medium), 130 dB (\square), 145 dB (\circ).

results obtained with the eduction methods (Figures 41c and 41e), on the other hand, show a more constant trend over all the frequency range. An exception is the increase in the low frequencies observed in the MM results and attributed to uncertainties, due to the small sample length compared to the acoustic wavelength and to small attenuation levels (SPILLERE; BRAGA, et al., 2021). All methods exhibit similar predictions for the liner's resonance at 130 dB, which should be around 1315 Hz, as mentioned in Section 3.2.2.

Among the three methods, the best agreement to the semiempirical model resistance predictions is obtained with the in-situ experimental results. This is an expected behaviour, since the model was built upon in-situ measurements (KRAFT et al., 1997; YU et al., 2008). This statement is also valid for the reactance results, as the model tends to underestimate the eduction experimental results in the low frequencies and overestimate them in frequencies above resonance.

Increasing the amplitude of the grazing acoustic wave to 145 dB leads to an increase of the resistance obtained experimentally with all methods, as expected, due to the liner non-linear behaviour (MELLING, 1973). Still, very good agreement is observed between the in-situ experimental results and the semiempirical model's predictions, which present an overall reasonable agreement with the eduction methods' results. The MM experimental results are mostly overestimated by the model, which matches better the KT algorithm results. A large spike is seen in the KT algorithm resistance results slightly below the resonance, which is likely to be caused by experimental uncertainty. Minor variations are found for the reactance between 130 dB and 145 dB, especially in the eduction methods' results (Figures 41d and 41f).

In general, the results from the simulations obtained with the eduction methods present good agreement with the reference curves for both 130 dB and 145 dB cases. The numerical results obtained with the in-situ do not capture the experimental trends obtained with the same technique, particularly for the resistance.

The MM method simulation results present very good agreement with the experiments for both resistance and reactance, even in the non-linear regime of 145 dB excitation. The increase in the resistance observed in the low-frequency range of the experimental curves is captured by the simulations at 145 dB. The slightly higher reactance results obtained with the MM method for the 130 dB source in comparison with the 145 dB are also represented by the simulations.

The simulation results obtained with the KT algorithm are rather constant over all

the frequency range for both SPLs. Good agreement is observed between simulations and experimental results at 130 dB. The increase in the resistance due to the higher SPL is captured by this technique in the simulations, although underestimating the experiments. As for the reactance, it is noticeable that the simulations capture the experimental trends, with the 130 dB results slightly higher than the 145 dB ones, except in the near-resonance range.

The in-situ technique numerical results for the resistance does not capture the effect of resonance, seen in the semiempirical model's predictions and in the experimental curves, and this becomes more evident in the case of 145 dB excitation. In general, the simulation results obtained with the in-situ technique underestimate the experimental ones. The reactance is well predicted by the simulations, especially at 130 dB, and the trend is well represented also at 145 dB. However, it is noticeable in the reactance results that the simulations slightly overestimate the experimental baseline for 145 dB. These trends can be explained by the fact that the numerical in-situ results are averaged over all cavities, while in the experiments, results from the in-situ technique are obtained for a single cavity near the sample edge closest to the acoustic source (see Figure 24a). Since the local resistance decreases as reactance increases at downstream cavities (SCHROEDER et al., 2021), the averaging of the numerical results affect their agreement to the experimental ones.

In the following Section 4.1.2, the grazing flow simulations carried out with the Sample A setup are presented.

4.1.2 Comparison of the Turbulent Boundary Layers

The comparison of the TBL measured experimentally with the simulations is made at the upstream end of the liner, at $x = 0$ m, where the grazing flow maximum speed in the experiments is $M \approx 0.3$. The inlet velocity and the turbulence tripping geometry were adjusted through a trial and error procedure to achieve a better alignment between the flow profile in the simulations and the experimental data. In the case where the best match was obtained, the inlet velocity was set to $M = 0.34$ and the tripping was positioned at $x = -676$ mm on the top wall, along with the transition from free-slip to no-slip BCs. The tripping had a height of 0.25 mm and a length of 2 mm. The TBL was not resolved on the bottom wall, as it was entirely set as slip BC. Figure 42 shows the effect of the tripping geometry by switching on the VLES solver at the specified x coordinate.

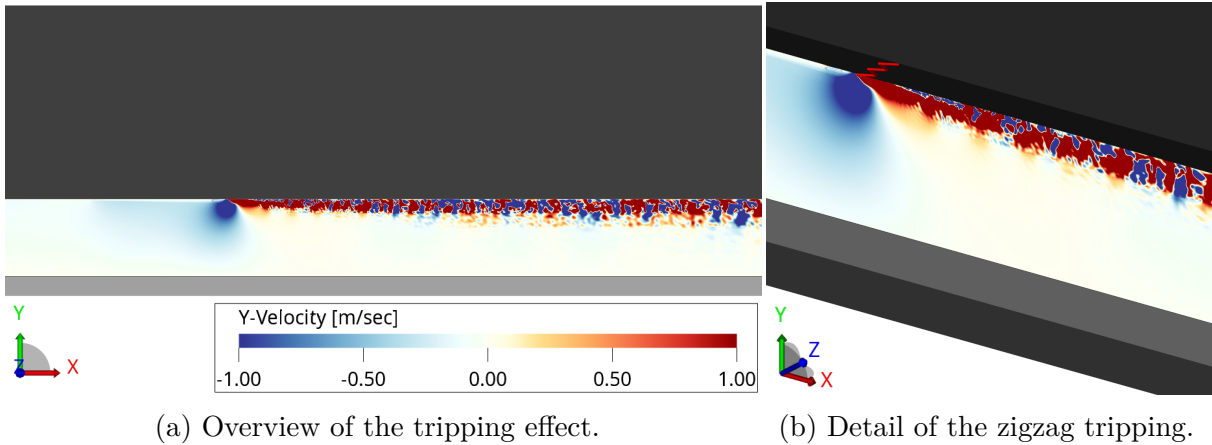


Figure 42 – Turbulent boundary layer triggered by the tripping geometry at $x = -676$ mm on the top wall.

Figure 43 shows the comparison between velocity profiles, as well as the fitting of the analytical model by [Schlichting and Gersten \(2017\)](#). The maximum Mach number is $M \approx 0.3$ on both the experimental and numerical profiles. Deviations can be seen between the two in the outer regions of the TBL. The parameters of the TBLs are summarized in [Table 7](#).

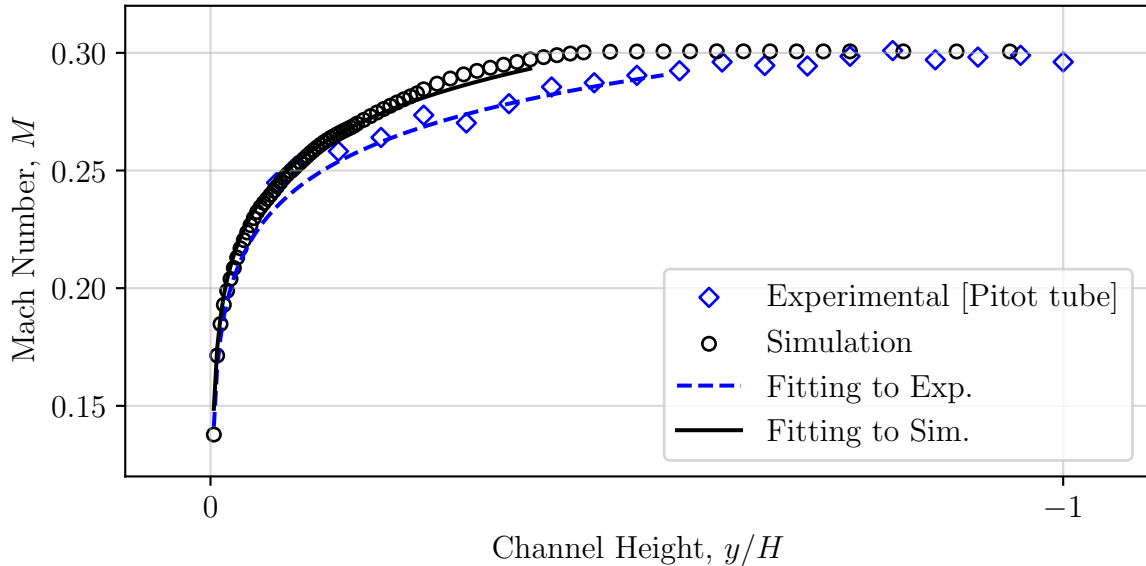


Figure 43 – Comparison of the flow profile measured experimentally by the Pitot tube with the simulations and analytical fitting, as per [Schlichting and Gersten \(2017\)](#).

The numerical TBL has a thickness of $\delta_{99} \approx 7.6$ mm, while the experimental one is $\delta_{99} \approx 11.2$ mm thick. Since the experimental curve was sampled by a Pitot tube, it lacks information of the inner region of the TBL, and for this reason the friction velocity is obtained from the analytical fitting to the experimental data. To maintain consistency

Table 7 – Characteristics of the turbulent boundary layers for Sample A.

	Experimental	Simulation
	UFSC	(Medium)
Maximum Mach Number M , -	0.301	0.301
Mean Mach Number \bar{M} , -	0.263	0.286
TBL Thickness δ_{99} , mm	11.212	7.641
TBL Displacement Thickness δ_1 , mm	1.011	0.726
TBL Momentum Thickness δ_2 , mm	0.828	0.593
Friction Velocity u_τ , m/s	4.092	4.260

in the comparisons, the friction velocity for the simulations was also calculated from its analytical fitting. It is found that $u_\tau \approx 4.26$ m/s for the numerical case and $u_\tau \approx 4.09$ m/s for the experimental one. Differences are found also in terms of integral boundary layer parameters, which are usually presented in a normalized form with respect to the diameter of the orifice d . For the numerical profile $\delta_1/d \approx 0.73$ and $\delta_2/d \approx 0.60$, while for the experimental $\delta_1/d \approx 1.01$ and $\delta_2/d \approx 0.83$.

The interaction between the turbulent flow and the orifice is strongly dependent on the integral TBL parameters (AVALONE; MANJUNATH, et al., 2019). As a baseline, Zhang and Bodony (2016) worked with about 5% deviation between experimental and numerical δ_1/d and less than 2% deviation for δ_2/d . In this work, almost 30% of deviation can be found for both δ_1/d and δ_2/d , which could affect the correlation between experimental and numerical acoustic results. Besides the real difference between the velocity profiles in the simulations and in the experiments, the lack of data close to the wall in the experimental case also harms the comparison of the TBL parameters, because it spoils the fitting of the analytical profile. The alignment between numerical and experimental flow profiles was further improved for Sample B cases, which will be presented in Section 4.2.2.

The turbulent flow interaction with the orifice leads to the formation of a circulation region inside the orifice, which affects the interaction of the acoustic wave with the liner (TAM; JU; WALKER, 2008; AVALONE; MANJUNATH, et al., 2019). A time-averaged flow-field is represented in Figure 44 for a streamwise slice at $z = 5$ mm. The figure shows the contour plot of the y component of the flow velocity and the streamlines inside the cavities and near the orifice. A counter clockwise circulation region appears inside the orifices, which forces the development of a clockwise flow circulation in the mid-region of the cavities' depth. Minor circulation regions also appear near the orifices next to the cavities' upstream divisions, which exhibit counter clockwise rotation, and deep inside the

cavity, whose behaviour is rather random. These findings agree with those in Tam, Ju, and Walker (2008) and Avallone, Manjunath, et al. (2019).

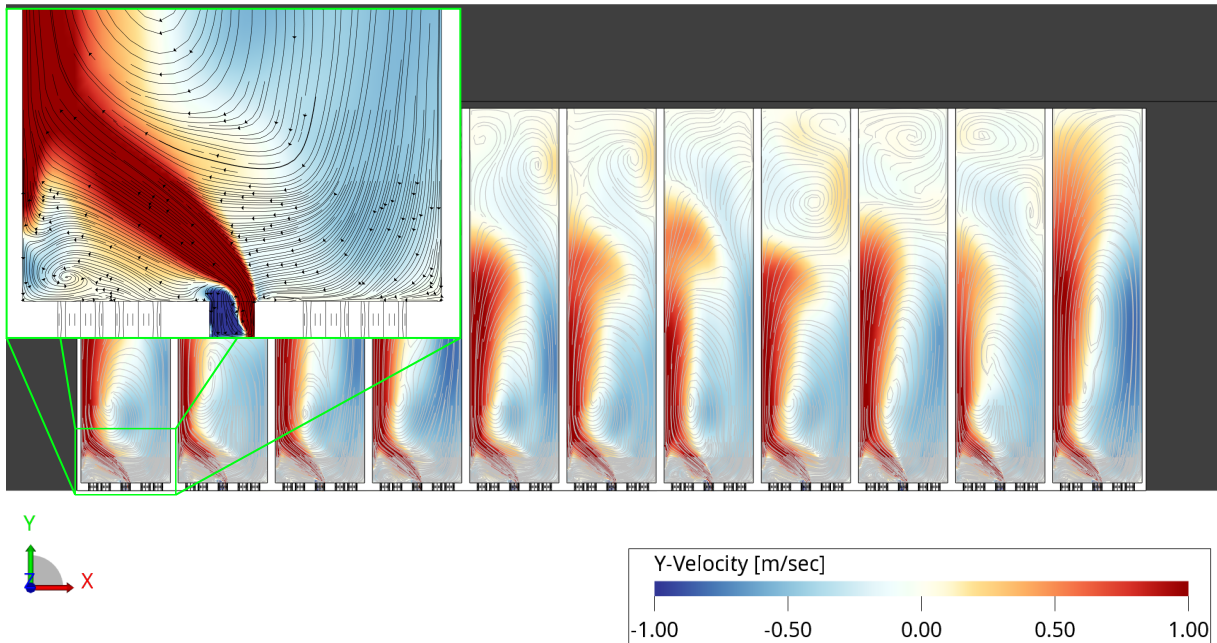


Figure 44 – Contour plot of the y velocity component of the flow, streamlines inside the cavities and detail of the near-orifice region.

The presence of the vortex inside the orifice can be responsible for an increase in the liner's resistance. Because of the recirculation effects, the oscillations induced by incident acoustic waves occur in a smaller effective area of the orifice. It is of primary importance to get a good representation of the fluid dynamics in this region of the model, which include the vortex dimensions and its interaction with the acoustic perturbations.

In the following Section 4.1.3, the effects of the $M = 0.3$ grazing flow on the impedance of Sample A are assessed.

4.1.3 Impedance in the Presence of Grazing Flow

Simulations were performed to evaluate the liner's impedance in the presence of a $M = 0.3$ grazing flow. These simulations were carried out with the same medium resolution setup, i.e., 25 cells/ d , used for the $M = 0$ simulations.

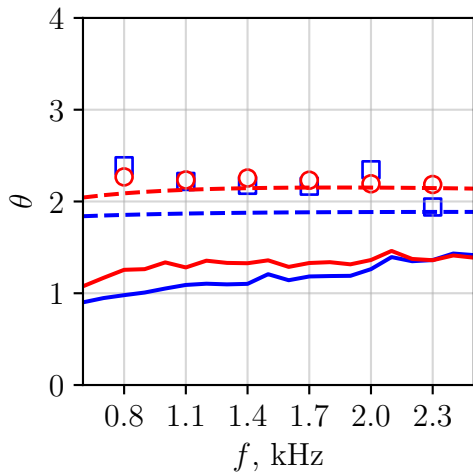
Figure 45 presents the simulations' impedance results obtained for acoustic sources at 130 dB and 145 dB positioned upstream of the liner, in comparison with the experimental measurements and with the semiempirical model predictions. For the semiempirical model predictions, the TBL parameters from the simulations were used as input.

The experimental results exhibit significantly higher value for the resistance when compared to the $M = 0$ results, which is expected due to the effects of the grazing flow (DEAN, 1974; SPILLERE; BRAGA, et al., 2021; BONOMO; QUINTINO; SPILLERE, et al., 2022). In this scenario, the grazing flow effects dominate the non-linear effects due to the increase in SPL, and there is no significant difference between the experimental values obtained for 130 dB and 145 dB. The effects of the SPL on the resistance measured in the presence of grazing flow are usually observed only for very high amplitude excitations (e.g., 160 dB), while reactance tends to remain unaffected (ZHANG; BODONY, 2016).

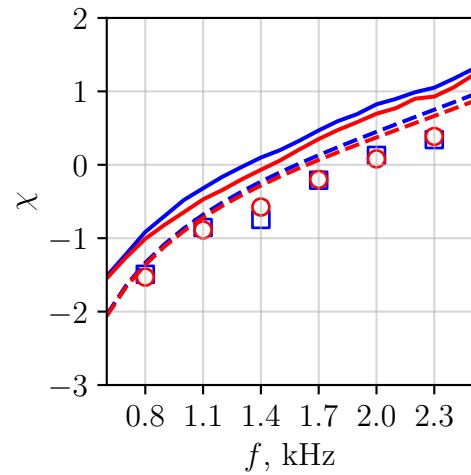
The $M = 0.3$ experimental results for the resistance obtained with the in-situ technique does not exhibit the near-resonance bump, as in the $M = 0$ cases. In the presence of the grazing flow, the resistance is more constant over all the frequency range, with a small increase in higher frequencies. The in-situ results tend to fall below those obtained by the eduction methods in lower frequencies, while they are slightly higher at higher frequencies. As for the reactance, a small difference is observed with increasing SPL in the presence of the grazing flow, with higher SPL leading to slightly higher resonance frequency. Both the 130 dB and 145 dB present a small shift towards the low frequencies when compared to the respective $M = 0$ results.

The impedance obtained experimentally with the eduction methods are consistent with what was observed in the $M = 0$ results. The MM method exhibits the same increase in the measured impedance in the lower frequencies, and remains rather constant with increasing frequencies. On the other hand, the results from the KT algorithm present a constant trend over the whole frequency range, although small uncertainties can be observed in the low frequencies. The reactance curves obtained with both the eduction methods tend to be higher than the resonance frequency obtained in the $M = 0$ cases. Overall, there is no significant effect of the increasing SPL on the reactance in the presence of the grazing flow, in agreement with previous observations (BONOMO; QUINTINO; SPILLERE, et al., 2022). It is worth noticing that there is a trend for the reactance curve to flatten, towards the zero horizontal line, when comparing the reactance results in the presence of grazing flow with the $M = 0$ case (see Figure 41). As one may notice, in frequencies below the resonance the $M = 0.3$ reactance results are higher than those observed for the $M = 0$ cases, while the opposite behaviour happens in frequencies above the resonance. These trends agree with previous works (DEAN, 1974).

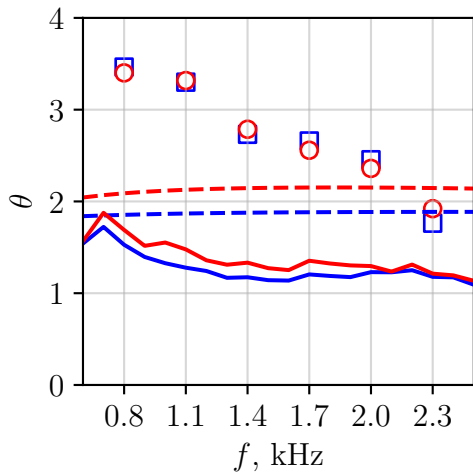
In the presence of the grazing flow, the predictions from the semiempirical model



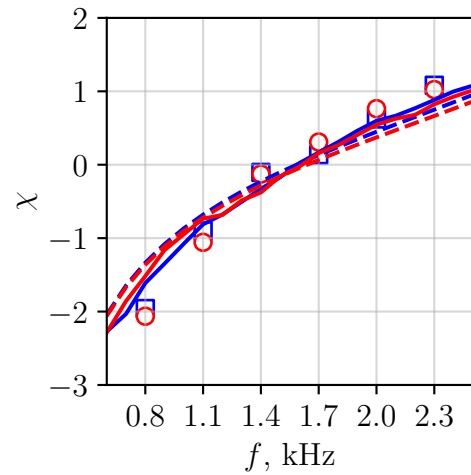
(a) Resistance, In-Situ.



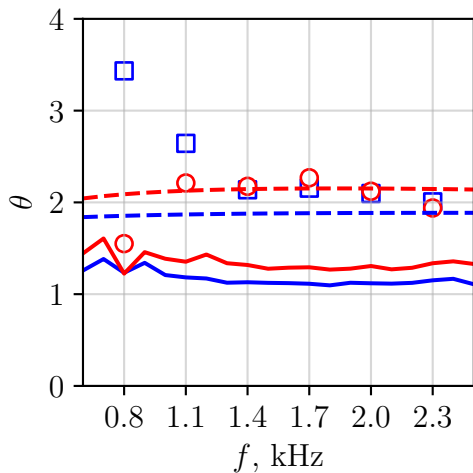
(b) Reactance, In-Situ.



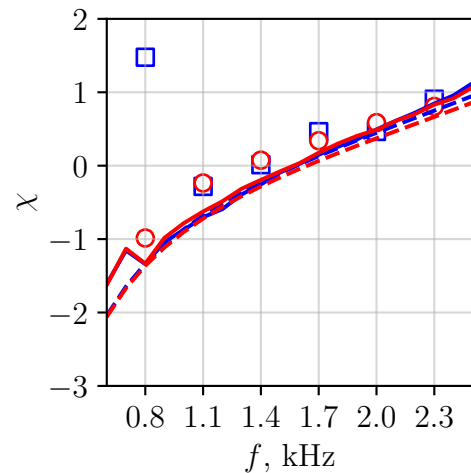
(c) Resistance, MM Method.



(d) Reactance, MM Method.



(e) Resistance, KT Algorithm.



(f) Reactance, KT Algorithm.

Figure 45 – Comparison of the impedance obtained from the $M = 0.3$ simulations of Sample A with an upstream acoustic source. **Blue** refers to the acoustic source at 130 dB, while **red** refers to 145 dB. Experimental (—); semiempirical (---); simulations (medium), 130 dB (\square), 145 dB (\circ).

for the resistance overestimate the experimental results, regardless of the impedance measurement method. When analysing the reactance, better agreement is found between the semiempirical model and the eduction methods' results, which is the opposite of what was found for the $M = 0$ cases. The model captures the trend obtained experimentally with the in-situ technique, although it is shifted to right in the frequency axis.

In general, the simulations show similar trends to the experimental results, although the former considerably overestimate the latter by approximately a factor of 2. The numerical results for the reactance are closer to the experimental baseline, exhibiting minor changes with respect to the $M = 0$ cases. The exceptions are the reactance values obtained from the simulations with the in-situ technique, which considerably overestimate the resonance frequency, when compared to both the model and the experiments.

The $M = 0.3$ simulation results obtained with the in-situ technique for the resistance are in good agreement with the semiempirical model's predictions. Good agreement is also verified between the model and the KT algorithm results above 1100 Hz. The resistance values obtained from the simulations with the MM method exhibit a large decreasing slope with increasing frequency, which is only verified for low frequencies in the experimental results.

To evaluate the effects of the change in the relative position of the acoustic source, the results obtained for both upstream and downstream acoustic sources are depicted in Figure 46, for 145 dB excitations. In this figure, the simulation results are compared against the experimental data, and also with predictions from the semiempirical model. However, it is worth highlighting that the semiempirical model's predictions are the same as those presented in Figure 45, since the source position relative to the liner is not taken into account by the model.

Experimentally, all the impedance assessment methods exhibit different results for both resistance and reactance with the change in the source's position. With respect to the results from the eduction methods, two main aspects can be highlighted: the overall values of the resistance increase when the source changes from upstream to downstream, getting closer to the semiempirical model's predictions; the reactance values get smaller in low frequencies, such that the upstream source results present better agreement with the semiempirical model's predictions. These findings are in line with previous works by [Renou and Aurégan \(2011\)](#) and [Spillere, Bonomo, et al. \(2020\)](#).

In contrast with the trends observed for the eduction methods, the resistance values

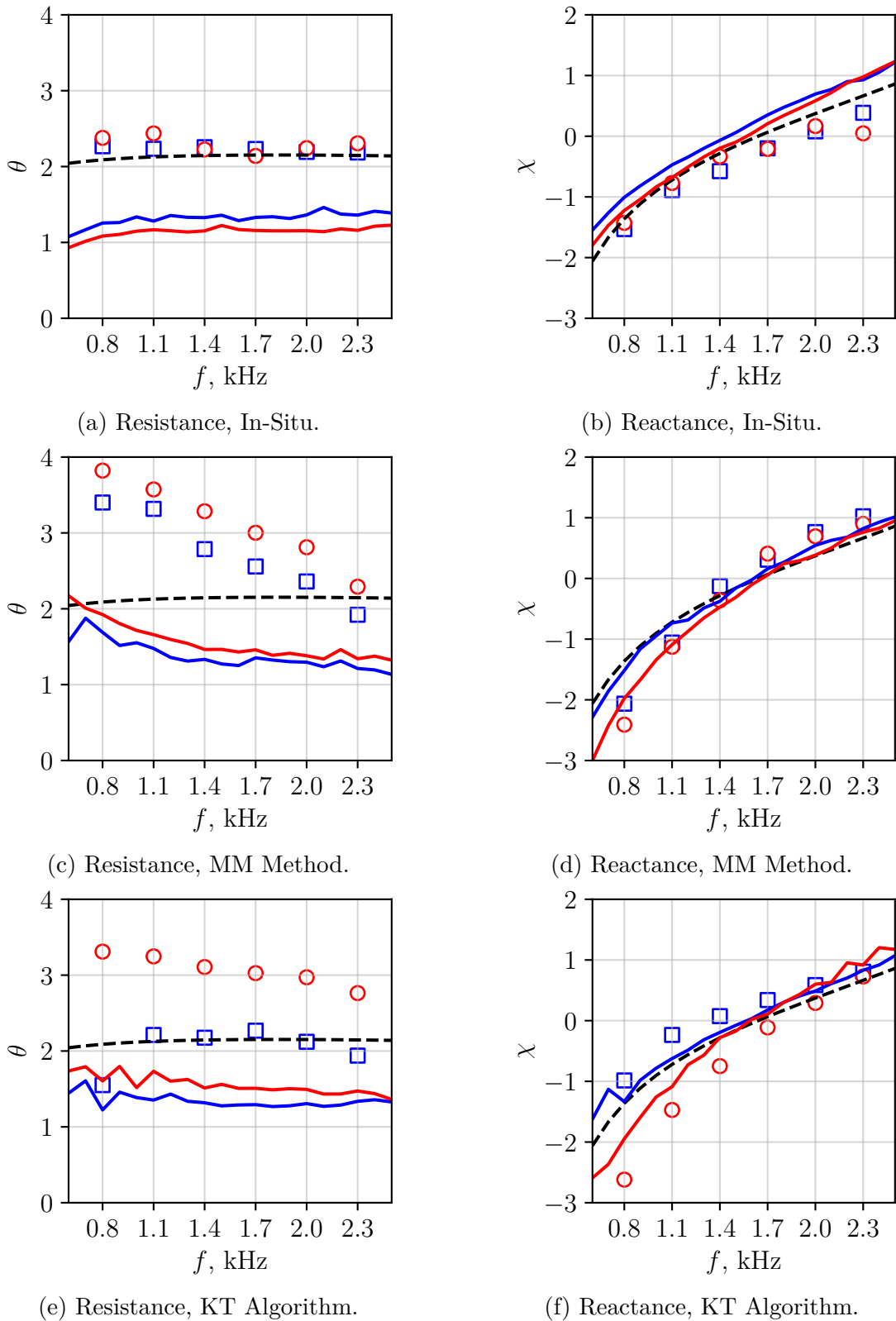


Figure 46 – Comparison of the impedance obtained from the $M = 0.3$ simulations of Sample A with the acoustic source at 145 dB. **Blue** refers to the upstream acoustic source, while **red** refers to downstream. Experimental (—); semi-empirical (---); simulations (fine), upstream (\square), downstream (\circ).

measured experimentally with the in-situ technique drop in the entire frequency range when the position of the acoustic source changes from upstream to downstream. On the other hand, the same behaviour observed in the eduction reactance results is verified in the in-situ curves. The works by [Boden et al. \(2017\)](#) and [Spillere, Braga, et al. \(2021\)](#) also highlight the difference in the predicted impedance by the in-situ technique for different acoustic source's positions. The results presented by [Spillere, Braga, et al. \(2021\)](#) are in agreement with the findings of this work for Sample A. On the other hand, the trends obtained by [Boden et al. \(2017\)](#) are opposite to those observed in this work, with both higher resistance and reactance observed for the downstream source. This behaviour might possibly be related to the different liner geometries considered, since Sample A is the same liner as in [Spillere, Braga, et al. \(2021\)](#).

The results from the simulations obtained with the in-situ technique are rather insensitive to the change in the acoustic source position, and show approximately the same trend for both acoustic source positions. Numerically, the impedance mismatch due to the change in the position of the source is observed only in the results obtained from the eduction methods. It is worth noticing that, especially for the KT algorithm results, the changes in the reactance values obtained from the simulations follow the experimental trends, with the downstream source curve lying below the upstream one in lower frequencies and crossing each other in higher frequencies.

Experimentally, all methods exhibit a mismatch in the impedance assessed with the change in the acoustic source's position with respect to the liner sample, while in the numerical simulations this is evident only in the eduction methods' results, especially in the KT algorithm ones. More important is to notice that the experimental results obtained with the in-situ technique suggest that the locally-reactive assumption made in the duct propagation models may be not correct. The reason is that the change in the source's position led to different impedance results, even though this particular method does not rely on any possibly ill-posed boundary condition.

Overall, the simulations overestimate the resistance values found in the experimental results. One of the possible causes for the simulations mismatches is insufficient refinement of the numerical scheme. The 25 cells/ d grid resolution delivers good impedance results for the $M = 0$ cases, as it was the case in [Schroeder et al. \(2021\)](#). As a matter of fact, [Manjunath et al. \(2018\)](#) results indicate approximately 40 cells/mm as a reasonable refinement parameter to perform grazing flow simulations, which is the equivalent of a

40 cells/ d resolution for this specific liner sample.

To assess the effects of the resolution on the mismatches between experiments and simulations, an additional case was simulated at 2 kHz with a higher 50 cells/ d refinement. The effects on the simulation results are shown in Figure 47. The higher resolution provides more reasonable results, with all methods presenting smaller resistance, which goes in the direction of the experimental curves. However, it is evident that the numerical results still overestimate the resistance, particularly those obtained with the MM method.

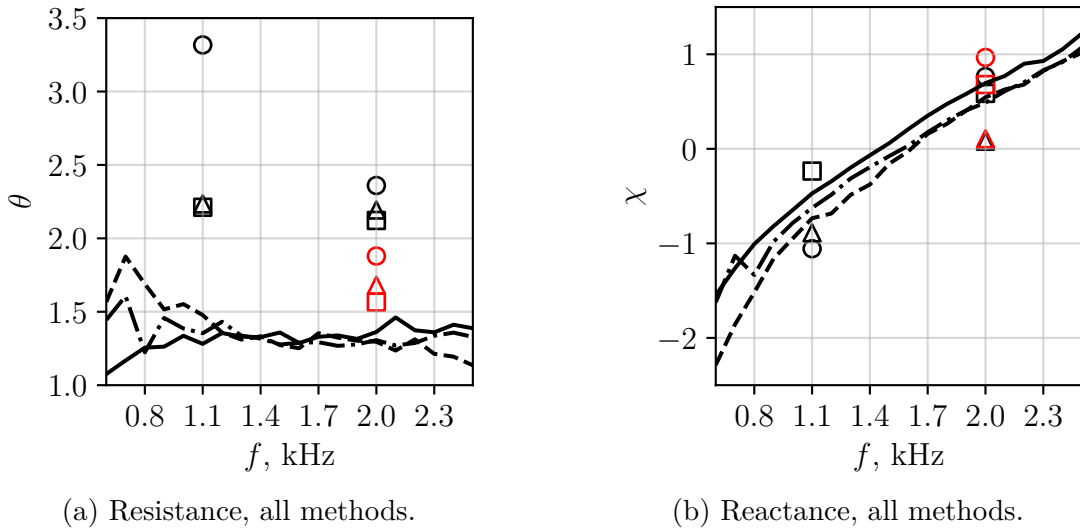


Figure 47 – Effect of finer resolution on the impedance obtained from the $M = 0.3$ simulations of Sample A, with an upstream acoustic source at 145 dB. **Black** refers to the medium resolution results, **red** refers to the fine resolution. Experimental, In-Situ (—), MM Method (---), KT Algorithm (-.-.); simulations, In-Situ (\triangle), MM Method (\circ), KT Algorithm (\square).

At this point, the remaining mismatch observed between the resistance values obtained experimentally and numerically could be addressed by a more representative numerical model of the UFSC test rig, since the computational setup for Sample A considered only half the channel height of the test rig and did not resolve the TBL on the bottom wall. Specifically, the MM method impedance education rely on the acoustic field measured in the rigid sections of the channel, which could be affected by a poor representation in the numerical model.

To investigate these effects, simulations were carried out with an improved version of the computational setup for Sample B. These results will be discussed in the following Section 4.2.

4.2 LINER SAMPLE B

The simulations with Sample B were performed based on the experience acquired with the work carried out with Sample A. All the following results were obtained with the *legacy solver* of the 2022-R1 release of the software ([POWERFLOW...](#), 2022). Some of the results from the simulations with Sample B are also available in [Pereira, Bonomo, Quintino, et al. \(2023\)](#).

4.2.1 Impedance in the Absence of Grazing Flow

The simulations for Sample B in the absence of grazing flow were carried out with the three grid resolutions presented in Table 4, i.e., coarse (10 cells/ d), medium (20 cells/ d) and fine (40 cells/ d). The different discretization levels were considered to assess the convergence of the results, as inadequate grid refinement can result in an inaccurate solution for the flow inside the liner's orifices, which is a potential cause for misleading the impedance measurements.

Figure 48 presents the impedance results obtained for acoustic sources at 145 dB, in comparison with the experimental measurements and with the semiempirical model predictions. As resolution increases, the numerical results for both resistance and reactance tend to decrease, which agrees with previous observations reported in the literature ([MANN et al., 2013](#); [PEREIRA; BONOMO; SILVA, et al., 2022](#)). However, it is observed that the resistance is more sensitive to the grid resolution level.

The simulations provide reasonable results for the impedance with all the three measurement techniques for the medium resolution level, and minor changes are verified between medium and fine resolution results. The results for the coarse resolution, on the other hand, neither agree with the experimental results nor with the model's prediction, showing that a minimum of 20 cells/ d should be used for a proper characterization of the liner in the absence of grazing flow, as a rule of thumb. Moreover, the accuracy of the predictions associated with the education methods are more affected by poor grid refinement, which mislead especially the low frequency resistance measurements.

The in-situ technique results are the less sensitive among all the methods to changes in grid resolution. Still, its effect is noticeable, especially in the resistance results. Considering the fine resolution results, there is reasonable consistency with the semiempirical model predictions. The resistance and reactance measured with the in-situ technique are shown

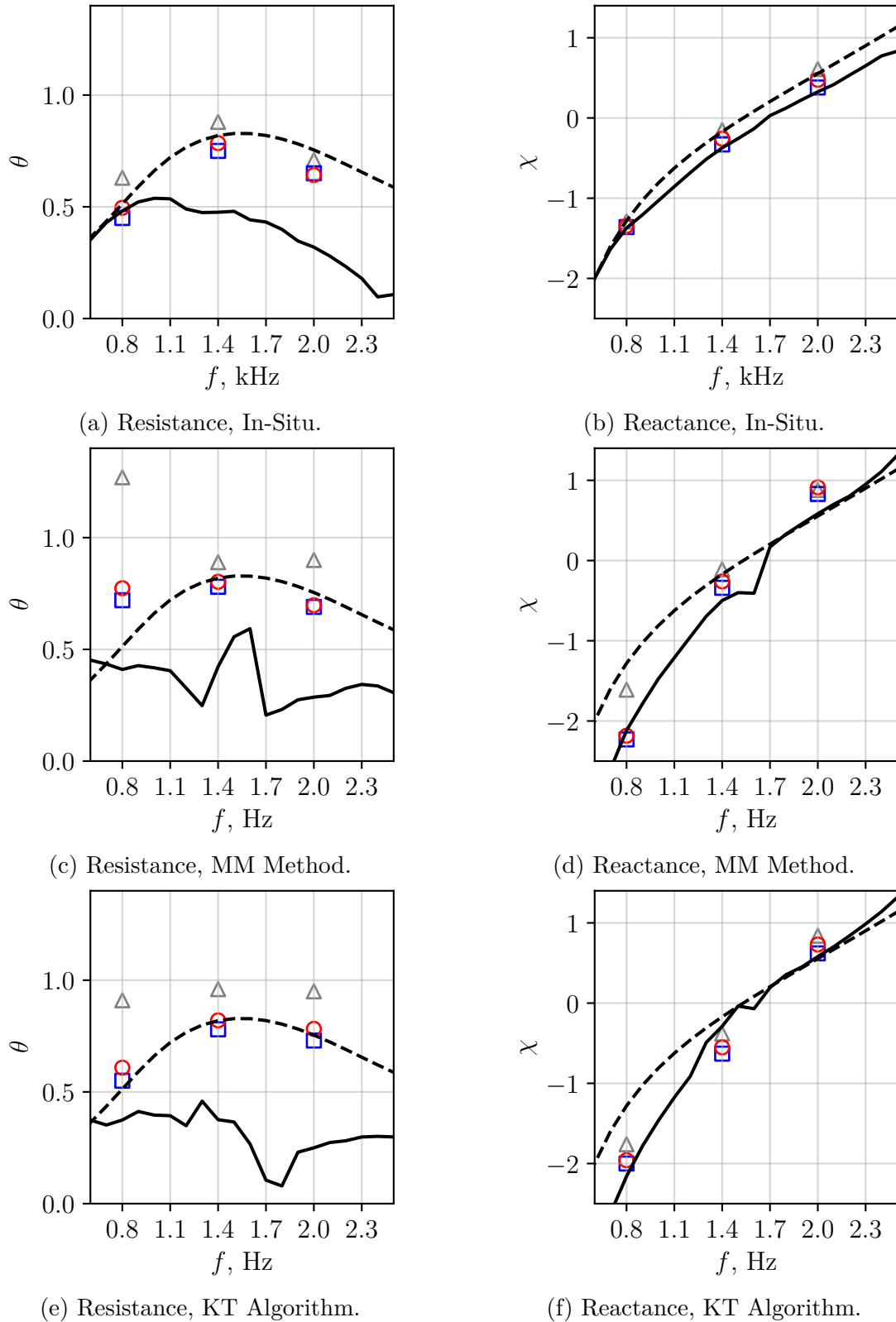


Figure 48 – Comparison of the impedance obtained from the $M = 0$ simulations of Sample B with the acoustic source at 145 dB: experimental (—); semiempirical model (---); simulations, coarse (\triangle), medium (\circ), fine (\square).

in Figures 48a and 48b, respectively.

The simulation result for 800 Hz agrees reasonably well with the experiments and the

model. As the frequency increases, the experimental curve and the semiempirical model's predictions deviate from each other, the latter overestimating the former. Apart from that, the trends of both the model and the experiments are very similar, which might be related to the fact that the Goodrich model was built upon in-situ measurements. The results of the simulations fall in between the two baselines, and there is better agreement with the semiempirical model. The reactance values match well with the Goodrich model's predictions, and present a small deviation from the experimental curve as the frequency increases. Nonetheless, the trends are well represented by the simulations, and the results are within a fair agreement with the reference values.

Figures 48c and 48d present the MM method results. These results exhibit a significant discrepancy between the experimental measurements and the semiempirical model predictions, particularly in the resistance plots. The generally constant trend exhibited by the MM method experimental resistance results is not captured by the Goodrich model, which can be justified by the fact that this model was built upon in-situ measurements. For the reactance, there is also a considerable deviation between the model and experimental results, especially at frequencies below resonance. The simulation results obtained with the MM method are the most sensitive to poor resolution levels, as observed by the significant changes in measured impedance with increasing resolution, particularly for the 800Hz case, where both resistance and reactance values decrease towards the reference curves. With respect to the finer resolution alone, the simulations show a rather constant trend for the resistance over all the frequencies considered, but overestimate the experimental results. Moreover, there is reasonable agreement with the semiempirical predictions for 1400 Hz and 2000 Hz, which is likely related to the bump presented by the model in the near resonance frequencies. Regarding the reactance, the simulations generally follow the experimental trend, except for a slight overprediction for the 2000 Hz case.

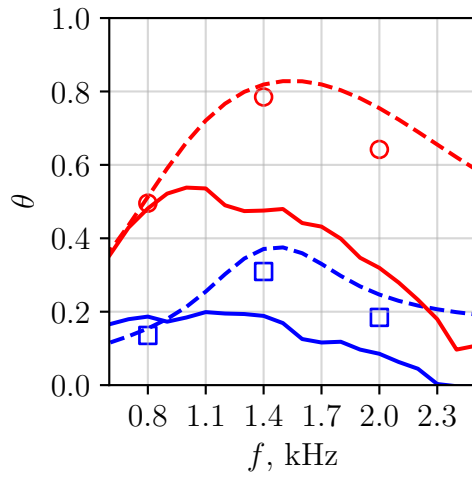
Figures 48e and 48f display the results obtained from the simulations using the KT algorithm. Similar to the MM method, the model and experimental results do not exhibit the same trends, particularly for the resistance plots. In this case, the model still overpredicts the experimental results, and so do the simulations. As with the MM method, the sensitivity to the grid refinement is significant. An increase in resolution to 40 cells/ d results in a close match between the simulation results and the semiempirical model predictions for the resistance, even in the 800 Hz case where the MM method diverges. Regarding the reactance, the simulations have better agreement with the experimental

curve, which matches reasonably the semiempirical model's predictions for frequencies above resonance. For frequencies below resonance, the model overestimates the experiments, as observed also in the comparison of the MM method results, and the results from the simulations present better agreement with the experiments.

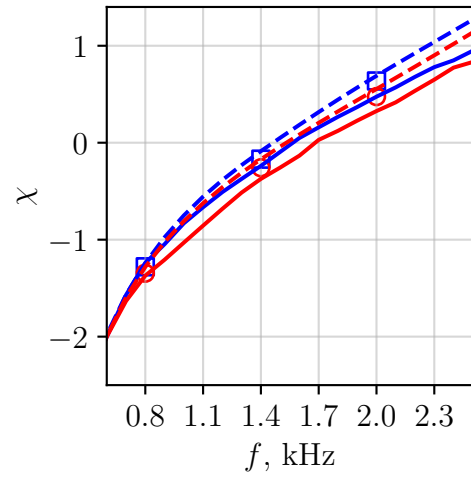
The comparison of the medium resolution results obtained at 145 dB for Samples A and B in the absence of the grazing flow reveals a few aspects. First, the correlation between the in-situ measurements and simulations is better for Sample B. This suggests that the approach to measure the impedance in the simulations applied for Sample B is more appropriate, and that the averaging of the results over all cavities might influence the correlation of the impedance. Also, it is questionable whether the position of the facesheet probe with respect to the orifices within a single cavity has an influence, even in the $M = 0$ scenario, since this aspect was only taken into account in the Sample B case. Second, the resistance results obtained from the simulations with the eduction methods for Sample A are in better agreement with the experiments than what is observed for Sample B. Overall, the simulations overestimate the experiments for Sample B, while very good agreement is observed, particularly for the MM method results, in the case of Sample A. Furthermore, although the experimental resistance results obtained with the KT algorithm for Sample A presented more scattering, the simulations captured reasonably better the experimental trends in that case. These observations agree with the hypothesis that the length of the modelled liner has an influence on the agreement of the eduction methods results (see Section 3.3.3). Since the eduction methods capture the overall effect of the liner on the acoustic field to determine the impedance, the higher L/L^* ratio found for Sample A could partially explain the better agreement of the numerical results with the experiments in that case.

Regardless the correlation between experimental and numerical results, in the case of Sample B, reasonable convergence in terms of the resolution can be observed for the medium resolution. To provide more solid evidence that a proper characterization of the liner in the absence of grazing flow can be obtained for a 20 cells/ d ratio, simulations with the medium resolution grid were also carried out for the acoustic source at 130 dB. These results are depicted in Figure 49, in comparison with the 145 dB results previously shown in Figure 48. With a lower SPL excitation, the results obtained for Sample B present a similar behaviour to those observed for Sample A. Overall, lower SPL leads to lower measured resistance and slightly higher reactance, and this is observed with all the three

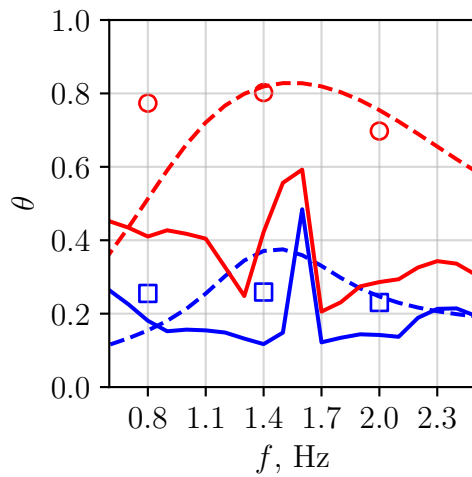
measurement methods.



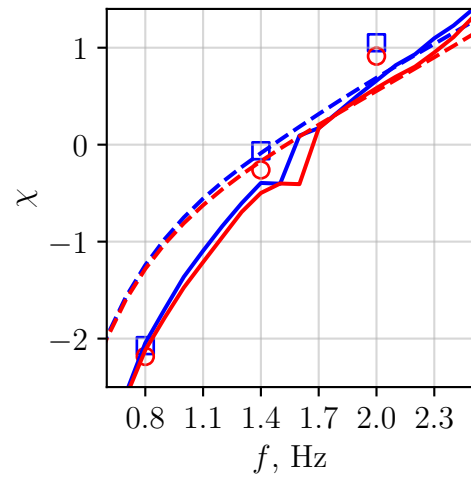
(a) Resistance, In-Situ.



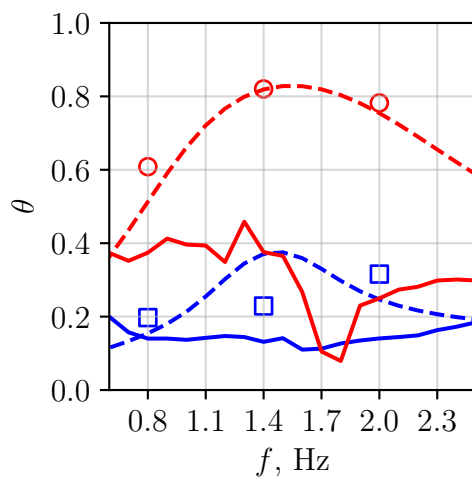
(b) Reactance, In-Situ.



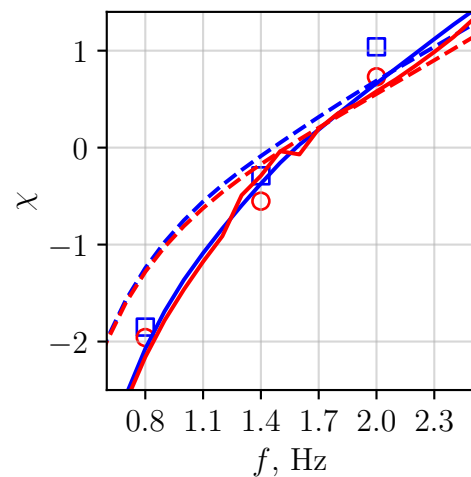
(c) Resistance, MM Method.



(d) Reactance, MM Method.



(e) Resistance, KT Algorithm.



(f) Reactance, KT Algorithm.

Figure 49 – Comparison of the impedance obtained from the $M = 0$ simulations of Sample B. **Blue** refers to the acoustic source at 130 dB, while **red** refers to 145 dB. Experimental (—); semiempirical (---); simulations (medium), 130 dB (\square), 145 dB (\circ).

The simulations' results obtained with in-situ at 130 dB present very good agreement with the semiempirical model, considering both resistance and reactance. Good agreement is also observed between simulations and experiments. At 130 dB, non-linear effects are less prominent, and good agreement is found between the eduction results from both experiments and simulations. Based on the results from both samples, it is reasonable to state that the numerical model is capable of making good prediction of liners' impedance, especially in the linear SPL regime. Moreover, the setup used for Sample A is computationally cheaper and equally capable.

In the following Section 4.2.2, the grazing flow simulations carried out with the Sample B setup are presented.

4.2.2 Comparison of the Turbulent Boundary Layers

The assessment of the TBL in the simulations is made at the upstream end of the liner, at $x = 0$ m, where the grazing flow maximum speed in the experiments is $M \approx 0.32$. In order to provide a reasonable match of the flow velocity field in the simulations with the experimental one, an inlet velocity BC corresponding to $M = 0.29$ was set in the simulations. The turbulence trippings, whose dimensions correspond to a height of 0.25 mm and a 2 mm length, was positioned at $x = -1.6$ m on both top and bottom walls, together with the transition from free-slip to no-slip BCs. In contrast with the simulations from Sample A, both top and bottom TBLs are triggered to develop towards the liner sample. Figure 50 shows the effect of the tripping geometries by switching on the VLES solver at the specified x coordinate.

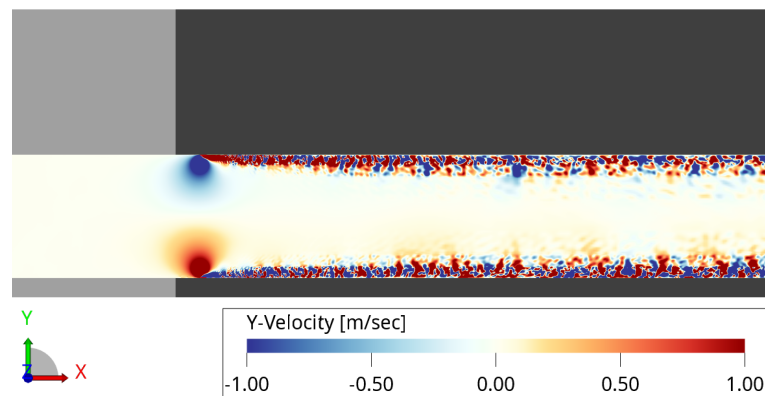


Figure 50 – Top and bottom turbulent boundary layers triggered by the tripping geometries at $x = -1.6$ m.

As the TBL develops on both walls in the simulations, the flow at the bulk of the

channel accelerates, such that the maximum velocity at $x = 0$ is $M \approx 0.32$, in line with the experimental measurements.

The comparison between the flow profiles measured in the experiments and in the simulations is shown in Figure 51. The experimental measurements made with the hot-wire anemometer present reasonable agreement with the Pitot tube data, which suggests a good reliability of both experimental techniques. However, the measurements from the anemometer are preferred against the Pitot tube data, since the former allows for a much more detailed assessment of the TBL, as it gets closer to the wall. It can be seen that the top and bottom TBLs from the simulations are not identical, the latter appearing less properly resolved. This is because the grid resolution next to the bottom wall is slightly less refined than the grid adjacent to the liner sample, close to the top wall (see Figure 35). This was done to save computational resources: next to the top wall, the resolution needs to be sufficiently high to solve the flow inside the liner's orifices, where important acoustic dissipation mechanisms take place.

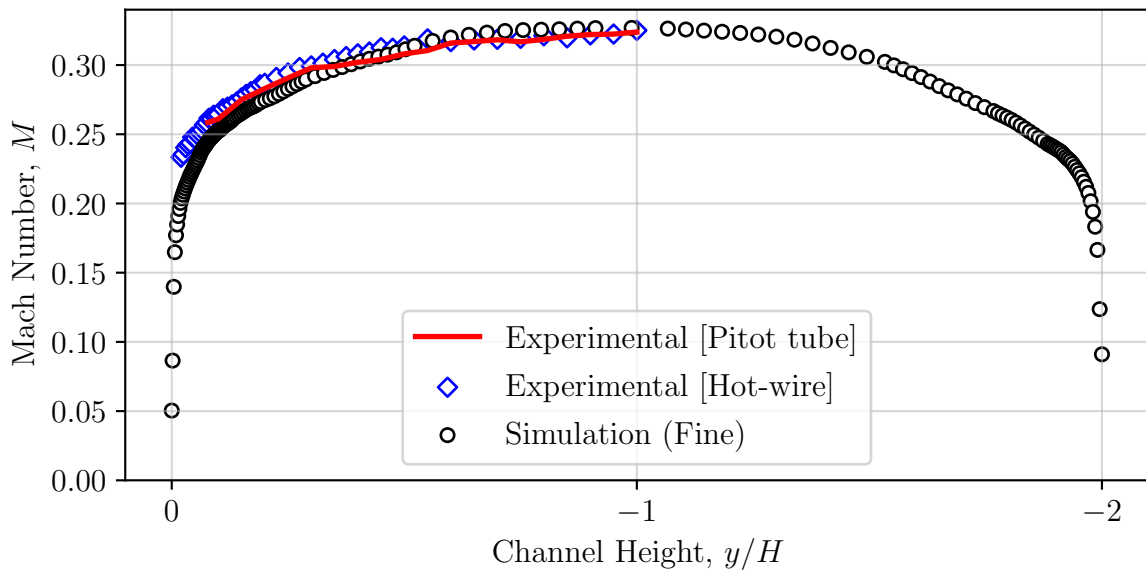


Figure 51 – Comparison of the flow profile measured experimentally by both the Pitot tube and the hot-wire anemometer with the simulations.

Figure 52 shows the comparison between the TBL in the experiments and the TBL assessed in the simulations, together with their respective fitting of the analytical profile, as per [Schlichting and Gersten \(2017\)](#). The flow profile assessed in the simulations present reasonable agreement with the experimental data, even for the medium resolution case. Instantaneous measurements from the fine resolution simulations also show reasonable agreement with the experimental baseline, although this simulation has not reached

statistical convergence to allow for a proper extraction of a mean profile and of the TBL parameters. For this reason, the analytical fitting of the fine resolution flow profile was omitted in Figure 52.

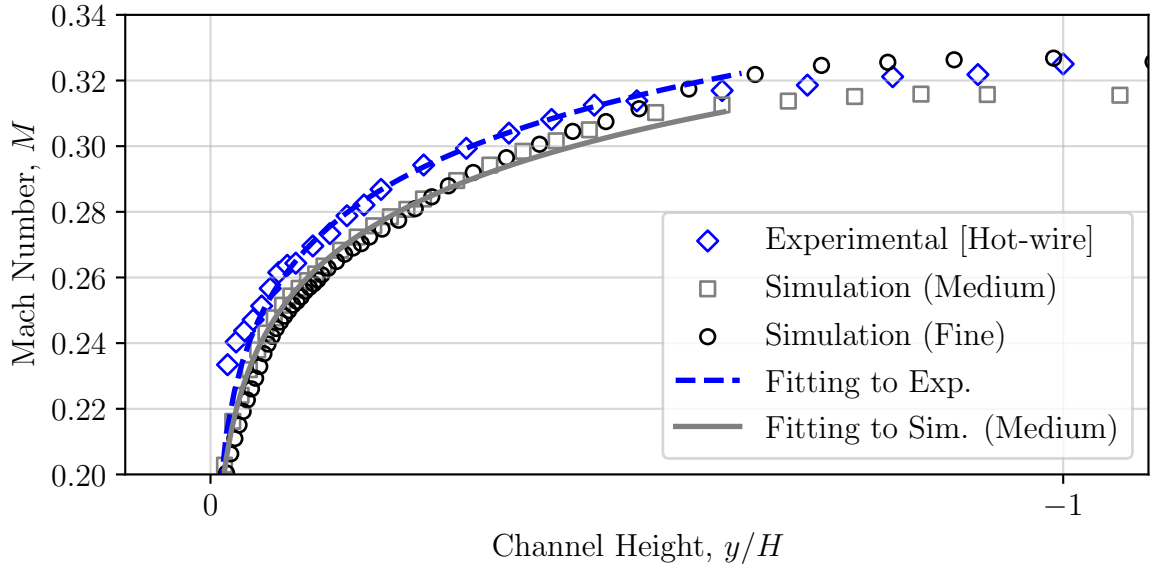


Figure 52 – Fitting of the analytical expression, as per Schlichting and Gersten (2017), to the turbulent boundary layers in the experiments and in the simulations.

The characterization of the TBLs in the experiments and in the simulations is made in terms of the parameters described in Table 8. The maximum Mach number M and the TBL thickness δ_{99} are obtained directly from the measured data. The mean Mach number \overline{M} , the TBL displacement thickness δ_1 and the TBL momentum thickness δ_2 are calculated by numerical integration of the data. Lastly, the δ_{99} obtained from each data set are used as input parameter to the analytical fitting for the calculation of the friction velocities u_τ . Although the sampling resolution was improved with the use of the hot-wire anemometer, the analysis still lacks information at distances close enough to the wall for a proper estimation of u_τ . To maintain consistency, the same approach was applied to estimate u_τ from the simulations.

The interaction between the turbulent flow and the orifice is strongly dependent on the integral TBL parameters δ_1 and δ_2 (AVALLONE; MANJUNATH, et al., 2019). In these cases, the integral parameters normalized by the orifice diameter are $\delta_1/d \approx 1.28$ and $\delta_2/d \approx 1.11$ for the experimental flow profile, while for the simulations (medium) $\delta_1/d \approx 1.35$ and $\delta_2/d \approx 1.07$. The relative difference between the two calculated δ_1/d is about 5.5%, and for the δ_2/d there is about 3.6% difference. These relative differences are in line with previous publications from correlated experimental and numerical assessments (ZHANG;

Table 8 – Characteristics of the turbulent boundary layers for Sample B.

	Experimental UFSC	Simulation (Medium)	Simulation (Fine)*
Maximum Mach Number M , -	0.325	0.316	0.327
Mean Mach Number \bar{M} , -	0.298	0.293	0.295
TBL Thickness δ_{99} , mm	12.456	12.042	13.493
TBL Displacement Thickness δ_1 , mm	1.269	1.338	1.730
TBL Momentum Thickness δ_2 , mm	1.099	1.060	1.349
Friction Velocity u_τ , m/s	4.420	4.300	4.248

* This simulation has not reached statistical convergence.

BODONY, 2016), and are an improvement from the Sample A setup (see Section 4.1.2). As for the TBL parameters estimated for the fine resolution simulation, greater deviations from the experimental reference values are observed. This is a consequence of the lack of statistical convergence of the mean flow profile from the fine simulation, which can be addressed by extending the sampling period. Due to time limitations, it was not possible to obtain the statistically converged data for the fine resolution flow profile.

The turbulent flow induces recirculation regions inside the liner's orifices, which is responsible for an increase in the liner's resistance by reducing the effective area of the orifice where the oscillation induced by incident acoustic wave takes place (ZHANG; BODONY, 2016; AVALONE; DAMIANO, 2021). Figure 53 shows a time-averaged result of the flow-field, where the contour plot represents the y component of the velocity. In the detail, it is possible to see the behaviour of the flow inside the orifices, similar to what was observed for Sample A in Figure 44.

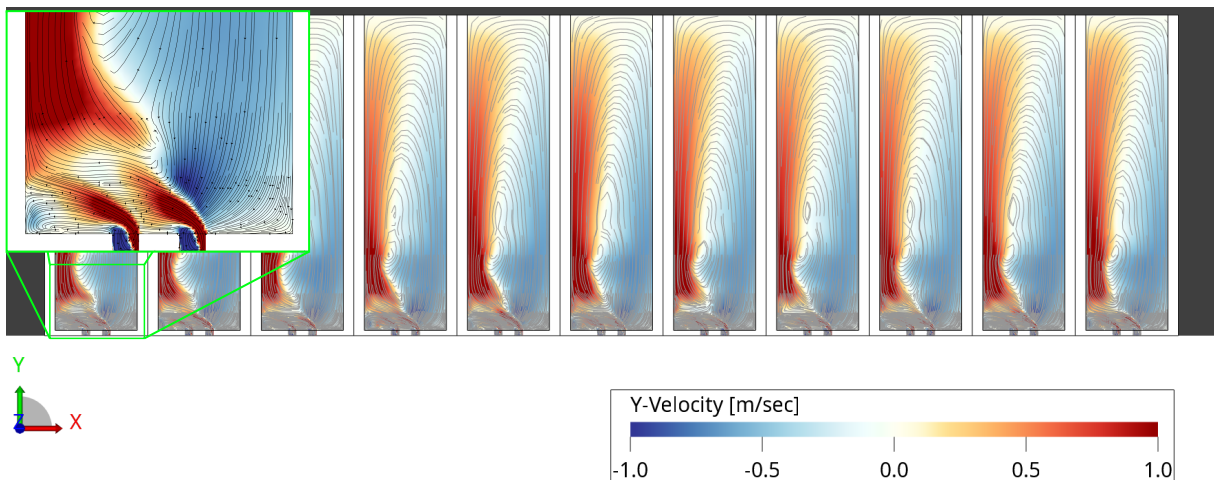


Figure 53 – Contour plot of the y velocity component of the flow, streamlines inside the cavities and detail of the near-orifice region.

In the following Section 4.2.3, the effects of the $M = 0.32$ grazing flow on the

impedance of Sample B are assessed.

4.2.3 Impedance in the Presence of Grazing Flow

To analyse the convergence of the grazing flow simulations, we followed a similar approach to the $M = 0$ cases. However, since the coarse resolution grid failed to match the reference values for $M = 0$, only medium and fine resolutions were considered in the following analysis.

Figure 54 presents the impedance results for $M = 0.32$ with an upstream acoustic source of 145 dB. The simulation results were compared with the experiments and with the semiempirical model's predictions. The semiempirical model's predictions showed very minor changes when using either the simulations' TBL parameters or the experimental ones as input, which suggests that the TBLs are in reasonable agreement for the acoustic analysis. The TBL parameters from the simulations were used as input for the semiempirical model.

Overall, the effects of the grazing flow can be observed in Figure 54 by the increase in the resistance values with respect to the no-flow case, exhibited by both the model and the experiments. The increase in the resistance due to the presence of the grazing flow is expected (BONOMO; QUINTINO; SPILLERE, et al., 2022; PEREIRA; BONOMO; SILVA, et al., 2022), and it is related to a reduction in the effective area of the orifice caused by recirculation effects, shown in Figure 53. The experimental results present good agreement with the semiempirical model's predictions, especially for the eduction methods. Nonetheless, the experimental resistance results for the in-situ technique underestimate considerably the model, which is most likely related to the uncertainties of this specific technique, e.g., leakages caused by imperfect sealing of the facesheet probe and the influence of the TBL near hydrodynamic field in the measurements and the position of the probe on the facesheet (the influence of the latter will be discussed in further sections). As for the reactance, the eduction methods and the model are in good agreement in frequencies above resonance, while deviate from each other in lower frequencies. This was also observed for the $M = 0$ results, and it is most likely related to the fact that the model was adjusted to in-situ measurements, which are better represented by the model.

The assessment of the simulation results shows that there is a general trend towards smaller resistance values with increasing resolution, similar to the observations for the $M =$

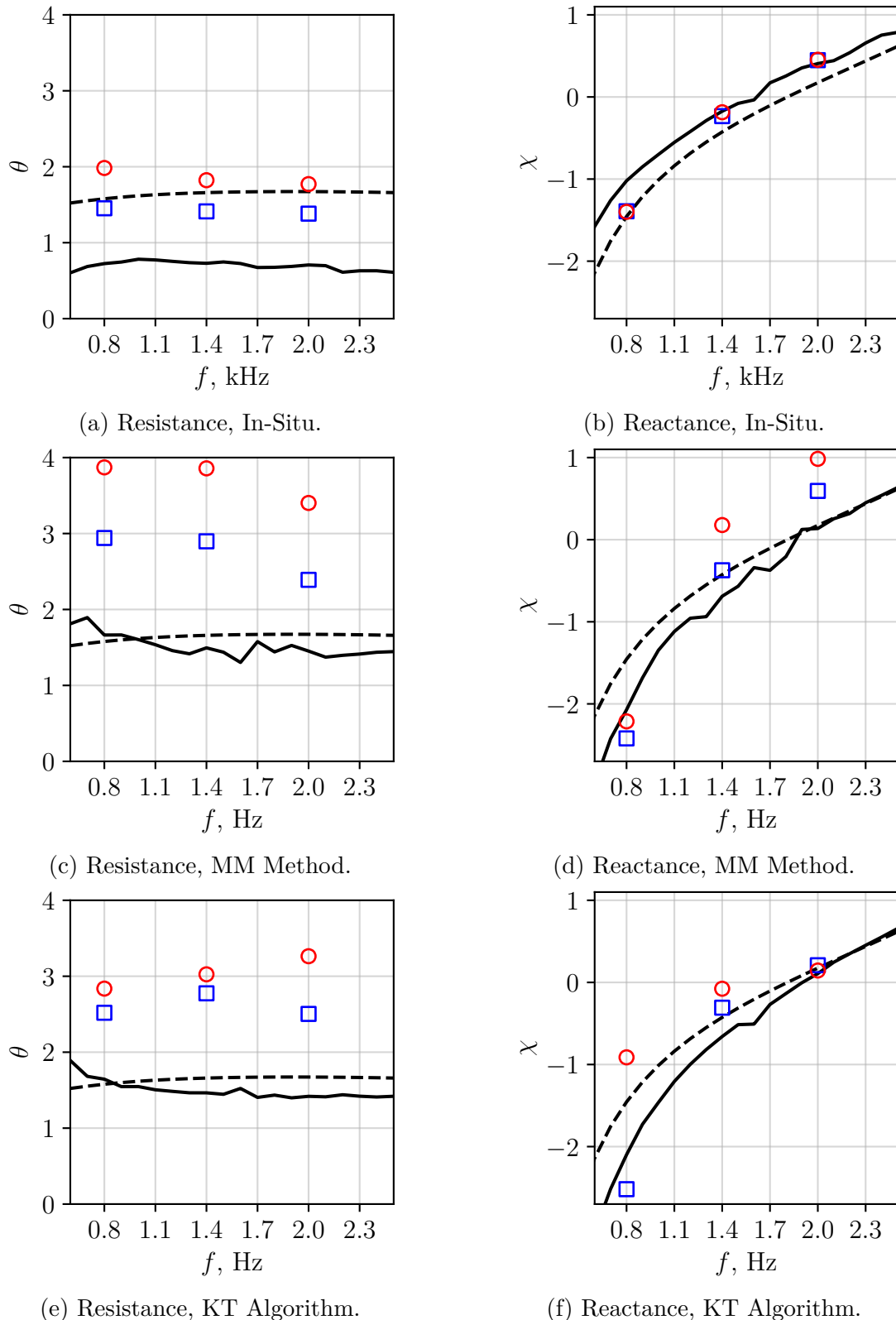


Figure 54 – Comparison of the impedance obtained from the $M = 0.32$ simulations of Sample B with an upstream acoustic source at 145 dB: experimental (—); semiempirical model (---); simulations, medium (○), fine (□).

0 cases. Once again, the eduction methods present greater sensitivity to the discretization level, especially the MM method, which overpredicts considerably the reference resistances

for the medium resolution cases. Considering the eduction methods, the medium resolution simulations do not provide a proper characterization of the impedance for the $M = 0.32$ cases, and even the fine resolution still overestimates the resistance by an approximate factor 2. This indicates that the computational setup needs to be improved for a proper match of the resistance with the eduction methods, either with finer resolution levels, with longer sampling times or with a longer model of the liner sample.

The eduction methods rely on measurements of the acoustic field in the channel, so it is important to make sure the acoustic field has reached its steady-state before sampling for the impedance. Furthermore, such a short sample in the simulations (only eleven cavities) might increase the uncertainties of the measurements.

Experiments were carried out in the UFSC test rig with the same liner, but with the first and the last eleven spanwise rows of cavities covered by speed tape, as schematically shown in Figure 55, such that only eleven spanwise rows would interact with the flow and acoustics.

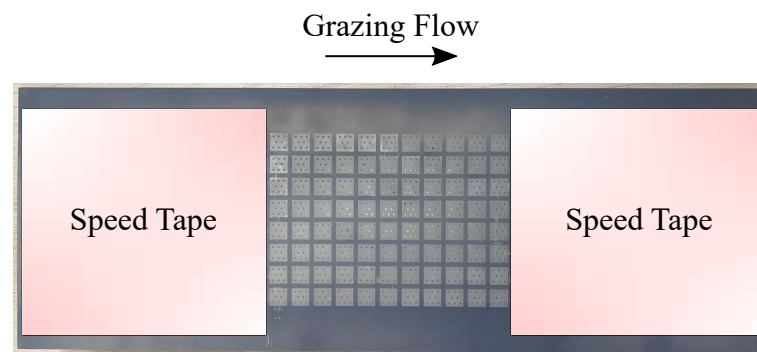


Figure 55 – Schematic representation of the liner Sample B partially covered with speed tape.

As depicted in Figure 56, the overall trends of the impedance measurements were not affected, but the curves exhibited considerable uncertainty levels in the form of spikes. The combined effects of the relative small sample length and the insufficient sampling time in the simulations are unclear, and should be further investigated.

The in-situ technique result remains the less sensitive among the methods to changes in grid resolution in the presence of grazing flow, and exhibits reasonable agreement with the semiempirical model's predictions, for both resistance and reactance. It is expected that the in-situ measurements are less sensitive to the acoustic field in the channel, and more to the grid resolution in the orifices. Still, a further increase in the resolution might be necessary for a proper convergence assessment of the in-situ results, since the change

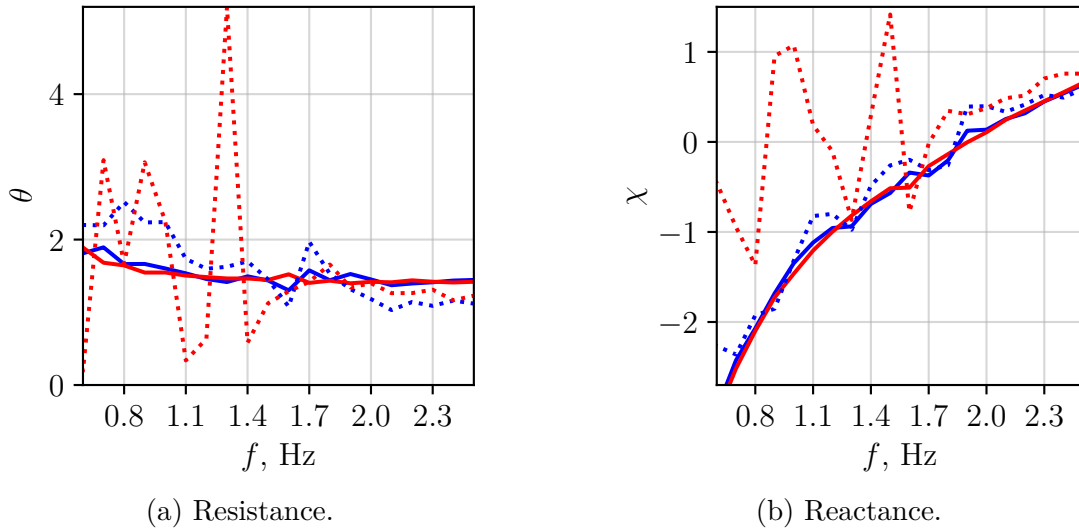


Figure 56 – Effect of the liner sample length on the impedance obtained from the $M = 0.32$ experiments of Sample B, with an upstream acoustic source at 145 dB. **Blue** refers to the MM method and **red** refers to the KT algorithm. Full sample (—), eleven cavities (.....).

from medium to fine grids brought the resistance down considerably. The results of the simulations from the eduction methods overestimate the resistance, even for the fine resolution. However, the reactance results are in reasonable agreement and the reference curves, especially with the experiments for the KT algorithm.

The effects of the position of the acoustic source in the impedance are shown in Figure 57. All the impedance assessment methods exhibit different results for the resistance with the change in the source's position, in which the downstream source induces higher resistance than its upstream counterpart. With respect to the eduction methods, although the downstream source experimental results are higher than the upstream ones, they are still in the range of the semiempirical model's predictions. The in-situ technique exhibits the highest sensitivity to the source position in terms of absolute values. Still, the downstream source experimental results for the in-situ remain considerably lower than the model.

The change of the acoustic source position also affects reactance, but mostly for the eduction methods results. Both eduction methods exhibit a drop in reactance when the source changes from upstream to downstream, especially in the frequency range below the resonance. On the other hand, the results obtained experimentally with the in-situ technique do not exhibit significant changes with respect to the source position.

It is worth to mention that the effects of the change in the acoustic source position

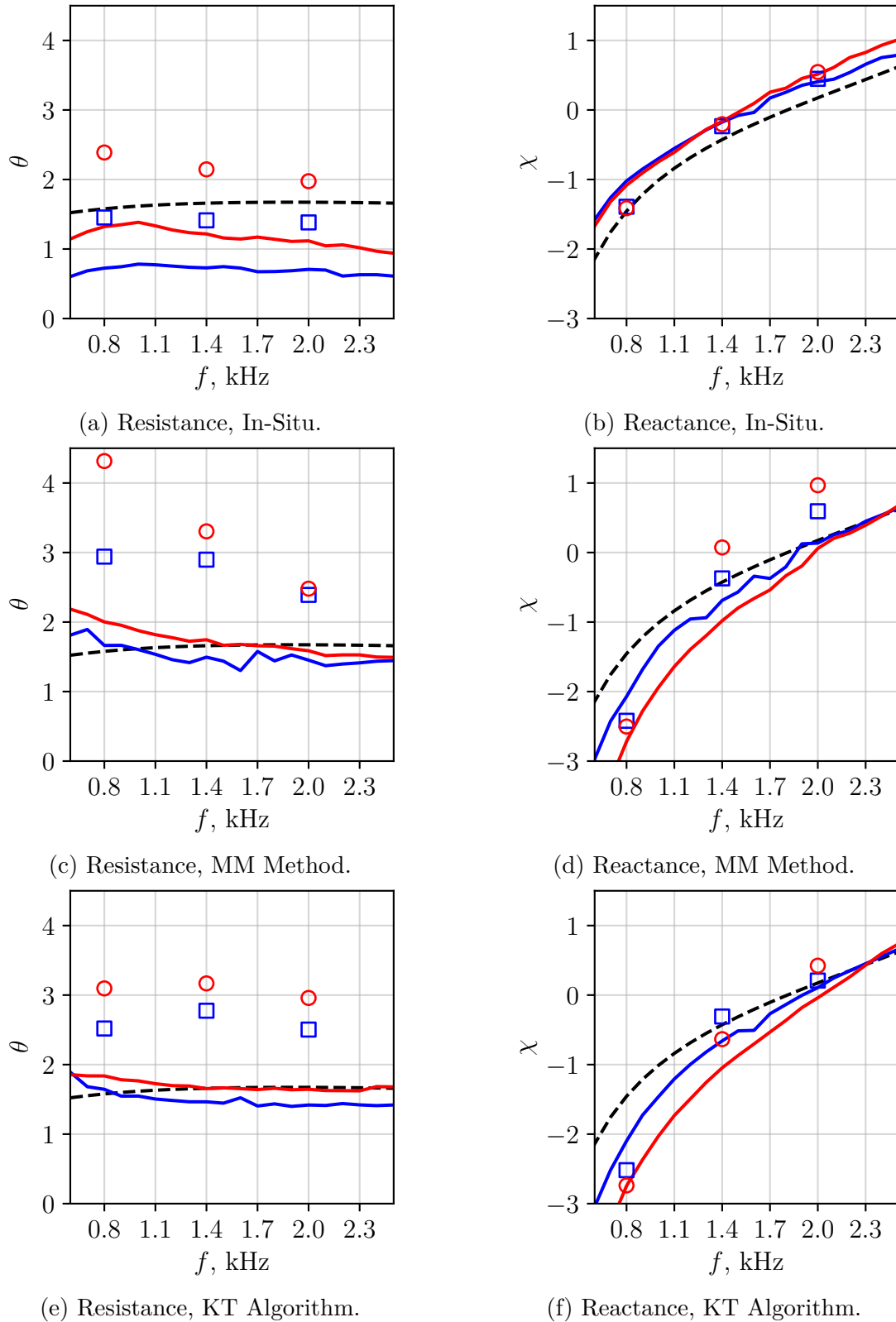


Figure 57 – Comparison of the impedance obtained from the $M = 0.32$ simulations of Sample B with the acoustic source at 145 dB. **Blue** refers to the upstream acoustic source, while **red** refers to downstream. Experimental (—); semi-empirical (---); simulations (fine), upstream (\square), downstream (\circ).

on the resistance measured experimentally with the in-situ technique for Sample A are opposed to the behaviour exhibited by Sample B. While in the case of Sample A the change from upstream to downstream led to a drop in the resistance (see Figure 46), the same change results in higher resistance values for Sample B. These observations are in line with the arguments presented in Section 4.1.2, i.e., the variation in the resistance observed in the in-situ measurements with the change in the source position might be dependent on the liner geometry.

Overall, the simulations are able to capture the same trends observed in the experiments. The differences between upstream and downstream resistance measured in the simulations with the in-situ technique are consistent with the ones observed in the experiments, and there is very good agreement between the experiments and the simulations for the reactance results.

The results obtained by the eduction methods in the simulations also change with respect to the source position. The resistances obtained from the MM method for the downstream source deviate more from the upstream results in lower frequencies. The KT algorithm, on the other hand, delivers a quite constant difference between upstream and downstream source results, both in the simulations and in the experiments. Regarding the reactance, the results from the KT algorithm in the simulations agree reasonably well with the experiments, with the downstream source values below the upstream ones, except in higher frequencies where the two curves cross and the upstream source results become higher. As for the MM method, the experimental trends from the experiments are not captured properly by the simulations, since the latter exhibit an opposite trend, i.e., the downstream source results higher than the upstream ones. This mismatch, which affects mainly the MM method, could also be caused by a combined effects of both a relative small sample length and insufficient sampling time.

4.3 A BRIEF DISCUSSION ABOUT THE MODEL'S CAPABILITIES

In the previous Sections 4.1 and 4.2, the acoustic results in the absence and in the presence of grazing flow were presented for two liner geometries.

Different parameters of the model were tested during the simulating process of these liners, in order to assess the agreement of the impedance numerical results with the experimental ones. In the following subsections, a brief discussion on the effects of each

parameter on the results is presented.

4.3.1 General Parameters of the Model and Their Effects

- **Grid refinement:** the effects of the grid refinement are major, especially for the resistance in the presence of grazing flow. The maximum resolution tested in this work was 50 cells/ d (Sample A), which was still not sufficient for a proper agreement of the measured resistance, particularly for the MM method in low frequencies. It is important to highlight that the orifice has two characteristic dimensions, namely the diameter and the facesheet thickness. The modelled Sample A has a $\tau/d = 0.8$ ratio, while $\tau/d \approx 0.64$ ratio is found for Sample B. The lower ratio observed for Sample B translates into a poorer discretization along τ , which agrees with the worse correlation found for this sample in comparison with Sample A, even at finer resolutions. On the other hand, 20 cells/ d appears to be the minimum resolution for a proper characterization of liners in the absence of grazing flow, at least for liners with similar τ/d to the ones considered in this work.
- **Agreement between numerical and experimental turbulent boundary layers:** based on the impedance obtained for both samples, the effect of the disagreement between numerical and turbulent boundary layers on the acoustic results is minor, to some extent. It is important to make it clear that the TBL parameters do play an important role on the acoustic measurements (KOOI; SARIN, 1981; BONOMO; QUINTINO; CORDIOLI, et al., 2023), but the range within these parameters varied in this work was insufficient for a proper assessment of these effects. Furthermore, to allow for a deeper look into these effects, it would be necessary to simulate one liner geometry with the same resolution level with different flow profiles, significantly varying the TBL parameters.
- **Modelling either half or full channel height:** it is unclear whether modelling the full channel improves the correlation between simulations and experiments in the presence of grazing flow. However, good agreement was observed between the numerical and experimental results for Sample A in the absence of grazing flow, with the half channel model. Since this setup is computationally cheaper, it is worth to perform further attempts with the half channel approach also for the grazing flow cases. Furthermore, previous works have presented good correlation

between numerical and experimental impedance results in the presence of a turbulent grazing flow with a half channel setup (AVALLONE; MANJUNATH, et al., 2019; AVALLONE; DAMIANO, 2021). Although in those works only in-situ measurements were considered for a single cavity resonator, they provide good evidence to support the use of half-channel setups.

- **Numerical precision of the solver:** the solver can be configured to use either single or double arithmetic precision. The double-precision solver is recommended by the software user’s guide for cases whose results are highly sensitive to tiny changes in variables (POWERFLOW..., 2022, p. 18), e.g., acoustic propagation. In the simulations performed in this work, the use of the double-precision solver did not improve the results, but increased significantly the computational cost.

As discussed in the topics above, considerable improvements in the acoustic results have been accomplished from increasing the refinement of the grid. The resolution of the grid impacts directly on the computational cost of the model, which is already expensive at the fine resolutions considered in this work. As previously shown in Figure 28, each refinement increment in the grid is performed by dividing the elements’ size by 2. Since the timestep in LBM simulations is linearly related to the smallest element size (refer to Section 3.3.1), the refinement of the grid results in double the number of timesteps required for a certain simulation. At the same time, for a given cubic volume and VR, the refinement of the grid leads to an increase in the number of elements by a 2^3 factor. The combined effect of both larger number of timesteps and grid elements translates into much higher computational cost, when refining the model.

Figure 58 depicts data measured from the acoustic simulations with the Sample B setup, for approximately 15×10^{-3} seconds of simulation time. As it can be seen in Figure 58a, the increase in the number of timesteps needed for the given simulation time follows a linear progression with increasing resolution. The data measured from the actual simulations (carried out for a maximum of 40 cells/ d) allow for an estimate of the number of timesteps necessary for a possible 80 cells/ d setup, which is double the 40 cells/ d value. On the other hand, an exponential increase is found for both the number of cells in the model and CPU hours necessary to accomplish the same simulation time (Figures 58b and 58c). These data are summarized in Table 9.

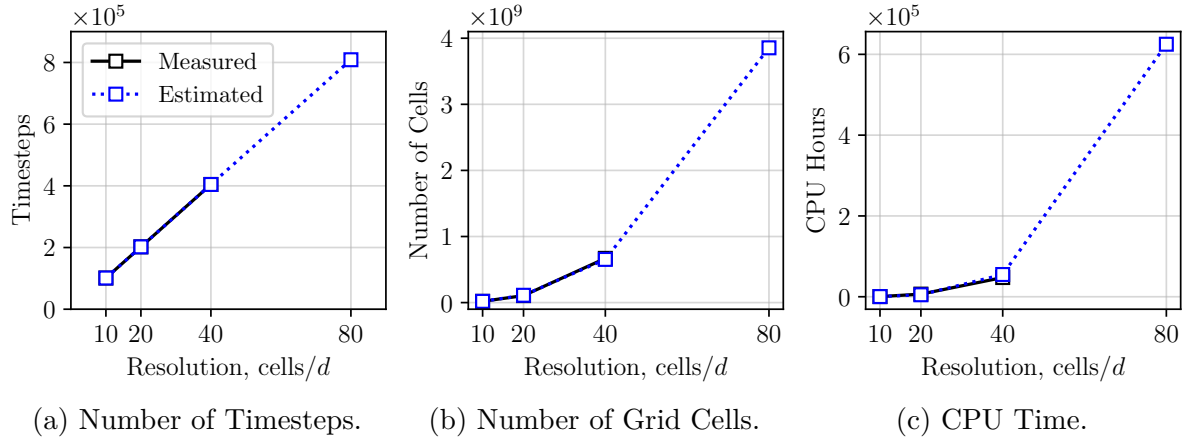


Figure 58 – Computational cost of the acoustic simulations with the Sample B setup: data measured from the actual acoustic simulations and forecast for further refinement.

Table 9 – Computational cost of 15×10^{-3} seconds of simulation time with the Sample B setup.

Resolution (cells/d)	No. of Timesteps $10110(\text{cells}/d) + 10.5$	No. of Cells $51659(\text{cells}/d)^{2.56}$	CPU Hours $0.133(\text{cells}/d)^{3.51}$
10	101,109	19,234,450	368
20	202,207	105,605,861	6,490
40	404,404	669,321,363	47,540
80*	808,811	3,855,525,347	625,021

* Estimated values based on expressions adjusted to the measured data.

Considering that the fine resolution setup was unable to provide good agreement of the acoustic results with the reference data, one might suggest that further refinement of the grid is necessary, at first. However, as shown above, a more refined version of the current model is too expensive. This is motivation for further investigations concerning the representativeness of the model to the real liner geometry, which could improve the convergence rate of the numerical results to the experimental ones without the need to increase the grid discretization level. Specifically, the shape of the orifices is of primary interest, and a brief discussion on the effect of this parameter on the numerical results is carried below.

4.3.2 Effect of the Orifice Shape on the Acoustic Results

Previous publications have shown that the manufacturing process of the liner can have great influence on its acoustic absorption properties (MURRAY; FERRANTE, et al., 2005). Moreover, the accuracy of the manufacturing process is of great relevance to key

parameters that affect the non-linear resistance of the liner, e.g., the POA and the discharge coefficient C_D (MELLING, 1973, p. 52). Specifically, the C_D depends on the ratio between τ and d , but also on the orifice shape, i.e., whether or not the holes are tapered, rounded or chamfered (JI et al., 2016; GUZMÁN-IÑIGO et al., 2019). Generally, sharp-edged holes have smaller C_D , which leads to higher resistance for a given frequency (MELLING, 1973; GUZMAN INIGO; MORGANS, 2022).

Given the influence of the orifice shape on the acoustic resistance, it is worth to investigate the shape of the real liner geometries tested in the UFSC test rig. Figure 59 depicts the facesheets of Samples A and B, with a detail of their orifice shapes.

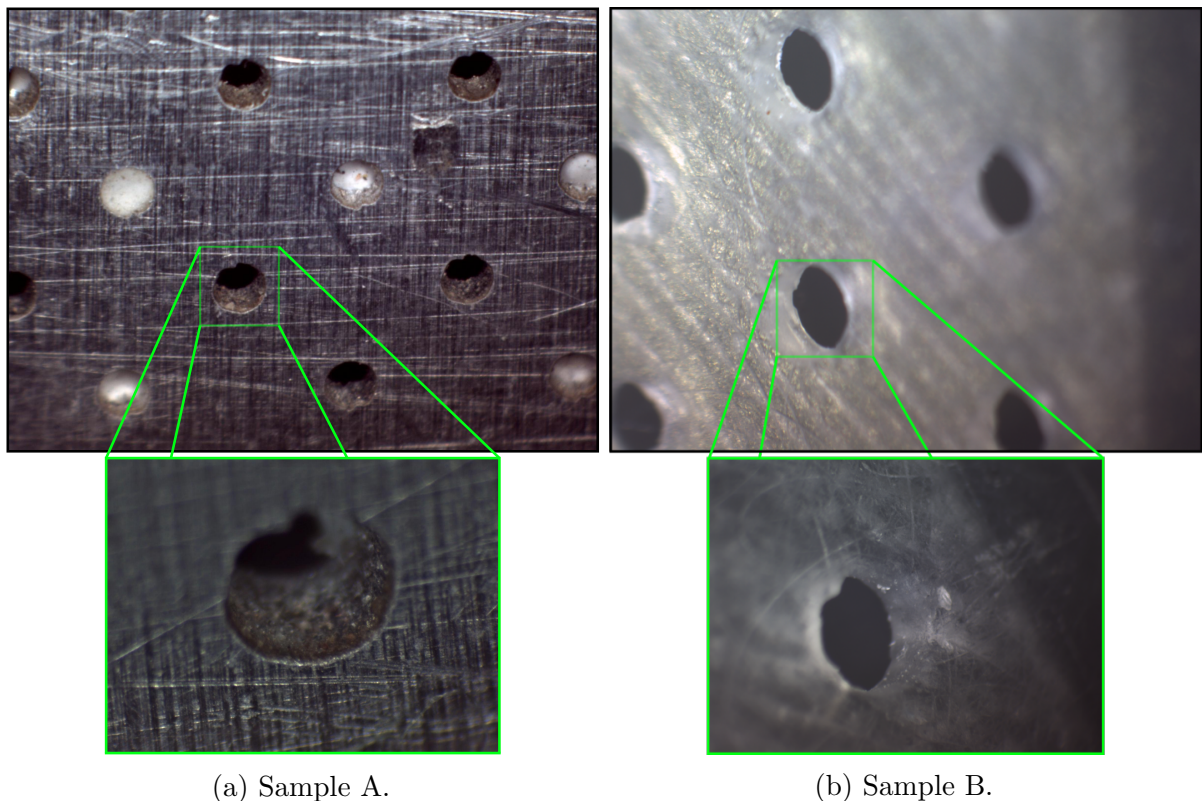


Figure 59 – Detail of the real liners' orifice shapes.

Based on Figure 59, it is noticeable that the orifice shapes are not regular, although it is not possible to determine their geometry precisely. The detailed orifice from Sample A looks sharp-edged, while it is harder to evaluate the one from Sample B due to the intrinsic transparency of the facesheet.

To investigate the effects of the orifice shape in the simulations, an alternative geometry was considered for Sample B. This geometry was generated by applying fillets to the edges of the orifices, with radii equivalent to 20 % of the facesheet thickness, as depicted in Figure 60. This number was randomly selected, with the single objective of

assessing the effect of this alternative shape on the measured impedance. All the other aspects of the simulations were kept constant.

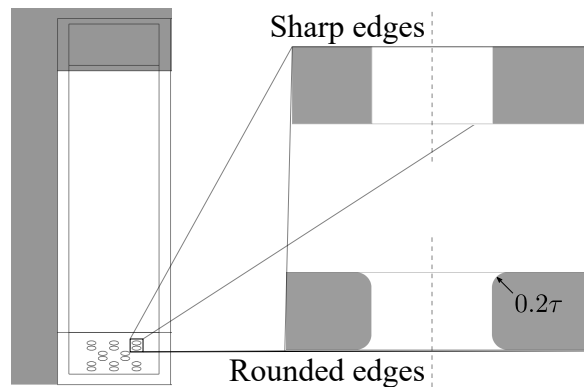


Figure 60 – Comparison between the original sharp-edged liner model and the alternative rounded-edges geometry.

Figures 61 and 62 present the results from the simulations with the rounded-edges geometry in comparison with previously shown sharp-edged results, both obtained from the medium resolution setup with an upstream source at 145 dB. The effects of the rounded-edges on the impedance results is noticeable, both in the absence and in the presence of the $M = 0.32$ grazing flow.

For the $M = 0$ scenario, better agreement between the resistance results from the simulations and the experiments is found, especially in the case of the MM method. It is also noticeable that the reactance results obtained for the rounded-edges setup is in better agreement with the experiments, when compared with the results from the sharp-edged geometry, regarding all methods.

In the presence of the $M = 0.32$, the resistance results obtained from the simulations with the original sharp-edged geometry overestimated considerably the experimental data, even in the case of the fine resolution setup. On the other hand, the results obtained for the geometry with the rounded-edges are in reasonable agreement with the experiments, even though they were obtained with a medium resolution setup. The resistance values, specifically, exhibit a very large drop, in comparison with the sharp-edged results.

These results show that the orifice shape has a major impact on the impedance results. This can partially explain the discrepancies observed in the previously shown results for the sharp-edged geometry, since it is expected that the orifice shapes on the real liners are not sharp, due to manufacturing processes. However, as the radius of the rounding was arbitrary, further analysis are necessary for more solid conclusions.

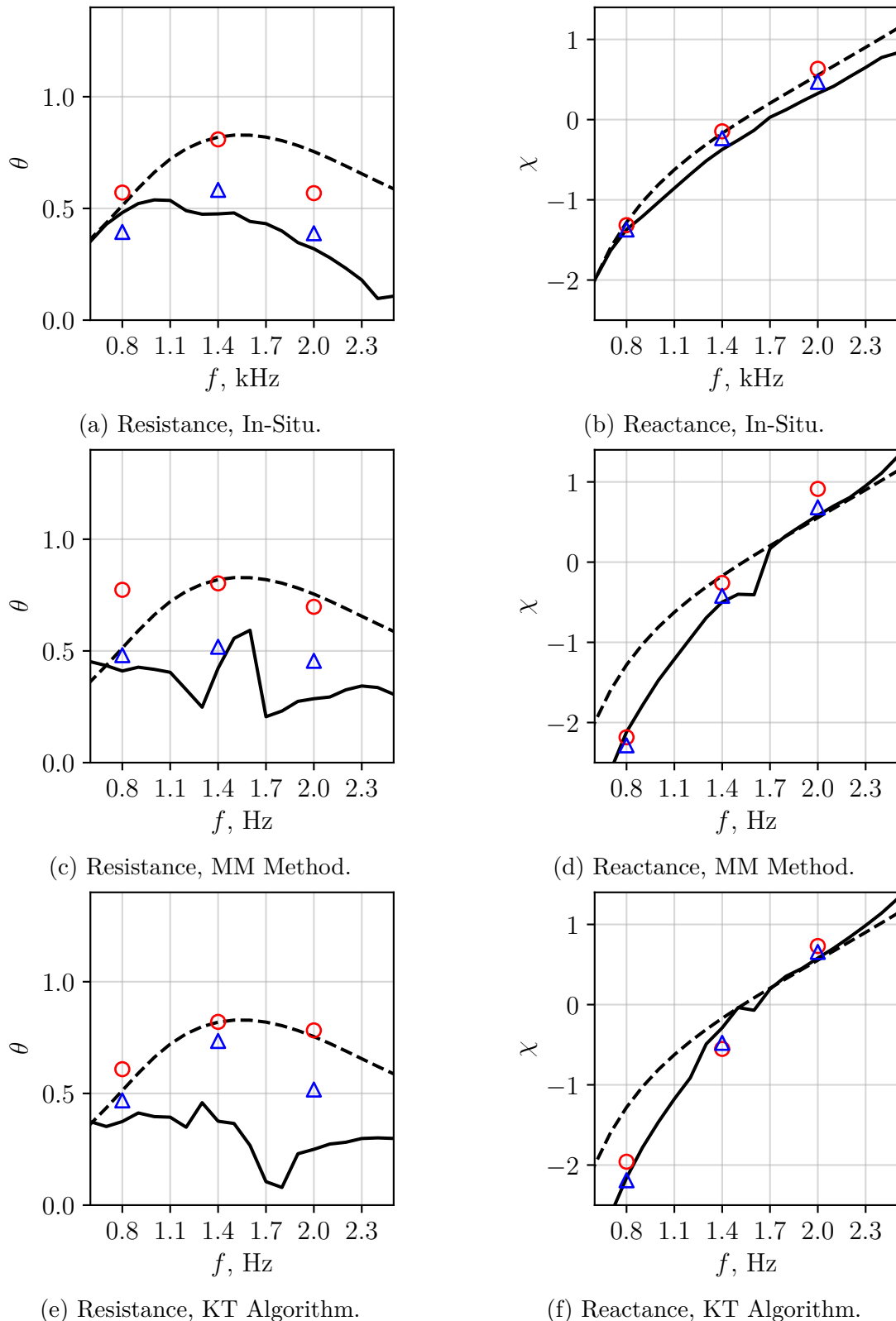


Figure 61 – Comparison of the impedance obtained from the $M = 0$ simulations of Sample B with the acoustic source at 145 dB. Experimental (—); semiempirical (---); simulations (medium), sharp edges (\circ), rounded edges (\triangle).

Moreover, simulations with the fine resolution setup are required to assess convergence of the impedance obtained for the rounded-edges geometry. Nonetheless, these results

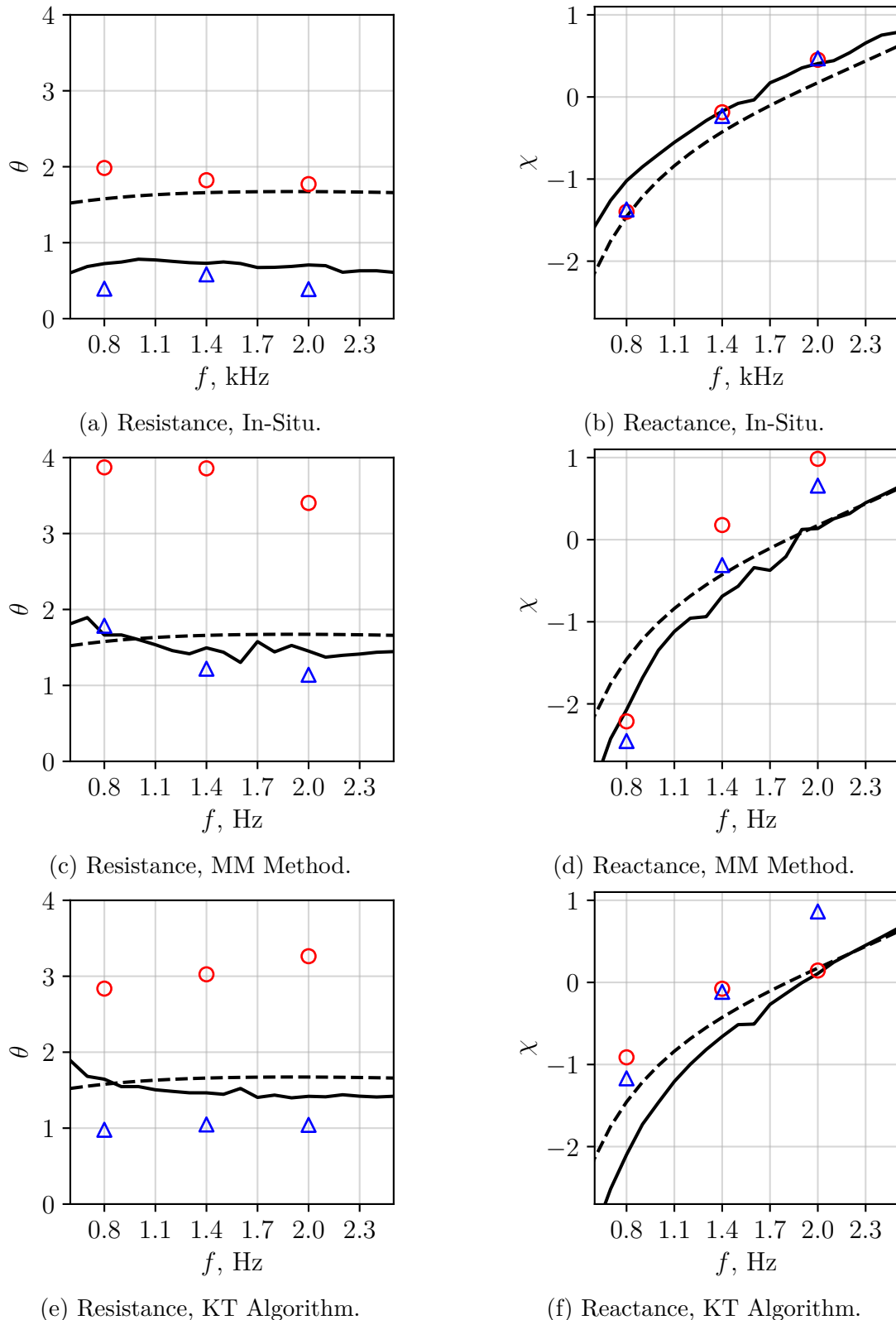


Figure 62 – Comparison of the impedance obtained from the $M = 0.32$ simulations of Sample B with an upstream acoustic source at 145 dB. Experimental (—); semiempirical (---); simulations (medium), sharp edges (\circ), rounded edges (\triangle).

show that pushing the resolution of the model is, perhaps, not the missing key factor for a proper match between the impedance obtained from simulations and experiments.

Apart from not matching properly the experimental impedance in the presence of grazing flow, the model presented in this work is still of great value to assess the liner's acoustic energy absorption mechanisms. As shown by the results presented previously in Sections 4.1.3 and 4.2.3, the model has demonstrated to be sensitive enough to capture different impedance measurements with different source positions, in the presence of grazing flow. In this sense, the following Chapter 5 uses the numerical model to provide a few insights into the absorption mechanisms of liners.

5 INSIGHTS ON SOUND ABSORPTION MECHANISMS OF LINERS

This chapter focuses on discussing various aspects of impedance assessment for liners. It begins by examining the application of the in-situ technique on the entire facesheet to understand how impedance varies in different scenarios. Next, it explores the acoustic-induced flow profile within the orifices using the triple decomposition procedure (refer to Section 2.4.2). Additionally, the discharge coefficient is estimated for different scenarios and the results are compared with previous data found in the literature. The following sections will discuss each of these aspects in the same order, providing a comprehensive analysis.

5.1 IMPEDANCE VARIATION ALONG THE LINER'S FACESHEET

Recent works have shown that different impedance measurement techniques might deliver different results for a given liner sample, especially in the presence of grazing flow (BONOMO; QUINTINO; CORDIOLI, et al., 2023). However, when liners are subjected to high SPL excitation, mismatches between different measurement methods are observed even in the absence of grazing flow (BONOMO; QUINTINO; SPILLERE, et al., 2022). The in-situ technique measures the local impedance using a single pair of microphones or probes, which may not accurately represent the properties of the whole sample. Conversely, the eduction methods provide a global assessment of the liner's impact on the acoustic field, resulting in an averaged impedance value for the sample. However, it should be noted that these global effects are the combined result of the local effects measured by the in-situ technique, which is of particular interest. It is expected a change in the measured impedance in the streamwise direction of the liners, due to the SPL attenuation provided by consecutive cavities (MOTSINGER; KRAFT, 1991; SCHROEDER et al., 2021), which can be assessed by the in-situ technique.

To evaluate how the SPL, resistance and reactance change along the sample, pressure time histories were evaluated along the whole facesheet of the liner in the simulations. Figure 63a shows 2D visualizations of the SPL on the liner facesheet for the 1400 Hz case. It is noticeable that the liner yields considerable attenuation, which results in a change in the measured resistance, presented by Figure 63b. In general, it is observed that the decrease in the SPL is followed by a decrease in the resistance. On the other hand, the

overall behaviour of the reactance is to increase towards the last cavities of the liner, as exhibited by Figure 63c.

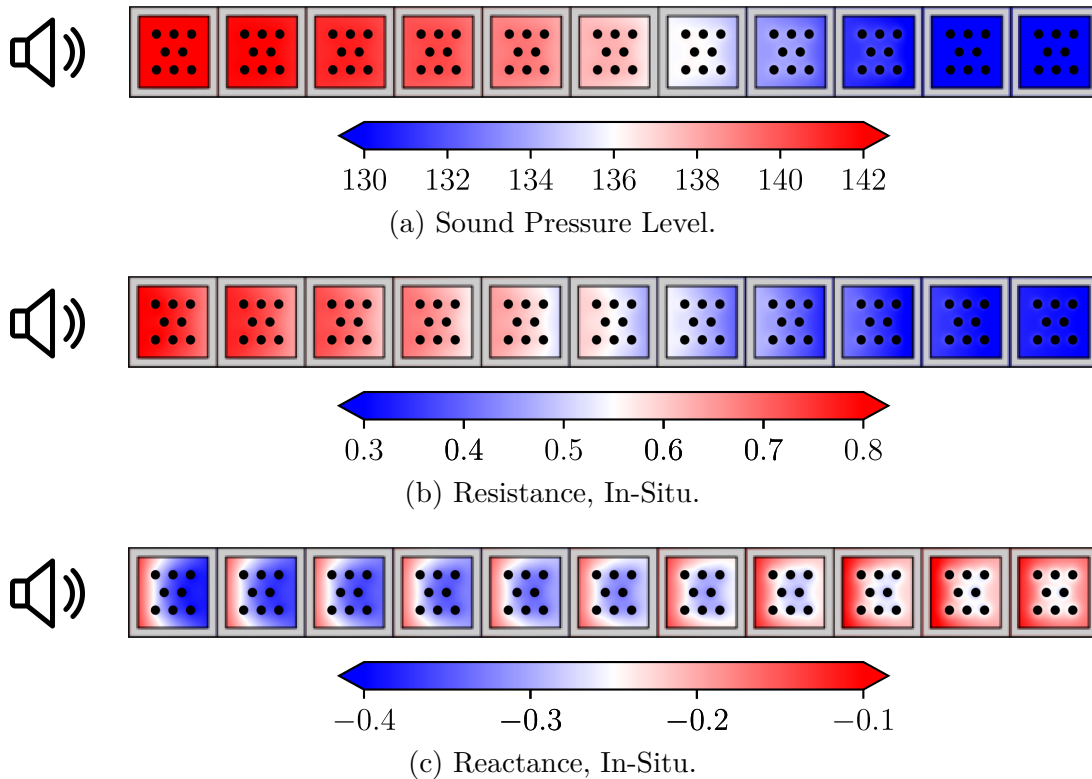


Figure 63 – Contour plots of the results obtained from the simulations (fine) on the facesheet of the liner. $M = 0$ at 1400 Hz acoustic excitation and 145 dB. The acoustic source is positioned upstream of the sample (left hand side of the plot).

Although the contour plots provide an overview of how these parameters change along the facesheet of the liner, line plots provide more detailed and quantitative information. To make these line plots, some of the probes used to make the contour plots were selected on the facesheet at a specific z coordinate. This z coordinate, shown by the red line in Figure 64, was chosen such that none of the probes would coincide with any of the orifices. The line plots obtained from these probes are shown in Figures 65 and 66 for the 1400 Hz and 2000 Hz cases, respectively. In these plots, the vertical white bars represent the partition walls, which separate each cavity from the adjacent ones.

From Figure 65a, one may notice that the liner attenuates more than 10 dB of the incoming acoustic amplitude along its length, considering the tonal excitation at 1400 Hz. The line plots reveal that the SPL slightly changes within the same cavity, reaching a maximum value in the near-orifice regions (centre of the cavity). This reflects in the semiempirical model's predictions for the resistance, exhibited in Figure 65b, which also

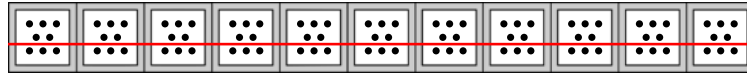


Figure 64 – Location of the facesheet probes along the sample for the line plots of SPL, resistance and reactance.

present a slightly parabolic shape with a maximum in the near-orifice regions. These predictions agree reasonably well with the measured resistance, although the trends within each cavity are different.

The resistance measured decays along the individual cavities, and the maximum value is not found in the near-orifice regions, but close to the left hand side partition wall. This is likely related to the fact that the wall regions act as a discontinuity, considering that the resistance from solid surfaces tend to infinity. As for the reactance, the plots shown in Figure 65c reveal that the measurements increase from the first cavity to the last one. This trend, which is not captured by the semiempirical model's predictions, was also observed in previous works (SCHROEDER *et al.*, 2021; PEREIRA; BONOMO; SILVA, *et al.*, 2022). More interestingly, is the change in the reactance within each individual cavity. Overall, the measured values tend to drop from the partition wall on the left hand side to the right hand side. The curves of the measured reactance also exhibit a parabolic shape, but with a minimum value, which occurs in the near-orifice regions.

Figure 66 shows the line plots for the 2000 Hz acoustic excitation. In this case, the liner provides less attenuation in comparison with the 1400 Hz case, which is closer to the resonance. As a consequence, a smaller variation of the mean resistance values is found along the sample. The reactance mean values, on the other hand, exhibit larger variation for the 2000 Hz case, when compared to the 1400 Hz one. The comparison between the 1400 Hz and the 2000 Hz cases shows the variation trends within each individual cavity are frequency dependent, especially for the SPL and the resistance. The assessment of the SPL for the 2000 Hz case shows a minimum value in the near-orifice regions, which is opposite to the maximum value found in the results for the 1400 Hz excitation. In contrast with a decaying resistance along each cavity, which can be observed in the 1400 Hz case, the 2000 Hz case exhibits an increasing resistance towards the right hand side partition walls.

The assessment of the resistance values along the facesheet reveals interesting trends,

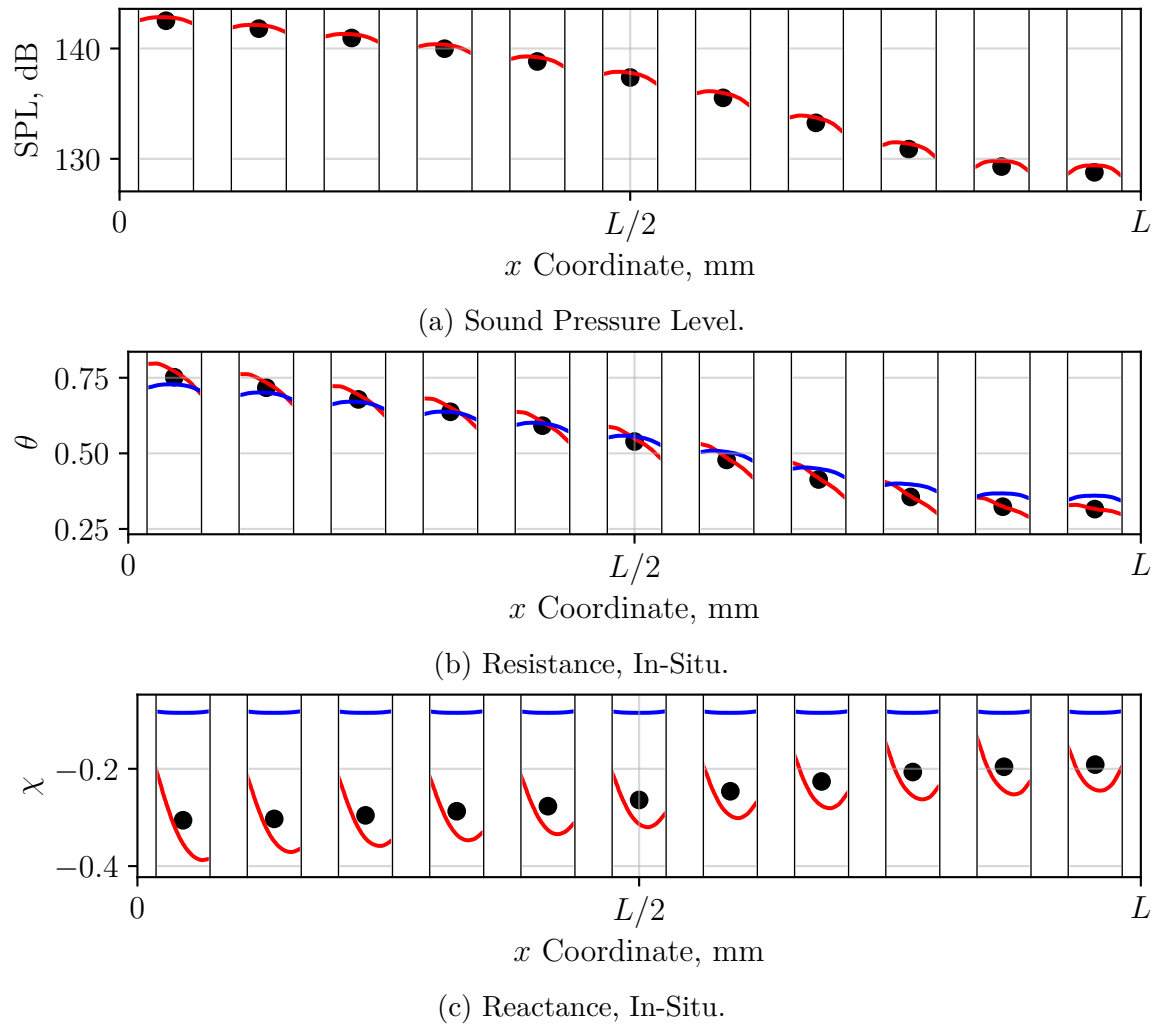
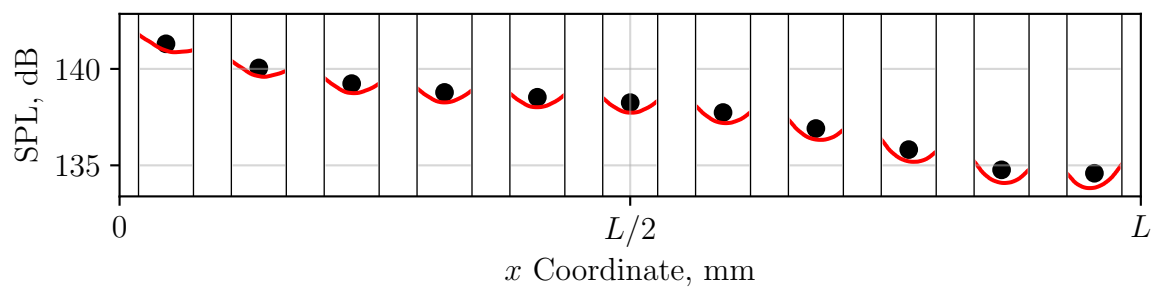
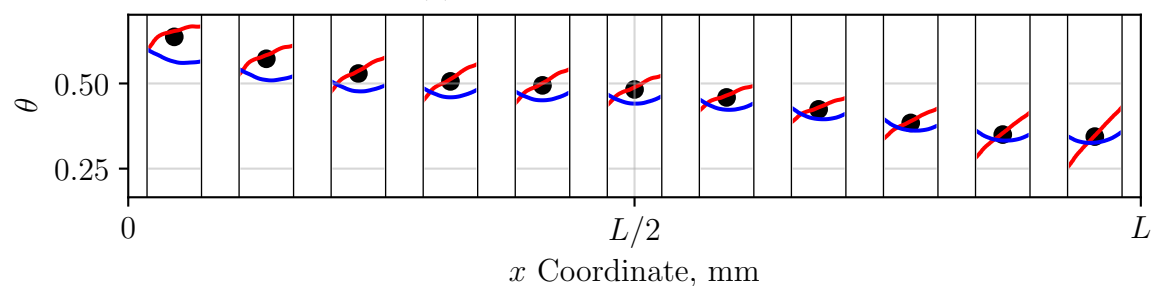


Figure 65 – Results along the liner sample obtained from the simulations (fine) on the facesheet. $M = 0$ at 1400 Hz acoustic excitation and 145 dB. The acoustic source is positioned upstream of the sample (left hand side of the plot). Simulation data (—); mean value of the simulation data (●); semiempirical model prediction, based on the measured SPL (—).

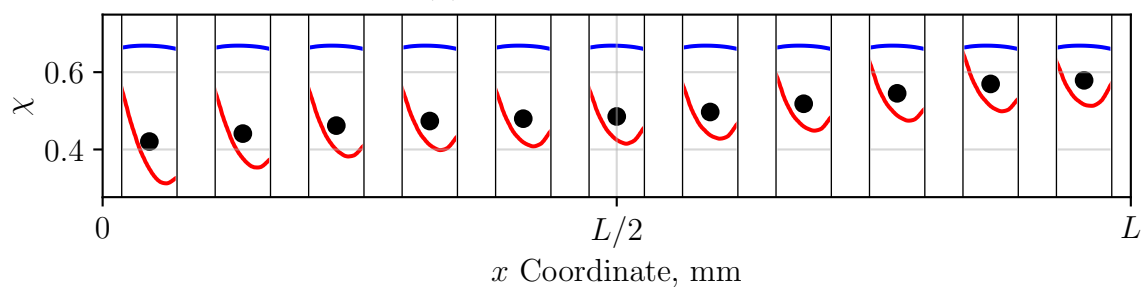
which can be related to previously shown impedance results. As shown in Figure 66b, there is a trend for lower resistance measurements for 2000 Hz at the position of the facesheet probe considered in the experiments (Figure 24b), which is on the left hand side of the orifices. In this sense, the experimental measurements tend to underestimate the resistance with respect to the mean value found for the cavity, which is similar to what is observed between the experiments and the model in Figure 48a. Conversely, resistance tends to be higher than the mean value of the cavity for frequencies below resonance at the probe's position, as depicted in Figure 65b for the 1400 Hz case. This is confirmed by the resistance results obtained for 800 Hz excitation, presented in Figure 67, which exhibit a steeper variation as a function of the x coordinate.



(a) Sound Pressure Level.



(b) Resistance, In-Situ.



(c) Reactance, In-Situ.

Figure 66 – Results along the liner sample obtained from the simulations (fine) on the facesheet. $M = 0$ at 2000 Hz acoustic excitation and 145 dB. The acoustic source is positioned upstream of the sample (left hand side of the plot). Simulation data (—); mean value of the simulation data (●); semiempirical model prediction, based on the measured SPL (—).

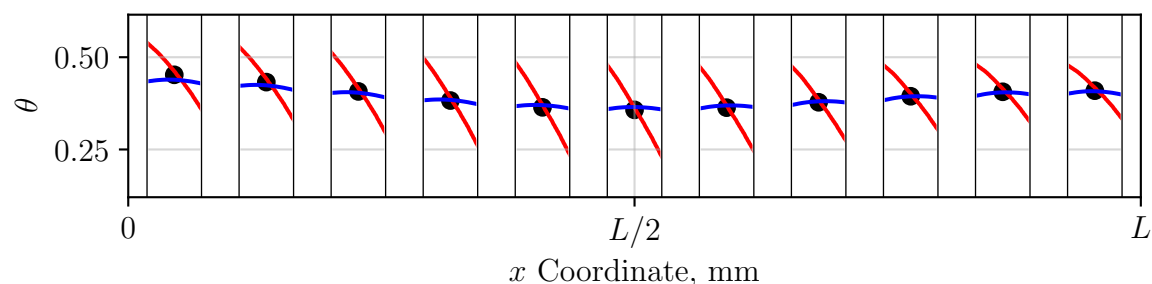


Figure 67 – Resistance along the liner sample obtained from the simulations (fine) on the facesheet. $M = 0$ at 800 Hz acoustic excitation and 145 dB. The acoustic source is positioned upstream of the sample (left hand side of the plot). Simulation data (—); mean value of the simulation data (●); semiempirical model prediction, based on the measured SPL (—).

Based on the arguments above, the results for 800 Hz should theoretically overestimate the semiempirical model's predictions. Surprisingly, they exhibit a nearly perfect match instead. This discrepancy can be attributed to a difference between the SPLs. While a 145 dB SPL is used as input for the model's estimations and as a target to the acoustic sources, the experimental measurements on the facesheet yield values of 142.9 dB, 142.0 dB, and 138.7 dB for 800 Hz, 1400 Hz, and 2000 Hz, respectively. Similarly for the simulations, the SPLs measured at an equivalent location on the facesheet are 143.11 dB, 142.56 dB, and 141.67 dB for the 800 Hz, 1400 Hz and 2000 Hz cases, as depicted in Figure 68.

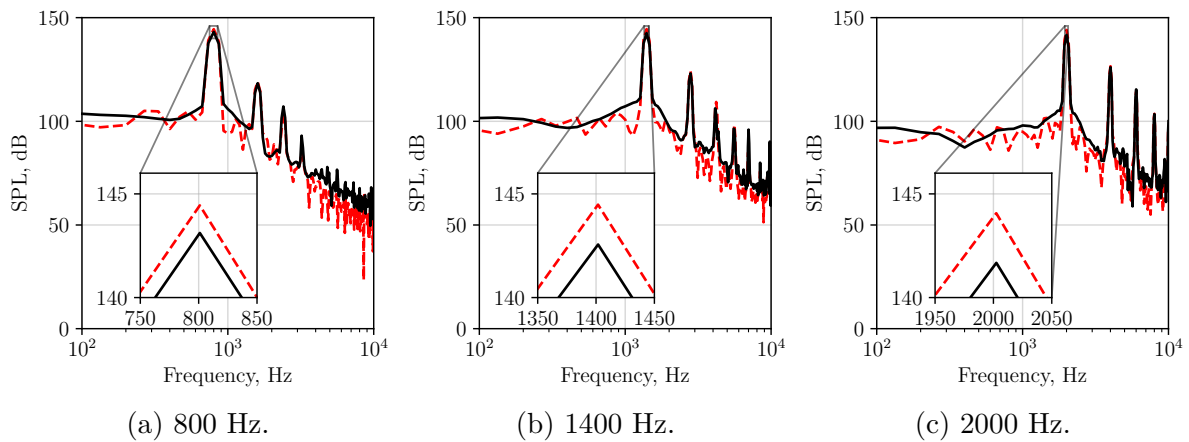


Figure 68 – Sound pressure level measured in the $M = 0$ simulations (fine) by the MM probe closest to the acoustic source (---) and by the in-situ facesheet probe (—).

After adjusting the SPL levels in the semiempirical model's predictions, we observe a notable improvement in agreement with the simulation results, as illustrated in Figure 69, in comparison with the predictions shown in Figure 48a for a constant value of 145 dB as input for all frequencies. However, a slight mismatch can still be observed between the simulated measurements and the semiempirical model's predictions, which aligns with the variations within individual cavities discussed earlier. The model's prediction for the experimentally corrected SPL demonstrates better agreement with the measurements, although a significant mismatch persists for frequencies above 1 kHz.

The same analysis was carried out for the $M = 0.32$ cases. The SPLs on the facesheet are shown in Figure 70, for both upstream (a) and downstream (b) acoustic sources with excitation frequency equal to 1400 Hz. Similarly to the $M = 0$ cases, the SPL largely varies along each cell. When the source is located downstream, the SPL decreases almost linearly along the liner sample, and almost 10 dB of attenuation is observed between the

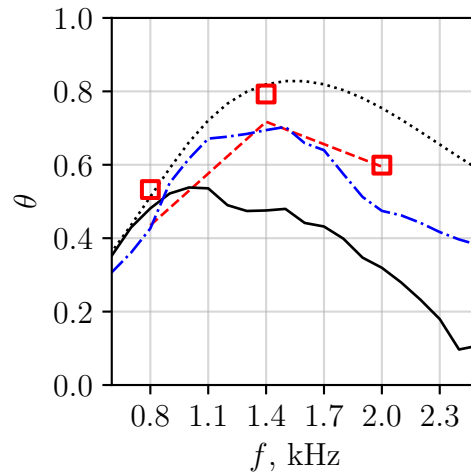
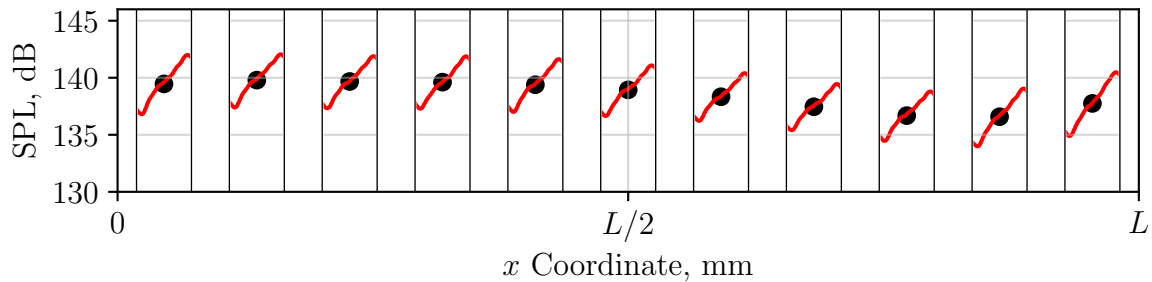
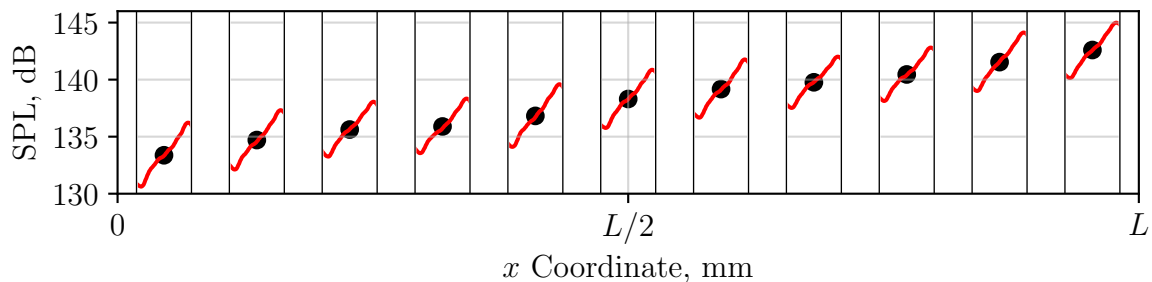


Figure 69 – Comparison of the liner’s impedance obtained from the simulations for $M = 0$ cases with the acoustic source at 145 dB: experimental (—); simulations, fine (\square); semiempirical model, constant 145 dB (.....); semiempirical model for experiments, corrected SPL (-.-.); semiempirical model for simulations, corrected SPL (-.-.-).

last cavity (downstream) and the first one (upstream). On the other hand, the attenuation along the cavities is smaller for the upstream source case.



(a) Upstream acoustic source (left hand side of the plot).



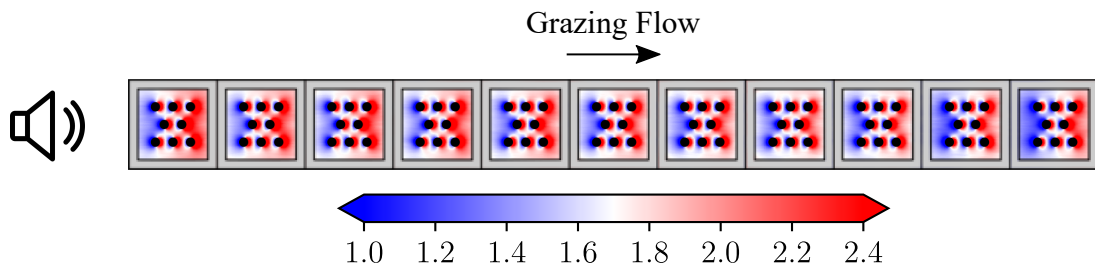
(b) Downstream acoustic source (right hand side of the plot).

Figure 70 – Sound pressure level along the liner sample obtained from the simulations (fine) on the facesheet. $M = 0.32$ at 1400 Hz acoustic excitation and 145 dB. Simulation data, fine (—); mean value of the simulation data.

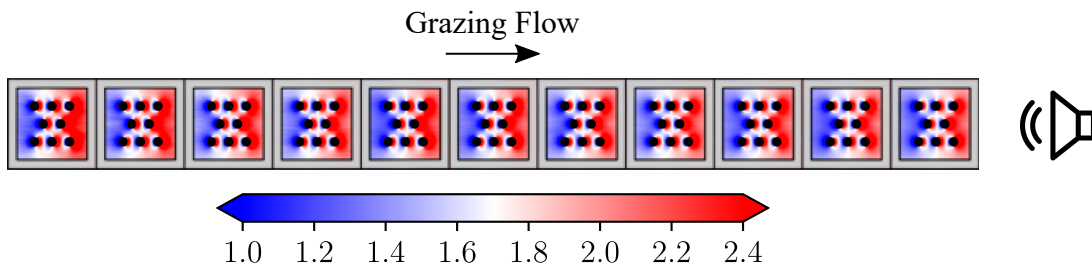
To further understand the differences between upstream and downstream sources, Figures 71 and 72 show the contour plots of the resistance and reactance, respectively,

obtained by applying the in-situ technique on the whole facesheet for the cases with excitation frequency equal to 1400 Hz.

The presence of the grazing flow largely affects the surface distribution of impedance. In these cases, for both upstream and downstream sources, the resistance increases from the most upstream to the most downstream part of each cell. From the surface distribution,

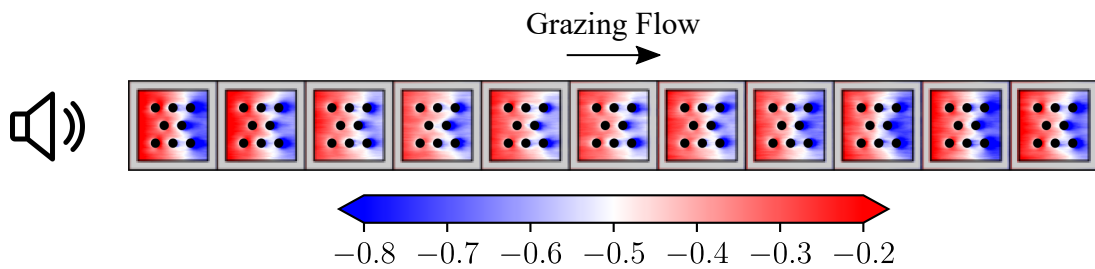


(a) Upstream acoustic source (left hand side of the plot).

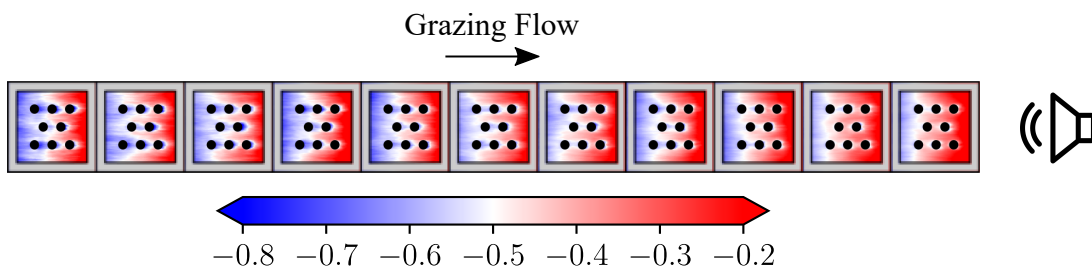


(b) Downstream acoustic source (right hand side of the plot).

Figure 71 – Contour plots of the resistance obtained from the simulations (fine) on the facesheet of the liner. $M = 0.32$ at 1400 Hz acoustic excitation and 145 dB.



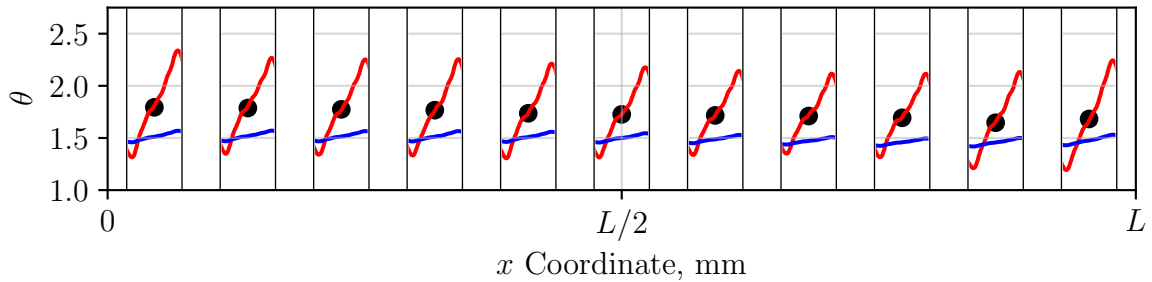
(a) Upstream acoustic source (left hand side of the plot).



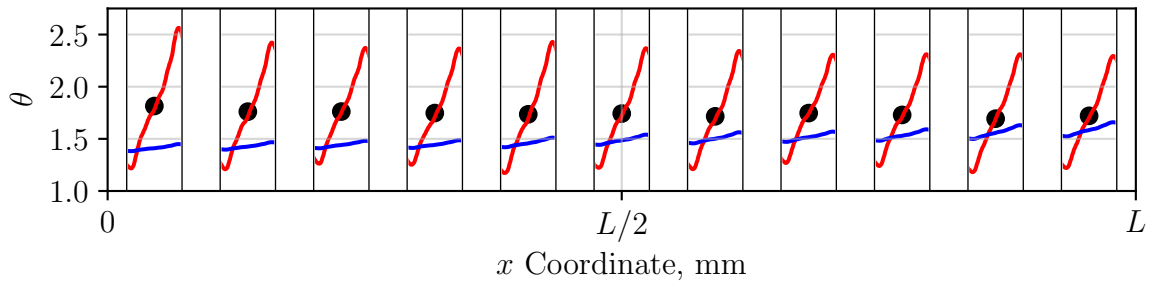
(b) Downstream acoustic source (right hand side of the plot).

Figure 72 – Contour plots of the reactance obtained from the simulations (fine) on the facesheet of the liner. $M = 0.32$ at 1400 Hz acoustic excitation and 145 dB.

it can be speculated that an effect of the interaction between the turbulent flow and the orifice, caused by the periodic inflow and outflow motions in the orifice due to the acoustic excitation, is one of the causes for the resistance variations. These findings are further quantified in Figure 73, where the line plots are depicted for both cases.



(a) Upstream acoustic source (left hand side of the plot).

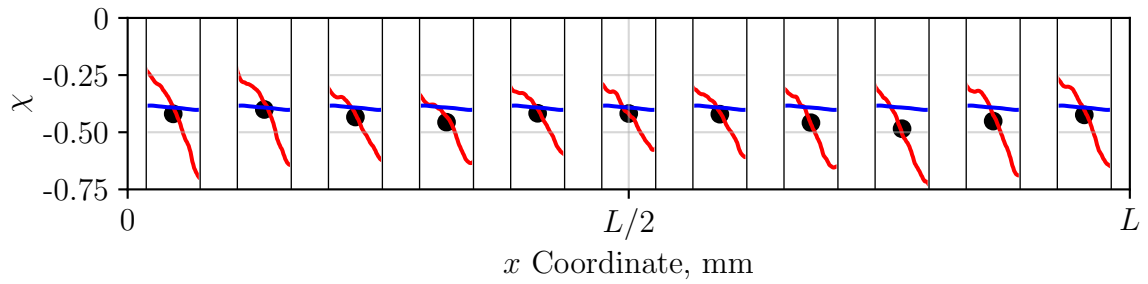


(b) Downstream acoustic source (right hand side of the plot).

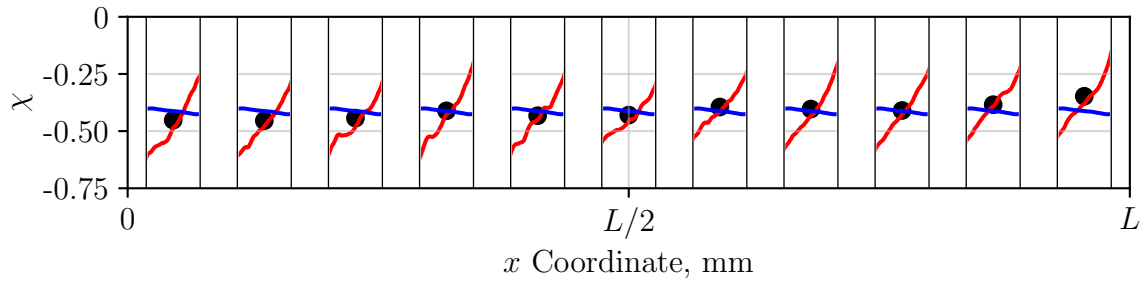
Figure 73 – Resistance along the liner sample obtained from the simulations (fine) on the facesheet by the in-situ technique. $M = 0.32$ at 1400 Hz acoustic excitation and 145 dB. Simulation data, fine (—); mean value of the simulation data, fine (●); semiempirical model prediction, based on the measured SPL (—).

The surface distributions displayed in Figure 72 show that the grazing flow also affects the reactance measurements. Interestingly, for the upstream acoustic source case, the reactance tends to drop from the most upstream portion to the downstream portions of the cavities. Conversely, the opposite behaviour is observed for the downstream source case. These findings are further detailed in Figure 74. The streamwise distribution of the mean reactance is rather uniform along the liner sample, for both upstream and downstream sources. However, the variation of the results within a single cavity is noticeably different from one case to the other.

Based on the discussions presented above, an additional experimental campaign was carried out to check whether these observations would stand. For this purpose, experimental data was obtained with the in-situ technique for facesheet probes positioned before and after the orifices, with respect to the grazing flow direction. Figure 75 shows the probe positions considered in the simulations, which are very close to the positions considered in



(a) Upstream acoustic source (left hand side of the plot).



(b) Downstream acoustic source (right hand side of the plot).

Figure 74 – Reactance along the liner sample obtained from the simulations (fine) on the facesheet by the in-situ technique. $M = 0.32$ at 1400 Hz acoustic excitation and 145 dB. Simulation data, fine (—); mean value of the simulation data, fine (●); semiempirical model prediction, based on the measured SPL (—).

the experiments. The main difference between the probes' positions between simulations and experiments, as mentioned previously, is that the third spanwise cavity is sampled in the experiments (see Figure 24b), while in the simulations the results were assessed in the first spanwise cavity.

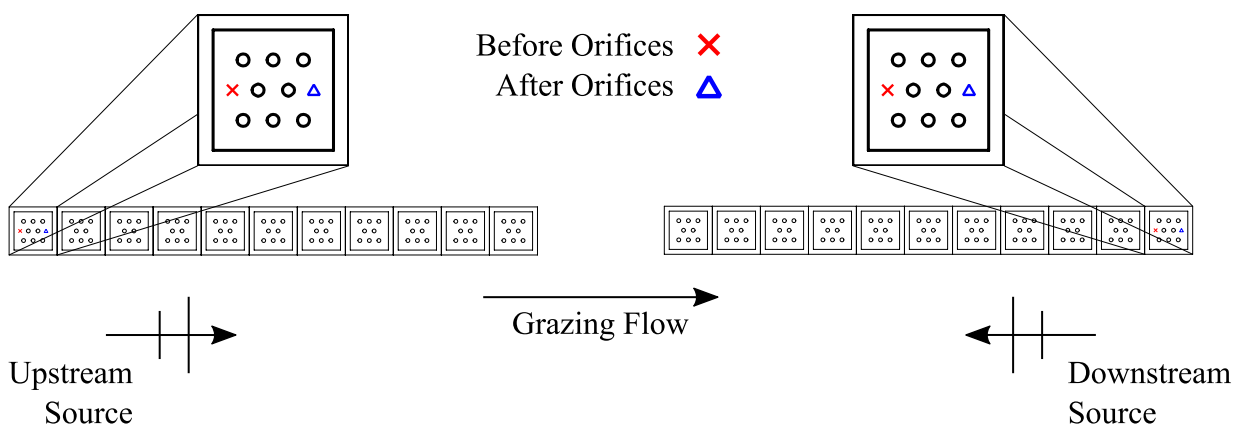


Figure 75 – Positions of the facesheet probes for the additional campaign.

Figure 76 exhibits the impedance results assessed before the orifices (BO) and after the orifices (AO) by both the experiments and the simulations. Despite the overestimated resistance exhibited by the simulations in some cases, which was previously discussed, the relative difference between BO and AO results is consistent for both the experiments and

the simulations. With respect to the resistance, the experiments confirm the frequency dependent trend, where BO results are higher below resonance and AO become higher above resonance. Furthermore, the results are also in good agreement in terms of reactance, with BO values higher than the AO ones for the entire frequency range.

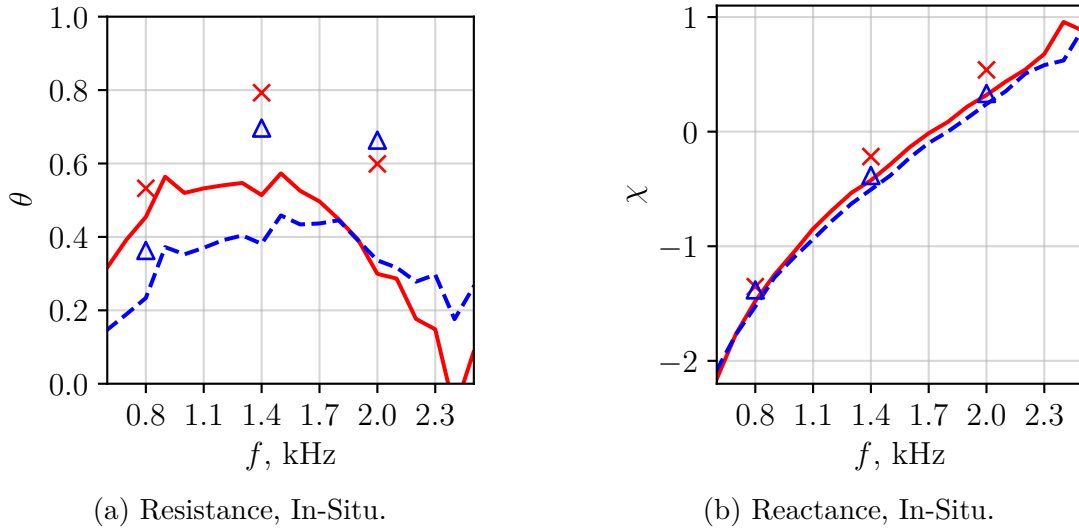


Figure 76 – Comparison of the impedance obtained from the $M = 0$ simulations of Sample B with an upstream acoustic source at 145 dB: experimental, before (—) and after (---) the orifices; simulations (fine), before (×) and after (△) the orifices.

Figures 77 and 78 present the results for the $M = 0.32$ cases considering upstream and downstream sources, respectively.

In the presence of the $M = 0.32$ grazing flow, the resistance trends are no longer frequency dependent, and AO results are higher than the BO ones for all frequencies, considering both upstream and downstream sources. This statement comprises both experiments and simulations, which once again are consistent in terms of relative difference between BO and AO resistance values.

Regarding the reactance, one can also observe the same consistency between the numerical and the experimental data. In the case of the upstream acoustic source, BO results are higher than the AO ones for all the frequencies analysed. In contrast, the reactance obtained for the downstream source exhibits an opposite behaviour. In this case, the experiments confirm that the AO reactance results are higher than the BO ones, which agrees with the previously shown contour plots from the simulations.

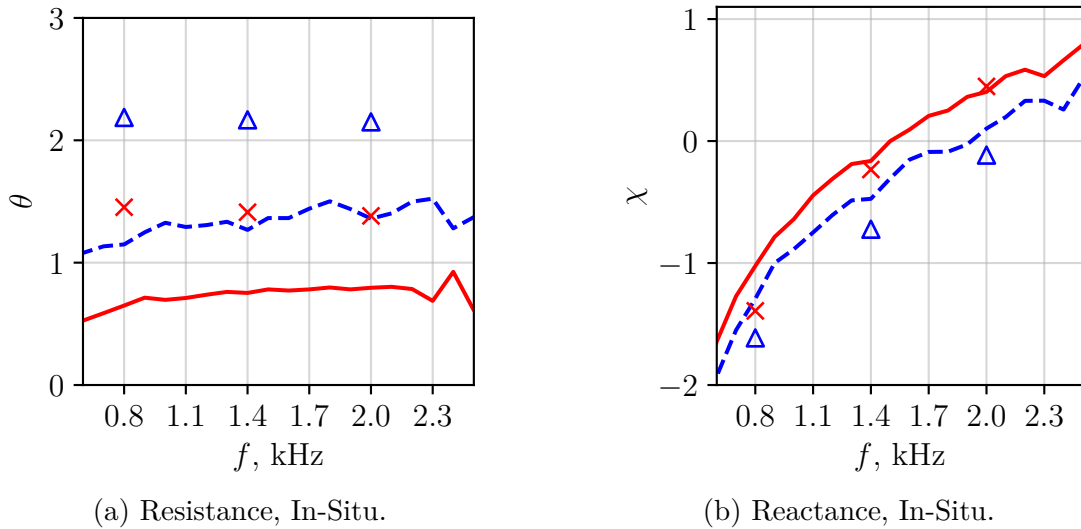


Figure 77 – Comparison of the impedance obtained from the $M = 0.32$ simulations of Sample B with an upstream acoustic source at 145 dB: experimental, before (—) and after (---) the orifices; simulations (fine), before (\times) and after (\triangle) the orifices.

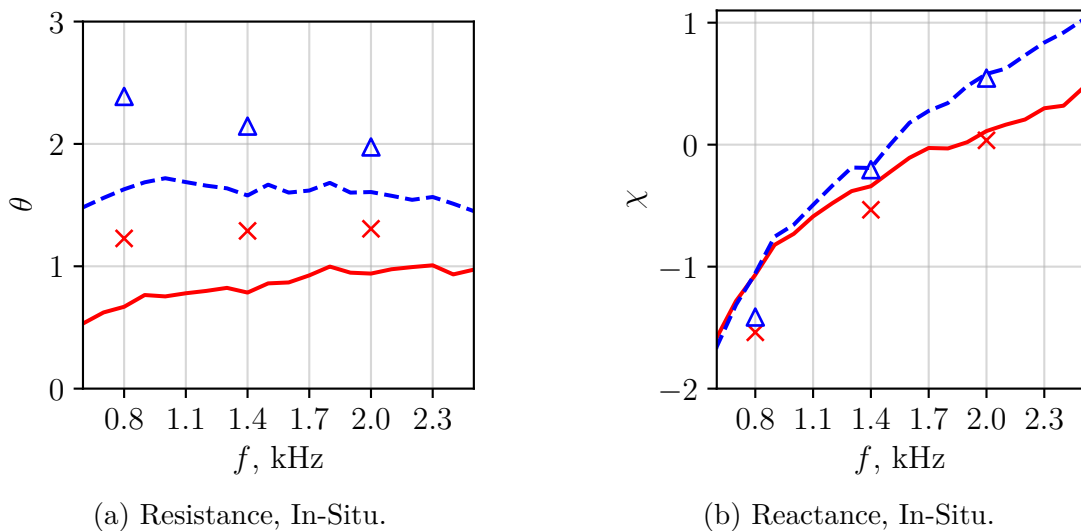


Figure 78 – Comparison of the impedance obtained from the $M = 0.32$ simulations of Sample B with a downstream acoustic source at 145 dB: experimental, before (—) and after (---) the orifices; simulations (fine), before (\times) and after (\triangle) the orifices.

5.2 IN-ORIFICE FLOW INDUCED BY ACOUSTICS

The flow profile within the orifices of the liner plays a crucial role on the impedance because the intrinsic viscous effects, which dominate in the orifices, largely contribute to the dissipation of acoustic energy.

Previous literature has identified certain effects resulting from the presence of grazing flow over the facesheet. For instance, it is known that during inflow and outflow cycles,

the asymmetry of the acoustic-induced flow occurs. This asymmetry is caused by flow recirculation (refer to Figures 44 and 53), and it leads to a reduction in the effective orifice area where the oscillation of the acoustic-induced flow happens. Consequently, the liner's resistance significantly increases in the presence of the grazing flow.

The simulation results of the impedance demonstrate the observed increase in resistance when the grazing flow is present. In order to analyse the effects on the flow profiles within the orifices, the triple decomposition procedure (illustrated in Figure 13) was applied to the velocity field. This procedure enables the assessment of the acoustic-induced velocities.

Figures 79 and 80 display contour plots of the magnitude of the acoustic-induced velocity, calculated as $\sqrt{\bar{u}^2 + \bar{v}^2 + \bar{w}^2}$, for Sample B. Figure 79 represents the velocity in the absence of grazing flow, while Figure 80 represents the velocity in the presence of the $M = 0.32$ grazing flow. Both figures refer to an upstream source with a frequency of 1400 Hz and an SPL of 145 dB. The displayed phase corresponds to the point of maximum velocity amplitude in the orifices of the most upstream cavity, during the inflow cycle.

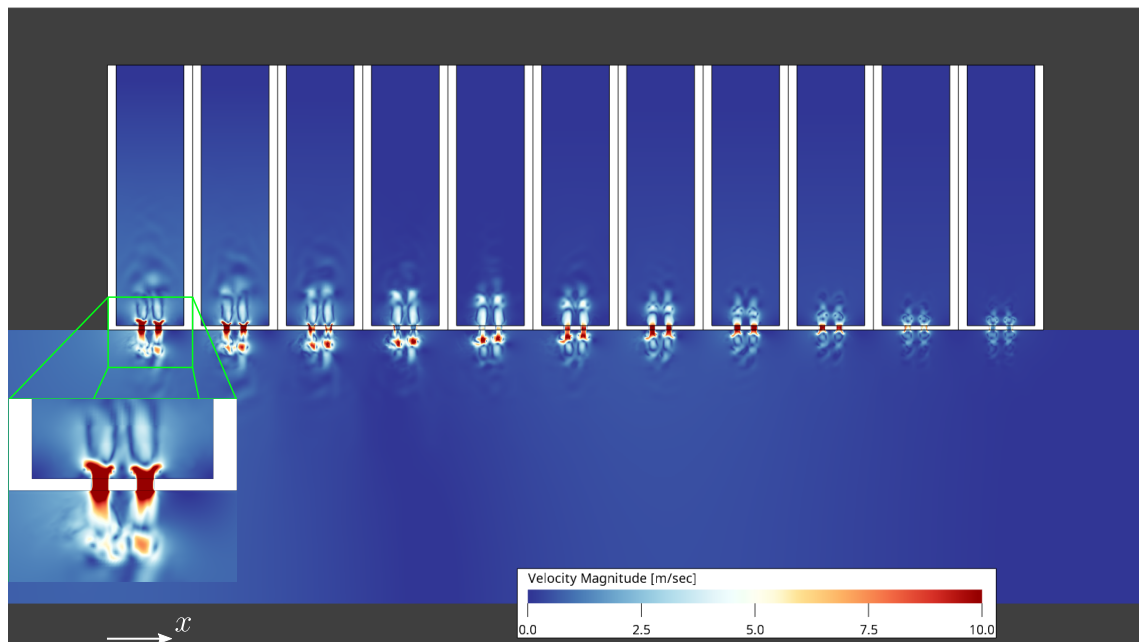


Figure 79 – Contour plot of the magnitude of the acoustic-induced velocity for Sample B in the absence of grazing flow. Case corresponds to a 1400 Hz acoustic source at 145 dB.

From the two figures it is possible to observe that the acoustic-induced flow is asymmetric inside the orifices, when the grazing flow is present. In this case, the acoustic

pressure perturbations manage to force the air through the openings only in their most downstream portions, while the most upstream portions are ‘blocked’ by the vortices. Conversely, the in-orifice flow is rather symmetric when the grazing flow is absent. These observations agree with previous works from the literature (ZHANG; BODONY, 2016; LÉON et al., 2019; AVALLONE; DAMIANO, 2021).

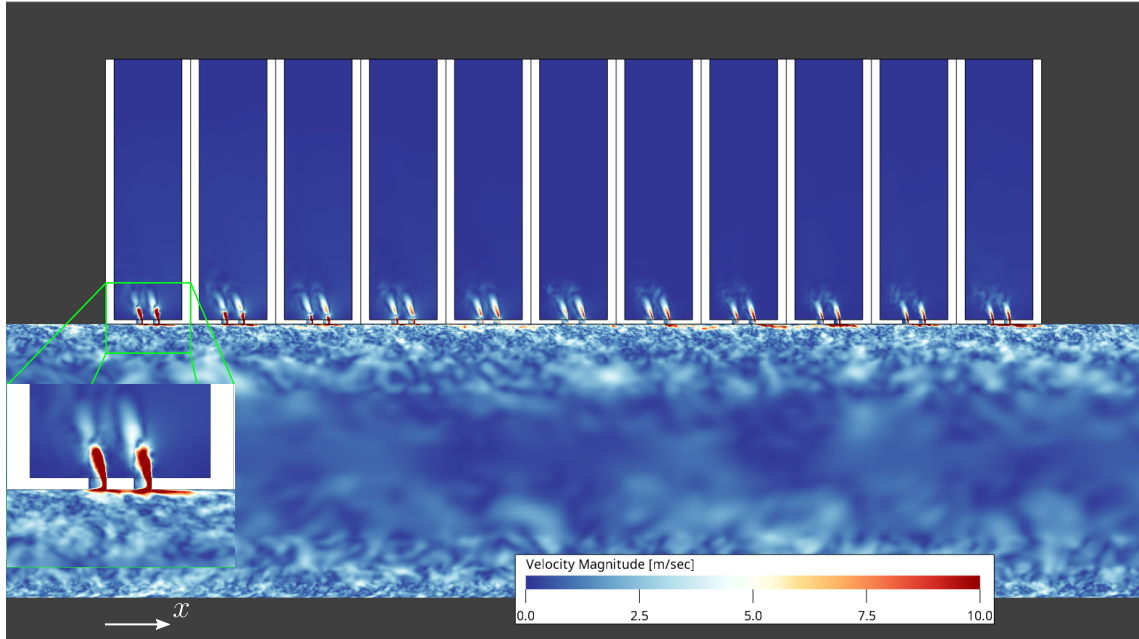


Figure 80 – Contour plot of the magnitude of the acoustic-induced velocity for Sample B in the presence of the $M = 0.32$ grazing flow. Case corresponds to a 1400 Hz upstream acoustic source at 145 dB.

To further investigate this phenomena and to verify whether the position of the acoustic source has any influence on the in-orifice flow, the y component of the acoustic-induced velocity was assessed in a spanwise plane (y normal), located in the mid-section of the orifices (see Figure 39b).

Figures 81 and 82 exhibit contour plots of the \bar{v} assessed in the orifices located in the mid-span of the liner, at the most upstream and downstream ends, respectively. The positive values refer to the maximum amplitude of \bar{v} during the inflow phase, while the negative values refer to the maximum amplitude of \bar{v} during the outflow phase. These plots correspond to the 1400 Hz excitation case, at 145 dB. The plots for 800 Hz and 2000 Hz show similar behaviour, and are depicted in Appendix B.

From Figure 81, it is possible to observe in more detail the change in spatial distribution of the flow’s core during inflow and outflow phases, due to the presence of the

grazing flow. The change in the position of the acoustic source does not alter the behaviour of the flow within the orifice. Although lower amplitudes are observed for the velocity in the downstream source case, this can be attributed to the lower SPL found in the most upstream end of the sample, as shown in Figure 70.

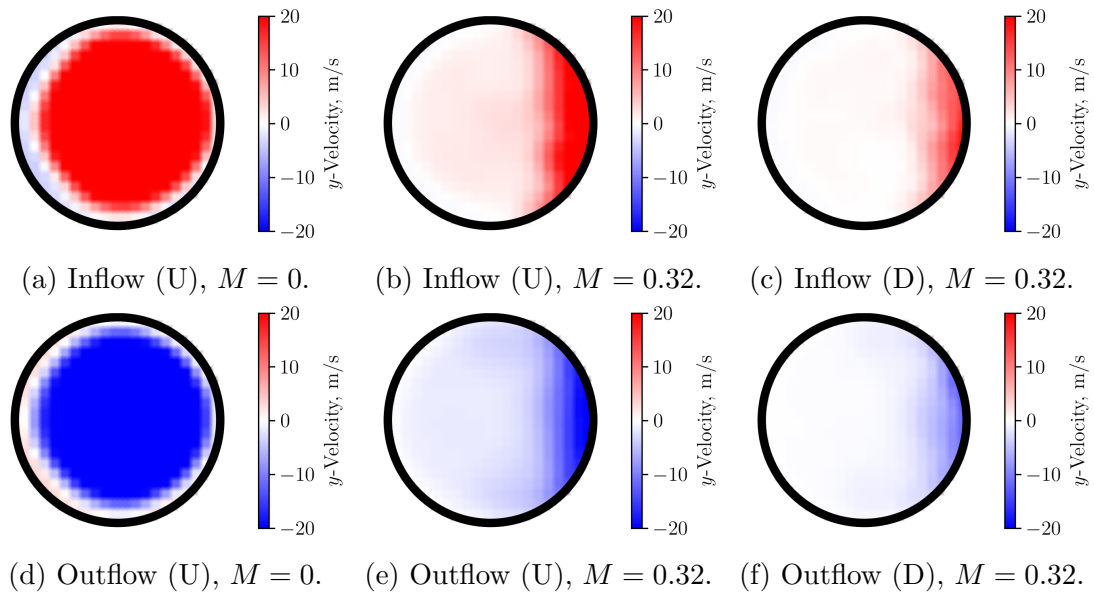


Figure 81 – Contour plots of \bar{v} , assessed in the most upstream orifice located in the mid-span of the liner. Data refers to a 1400 Hz acoustic source at 145 dB. Upstream (U) and downstream (D) acoustic sources.

A similar analysis can be performed for the orifice at the most downstream end of the liner, shown in Figure 82. In this case, lower amplitude is found for the velocity in the core of the flow in the $M = 0$ case, due to the liner's attenuation. The magnitude of \bar{v} for the downstream source case is higher in the most downstream orifice, as expected. Still, no remarkable influence of the source's position can be seen in the velocities' distributions. Interestingly, the amplitude of the oscillations for the upstream source case does not decay as much from the most upstream to the most downstream orifice, which agrees with the low SPL attenuation along the sample observed previously in Figure 70.

In order to quantify these data, the in-orifice velocity profiles were extracted from the streamwise plane (see Figure 39a) in the mid-section of the orifices. Figure 83 depicts the in-orifice flow profiles extracted from the cases with 1400 Hz excitations at 145 dB. In this figure, the phases of maximum amplitudes in both inflow and outflow cycles are shown. For the $M = 0.32$ cases, the orifices closest to the acoustic sources were considered, such that the highest possible SPL was accounted for.

Figure 83a depicts the y component of the phase-locked velocity v_{PL} , which corre-

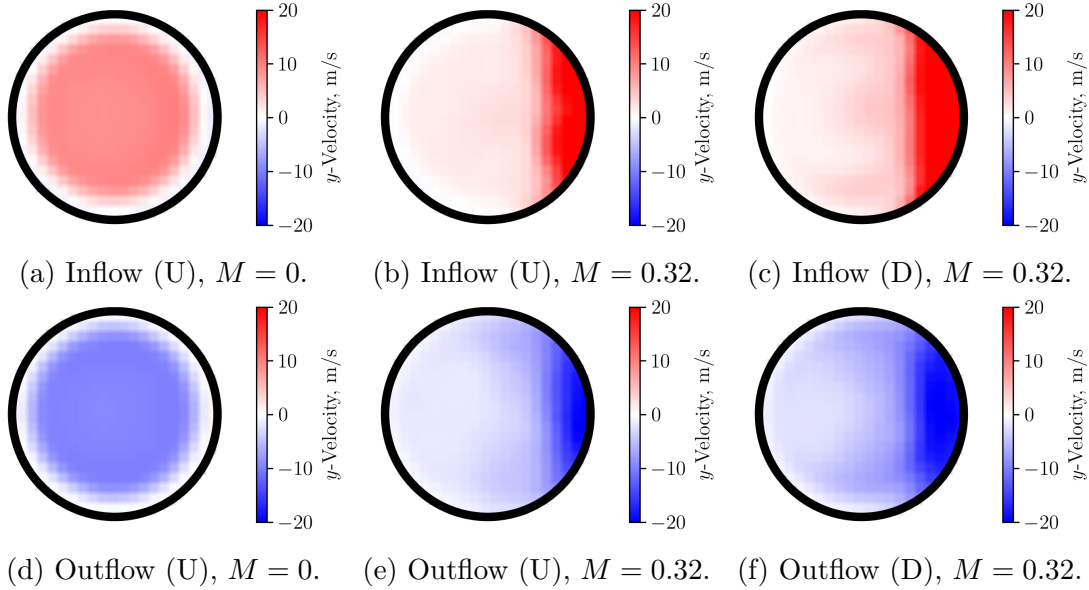
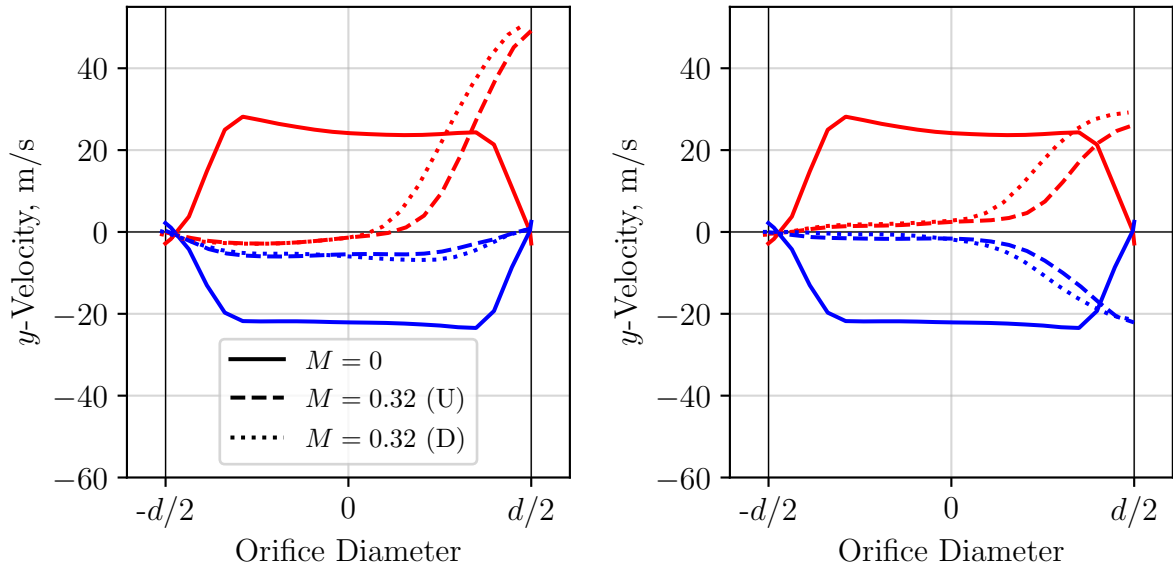


Figure 82 – Contour plots of \bar{v} , assessed in the most downstream orifice located in the mid-span of the liner. Data refers to a 1400 Hz acoustic source at 145 dB. Upstream (U) and downstream (D) acoustic sources.

sponds to the phase-averaged effect of both acoustic waves and grazing flow, combined. For the $M = 0$ case, it is evident that both inflow and outflow phases exhibit a symmetrical pattern around the orifice centre. When the grazing flow is present, the profiles become highly asymmetric. Furthermore, the maximum amplitude observed for the inflow cycles are much higher than what is seen for the outflow cycles. This behaviour is due to the effect of the quasi-steady vortex, which acts in favour of the acoustic wave during the inflow cycle at the downstream edge of the orifice, and against the acoustic wave during the outflow cycle.

By removing the mean effect of the grazing flow, the y components of the acoustic-induced velocities \bar{v} are obtained, and are exhibited in Figure 83b.

From these results, it is clear that $v_{PL} = \bar{v}$ for the $M = 0$ case. However, in the presence of the $M = 0.32$ grazing flow, the \bar{v} profiles exhibit considerable oscillations only at the most downstream portion of the orifice, as previously observed in Figures 80, 81 and 82. These profiles are rather symmetric with respect to the horizontal zero line, with a slightly lower amplitude observed for the outflow cycles. This effect can be attributed to a loss in the acoustic energy due to viscous dissipations. Nonetheless, these plots enlighten the fact that the maximum amplitude for both inflow and outflow cycles are equivalent between the $M = 0$ and $M = 0.32$ cases, disregarding the position of the acoustic source. These observations are complementary to those in [Avallone and Damiano \(2021\)](#).



(a) Phase-locked velocity v_{PL} , y component. (b) Acoustic-induced velocity \bar{v} , y component.

Figure 83 – In-orifice velocity profiles from the maximum and minimum value phases, induced by a 1400 Hz acoustic excitation at 145 dB. Inflow cycles are in red, outflow cycles are in blue.

Taking a closer look in Figure 83b reveals that the downstream source case exhibits slightly higher velocity amplitude than the upstream source case, at least during the inflow cycle. Intuitively, this translates into a slightly larger resistance for the latter, which was confirmed by the results in Figure 73.

As it can be seen in Figure 70, there is lower SPL in the first cavity for the upstream source case when compared with the last cavity for the downstream source case, which might be the cause for the higher \bar{v} values found for the latter. Although higher SPL typically translates into higher resistance, at least for the $M = 0$ scenario, this might not be the case when the grazing flow is present, since the flow effects dominate.

With the grazing flow over the liner, the key parameter for the resistance results seems to be the effective orifice area where the acoustic-induced oscillation takes place, which is related to the quasi-steady vortices. In this sense, the higher SPL acoustic waves manage to ‘push’ the flow through a larger area of the orifice and through a greater portion of the vortex, which results in relative lower resistance.

5.3 ASSESSMENT OF THE DISCHARGE COEFFICIENT

As discussed in the previous Section 4.3, the discharge coefficient C_D is an important parameter from the impedance point of view, especially regarding the resistance. It

quantifies the differences found for the in-orifice flow patterns observed in the previous Section 5.2 for different scenarios. It can be interpreted as an orifice open-area correction, due to the formation of the *vena contracta* during inflow and outflow phases when grazing flow is absent (SPILLERE, 2017, p. 63). However, with the presence of the grazing flow, the assessment of the *vena contracta* is not straightforward.

Generally, there is not a well-defined method to obtain the C_D for acoustic liners (TAM; KURBATSKII, 2000), and a wide range of values are reported in the literature. Zinn (1970) performed a theoretical study on resonators and found $C_D \approx 0.61$ for sharp-edged orifices, when subjected to high Reynolds flows. The canonical work on liners, by Melling (1973), reports discharge coefficients for perforated plates with a 7.5% POA ranging from 0.62 to about 0.80, depending on the assessment method. The classical model by Mottsinger and Kraft (1991) adopts $C_D = 0.76$, which is a common assumption found in other texts regarding acoustic liners. Under high acoustic loadings (i.e., for near-resonance frequencies and/or at high SPL), Zhang and Bodony (2012) obtained $C_D \approx 0.70$ with a numerical approach in the absence of grazing flow. In less severe acoustic loadings, values up to 0.86 were obtained. In contrast, for the liner Sample B considered in this work, the C_D obtained from the expression given in the Goodrich semiempirical model is approximately 0.83 (refer to Section 2.3), disregarding the frequency/SPL of the excitation and whether grazing flow is present or not.

Based on the velocity profiles exhibited in the previous Section 5.2, it is possible to estimate the C_D from the simulations. For this purpose, an alternative mathematical definition for the C_D , presented by Park and Mongeau (2007), was considered. The expression can be translated into the ratio of the real flow rate through the orifice by the ideal flow rate, in the form of

$$C_D(t) = \frac{\int \bar{\bar{v}}(\mathbf{x}, t) dS}{Sv_{ac}}, \quad (5.1)$$

where v_{ac} is the ideal flow velocity induced by the acoustic waves. It is important to consider that, since $\bar{\bar{v}}(\mathbf{x}, t)$ is time-dependent, so is the C_D . However, in the following analysis, only the maximum value of the C_D is taken into account, which corresponds to the phase of the maximum flow rate through the orifice.

To determine v_{ac} , the approach based on the Bernoulli's equation for an inviscid and incompressible fluid is considered, which was also employed by Ingard (1970). The velocity

is estimated by

$$v_{ac} \approx \sqrt{\frac{2P_o}{\rho_0}}, \quad (5.2)$$

where $P_o = \sqrt{2}p_{ref}10^{\frac{SPL_f}{20}}$, as a function of the SPL measured on the facesheet.

The C_D was estimated from the simulations for all the orifices and averaged per cavity. These results are shown in Figure 84 for different cases. From these results, it is noticeable that the C_D obtained for the $M = 0$ cases are frequency dependent. At 800 Hz, the results are rather constant over all the cavities, and are close to 0.40. The relative low value can be explained by the fact that, even though the liner was excited by a high SPL incident wave, it is not capable of providing reasonable attenuation, such that the acoustic-induced flow rate within the orifices is reasonably compromised with respect to the ideal prediction. On the other hand, the 1400 Hz and 2000 Hz excitations promote an averaged C_D over all cavities of approximately 0.67 and 0.56, respectively. It is worth noticing that these trends are reversed, in comparison with those observed in Zhang and Bodony (2012), which showed lower C_D for near-resonance frequencies. However, in that work, the C_D was obtained by an expression based exclusively upon the δ_1 inside the orifice, and did not take into account any difference in the velocity magnitude inside the core of the jet flow. Consequently, the approach described in Zhang and Bodony (2012) can deliver a lower C_D because of a higher δ_1 for a near-resonance excitation, even if a relative higher mass flow rate is observed.

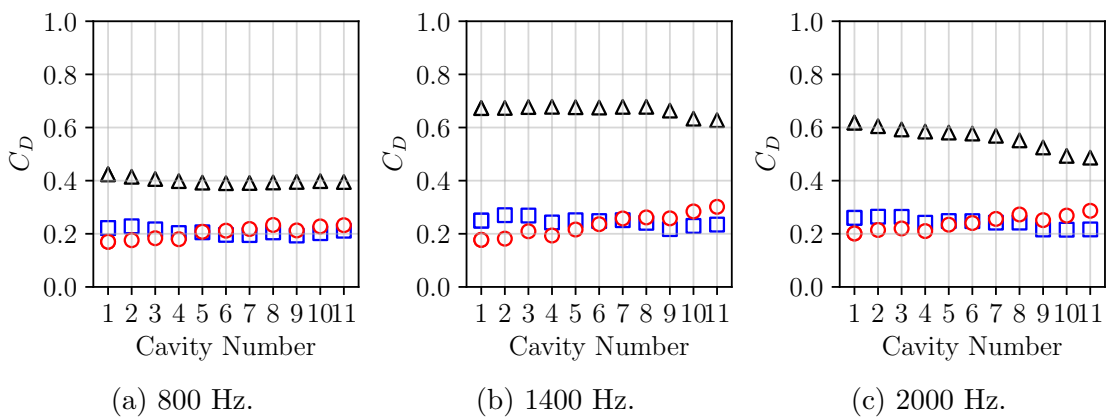


Figure 84 – Discharge coefficient estimated from the simulations (fine) with the acoustic source at 145 dB. v_{ac} estimated with the Bernoulli’s approach. $M = 0$ (Δ); $M = 0.32$, upstream source (\square); $M = 0.32$, downstream source (\circ).

When the grazing flow is present, a significant drop in the C_D can be observed. In these cases, the averaged values for upstream sources are 0.21, 0.25 and 0.24, for 800 Hz, 1400 Hz and 2000 Hz, respectively. For the downstream source cases, it is found 0.20, 0.23

and 0.24, for the respective frequencies. It can be seen that the C_D values slightly decrease from the liner end which is closest to the acoustic source to the opposite side. This is likely related to a change in the SPL, and consequently in the flow rate inside the orifices along the sample, although the range in which the variations occur is quite small. Apart from that, the overall behaviour of the C_D along the sample does not exhibit any dependency on the position of the source.

The results obtained for each orifice for $M = 0$ were plotted against the reference data presented by Melling (1973), which were obtained experimentally by Johansen and Southwell (1930) with steady flow measurements. These plots, exhibited in Figure 85, are shown as a function of the square root of the in-orifice Reynolds number. Also, the results are divided in different trends with respect to the d/D ratio, where D is the diameter of the inscribed circumference in the downstream enclosure of the flow. In the case of the liner Sample B, it is considered that $D = l$, since the cavity is squared.

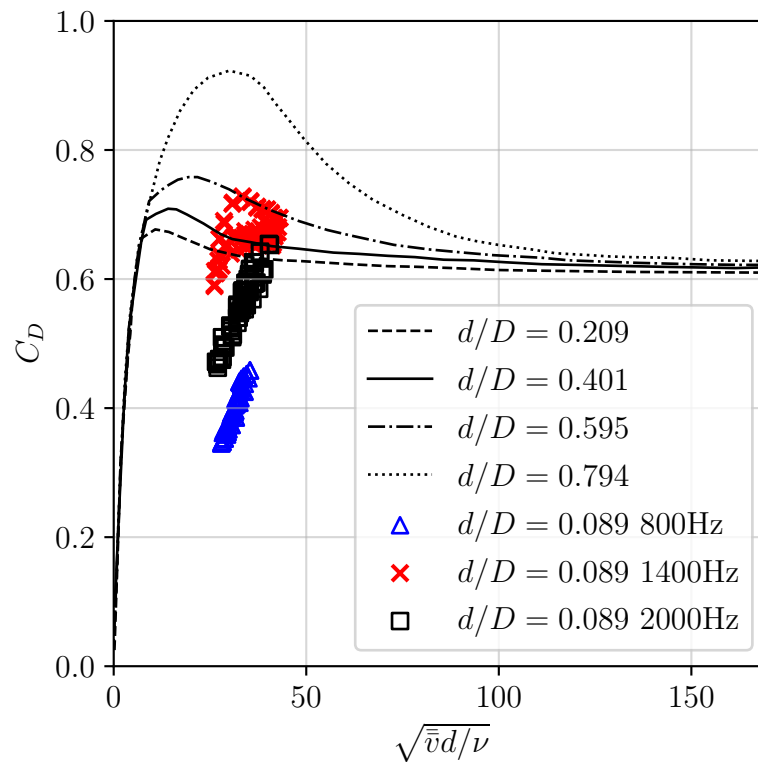


Figure 85 – Comparison of the discharge coefficient estimated from the $M = 0$ simulations (fine) with reference data obtained from Melling (1973), represented by the black lines. Simulation results (scatter points) refer to the acoustic source at 145 dB. v_{ac} estimated with the Bernoulli's approach.

The comparison between the simulations results for the C_D and the reference data reveals reasonable agreement, depending on the frequency analysed. From the available

reference data, the curve which is more closely related to the $d/D \approx 0.089$ relation found for the Sample B is represented by the dashed line, for which $d/D = 0.209$. From the Reynolds numbers obtained for the orifices in the simulations, the dashed line suggests an approximate value of 0.63 for the C_D , which is in good agreement with the averaged value of 0.67 found for the 1400 Hz case. Other frequencies are unable to induce flow rates as high as those found for 1400 Hz, although impinging in the facesheet with similar SPL, and this reduces the values found for the C_D .

Different approaches can be found in the literature to estimate v_{ac} , which not necessarily agree with the predictions from Equation 5.2. Consequently, these alternative approaches deliver different C_D values. One of these alternative approaches is that considered by Léon et al. (2019).

The approach considered by Léon et al. (2019) relies on a SDOF damped system analogy to the liner. Besides the SPL measured on the facesheet, the method depends on the quality factor Q to estimate v_{ac} . The Q parameter is inversely proportional to the resonator's resistance, and typical values for the quality factor of liners in the absence of grazing flow are $Q \approx 10$ (ZHANG; BODONY, 2016). Based on the geometrical parameters of Sample B, it is possible to estimate $Q \approx 13.9$ with the expression found in Morse and Ingard (1986, p. 490). However, as stated by Léon et al. (2019), non-linear effects induced by a high SPL and by grazing flow significantly increase the orifice resistance and thus decrease the value of Q , yielding $Q \approx 1$. This imposes a challenge to the definition of a proper Q value valid for the whole liner, even in the absence of grazing flow. It has been shown in Section 5.1 that the SPL and the resistance change along the facesheet considerably, so ideally the Q factor should vary as well. Since Léon et al. (2019) considered a constant Q value for their analysis, this approach is rather inaccurate for the purposes of this work. A more suitable estimation for the C_D along the liner sample with this method would require a formal relation between Q and the measured resistance, which was not investigated in this work.

6 CONCLUSIONS

This work focused on the development of a high-fidelity numerical model for acoustic liners, which was used to assess the liners' impedance in the absence and in the presence of subsonic turbulent grazing flows. Two liner geometries were simulated and their impedance was assessed in different scenarios with three measurement techniques, namely the in-situ technique, the mode matching method and the KT algorithm. The numerical results were compared with experimental data obtained at the UFSC test rig and with predictions from a semiempirical model. Overall, the effects of the frequency and sound pressure level of the acoustic source, as well as its relative position to the sample, were investigated.

The impedance results from the simulations in the absence of grazing flow showed good agreement with the reference data. The minimum resolution of 20 elements across the diameter of the liners' orifices was considered proper for the simulations in this scenario. The non-linear effects of high sound pressure level acoustic waves were captured by the numerical model. The different impedance measurement techniques delivered slightly divergent values, especially in the high sound pressure level non-linear regime, both in the experiments and in the simulations.

In the presence of grazing flow, the numerical results presented fair agreement with the reference data in terms of the resistance, and a reasonable agreement in terms of the reactance. Specifically, the resistance was quite overestimated by the simulations, and in some cases a good match was observed with the semiempirical predictions, but not with the experiments. Nonetheless, the model was able to capture the general trends observed in the experiments in terms of impedance, and that includes the resistance part.

In general, the non-linear effect of the grazing flow acts to increase the resistance, which was reproduced in the numerical results. For these cases, a maximum resolution of 50 elements per orifice diameter was adopted, but the results suggested that a higher resolution is necessary to correctly capture the dissipative effects associated with the resistance.

Several parameters from the numerical model were investigated as an attempt to improve the agreement between the results from the simulations and the experiments. The most important features were found to be the resolution of the grid, the use of an alternative solver (more adequate for acoustic simulations) and, particularly, the proper representation of the orifice profiles in the model. The impedance results were found to be

very sensitive to the orifice shape, and a significant drop in the resistance was observed for a liner with rounded orifice edges. In this work, no detailed assessment of the orifice shapes in the real samples was performed, which compromised a trustful conclusion regarding this particular effect. However, it was possible to conclude that the agreement of the numerical results could significantly improve if the orifice shapes of the real liner were replicated in the model.

Furthermore, the simulations were capable of capturing different impedance measurements in the presence of grazing flow when the position of the acoustic source changed, with respect to the sample. Typically, higher resistance was found for downstream sources in the experiments, and this trend was also observed in the numerical results.

From the numerical model, some aspects regarding the flow-acoustic interactions were observed, such as the variation of the impedance measured along the facesheet, the effect of a grazing turbulent boundary layer on the acoustic-induced flow within the liner's orifices and the discharge coefficient in each scenario. These observations were performed considering different acoustic source positions, in order to assess any potential cause for the impedance upstream-downstream mismatch.

It was observed that the measured impedance varies significantly along the liner's facesheet, even in the absence of grazing flow. The variation of the impedance happens not only between cavities, but within a single cavity. This effect was found to be frequency dependent, and it was confirmed by the experiments. In the presence of grazing flow, a considerable influence of the orifice near-wake was verified, and typical resistance values were found to be higher downstream from the orifices. Interestingly, a dependence on the acoustic source's position was found in the reactance results, which tend to be higher upstream from the orifices, for an upstream source, and lower, for a downstream source. These results were also confirmed experimentally.

The assessment of the acoustic-induced flows within the orifices revealed that the key parameter from the impedance point of view, in the presence of grazing flow, is the effective open area in which the flow oscillations take place. This area is a function of the turbulent boundary layer parameters and of the sound pressure level of the incident acoustic wave. The grazing turbulent boundary layer generates a recirculation region inside the liner's orifices, i.e., a vortex. The presence of this vortex acts to reduce the area in which the acoustic-induced oscillations happen, likely due to inertial effects of the flow. Consequently, typical resistance measurements are considerably higher in this scenario.

Generally, the resistance measured in the absence of grazing flow is proportional to the acoustic-induced velocity inside the orifices, which is a frequency dependent parameter, also directly related to the sound pressure level. However, with the presence of the vortex, a higher sound pressure level acts to reduce the overall resistance, as the higher acoustic particle velocities are able to overcome the inertial effects of the mean flow and to push the acoustic-induced flow through a larger portion of the vortex. Furthermore, in the presence of grazing flow, the acoustic-induced flow inside the orifices was found to be considerably less sensitive to the frequency of the incident acoustic waves. From these observations, no considerable difference was found in the in-orifice flow when changing the position of the acoustic source.

The analysis of the discharge coefficient allowed for a quantitative estimate of the flow rate induced by the acoustics through the liner's orifices. A frequency dependence of the discharge coefficient was found in the absence of grazing flow. Conversely, the presence of grazing flow eliminates this dependence. The discharge coefficient calculated in the presence of grazing flow was found to be significantly smaller than that obtained when the grazing flow was absent. Once again, no considerable difference was found in these results when changing the position of the acoustic source.

6.1 FUTURE WORKS

In this section, some possibilities to continue the study of acoustic liners with high-fidelity simulations are provided:

- To perform simulations with a broadband acoustic source, which would allow for the impedance assessment in a wide range of frequencies with relative low computational cost;
- To simulate a longer liner, such that the effects of small sample lengths for low frequencies are mitigated;
- To improve the method of imposing the acoustic source in the simulation domain, such that the length of the channel can be reduced and the simulation time enhanced;
- To assess the effects of different turbulent boundary layers on the liner's in-orifice flow profiles, and;

- To simulate a properly characterized real liner in terms of its orifice shapes.

BIBLIOGRAPHY

- AURÉGAN, Y.; STAROBINSKI, R.; PAGNEUX, V. Influence of grazing flow and dissipation effects on the acoustic boundary conditions at a lined wall. **The Journal of the Acoustical Society of America**, Acoustical Society of America (ASA), v. 109, p. 59–64, 1 Jan. 2001. DOI: [10.1121/1.1331678](https://doi.org/10.1121/1.1331678). Cit. on p. 40.
- AVALLONE, F.; DAMIANO, C. Acoustic-induced velocity in a multi-orifice acoustic liner grazed by a turbulent boundary layer. **AIAA Aviation Forum**, 2021. DOI: [10.2514/6.2021-2169](https://doi.org/10.2514/6.2021-2169). Cit. on pp. 48, 52, 53, 64, 74, 79, 81, 106, 114, 134, 136.
- AVALLONE, F.; MANJUNATH, P.; RAGNI, D.; CASALINO, D. Lattice-boltzmann very large eddy simulation of a multi-orifice acoustic liner with turbulent grazing flow. **25th AIAA/CEAS Aeroacoustics Conference**, 2019. DOI: [10.2514/6.2019-2542](https://doi.org/10.2514/6.2019-2542). Cit. on pp. 30, 52, 74, 77, 90, 91, 105, 114.
- BAKE, F.; KNOBLOCH, K. Novel liner concepts. **CEAS Aeronautical Journal**, Springer-Verlag Wien, v. 10, p. 123–136, 1 Mar. 2019. DOI: [10.1007/s13272-019-00380-7](https://doi.org/10.1007/s13272-019-00380-7). Cit. on p. 29.
- BERTSCH, L.; SNELLEN, M.; ENGHARDT, L.; HILLENHERMS, C. Aircraft noise generation and assessment: executive summary. **CEAS Aeronautical Journal**, v. 10, p. 3–9, 2019. DOI: [10.1007/s13272-019-00384-3](https://doi.org/10.1007/s13272-019-00384-3). Cit. on p. 27.
- BHATNAGAR, P. L.; GROSS, E. P.; KROOK, M. A Model for Collision Processes in Gases. I. Small Amplitude Processes in Charged and Neutral One-Component Systems. **Physical Review**, American Physical Society, v. 94, p. 511, 3 May 1954. DOI: [10.1103/PhysRev.94.511](https://doi.org/10.1103/PhysRev.94.511). Cit. on p. 70.
- BODEN, H.; CORDIOLI, J. A.; SPILLERE, A.; SERRANO, P. Comparison of the effect of flow direction on liner impedance using different measurement methods. **23rd AIAA/CEAS Aeroacoustics Conference**, 2017. DOI: [10.2514/6.2017-3184](https://doi.org/10.2514/6.2017-3184). Cit. on pp. 30, 40, 41, 96.
- BONOMO, L. A.; QUINTINO, N. T.; CORDIOLI, J. A., et al. A Comparison of Impedance Education Test Rigs with Different Flow Profiles. **AIAA Aviation Forum**, 2023. DOI: [10.2514/6.2023-3346](https://doi.org/10.2514/6.2023-3346). Cit. on pp. 113, 121.

- BONOMO, L. A.; QUINTINO, N. T.; SPILLERE, A.; CORDIOLI, J. A.; MURRAY, P. B. A Comparison of In-Situ and Impedance Eduction Experimental Techniques for Acoustic Liners with Grazing Flow and High SPL. **28th AIAA/CEAS Aeroacoustics 2022 Conference**, 2022. DOI: [10.2514/6.2022-2998](https://doi.org/10.2514/6.2022-2998). Cit. on pp. [29](#), [30](#), [36](#), [38](#), [41](#), [46](#), [57](#), [63](#), [64](#), [92](#), [107](#), [121](#).
- BONOMO, L. A.; SPILLERE, A. M. N.; CORDIOLI, J. A. Parametric Uncertainty Analysis for Impedance Eduction Based on Prony's Method. **AIAA Journal**, v. 58, n. 8, p. 3625–3638, 2020. DOI: [10.2514/1.J059071](https://doi.org/10.2514/1.J059071). Cit. on pp. [61](#), [159](#).
- BONOMO, L. A. **Análises de Incertezas e de Sensibilidade Global para Educação de Impedância Acústica**. 2021. S. 127. Mestrado em Engenharia Mecânica – Universidade Federal de Santa Catarina, Florianópolis. Cit. on pp. [28](#), [29](#), [57](#), [58](#).
- BRAMBLEY, E. J. Well-Posed Boundary Condition for Acoustic Liners in Straight Ducts with Flow. **AIAA Journal**, v. 49, n. 6, p. 1272–1282, 2011. DOI: [10.2514/1.J050723](https://doi.org/10.2514/1.J050723). Cit. on pp. [40](#), [160](#).
- CASALINO, D.; DIOZZI, F.; SANNINO, R.; PAONESSA, A. Aircraft noise reduction technologies: A bibliographic review. **Aerospace Science and Technology**, Elsevier Masson, v. 12, p. 1–17, 1 Jan. 2008. DOI: [10.1016/J.AST.2007.10.004](https://doi.org/10.1016/J.AST.2007.10.004). Cit. on p. [28](#).
- CASALINO, D.; HAZIR, A.; MANN, A. Turbofan broadband noise prediction using the lattice boltzmann method. **AIAA Journal**, American Institute of Aeronautics and Astronautics Inc., v. 56, p. 609–628, 2 2018. DOI: [10.2514/1.J055674](https://doi.org/10.2514/1.J055674). Cit. on p. [70](#).
- CHEN, H.; FILIPPOVA, O., et al. Grid refinement in lattice Boltzmann methods based on volumetric formulation. **Physica A: Statistical Mechanics and its Applications**, v. 362, n. 1, p. 158–167, 2006. DOI: [10.1016/j.physa.2005.09.0](https://doi.org/10.1016/j.physa.2005.09.0). Cit. on p. [73](#).
- CHEN, H.; CHEN, S.; MATTHAEUS, W. Recovery of the Navier-Stokes Equations Using a Lattice-Gas Boltzmann Method. **Physical Review A**, v. 45, May 1992. DOI: [10.1103/PhysRevA.45.R5339](https://doi.org/10.1103/PhysRevA.45.R5339). Cit. on p. [72](#).
- DAI, X.; AURÉGAN, Y. Acoustic of a perforated liner with grazing flow: Floquet-Bloch periodical approach versus impedance continuous approach. **The Journal of the Acoustical Society of America**, v. 140, p. 2047, 2016. DOI: [10.1121/1.4962490](https://doi.org/10.1121/1.4962490). Cit. on p. [40](#).

DASSAULT SYSTÈMES. **PowerFLOW 2021 User's Guide**. English. Version 2021 Refresh2, 2021. 90 pp. Cit. on p. 85.

DASSAULT SYSTÈMES. **PowerFLOW 2022 User's Guide**. English. Version 2022 Refresh1, 2022. 108 pp. Cit. on p. 98.

DASSAULT SYSTÈMES. **PowerFLOW 2022 User's Guide: PowerCASE User's Guide**. Version 2022 Refresh1, 2022. 709 pp. Cit. on p. 114.

DEAN, P. D. An in situ method of wall acoustic impedance measurement in flow ducts. **Journal of Sound and Vibration**, Academic Press, v. 34, 97–in6, 1 May 1974. DOI: [10.1016/S0022-460X\(74\)80357-3](https://doi.org/10.1016/S0022-460X(74)80357-3). Cit. on pp. 29, 38, 39, 56–58, 92.

ELNADY, T.; BODÉN, H.; ELHADIDI, B. Validation of an Inverse Semi-Analytical Technique to Educe Liner Impedance. **AIAA Journal**, v. 47, n. 12, p. 2836–2844, 2009. DOI: [10.2514/1.41647](https://doi.org/10.2514/1.41647). Cit. on pp. 29, 38, 39, 58, 159.

ELNADY, T.; BODÉN, H. An Inverse Analytical Method for Extracting Liner Impedance from Pressure Measurements. **10th AIAA/CEAS Aeroacoustics Conference**, 2004. DOI: [10.2514/6.2004-2836](https://doi.org/10.2514/6.2004-2836). Cit. on pp. 57, 58.

EVERSMAN, W. The Effect of Mach Number on the Tuning of an Acoustic Lining in a Flow Duct. **The Journal of the Acoustical Society of America**, v. 48, 2A, p. 425–428, 1970. DOI: [10.1121/1.1912148](https://doi.org/10.1121/1.1912148). Cit. on pp. 29, 36, 39, 56.

FERRANTE, P.; DE ROECK, W.; DESMET, W.; MAGNINO, N. Back-to-back comparison of impedance measurement techniques applied to the characterization of aero-engine nacelle acoustic liners. **Applied Acoustics**, v. 105, p. 129–142, 2016. DOI: <https://doi.org/10.1016/j.apacoust.2015.12.004>. Cit. on pp. 38, 58.

GABARD, G.; ASTLEY, R. A computational mode-matching approach for sound propagation in three-dimensional ducts with flow. **Journal of Sound and Vibration**, v. 315, n. 4, p. 1103–1124, 2008. DOI: <https://doi.org/10.1016/j.jsv.2008.02.015>. Cit. on p. 59.

GOLDSTEIN, S. Fluid mechanics in the first half of this century. **Annual Review of Fluid Mechanics**, Annual Reviews 4139 El Camino Way, PO Box 10139, Palo Alto, CA 94303-0139, USA, v. 1, n. 1, p. 1–29, 1969. Cit. on p. 7.

- GUESS, A. W. Calculation of perforated plate liner parameters from specified acoustic resistance and reactance. **Journal of Sound and Vibration**, Academic Press, v. 40, p. 119–137, 1 May 1975. DOI: [10.1016/S0022-460X\(75\)80234-3](https://doi.org/10.1016/S0022-460X(75)80234-3). Cit. on pp. 29, 36, 42.
- GUO, Z.; SHU, C. **Lattice Boltzmann method and its application in engineering**. Singapore, Singapore: World Scientific Publishing, May 2013. (Advances In Computational Fluid Dynamics). Cit. on pp. 68, 69.
- GUZMAN INIGO, J. G.; MORGANS, A. Influence of the Shape of a Short Circular Hole with Bias Flow on Its Acoustic Response. **28th AIAA/CEAS Aeroacoustics 2022 Conference**, American Institute of Aeronautics and Astronautics, Reston, Virginia, June 2022. DOI: [10.2514/6.2022-2997](https://doi.org/10.2514/6.2022-2997). Cit. on p. 116.
- GUZMÁN-IÑIGO, J.; YANG, D.; JOHNSON, H. G.; MORGANS, A. S. Sensitivity of the Acoustics of Short Circular Holes with Bias Flow to Inlet Edge Geometries, 2019. DOI: [10.2514/1.J057996](https://doi.org/10.2514/1.J057996). Cit. on p. 116.
- HERSH, A. S.; WALKER, B. E.; CELANO, J. W. Helmholtz Resonator Impedance Model, Part 1: Nonlinear Behavior. **AIAA Journal**, v. 41, n. 5, p. 795–808, 2003. DOI: [10.2514/2.2041](https://doi.org/10.2514/2.2041). Cit. on p. 52.
- HOCHMANN, D.; SADOK, M. Theory of synchronous averaging. In: 2004 IEEE Aerospace Conference Proceedings (IEEE Cat. No.04TH8720). 2004. v. 6, 3636–3653 vol.6. DOI: [10.1109/AERO.2004.1368181](https://doi.org/10.1109/AERO.2004.1368181). Cit. on p. 53.
- HOLMBERG, A.; ÅBOM, M.; BODÉN, H. Accurate experimental two-port analysis of flow generated sound. **Journal of Sound and Vibration**, v. 330, n. 26, p. 6336–6354, 2011. DOI: <https://doi.org/10.1016/j.jsv.2011.07.041>. Cit. on p. 59.
- HUANG, J. A Review of Stereolithography: Processes and Systems. **Processes**, v. 8, p. 1138, Sept. 2020. DOI: [10.3390/pr8091138](https://doi.org/10.3390/pr8091138). Cit. on p. 66.
- HUFF, D. L. **Noise Reduction Technologies for Turbofan Engines**. 2007. Cit. on p. 27.
- ICAO. In: 2019 Environmental Report: Aviation and Environment. 2019. Chapter two: Aircraft Noise. Cit. on p. 27.

INGARD, U. Influence of Fluid Motion Past a Plane Boundary on Sound Reflection, Absorption, and Transmission. **The Journal of the Acoustical Society of America**, Acoustical Society of America/ASA, v. 31, p. 1035–1036, 7 July 1959. DOI:

[10.1121/1.1907805](https://doi.org/10.1121/1.1907805). Cit. on pp. 40, 160.

INGARD, U. Nonlinear Distortion of Sound Transmitted through an Orifice. **J Acoust Soc Am**, v. 48, p. 32–33, 1970. DOI: [10.1121/1.1912106](https://doi.org/10.1121/1.1912106). Cit. on p. 138.

JI, C.; ZHAO, D.; HAN, N.; LI, J. Parametric Measurements of the Effect of In-Duct Orifice Edge Shape on Its Noise Damping Performance. **Journal of Sound and Vibration**, Academic Press, v. 384, p. 130–145, Dec. 2016. DOI:

[10.1016/J.JSV.2016.08.007](https://doi.org/10.1016/J.JSV.2016.08.007). Cit. on p. 116.

JING, X.; PENG, S.; SUN, X. A straightforward method for wall impedance education in a flow duct. **The Journal of the Acoustical Society of America**, Acoustical Society of America (ASA), v. 124, p. 227–234, 1 July 2008. DOI: [10.1121/1.2932256](https://doi.org/10.1121/1.2932256). Cit. on pp. 38, 39, 60, 61, 160.

JOHANSEN, F. C.; SOUTHWELL, R. V. Flow through pipe orifices at low Reynolds numbers. **Proceedings of the Royal Society of London. Series A, Containing Papers of a Mathematical and Physical Character**, v. 126, n. 801, p. 231–245, 1930. DOI: [10.1098/rspa.1930.0004](https://doi.org/10.1098/rspa.1930.0004). Cit. on p. 140.

JONES, M. G.; PARROTT, T. L.; WATSON, W. R. Comparison of acoustic impedance education techniques for locally-reacting liners. **9th AIAA/CEAS Aeroacoustics Conference and Exhibit**, 2003. DOI: [10.2514/6.2003-3306](https://doi.org/10.2514/6.2003-3306). Cit. on p. 39.

JONES, M. G.; WATSON, W. R.; PARROTT, T. L.; SMITH, C. D. Design and evaluation of modifications to the NASA Langley flow impedance tube. **10th AIAA/CEAS Aeroacoustics Conference**, v. 1, p. 451–463, 2004. DOI:

[10.2514/6.2004-2837](https://doi.org/10.2514/6.2004-2837). Cit. on pp. 38, 47, 52.

JONES, M.; WATSON, W. On the Use of Experimental Methods to Improve Confidence in Educated Impedance. **17th AIAA/CEAS Aeroacoustics Conference (32nd AIAA Aeroacoustics Conference)**, 2011. DOI: [10.2514/6.2011-2865](https://doi.org/10.2514/6.2011-2865). Cit. on pp. 29, 46.

JONES, M. G.; BROWN, M. C.; HOWERTON, B. M.; BECKER, L. E. Over-the-Rotor Liner Investigation via the NASA Langley Normal Incidence Tube, 2019. Cit. on p. 38.

JONES, M. G.; TRACY, M. B.; WATSON, W. R.; PARROTT, T. L. Effects of liner geometry on acoustic impedance. **8th AIAA/CEAS Aeroacoustics Conference and Exhibit**, American Institute of Aeronautics and Astronautics Inc., 2002. DOI: [10.2514/6.2002-2446](https://doi.org/10.2514/6.2002-2446). Cit. on pp. 29, 36.

KOOI, J.; SARIN, S. An experimental study of the acoustic impedance of Helmholtz resonator arrays under a turbulent boundary layer. **7th Aeroacoustics Conference**, 1981. DOI: [10.2514/6.1981-1998](https://doi.org/10.2514/6.1981-1998). Cit. on pp. 29, 36, 38, 39, 42, 64, 113.

KOTAPATI, R. et al. The Lattice-Boltzmann-VLES Method for Automotive Fluid Dynamics Simulation, a Review. In: SIAT 2009. The Automotive Research Association of India, Jan. 2009. DOI: <https://doi.org/10.4271/2009-26-0057>. Cit. on p. 74.

KRAFT, R. et al. Acoustic Treatment Impedance Models for High Frequencies. In: 3RD AIAA/CEAS Aeroacoustics Conference. American Institute of Aeronautics and Astronautics, May 1997. (Aeroacoustics Conferences). DOI: [10.2514/6.1997-1653](https://doi.org/10.2514/6.1997-1653). Cit. on pp. 42, 87.

KRÜGER, T. et al. **The Lattice Boltzmann Method**. Springer International Publishing, 2017. DOI: [10.1007/978-3-319-44649-3](https://doi.org/10.1007/978-3-319-44649-3). Cit. on pp. 46, 69–72.

KUMARESAN, R. On the zeros of the linear prediction-error filter for deterministic signals. **IEEE Transactions on Acoustics, Speech, and Signal Processing**, v. 31, n. 1, p. 217–220, 1983. DOI: [10.1109/TASSP.1983.1164021](https://doi.org/10.1109/TASSP.1983.1164021). Cit. on p. 61.

KUMARESAN, R.; TUFTS, D. Estimating the parameters of exponentially damped sinusoids and pole-zero modeling in noise. **IEEE Transactions on Acoustics, Speech, and Signal Processing**, v. 30, n. 6, p. 833–840, 1982. DOI: [10.1109/TASSP.1982.1163974](https://doi.org/10.1109/TASSP.1982.1163974). Cit. on p. 61.

KUNDU, P. K.; COHEN, I. M.; DOWLING, D. R. **Fluid Mechanics**. 6. ed.: Academic Press, 2015. Cit. on p. 65.

LAFONT, V.; MÉRY, F.; REULET, P.; SIMON, F. Surface temperature measurement of acoustic liners in the presence of grazing flow and thermal gradient. **Experiments in Fluids**, Springer Science and Business Media Deutschland GmbH, v. 62, 4 Apr. 2021. DOI: [10.1007/s00348-021-03184-w](https://doi.org/10.1007/s00348-021-03184-w). Cit. on p. 29.

LÉON, O.; MÉRY, F.; PIOT, E.; CONTE, C. Near-wall aerodynamic response of an acoustic liner to harmonic excitation with grazing flow. **Experiments in Fluids**, Springer Verlag, v. 60, 9 Sept. 2019. DOI: [10.1007/s00348-019-2791-5](https://doi.org/10.1007/s00348-019-2791-5). Cit. on pp. [29](#), [36](#), [38](#), [54](#), [134](#), [141](#).

LEVENBERG, K. A method for the solution of certain non-linear problems in least squares. **Quarterly of Applied Mathematics**, v. 2, p. 164–168, 1944. DOI: [10.1090/qam/10666](https://doi.org/10.1090/qam/10666). Cit. on p. [59](#).

LIGHTHILL, S. J. Acoustic streaming. **Journal of Sound and Vibration**, v. 61, n. 3, p. 391–418, 1978. DOI: [https://doi.org/10.1016/0022-460X\(78\)90388-7](https://doi.org/10.1016/0022-460X(78)90388-7). Cit. on p. [33](#).

MANJUNATH, P.; AVALLONE, F.; CASALINO, D.; RAGNI, D.; SNELLEN, M. Characterization of Liners using a Lattice-Boltzmann Solver. **2018 AIAA/CEAS Aeroacoustics Conference**, 2018. DOI: [10.2514/6.2018-4192](https://doi.org/10.2514/6.2018-4192). Cit. on pp. [46–48](#), [70](#), [74](#), [79](#), [96](#).

MANN, A.; PÉROT, F.; KIM, M. S.; CASALINO, D. Characterization of acoustic liners absorption using a lattice-Boltzmann method. In: p. 256. DOI: [10.2514/6.2013-2271](https://doi.org/10.2514/6.2013-2271). Cit. on pp. [46](#), [98](#).

MARQUARDT, D. W. An Algorithm for Least-Squares Estimation of Nonlinear Parameters. **Journal of the Society for Industrial and Applied Mathematics**, v. 11, n. 2, p. 431–441, 1963. DOI: [10.1137/0111030](https://doi.org/10.1137/0111030). Cit. on p. [59](#).

MELLING, T. The acoustic impedance of perforates at medium and high sound pressure levels. **Journal of Sound and Vibration**, v. 29, n. 1, p. 1–65, 1973. DOI: [https://doi.org/10.1016/S0022-460X\(73\)80125-7](https://doi.org/10.1016/S0022-460X(73)80125-7). Cit. on pp. [36](#), [38](#), [46](#), [52](#), [56](#), [87](#), [116](#), [138](#), [140](#).

MÉRY, F. et al. Experimental assessment of the effect of temperature gradient across an aeroacoustic liner. **Journal of Aircraft**, American Institute of Aeronautics and Astronautics Inc., v. 56, p. 1809–1821, 5 2019. DOI: [10.2514/1.C035157](https://doi.org/10.2514/1.C035157). Cit. on pp. [29](#), [36](#).

MORSE, P.; INGARD, K. **Theoretical Acoustics**. Princeton University Press, 1986. (International series in pure and applied physics). Cit. on p. [141](#).

MOTSINGER, R. E.; KRAFT, R. E. Aeroacoustics of Flight Vehicles: Theory and Practice. In: 1991. 2: Noise Control Design and Performance of Duct Acoustic Treatment. Cit. on pp. [33](#), [34](#), [36](#), [37](#), [42](#), [46](#), [58](#), [121](#), [138](#).

MURRAY, P.; DI GIULIO, M. Development and validation of a single degree of freedom perforate impedance model under high SPL and grazing flow. **28th AIAA/CEAS Aeroacoustics 2022 Conference**, American Institute of Aeronautics and Astronautics, June 2022. DOI: [10.2514/6.2022-2929](#). Cit. on p. [29](#).

MURRAY, P. B.; ASTLEY, R. J. Development of a single degree of freedom perforate impedance model under grazing flow and high SPL. **18th AIAA/CEAS Aeroacoustics Conference**, 2012. DOI: [10.2514/6.2012-2294](#). Cit. on pp. [29](#), [36](#).

MURRAY, P. B.; FERRANTE, P.; SCOFANO, A. Manufacturing process and boundary layer influences on perforate liner impedance. **Collection of Technical Papers - 11th AIAA/CEAS Aeroacoustics Conference**, v. 1, p. 647–663, 2005. DOI: [10.2514/6.2005-2849](#). Cit. on p. [115](#).

MYERS, M. On the acoustic boundary condition in the presence of flow. **Journal of Sound and Vibration**, v. 71, n. 3, p. 429–434, 1980. DOI: [10.1016/0022-460X\(80\)90424-1](#). Cit. on pp. [40](#), [160](#).

PARK, J. B.; MONGEAU, L. Instantaneous orifice discharge coefficient of a physical, driven model of the human larynx. **The Journal of the Acoustical Society of America**, v. 121, n. 1, p. 442–455, Jan. 2007. Publisher: AIP Publishing. DOI: [10.1121/1.2401652](#). Cit. on p. [138](#).

PEREIRA, L. M.; BONOMO, L. A.; QUINTINO, N. T., et al. Validation of High-Fidelity Numerical Simulations of Acoustic Liners Under Grazing Flow. **AIAA Aviation Forum**, 2023. DOI: [10.2514/6.2023-3503](#). Cit. on p. [98](#).

PEREIRA, L. M.; BONOMO, L. A.; SILVA, A. R. da; CORDIOLI, J. A.; AVALLONE, F. Lattice-Boltzmann Numerical Investigation of a Realistic Multi-Cavity Acoustic Liner with Grazing Flow Interactions. **28th AIAA/CEAS Aeroacoustics Conference**, 2022. DOI: [10.2514/6.2022-2967](#). Cit. on pp. [85](#), [98](#), [107](#), [123](#).

PIERCE, A. D. **Acoustics: An introduction to its physical principles and applications**. New York, NY: American Institute of Physics, Dec. 1989. Cit. on pp. [33](#), [34](#).

RANDALL, R. B. Vibration-based condition monitoring - industrial, automotive and aerospace applications, second edition. In: 2. ed. Hoboken, NJ: Wiley-Blackwell, June 2021. 5.3.1 Time Synchronous Averaging. Cit. on p. [53](#).

RENOU, Y.; AURÉGAN, Y. Failure of the Ingard–Myers boundary condition for a lined duct: An experimental investigation. **The Journal of the Acoustical Society of America**, Acoustical Society of America (ASA), v. 130, p. 52–60, 1 July 2011. DOI: [10.1121/1.3586789](#). Cit. on pp. [30](#), [34](#), [40](#), [94](#), [160](#).

RIENSTRA, S. W.; SINGH, D. K. Nonlinear Asymptotic Impedance Model for a Helmholtz Resonator of Finite Depth. **AIAA Journal**, American Institute of Aeronautics and Astronautics (AIAA), v. 56, n. 5, p. 1792–1802, May 2018. DOI: [10.2514/1.j055882](#). Cit. on p. [36](#).

ROLLS-ROYCE LTD. The jet engine. In: 5. ed.: Rolls Royce Technical Publications Department, 1996. Chapter 19: Noise suppression. Cit. on p. [28](#).

RONCEN, R. et al. Wavenumber-Based Impedance Eduction with a Shear Grazing Flow. **AIAA Journal**, v. 58, n. 7, p. 3040–3050, 2020. DOI: [10.2514/1.J059100](#). Cit. on p. [41](#).

SCHLICHTING, H.; GERSTEN, K. Internal Flows. In: BOUNDARY-LAYER Theory. Berlin, Heidelberg: Springer Berlin Heidelberg, 2017. P. 519–556. Cit. on pp. [65](#), [66](#), [89](#), [104](#), [105](#).

SCHROEDER, L. **Análise do tratamento acústico de motores aeronáuticos utilizando o método de lattice-Boltzmann**. 2020. S. 80. Trabalho de Conclusão de Curso - Graduação em Engenharia Mecânica – Universidade Federal de Santa Catarina, Florianópolis. Cit. on p. [77](#).

SCHROEDER, L. et al. Numerical Investigation of Acoustic Liners Experimental Techniques using a Lattice-Boltzmann Solver. **AIAA Aviation Forum**, American Institute of Aeronautics and Astronautics (AIAA), Aug. 2021. DOI: [10.2514/6.2021-2144](#). Cit. on pp. [30](#), [46–49](#), [58](#), [74](#), [75](#), [77](#), [79](#), [85](#), [88](#), [96](#), [121](#), [123](#).

SCIPY v1.9.0 Manual. 2022. Optimization and root finding (scipy.optimize). Cit. on p. [59](#).

SHAN, X.; YUAN, X. F.; CHEN, H. Kinetic theory representation of hydrodynamics: a way beyond the Navier–Stokes equation. **Journal of Fluid Mechanics**, Cambridge University Press, v. 550, p. 413–441, 2006. DOI: [10.1017/S0022112005008153](https://doi.org/10.1017/S0022112005008153). Cit. on p. 70.

SILVA, A. R. da; GRECO, G. F. Computational investigation of plane wave reflections at the open end of subsonic intakes. **Journal of Sound and Vibration**, Academic Press, v. 446, p. 412–428, Apr. 2019. DOI: [10.1016/j.jsv.2019.01.044](https://doi.org/10.1016/j.jsv.2019.01.044). Cit. on pp. 70–72, 74.

SINGH, D. K.; RIENSTRA, S. W. Nonlinear asymptotic impedance model for a Helmholtz resonator liner. **Journal of Sound and Vibration**, v. 333, n. 15, p. 3536–3549, 2014. DOI: <https://doi.org/10.1016/j.jsv.2014.03.013>. Cit. on p. 52.

SMITH, M. J. T. Aircraft Noise. In: Cambridge University Press, 1989. Chapter 4: Power-plant noise control. (Cambridge Aerospace Series). DOI: [10.1017/CB09780511584527](https://doi.org/10.1017/CB09780511584527). Cit. on pp. 27, 28, 33, 36, 67.

SPARROW, V. et al. Aviation Noise Impacts White Paper: State of the Science 2019: Aviation Noise Impacts. In: ICAO Environmental Report-Aviation and Environment 2019. Sept. 2019. P. 44–61. Cit. on p. 27.

SPILLERE, A.; REIS, D.; CORDIOLI, J. A systematic review of semi-empirical acoustic liner models under grazing flow and high SPL. **The 22nd International Congress on Acoustics**, Sept. 2016. Cit. on p. 36.

SPILLERE, A. M.; BRAGA, D. S., et al. Design of a single degree of freedom acoustic liner for a fan noise test rig. **International Journal of Aeroacoustics**, SAGE Publications Inc., v. 20, p. 708–736, 5-7 Sept. 2021. DOI: [10.1177/1475472X211023831](https://doi.org/10.1177/1475472X211023831). Cit. on pp. 38, 47, 48, 64, 66, 67, 87, 92, 96.

SPILLERE, A. M.; MEDEIROS, A. A.; CORDIOLI, J. A. An improved impedance education technique based on impedance models and the mode matching method. **Applied Acoustics**, v. 129, p. 322–334, 2018. DOI: <https://doi.org/10.1016/j.apacoust.2017.08.014>. Cit. on pp. 38, 59, 159.

SPILLERE, A. M. N. **Towards Optimal Design of Acoustic Liners in Turbofan Aero-Engines**. 2017. S. 160. Mestrado em Engenharia Mecânica – Universidade Federal de Santa Catarina, Florianópolis. Cit. on pp. 34, 35, 42, 43, 138.

- SPILLERE, A. M. N.; BONOMO, L. A.; CORDIOLI, J. A.; BRAMBLEY, E. J. Experimentally testing impedance boundary conditions for acoustic liners with flow: Beyond upstream and downstream. **Journal of Sound and Vibration**, Academic Press, v. 489, Dec. 2020. DOI: [10.1016/j.jsv.2020.115676](https://doi.org/10.1016/j.jsv.2020.115676). Cit. on pp. [40](#), [58](#), [59](#), [63](#), [94](#), [159](#), [160](#).
- SUCCI, S. **The Lattice Boltzmann Equation for Fluid Dynamics and Beyond**. 1. ed.: Clarendon Press, 2001. P. 304. Cit. on p. [69](#).
- TAM, C. K.; JU, H.; JONES, M. G.; WATSON, W. R.; PARROTT, T. L. A computational and experimental study of slit resonators. **Journal of Sound and Vibration**, Academic Press, v. 284, p. 947–984, 3-5 June 2005. DOI: [10.1016/j.jsv.2004.07.013](https://doi.org/10.1016/j.jsv.2004.07.013). Cit. on pp. [45](#), [48](#).
- TAM, C. K.; KURBATSKII, K. A.; AHUJA, K. K.; GAETA, R. J. A numerical and experimental investigation of the dissipation mechanisms of resonant acoustic liners. **Journal of Sound and Vibration**, Academic Press, v. 245, p. 545–557, 3 Aug. 2001. DOI: [10.1006/jsvi.2001.3571](https://doi.org/10.1006/jsvi.2001.3571). Cit. on pp. [38](#), [45](#).
- TAM, C. K. W.; KURBATSKII, K. A. Microfluid Dynamics and Acoustics of Resonant Liners. **AIAA Journal**, v. 38, n. 8, p. 1331–1339, 2000. DOI: [10.2514/2.1132](https://doi.org/10.2514/2.1132). Cit. on pp. [44](#), [45](#), [48](#), [138](#).
- TAM, C. K.; JU, H.; JONES, M. G.; WATSON, W. R.; PARROTT, T. L. A computational and experimental study of resonators in three dimensions. **Journal of Sound and Vibration**, v. 329, p. 5164–5193, 24 Nov. 2010. DOI: [10.1016/j.jsv.2010.06.005](https://doi.org/10.1016/j.jsv.2010.06.005). Cit. on pp. [45](#), [46](#).
- TAM, C. K.; JU, H.; WALKER, B. E. Numerical simulation of a slit resonator in a grazing flow under acoustic excitation. **Journal of Sound and Vibration**, Academic Press, v. 313, p. 449–471, 3-5 June 2008. DOI: [10.1016/j.jsv.2007.12.018](https://doi.org/10.1016/j.jsv.2007.12.018). Cit. on pp. [48](#), [90](#), [91](#).
- TAM, C. K.; PASTOUCHENKO, N. N.; JONES, M. G.; WATSON, W. R. Experimental validation of numerical simulations for an acoustic liner in grazing flow: Self-noise and added drag. **Journal of Sound and Vibration**, Academic Press, v. 333, p. 2831–2854, 2014. DOI: [10.1016/j.jsv.2014.02.019](https://doi.org/10.1016/j.jsv.2014.02.019). Cit. on pp. [30](#), [50](#).

TEIXEIRA, C. M. Incorporating Turbulence Models into the Lattice-Boltzmann Method. **International Journal of Modern Physics C**, v. 09, n. 08, p. 1159–1175, 1998. DOI: [10.1142/S0129183198001060](https://doi.org/10.1142/S0129183198001060). Cit. on p. 74.

TEMKIN, S. **Elements of Acoustics**. Nashville, TN: John Wiley & Sons, Apr. 1981. Cit. on pp. 35, 36.

WATSON, W.; JONES, M.; PARROTT, T. A Quasi-3-D Theory for Impedance Eduction in Uniform Grazing Flow. **11th AIAA/CEAS Aeroacoustics Conference**, 2005. DOI: [10.2514/6.2005-2848](https://doi.org/10.2514/6.2005-2848). Cit. on p. 50.

WATSON, W. R.; CARPENTER, M. H.; JONES, M. G. Performance of Kumaresan and Tufts Algorithm in Liner Impedance Eduction with Flow. **AIAA Journal**, American Institute of Aeronautics and Astronautics, v. 53, p. 1091–1102, 4 Feb. 2015. DOI: [10.2514/1.J053705](https://doi.org/10.2514/1.J053705). Cit. on pp. 29, 38, 61.

WENG, C.; SCHULZ, A.; RONNEBERGER, D.; ENGHARDT, L.; BAKE, F. Flow and Viscous Effects on Impedance Eduction. **AIAA Journal**, v. 56, n. 3, p. 1118–1132, 2018. DOI: [10.2514/1.J055838](https://doi.org/10.2514/1.J055838). Cit. on p. 40.

WINKLER, J.; MENDOZA, J. M.; REIMANN, C. A.; HOMMA, K.; ALONSO, J. S. High fidelity modeling tools for engine liner design and screening of advanced concepts. **International Journal of Aeroacoustics**, v. 20, n. 5-7, p. 530–560, 2021. DOI: [10.1177/1475472X211023884](https://doi.org/10.1177/1475472X211023884). Cit. on p. 44.

WOLF-GLADROW, D. A. **Lattice-gas cellular automata and lattice Boltzmann models**. 2000. ed. New York, NY: Springer, Sept. 2006. (Lecture notes in mathematics). Cit. on p. 71.

YAKHOT, V.; ORSZAG, S. A. Renormalization group analysis of turbulence. I. Basic theory. **Journal of Scientific Computing**, Springer Science and Business Media LLC, v. 1, n. 1, p. 3–51, 1986. DOI: [10.1007/bf01061452](https://doi.org/10.1007/bf01061452). Cit. on p. 74.

YU, J.; RUIZ, M.; KWAN, H. W. Validation of Goodrich perforate liner impedance model using NASA langley test data. **14th AIAA/CEAS Aeroacoustics Conference**, 2008. DOI: [10.2514/6.2008-2930](https://doi.org/10.2514/6.2008-2930). Cit. on pp. 36, 42, 48, 49, 87.

ZHANG, Q.; BODONY, D. J. Numerical investigation and modelling of acoustically excited flow through a circular orifice backed by a hexagonal cavity. **Journal of Fluid Mechanics**, Cambridge University Press, v. 693, p. 367–401, 2012. DOI:

[10.1017/jfm.2011.537](https://doi.org/10.1017/jfm.2011.537). Cit. on pp. 48, 138, 139.

ZHANG, Q.; BODONY, D. J. Numerical investigation of a honeycomb liner grazed by laminar and turbulent boundary layers. **Journal of Fluid Mechanics**, Cambridge University Press, v. 792, p. 936–980, Mar. 2016. DOI: [10.1017/jfm.2016.79](https://doi.org/10.1017/jfm.2016.79). Cit. on

pp. 30, 47, 51, 54, 90, 92, 105, 106, 134, 141.

ZHANG, Q.; BODONY, D. J. Numerical simulation of two-dimensional acoustic liners with high-speed grazing flow. **AIAA Journal**, v. 49, p. 365–382, 2 Feb. 2011. DOI:

[10.2514/1.J050597](https://doi.org/10.2514/1.J050597). Cit. on pp. 49, 50.

ZHOU, L.; BODÉN, H. A systematic uncertainty analysis for liner impedance reduction technology. **Journal of Sound and Vibration**, v. 356, p. 86–99, 2015. DOI:

<https://doi.org/10.1016/j.jsv.2015.07.001>. Cit. on p. 58.

ZINN, B. T. A theoretical study of non-linear damping by helmholtz resonators. **Journal of Sound and Vibration**, v. 13, n. 3, p. 347–356, 1970. DOI:

[10.1016/S0022-460X\(70\)80023-2](https://doi.org/10.1016/S0022-460X(70)80023-2). Cit. on p. 138.

APPENDIX A – TWO-DIMENSIONAL DUCT ACOUSTIC PROPAGATION MODEL WITH LINERS

Considering a rectangular cross sectional duct, we take a streamwise slice to represent the two-dimensional duct acoustic propagation model, as shown in Figure A.1. The duct is divided into three sections: section (1) is the rigid-walled region bounded by streamwise coordinates $x = x_0$ and $x = x_1$; section (2) is bounded by $x = x_1$ and $x = x_2$ with an acoustic liner; section (3) is the rigid-walled region bounded by $x = x_2$ and $x = x_3$. Uniform inviscid grazing flow is assumed in the positive x coordinate direction (ELNADY; BODÉN; ELHADIDI, 2009).

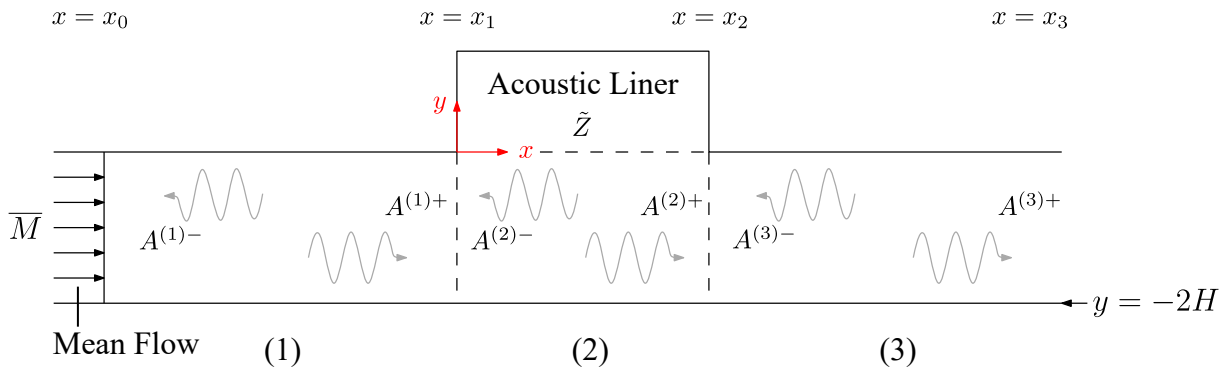


Figure A.1 – Two-dimensional model of the duct acoustic field.

Considering acoustic modes in the form $\tilde{p}(y)e^{i(\omega t \pm kx)}$, the propagation inside the duct is governed by the linear convective Helmholtz equation (BONOMO; SPILLERE, et al., 2020; SPILLERE; BONOMO, et al., 2020):

$$\left(ik + \overline{M} \frac{\partial}{\partial x}\right)^2 \tilde{p} - \frac{\partial^2 \tilde{p}}{\partial x^2} - \frac{\partial^2 \tilde{p}}{\partial y^2} = 0. \quad (\text{A.1})$$

Equation A.1 has an infinite number of solutions, which must satisfy the boundary conditions of the system. Each solution represents a transverse mode of order m that propagates only above its cut-on frequency, given by

$$f_c = \frac{mc_0}{4H} \sqrt{1 \mp \overline{M}^2}, \quad (\text{A.2})$$

for downstream and upstream propagation, respectively (SPILLERE; MEDEIROS, et al., 2018). Numerically, finite difference schemes can be applied to solve Equation A.1. Details on this procedure are discussed by Spillere, Bonomo, et al. (2020).

The solution for Equation A.1 is given by the sum of infinite modes which propagate in both x directions, in the form

$$\tilde{p}(x, y) = \sum_{m=1}^{\infty} \left(A_m^{(j)+} \psi_m^{(j)+}(y) e^{-i\zeta_m^{(j)+} x} + A_m^{(j)-} \psi_m^{(j)-}(y) e^{-i\zeta_m^{(j)-} x} \right). \quad (\text{A.3})$$

In Equation A.3, index $j = 1, 2, 3$ refer to the duct sections. The axial modes ζ_m^+ propagate in the positive x direction with amplitude A_m^+ . Similarly, axial modes ζ_m^- propagate in the negative x direction with amplitude A_m^- . The respective modal shapes are represented by ψ_m^\pm .

The parameters $\zeta_m^{(j)\pm}$ and $\psi_m^{(j)\pm}$ are determined by applying suitable boundary conditions to each one of the duct's sections. On the rigid walls, the acoustic particle velocity vanishes, that is,

$$\frac{\partial \tilde{p}}{\partial y} = 0. \quad (\text{A.4})$$

On the lined wall, impedance \tilde{Z} must be taken into account. However, in the presence of grazing flow the \tilde{Z} perceived by the acoustic field changes, represented by an effective \tilde{Z}_{eff} (SPILLERE; BONOMO, et al., 2020). The relation between \tilde{Z} and \tilde{Z}_{eff} can be modelled by different approaches (INGARD, 1959; BRAMBLEY, 2011; RENO; AURÉGAN, 2011). A classical relation is given by Ingard (1959), later modified by Myers (1980). The Ingard-Myers boundary condition is defined by

$$\frac{\partial \tilde{p}}{\partial y} = \frac{1}{i\omega \tilde{Z}} \left(i\omega + \bar{M} \frac{\partial}{\partial x} \right)^2 \tilde{p}, \quad (\text{A.5})$$

whose application leads to the following eigenvalue problem, which explicitly relates \tilde{Z} and the wavenumbers measured in the lined section (JING et al., 2008):

$$\frac{ik}{\tilde{Z}} \left\{ \frac{1}{1 - \bar{M}^2} \left[1 \mp \bar{M} \sqrt{1 - \frac{1 - \bar{M}^2}{k^2} (\alpha_m^\pm)^2} \right] \right\}^2 = \alpha_m^\pm \tan(\alpha_m^\pm 2H), \quad (\text{A.6})$$

where α_m^\pm are the m -th transverse wavenumbers. The axial wavenumbers are related to the transverse wavenumbers by the dispersion relation (JING et al., 2008):

$$\zeta_m^\pm = \frac{-\bar{M}k \pm \sqrt{k^2 - (1 - \bar{M}^2) (\alpha_m^\pm)^2}}{1 - \bar{M}^2}. \quad (\text{A.7})$$

**APPENDIX B – CONTOUR PLOTS OF THE IN-ORIFICE
ACOUSTIC-INDUCED VELOCITY**

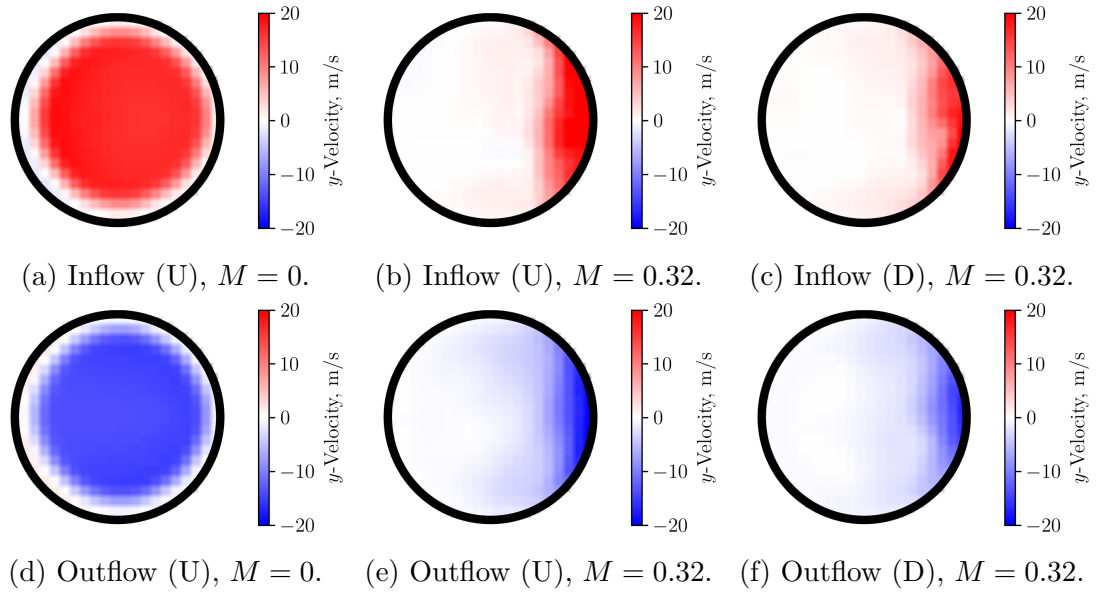


Figure B.1 – Contour plots of \bar{v} , assessed in the most upstream orifice located in the mid-span of the liner. Data refers to a 800 Hz acoustic source at 145 dB. Upstream (U) and downstream (D) acoustic sources.

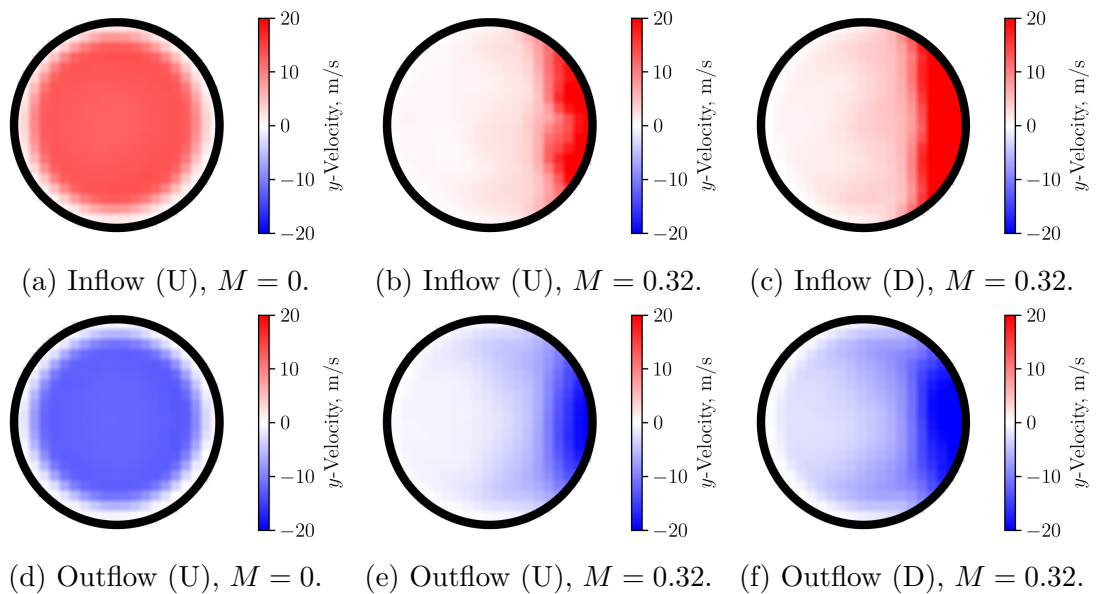


Figure B.2 – Contour plots of \bar{v} , assessed in the most downstream orifice located in the mid-span of the liner. Data refers to a 800 Hz acoustic source at 145 dB. Upstream (U) and downstream (D) acoustic sources.

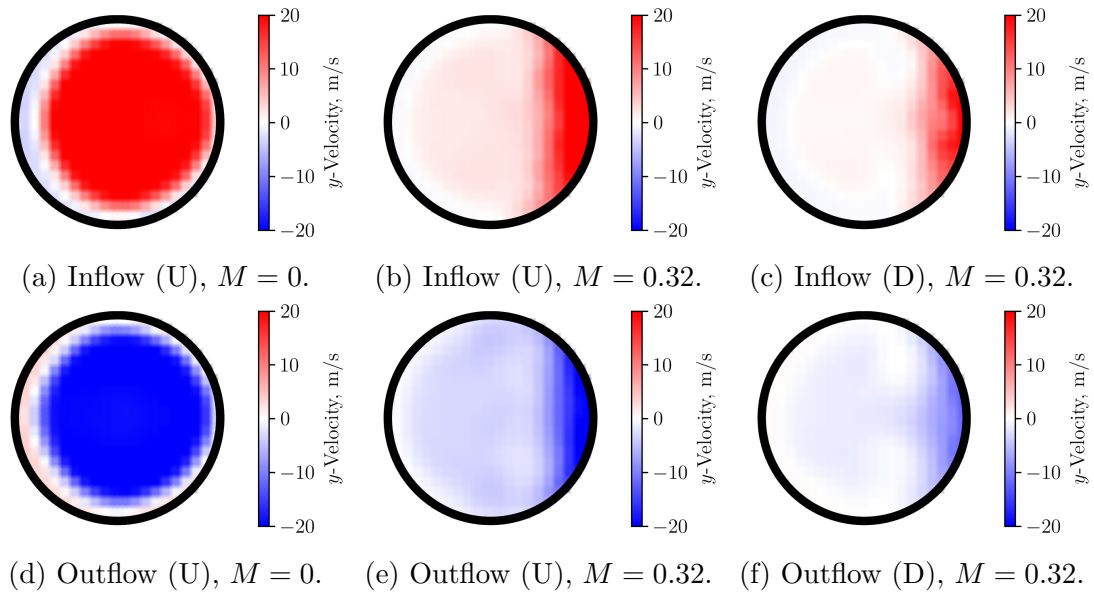


Figure B.3 – Contour plots of \bar{v} , assessed in the most upstream orifice located in the mid-span of the liner. Data refers to a 2000 Hz acoustic source at 145 dB. Upstream (U) and downstream (D) acoustic sources.

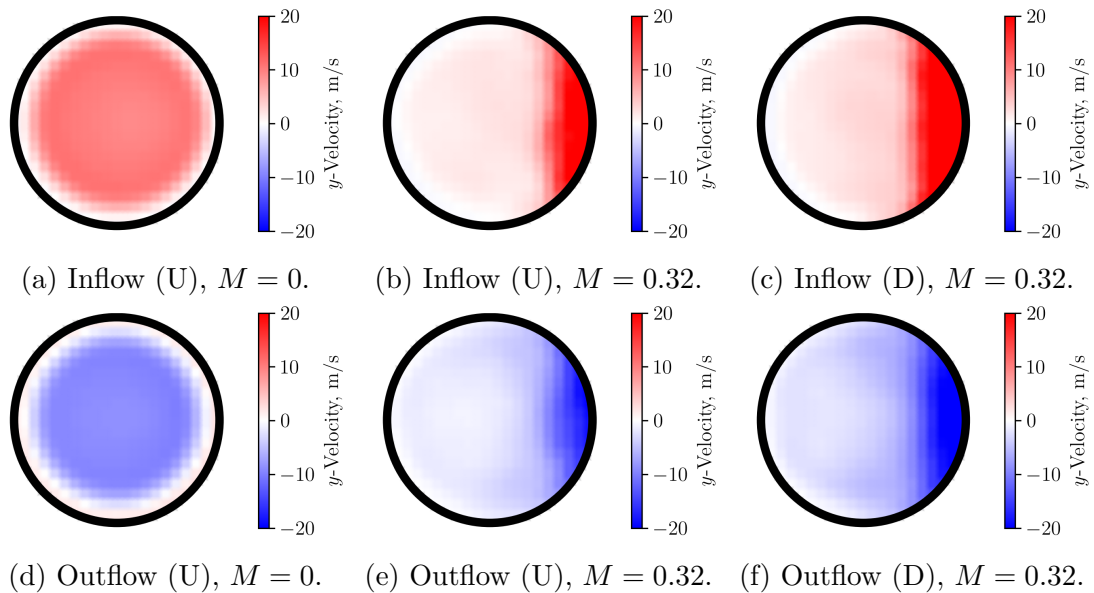


Figure B.4 – Contour plots of \bar{v} , assessed in the most downstream orifice located in the mid-span of the liner. Data refers to a 2000 Hz acoustic source at 145 dB. Upstream (U) and downstream (D) acoustic sources.